



UNIVERSITY OF
LIVERPOOL

BIOMECHANICS AND BIOCHEMISTRY OF THE AORTA IN CHRONIC AORTIC DISSECTION

Thesis submitted in accordance with the requirements of
the University of Liverpool for the degree of Doctor of Philosophy by

Phakakorn Panpho

March 2021

Acknowledgements

Firstly, I would like to thank to Ministry of Higher Education Science, Research and Innovation (MHESI) and Pibulsongkram Rajabhat University (PSRU), Thailand for granting me the scholarship to undertake this PhD programme in University of Liverpool, UK, along with the Office of Educational Affairs, Royal Thai Embassy for being responsible for my academic life.

I would like to express my sincerest gratitude for support, understanding and encouragement received from Dr Riaz Akhtar, Dr Jill Madine and Mr. Mark Field through my PhD. I have undertaken this PhD project under their supervisions. Their unwavering contribution of time and knowledge into my project has been the greatest experience of my educational life.

I am extremely grateful for mental and physical support I have received from Dr Jill Madine who I know will always provide the utmost help whenever it is needed. This appreciation also goes to Dr Ya Hua Chim and Dr Hannah A. Davies.

My appreciation goes to Professor Ying Yang in Keele University for contribution and support with creep testing and Dr Kerstin Mader and Professor Chris Sammon in Sheffield Hallam University for the opportunity to benefit from her expertise in FTIR. They not only provide the help but they also were a major supplier of snack and coffee.

I was lucky to receive help from Dr Geraghty, Brendan who expertise in tensile testing and Dr Steve Barrett for his assistance in the image analysis. My sincere gratitude to

Mr Dave Atkinson and Mrs Angela Platt-Higgins for their kind support and assistance for my research in Liverpool.

I also would like to thank Ms Deborah Harrington, Mr Vipin Mehta, and Mr Manoj Kuduvalli, Sarah Shirley and all staffs in operation theatres at Liverpool Heart and Chest Hospital who have assisted during collecting the tissues. I are also grateful to Mr Omar Nawaytou and Mr Amer Hark (Liverpool Heart and Chest Hospital) for their assistance in interpreting the surgical data.

Living more than 5,000 miles away from home for four years would not have been as warm without the friendship of my colleagues at the University of Liverpool, past and present, for their support and advice. A very special thanks to Dr Zhuo Chang, Dr Zhuola, Dr Ahmed Kazaili, Dr Benjamin John Peek, Dr PK, Michael Ward and Martin Hossack. I would like to extend my special gratitude to Dr Suppanit Jarernsuk, our friends in Thailand and my Thai friends in Chaba Chaba Thai restaurant for their love and support.

Words cannot express how grateful I am for my family. A special thanks to my aunts (Por and Aeed) for all their supplier of Thai food. To my dear mother, thank you for her love, encouragement, patience and inspiration my mother has provided me. She instilled in me the belief that through hard work, anything is possible.

Thank you to you all.

BIOMECHANICS AND BIOCHEMISTRY OF THE AORTA IN CHRONIC AORTIC DISSECTION

Author: Phakakorn Panpho

Abstract

Chronic aortic dissection (AD) is defined as being one in which there is a tear which originates in aortic wall and has been present for more than 30 days. Chronic AD tends to be associated with a weakened aortic wall. Eventually the degenerated, weakened aortic wall may rupture. Although tensile or biaxial testing techniques have previously been used *in vitro* for biomechanical testing of AD tissues at the macro-scale, little is known about how localised changes in aortic structure and biomechanics contribute to progression of chronic AD. To find a way to address this challenge, the nanoindentation technique and ball indentation tests were used to investigate localised mechanical properties and time-dependent deformation behaviour respectively, of human aortic tissue samples from chronic AD patients.

Using ovine aortic tissue as a model, the utility of the nanoindentation technique and ball indentation methods were validated and optimised. The data were correlated with conventional uniaxial indentation testing. Further, the mechanical properties and

biochemical composition (collagen, elastin and GAG) were correlated across the entire aortic length.

The human tissue work characterised the biomechanics, biochemistry, and histology of the dissection flap (FP), true lumen outer wall (TL) and false lumen outer wall (FL) in chronic dissection. These micromechanical properties and biochemical properties were compared with clinical data (interval of index event to operation (IIEO) and aortic growth rate). The main outcome of this thesis was the demonstration of how structural properties of dissection tissues within the aortic wall alter with time. FP and TL are stiffer with the arrangement of elastin fibres being highly compact, long, and aligned, whereas the FL was more compliant with localised loss of elastic fibres and increased elastin fragmentation that correlated with IIEO. Overall, the findings of this thesis suggest that indications for surgery in chronic AD, which are currently based on aortic size, may be independent of features such as aetiology, aortic dimensions, and anatomical segment.

List of Publications and Conferences

Publications

Phakakorn Panpho, Brendan Geraghty, Ya Hua Chim, Hannah A. Davies, Mark L. Field, Jillian Madine, Riaz Akhtar, 'Macro- and Micro-mechanical Properties of the Ovine Aorta: Correlation with Regional Variations in Collagen, Elastin and Glycosaminoglycan Levels', Journal of the Artery Research, Vol. 25,

DOI: <https://doi.org/10.2991/artres.k.191114.003>; ISSN 1872-9312; eISSN 1876-4401

Conferences

P. Panpho, M. Field, J. Madine, R. Akhtar, 'regional variations in the micromechanical properties of the ovine aorta', the 24th Annual Conference of the Section of Bioengineering of the Royal Academy of Medicine, BinI2018, 2018, Ireland.

P. Panpho, M. Field, J. Madine, R. Akhtar, 'Correlation between regional variations in the micromechanical and biochemical properties of the ovine aorta', the 2018 World Congress of Biomechanics, WCB2018, 2018, Dublin, Ireland.

P. Panpho, M. Field, J. Madine, R. Akhtar, 'Regional variations in the micromechanical and biochemical properties of the ovine aorta', the 26th Northern Cardiovascular Research Group Meeting, Newcastle upon Tyne, UK.

P. Panpho, M. Field, J. Madine, R. Akhtar, 'Regional variations in the micromechanical and biochemical properties of the ovine aorta', The BioMedEng18 conference, BioMedEng18, 2018, London, UK. 'BHF travel awards'.

P. Panpho, M. Field, J. Madine, R. Akhtar, 'Regional variations in the micromechanical and biochemical properties of the ovine aorta', the ARTERY18 Conference, 2018, Guimarães, Portugal.

P. Panpho, Mader, K.T, Sammon C., Field, M., Madine, J., Akhtar, R. 'Infrared Imaging as a histopathological tool for aortic dissections', The Northern Vascular Biology Forum (NVBF 2019) Conference, 2019, Sheffield, U.K.

P. Panpho, M. Field, J. Madine, R. Akhtar, 'The mechanical properties of the ovine aorta at the macro- and micro- scale correlation with regional variations in collagen, elastin and glycosaminoglycan levels', The 14th international symposium in Biomechanics in Vascular Biology and Cardiovascular Disease, 2019, Imperial College London, UK. 'BHF travel awards'.

P. Panpho, M. Field, J. Madine, R. Akhtar, 'Regional variations of biomechanical properties of the ovine aorta at the macro- and micro- scale correlation with in collagen, elastin and glycosaminoglycan levels', The 27th Northern Cardiovascular Research Group Meeting, 2019, Leeds University, UK.

P. Panpho, M. Field, J. Madine, R. Akhtar, 'Mechanical properties of the ovine aorta: macro- to micro- scale correlation with regional variations in collagen, elastin and glycosaminoglycan levels', The BioMedEng19 conference, BioMedEng19, 2019, London, UK. 'BHF travel awards'.

P. Panpho, M. Field, J. Madine, R. Akhtar, 'Creep behaviour and biochemical data of chronic aortic dissection', The ARTERY19 Conference, 2019, Budapest, Hungary.

Structure of Thesis

This thesis is composed of seven main chapters:

Chapter 1 provides the purpose of this research, aims and objectives of this this thesis.

Chapter 2 provides comprehensive background information on aortic dissection, dissection flap morphology changes from the acute to the chronic phase, aortic anatomy, structure and components of the aorta, and biomechanical testing from the macroscopic to the nanoscopic length scales as well as the biomechanical and biochemical properties of the chronically dissected aorta.

Chapter 3 demonstrates sample preparation for ovine models and human chronic tissues and detailed experimental methods of nanoindentation testing, creep testing (time-dependent deformation), biochemical, histological analysis and FTIR.

Chapter 4 explores the mapping the biomechanical properties across the entire length of the ovine aorta at the macro scale (via uniaxial tensile testing) and micro scale (via nanoindentation). The mechanical property data are compared with collagen, elastin and GAG levels measured across the different regions.

Chapter 5 demonstrates the utility of the nanoindentation (which is explained in detail in Chapter 4) as a tool for characterising the properties of small-scale biological samples and the ball indentation for investigating the behaviour of dissection flap, true and false lumen changes with time-dependent deformation (creep). This chapter focusses on human tissues from chronic dissection patients and correlates these

properties with biochemical properties and histological analysis. This chapter also compares the biomechanical, biochemical properties with clinical data (interval of index event to operation (IIEO) and the growth rate).

Chapter 6 summarises the main key findings of this thesis and provides future work in this thesis.

Contribution of Authors

Authors contributing to this thesis include: Miss Phakakorn Panpho (PP), Dr Riaz Akhtar (RA), Dr Jillian Madine (JM), Dr Brendan Geraghty, (BG), Dr Steve Barrett (SB), Dr Ya Hua Chim (YHC) Dr Hannah A. Davies (HAD) and Angela Platt-Higgins (AP) from the University of Liverpool (UoL), UK; Dr Mark L. Field (MLF), Mr Omar Nawayto (ON) and Mr Amer Harky from (AH) Liverpool Heart Chest Hospital (LHCH), U.K.; Professor Ying Yang (YY) and Homayemem K.Weli (HKW) from Keele University (KU); Professor Chris Sammon (CS) and Dr Kerstin Mader (KM) from Sheffield Hallam University (SHU).

The uniaxial tensile testing collaborated with BG, nanoindentation testing collaborated with RA and biochemical assay (ovine aortic tissues) collaborated with JM, YHC and HAD in UoL shown in Chapter 4 was conducted in UoL. Some of work presented in this chapter has been published in the Journal of Artery Research in March 2019 (Panpho et al., 2019).

The ball indentation presented in Chapter 4 (ovine aortic tissues) and 5 (chronic AD tissues) was conducted in KU in collaboration with YY and HKW in KU.

The histological work presented in Chapter 4 and 5 was conducted in UoL in collaboration with AP in UoL.

The FTIR presented in Chapter 4 and 5 (animal tissues) and Chapter 5 (chronic AD tissues) was conducted in SHU in collaboration with CS and KM in SHU.

The work in image analysis using software Image SXM (Chapter 5) was conducted in collaboration with SB in UoL SB wrote the image analysis code and conducted the analysis.

The clinical data presented in Chpater5 was conducted in collaboration with MLF, ON and AH in LHCH.

Contents

Acknowledgements	ii
Abstract	iv
List of Publications and Conferences.....	vi
Publications.....	vi
Conferences	vi
Structure of Thesis	ix
Contribution of Authors	xi
List of Figures	xviii
List of Tables	xxxii
Abbreviation	xxxii
Chapter 1 Introduction	1
1.1 Motivation.....	2
1.2 Aims and Objectives.....	6
References	8
Chapter 2 Background and Literature Review.....	11
2.1 The Aorta: Anatomy, Structure and Composition	12
2.1.1 Aortic anatomy	12
2.1.2 The structure of the aortic wall	18
2.1.3 The components of the aorta	21
2.2 The definition of Aortic dissection.....	28

2.2.1 The classification systems for aortic dissection	29
2.3 Dissection Flap	34
2.4 Treatment of Aortic Dissection	35
2.5 Biomechanical properties of the aortic wall	36
2.6 Biomechanical testing <i>in vitro</i> across the length scale	39
2.6.1 Uniaxial tensile testing	39
2.6.2 Biaxial tensile testing	44
2.6.3 Nanoindentation Testing	45
2.7 The biomechanical and biochemical behaviours of aortic dissection	51
2.7.1 The biomechanical behaviours of aortic dissection	51
2.7.2 The biochemical behaviours of aortic dissection	53
2.8 Summary	56
References	58
Chapter 3 Materials and Methods.....	80
3.1 Materials	81
3.1.1 Ovine aortic tissue preparation	81
3.2.1 Human chronic AD tissue harvest and sample preparation	85
3.2 Methods	87
3.2.1 Biomechanical testing	87
3.2.2 Biochemical analysis	96
3.2.3 FTIR analysis	98

3.2.4 Histological analysis	99
3.2.5 Statistical analysis	103
References	105
Chapter 4 Macro- and micro mechanical properties of the ovine aorta: Correlation with regional variations in collagen, elastin and glycosaminoglycan Levels.....	108
4.1 Introduction	109
4.2 Results	111
4.2.1 Regional variations in the uniaxial behaviour of the ovine aorta.....	111
4.2.2 Micromechanical behaviour of ovine aortic tissue	113
4.2.3 Comparison of micromechanical and macromechanical behaviour	117
4.2.4 Creep behaviour (time-dependent deformation)	119
4.2.5 Biochemical analysis	122
4.2.6 FTIR analysis	125
4.3. Discussion.....	132
4.4. Limitations.....	137
4.5. Conclusions	137
References	139
Chapter 5 Micromechanical properties, time-dependent deformation and biochemical properties of chronic aortic dissection tissues	144
5.1 Introduction	145
5.2 Results	150

5.2.1 Patients and demographics	150
5.2.2 Biomechanical findings	152
5.2.3 Biochemical analysis	160
5.2.4 Histological analysis	162
5.2.5 FTIR analysis	167
5.2.6 Correlations of biomechanical data with clinical data	172
5.2.7 Correlations of biochemical data, histological findings with clinical data	176
5.3. Discussion.....	178
5.4. Limitations.....	182
5.5. Conclusions	183
References	184
Chapter 6 Summary of Findings, Conclusions and Future Work	189
6.1 Summary of findings	190
6.2 Conclusions	193
6.3 Future work.....	194
6.3.1 Micromechanical properties and biochemical properties across the layer of aortic wall.....	194
6.3.2 Characterisation of behaviours changes with time-dependent deformation at adventitial layer	195
6.3.3 Measurement of the specific of PGs/GAGs	195
6.3.4 Development of FTIR to quantify more chemical species	195

6.3.5. Quantifying of the inflammatory reactions and fibrosis	196
6.3.6 Characterisation of micromechanical behaviours and biochemical changes in patients with acute and sub-acute AD.....	196
6.3.7 Measurement of follow-up clinical data.....	196
References	197
Appendix A	198
Appendix B.....	209

List of Figures

Chapter 1

Figure 1.1 Schematic representation of aortic dissection: (A) The formation of the tear occurs in the intimal layer. (B) The cross section of aortic dissection with false lumen outer wall (FL), true lumen outer wall (TL) and dissection flap (FP) marked. (C) The Stanford classification.....	3
--	---

Chapter 2

Figure 2.1 Sketch of anatomical aorta in different sections: 1) aortic root, 2) ascending, 3) aortic arch 4) descending thoracic 5) abdominal aorta.	13
Figure 2.2 The normal anatomy of the aortic root. Adapted from Kirali and Günay (2017).....	14
Figure 2.3 The aortic arch. Figure adapted from Drake et al. (2009).	16
Figure 2.4 The anatomy of descending aorta along the spine cord: (A) The descending aorta spans from the fifth and twelfth thoracic vertebra (T5–T12) and (B) The abdominal aorta begins the first to fourth lumbar vertebra (L1-4). Figure adapted from Richardon et al. (2019).....	17
Figure 2.5 The layers and major components of the normal aortic wall: tunica intima, tunica media and tunica adventitia layer. Figure drawn by the author based on Britannica (2010).....	18

Figure 2.6 Schematic drawing of a medial lamellar unit (MLU) composed of paired elastic laminae with an embedded SMC, collagen and elastin fibres, as well as GAGs. Figure drawn by the author based on Humphrey (2013).	20
Figure 2.7 Collagen fibrils present a repeating banding pattern known as the D-period (~ 67 nm) which is formed by staggered parallel aligned collagen molecules (length = 300nm; diameter = 1.5 nm). Figure adapted from Sherman et al. (2015).	21
Figure 2.8 Schematic diagram of an elastic fibre assembled by the outer fibrillin microfibrillar mantle with characteristic repeating structures and inner amorphous crosslinked elastin. Adapted from Gasser (2017).	23
Figure 2.9 A schematic model of the proposed structure of a collection of proteoglycans. A typical proteoglycan monomer consists of a core protein which is attached to a variable number of glycosaminoglycans side chains. Glycosaminoglycans influence viscoelasticity and residual stress, which plays a significant role in arterial homeostasis and in correlation with aortic pathogenesis such as aortic aneurysm and dissection (Wight, 1989, Cherchi et al., 1990, Schriebl et al., 2015).	27
Figure 2.10 Schematic representation of aortic dissection: (A) The cross section of aortic dissection with FL, TL and FP marked. (B) The formation of tear occurs in the intimal layer in the majority of AD cases. (C) In some cases, blood enters the tear, flows through the dissection and re-enters the true lumen.	29
Figure 2.11 The DeBakey classification localisation. Adapted from Huh et al. (2013).	31
Figure 2.12 The Stanford classification. Adapted from Huh et al. (2013).	32
Figure 2.13 The classification systems of AD with signs of evolving dissections from classes 1-5. Class 1: classic AD with TL and FL without communicating between two	

lumina; class 2: intramural haemorrhage; class 3: ulceration of aortic plaque following plaque rupture; class 4: subtle or discrete AD with bulging of the aortic wall; class 5: traumatic AD. Figure adapted from Erbel et al. (2001).	33
Figure 2.14 CT image demonstrating the morphological change during the transition from acute to chronic dissection (a, b) Curly flaps are observed in acute phase (0-14 days) compared with (c) straight flap in chronic phase (after 12 months). Decreased flap motion over time is presented by two orange triangle head and flap straightening over time is represented by a green star. Adapted from Peterss et al. (2016).....	35
Figure 2.15 A schematic model of the main dominating stresses in the aortic wall: circumferential and axial stresses.....	36
Figure 2.16 Typical stress-stretch curve for the aortic wall with key points marked. The incremental elastic modulus (E_{inc}) is defined as the ratio between the change of applied force ($\Delta\sigma$) and the change in the elongation ($\Delta\epsilon$). The stress (σ) is the force applied (F) to tissue, divided by the cross-sectional area of tissue (A) and the strain (ϵ) is the ratio between the specimen stretch (ΔL) divided by the original length (L_0).	37
Figure 2.17 A schematic diagram showing (A) Typical tensile test specimen in the form of a rectangular strip or a dumb-bell or dog-bone shaped specimen and (B) Typical sample set up for uniaxial tensile testing. Samples are typically connected to notched mechanical clamps to protect against slipping of the sample.	40
Figure 2.18 Schematic demonstrating showing: (A) the process of nanoindentation testing and (B) a typical nanoindentation load-displacement curve. Load is applied while the load displacement and displacement-time are recorded. h_{max} is indentation depth; h_c is contact depth, h_f is final depth and S is the contact stiffness calculated from change in load (P) and displacement (h) as shown.	46

Figure 2.19 Schematic presenting indenter tips for nanoindentation of specimens: (1) Berkovich, (2) a large diameter spherical tip, (3) a small diameter spherical tip and (4) flat punch. The selection of the geometric indenter is significant for determining the modes of deformation.	48
--	----

Chapter 3

Figure 3.1 Schematic representation of the experimental approach for ovine model: (A) The aortic locations where the tissue was taken from for nanoindentation testing. Samples were extracted from aortic root through to the celiac artery. (B) Schematic representation of longitudinal indentation of side view of aortic biopsy specimen with adventitial and intimal faces marked and circumferential indentation of aortic sections for nanoindentation testing. The specimen holder and the orientation of the flat-ended cylindrical punch are also shown. (C) Schematic representation of tensile set up using mechanical clamps and sample for testing hydrated with phosphate buffered saline (PBS) in the liquid cell. (D) Schematic representation of tissue preparation for FTIR analysis. (E) Schematic representation of tissue preparation and an assembled specimen holder for creep behaviour testing.	82
---	----

Figure 3. 2 Schematic diagram of the tensile set up: (A) The mechanical clamps: the upper clamp was moved whilst the lower clamp remained fixed in position. (B) Sample for testing hydrated with PBS in the liquid cell.	88
--	----

Figure 3.3 Typical stress-strain relationship showing the points on the curve which were used to calculate physiological elastic modulus (PE), tangent modulus (TM) at 0.5 strain, maximum elastic modulus (ME) and failure stress.	89
--	----

Figure 3.4 Schematic representation of the experimental approach for nanoindentation in human chronic AD: (A) The dissection tissue types used for nanoindentation testing: flap (inner:intima, outer:medial face); true lumen outer wall (inner:intimal, outer:adventitial face) and false lumen outer wall (inner:medial, outer:adventitial face). Samples were tested on both sides (the inner and outer side of the tissue). (B) Schematic representation of the side view of specimen holder with a flat-ended cylindrical punch showing tip direction, (C) The top view of 16 indentations with 200 μ m of spacing on the adventitia surface and partial submersion of the samples in PBS.....	93
Figure 3.5 Schematic representation of the experimental approach for creep behaviour testing: (A) The disassembled specimen holder and spherical ball, (B) Completely assembled specimen holder and (C) Instrument system consisted of incubator; long focal distance microscope connected with CCD video camera and image analysis system.....	95
Figure 3.6 Schematic representation of indentation of the aortic tissue by the weight of spherical ball. All parameters are used to calculate the elastic modulus of aortic tissue.	96
Figure 3.7 Image processing procedure to obtain percentage of elastin and collagen: (A) VVG stained image for elastin (B) RGB binary image of chronic AD (C) PSR stained image for collagen (D) Binary black and white image. Scale bar indicates 20 μ m.	101
Figure 3.8 Example of the three grades of elastin fragmentation: (A), (B) and (C) demonstrates grades I, II and III, respectively.	102

Chapter 4

Figure 4.1 The true stress–strain relationship extracted from: (A) ascending, (B) upper thoracic region, (C) upper abdominal region and (D) comparison of average stress–strain behaviour for the three main regions (n = 9 samples per region).111

Figure 4.2 Box-whisker plots presented for the macro-mechanical data for the 3 aortic regions (the ascending (ASC), upper thoracic (UT) and upper abdominal aorta (UA)) that were tested (n=9 samples/region): A) PE (B) Tangent modulus at 0.5 strain (C) ME (D) Failure stress. All values are shown with boxes representing the 25th and 75th percentiles of data. Whiskers represent the 5th and 95th percentiles of data. NS = Not significant.113

Figure 4.3 Micromechanical properties of the medial layer (circumferential orientation), shown for the ascending (ASC), upper thoracic (UT) and upper abdominal aorta (UA): (A) G' (B) G'' and (C) $\tan(\delta)$. Symbols represent the mean values and error bars represent the standard deviation.115

Figure 4.4 Longitudinal micromechanical properties across the ovine aorta as a function of distance from the aortic root to celiac region (A) G' -distance (B) G'' -distance were found to have a high positive correlation (Pearson correlation coefficient, G' -distance: $R = 0.97$, $p=0.000028$ and $R=0.97$, $p=0.000016$ for adventitia and intima, respectively. G'' -distance: $R = 0.95$, $p=0.00089$ for adventitia and $R=0.94$, $p=0.00035$ for intima) (C) the relationship between $\tan(\delta)$ and distance. The data are averaged from 81 samples (n=9/region with 3 samples/animal) shown as mean \pm SD.117

Figure 4.5 Comparison of trends obtained via circumferential testing of the medial layer using oscillatory nanoindentation (elastic modulus) with PE values obtained via uniaxial tensile testing, for the ascending, upper thoracic and upper abdominal aorta, shown as a function of distance (length) from the heart.	118
Figure 4.6 Side view of the deformed aortic tissue with the ball indentation method. Image was acquired using a long focal distance microscope. Scale bar is 200µm....	119
Figure 4.7 Optical images showing central deformation of the ovine aorta over five hours in the ascending and descending regions. Scale bar is 200µm.	120
Figure 4.8 Time-dependent deformation (creep behaviour) of the ovine aortic wall for the ascending and descending regions over five hours.	121
Figure 4.9 Box-whisker plots presented for the elastic modulus determined with the ball-indentation technique for the ascending and descending (n=2 samples/region). All values are shown with boxes representing the 25th and 75th percentiles of data. Whiskers represent the 5th and 95th percentiles of data. There was significant difference with a 95% confidence interval, determined by one way ANOVA with a Bonferroni test.....	122
Figure 4.10 Biochemical properties across the ovine aorta as a function of distance from the aortic root (A) Collagen levels were found to be positively correlated with distance (Pearson correlation coefficient, $R=0.88$, $p=0.00187$) (B) GAG levels and (C) Elastin levels showed a negative relationship with distance (Pearson correlation coefficient, GAG level-distance: $R=-0.84$, $p=0.0043$ and elastin level-distance: $R=-0.89$, $p=0.001$). All biochemical data are expressed as µg/mg of wet tissue weight from 81 samples (n=9/region with 3 samples/animal) shown as mean ±SD.....	123

Figure 4.11 Comparison between biochemical properties (collagen, GAG and elastin levels) and elastic modulus determined with nanoindentation in the longitudinal orientation (A) Collagen (B) GAG and (C) elastin. Data are shown as mean \pm SD.....	124
Figure 4.12 (A) Comparison of spectral profiles of 2nd derivative reference of collagen and elastin with (B) extracted spectral signatures from MCR-ALS analysis. Overview FTIR image of a sheep aorta section showing from (C) overall distribution map of tissue section, (D) MCR-ALS factor 1 refers to collagen (E) MCR-ALS factor 4 refers to elastin. Red rectangle represents transverse image that was used to more analyse for FTIR across the layer of aortic wall.	128
Figure 4.13 (A) Comparison of spectral profiles of 2nd derivative reference spectra of Collagen and Elastin with (B) extracted spectral signatures from MCR-ALS analysis. Transverse FTIR image across the aortic wall of the same ovine aorta section shown in Figure 3.13 (highlighted in red box) showing (C) distribution maps of the tissue overall and H & E stain, (D) MCR-ALS factor 1 and Picrosirius red stain and (E) MCR-ALS factor 2 and VVG stain (Scale bar = 100 μ m).....	131

Chapter 5

Figure 5.1 Contrast-enhanced computed tomography images demonstrating the morphology of patient ID:05-00064-18 with chronic type B dissection in (A) axial plane, (B) coronal plane and (C) sagittal plane.....	148
Figure 5.2 Contrast-enhanced computed tomography images demonstrating the morphology of patient ID:05-00017-19 with chronic type B dissection in (A) axial plane, (B) coronal plane and (C) sagittal plane.....	149

Figure 5.3 Micromechanical properties for the adventitial and intimal face for FP, TL and FL in longitudinal orientation: (A) G' (B) G'' and (C) $\tan(\delta)$. All values are shown with boxes representing the 25th and 75th percentiles of data. Whiskers represent the 5th and 95th percentiles of data and the middle horizontal lines represent the median value. Each point within the plot represents an individual patient for the variable specified. A p-value below 0.05 was considered as statistically significant.

.....152

Figure 5.4 Images showing deformation for chronic aortic dissection tissues with no ball, under ball at 0 minute and 300 minutes: (A) FP, (B) TL and (c) FL. Scale bar represents 200 μm154

Figure 5.5 Central displacement deformation–time relationship extracted from: (A) FP (n=10), (B) TL (n=6), (c) FL (n=5) and (D) all FP, TL, FL in one graph. One measurement per tissue sample.155

Figure 5.6 Box-whisker plots presented for the central deformation of chronic aortic dissection tissues between the three tissue types: FP (n=10), TL (n=6) and FL (n=5). The tissues were collected from ascending FP, TL (n=1) and FL (n=3) and descending sections FP (n=9), TL (n=5) and FL (n=2) from 14 patients. The Marfan syndromes were grouped by tissues type: FP (n=3), TL (n=1), and FL (n=2). All values are shown with boxes representing the 25th and 75th percentiles of data. Whiskers represent the 5th and 95th percentiles of data and the middle horizontal line represents the median. Each point within the plot represents a patient sample for the variable specified. .156

Figure 5.7 Box-whisker plots presented for elastic modulus for FP (n=10), TL (n=6) and FL (n=5). The tissues were collected from ascending FP, TL (n=1) and FL (n=3) and descending sections FP (n=9), TL (n=5) and FL (n=2) for 14 patients. Patients with

Marfan syndrome are marked FP (n=3), TL (n=1), and FL (n=2). All values are shown with boxes representing the 25th and 75th percentiles of data. Whiskers represent the 5th and 95th percentiles of data and the middle horizontal line represents the median. Each point within the plot represents a patient sample for the variable specified.157

Figure 5.8 Comparison of trends of elastic modulus obtained via nanoindentation testing at the medial layer with elastic modulus values obtained via non-destructive ball testing for FP and FL.....159

Figure 5.9 Boxplots of biochemical data between the three tissue types: FP (n=10), TL (n=9) and FL (n=5). These tissue types were collected from ascending FP, TL (n=1) and FL (n=3) and descending sections FP (n=9), TL (n=8) and FL (n=2) during replacement surgery from 16 patients. Marfan patients were grouped by tissue type: FP (n=3), TL (n=2), and FL (n=2). All data are represented as box plots representing the 25th and 75th percentiles of data. Whiskers represent the 5th and 95th percentiles of data and the middle horizontal lines represent the median value. Each point within the plot represents an individual patient for the variable specified. Variables acquired from the specimens were: (A) collagen levels (B) GAG level (C) elastin levels and (D) collagen/elastin ratio levels. The non-parametric Mann-Whitney analyses were performed to determine whether they were significantly different between groups.161

Figure 5.10 Box-whisker plots presented for: (A) Percentage of collagen per tissue section area and (B) Percentage of elastin per tissue section between the three tissue types: FP (n=10), TL (n=8) and FL (n=5). All values are shown with boxes representing the 25th and 75th percentiles of data. Whiskers represent the 5th and 95th percentiles

of data and the middle horizontal line represents the median. Each point within the plot represents an individual patient for the variable specified.	163
Figure 5.11 Example elastin fragmentation for chronic AD tissues: (A), (B) and (C) demonstrates TL, FP and FL, respectively. Scale bar is 20µm.	164
Figure 5.12 Percentage of elastin fragmentation graded by age for: (A) flap (FP), (B) true lumen outer wall (TL) and (C) false lumen outer wall (FL).....	165
Figure 5.13 Representative histology sections stained to reveal GAG (Blue) for: (A) flap (FP), (B) true lumen outer wall (TL) and (C) false lumen outer wall (FL). Scale bar 20µm.	166
Figure 5.14 (A) Comparison of spectral profiles of 2nd derivative reference of collagen and elastin with (B) extracted spectral signatures from MCR-ALS analysis for patient 05-00064-18 (C) extracted spectral signatures from MCR-ALS analysis for patient 05-00017-19.	168
Figure 5.15 Overview FTIR images of the chronic aortic tissues (patient ID:05-00064-18): Flap, True and False Lumen outer wall showing (A) Overall distribution maps of the tissue sections shown alongside H & E stain, (B) MCR-ALS factor 2 and VVG stain and (C) MCR-ALS factor 4 and Picrosirius red stain (Scale bar = 100 µm).	170
Figure 5.16 FTIR images of the chronic aortic tissues (patient ID 05-00017-19): Flap, True and False Lumen outer showing (A) distribution maps of general tissue and H & E stain, (B) MCR-ALS factor 4 and VVG stain and (C) MCR-ALS factor 3 and Picrosirius red stain (Scale bar = 100 µm).	171
Figure 5.17 The correlation between elastic modulus obtained from both techniques, central deformation obtained from ball indentation with IIEO for FP (n=10 samples). A, B presented the correlation IIEO with intimal and media surface from	

nanoindentation technique (NI). C showed the correlation IIEO with elastic modulus obtained from the ball indentation (BI). D presented the relationship between central deformation with IIEO. This figure shows the most important correlations. Additional correlations are shown in Figure B1, B2 in Appendix B.	173
Figure 5.18 Correlation between mechanical findings with growth rate shown (A) central deformation obtained from ball indentation in FL (n=5 samples) and (B) central deformation obtained from ball indentation in TL (n=6 samples) and (C) elastic modulus from nanoindentation method in FL (n=5 samples). This figure shows the most important correlations. Additional correlations are shown in Figure B3, B4 in Appendix B.	175
Figure 5.19 Relationships between biochemical findings with IIEO shown (A) collagen in FL (n=5 samples), (B) collagen/elastin ratio in FL (n=5 samples) and (C) collagen in FP (n=10 samples). This figure shows the most important correlations. Additional correlations are shown in Figure B5 in Appendix B.	176
Figure 5.20 Relationships between biochemical and histological findings with growth rate shown (A) elastin in FL (n=5 samples) and (B) percentage elastin per tissue section area in FL (n=5 samples). This figure shows the most important correlations. Additional correlations are shown in Figure B6 in Appendix B.	177
Figure 5.21 Summary schematic highlighting the biomechanical and biochemical properties between FP, TL and FL chronic AD tissues. Overall, FP and TL were stiffer with the arrangement of elastin fibres being highly compact, long, and aligned, whereas FL is more compliant with localized loss of the elastic fibres and increasing elastin fragmentation that correlates with time of illness.	179

List of Tables

Chapter 3

Table 3.1 A list of chronic AD was used for each experiment.	86
---	----

Chapter 4

Table 4.1 The representative factor index after MCR-ALS analysis in the spectral region 950-1600 cm ⁻¹ for the overview FTIR imaging data sets.	126
Table 4.2 Representative factor index after MCR-ALS analysis in the spectral region 950-1600 cm ⁻¹ for the transverse FTIR imaging data sets.	129

Chapter 5

Table 5. 1 Clinical characteristics for the chronic patients, grouped by tissue type. Data are displayed as Mean \pm Standard deviation and <i>n</i> represents number of patients. FP, flap tissues; TL, true lumen outer wall tissues; FL, false lumen outer wall tissues. ...	151
--	-----

Abbreviation

AAA	Abdominal aortic aneurysm
AAAs	Abdominal aortic aneurysms
AD	Aortic dissection
ATAA	Ascending thoracic aortic aneurysm
ATAD	Ascending thoracic aortic dissection
BAV-A	Bicuspid aortic valve aneurysm
CMD	Cystic medial degeneration
CT	Computerised tomography
CS	Chondroitin sulfate
DA	Degenerative aneurysm
DS	Dermatan sulfate
ECs	Endothelial cells
FL	False lumen outer wall
FP	Flap
FTIR	Fourier transform infrared

GAGs	Glycosaminoglycans
HA	Hyaluronic acid
Hep	Heparin
HS	Heparin sulfate
IEL	Internal elastic lamina
IIEO	Interval of index event to operation
IRAD	International Registry of Aortic Dissection
KS	Keratan sulfate
LBIH	Liverpool Bio-Innovation Hub Biobank
LHCH	Liverpool heart chest hospital
MCR-ALS	Multivariate curve resolution-alternating least squares
ME	Maximum elastic modulus
MLU	Medial lamellar units
MMP	Matrix metalloproteinases
MRI	Magnetic resonance imaging
NIPALS	Non-linear iterative partial least squares
PBS	Phosphate buffered saline

PE	Physiological elastic modulus
PGs	Proteoglycans
PSR	Picrosirius red
SMCs	Smooth muscle cells
STJ	Sinotubular junction
TAA	Thoracic aortic aneurysm
TAD	Thoracic aortic dissection
TM	Tangent modulus
TL	True lumen outer wall
VVG	Verhoeff-Van Gieson

Chapter 1

Introduction



This chapter introduces the motivation of this research. The aims and objectives of this thesis are presented.

1.1 Motivation

Aortic dissection (AD) is a significant cardiovascular health problem, a rare, life-threatening disease and its outcome is high mortality and morbidity. The incidence of aortic dissection is 3-6 per 100,000 people per year in the general population (Olsson et al., 2006, Peterss et al., 2016). The incidence of AD is typically higher in men as compared to women (Sampson et al., 2014, Erbel et al., 2014). 40% of patients with AD are aged between 60 and 74 but 27% are aged between 17 to 59 years. Individuals of all ages are hence affected (Bashir et al., 2017).

AD begins with an intimal tear allowing blood to enter the aortic wall leading to the splitting of aortic layers and creating the false lumen from the true lumen by the septum which is referred to as the dissection flap (Figure 1.1A, B). Generally, AD is classified based on the anatomical location of the dissection by the Stanford classification criteria: Type A (originating at the ascending aorta) and Type B (originating at the descending aorta) (Figure 1.1C).

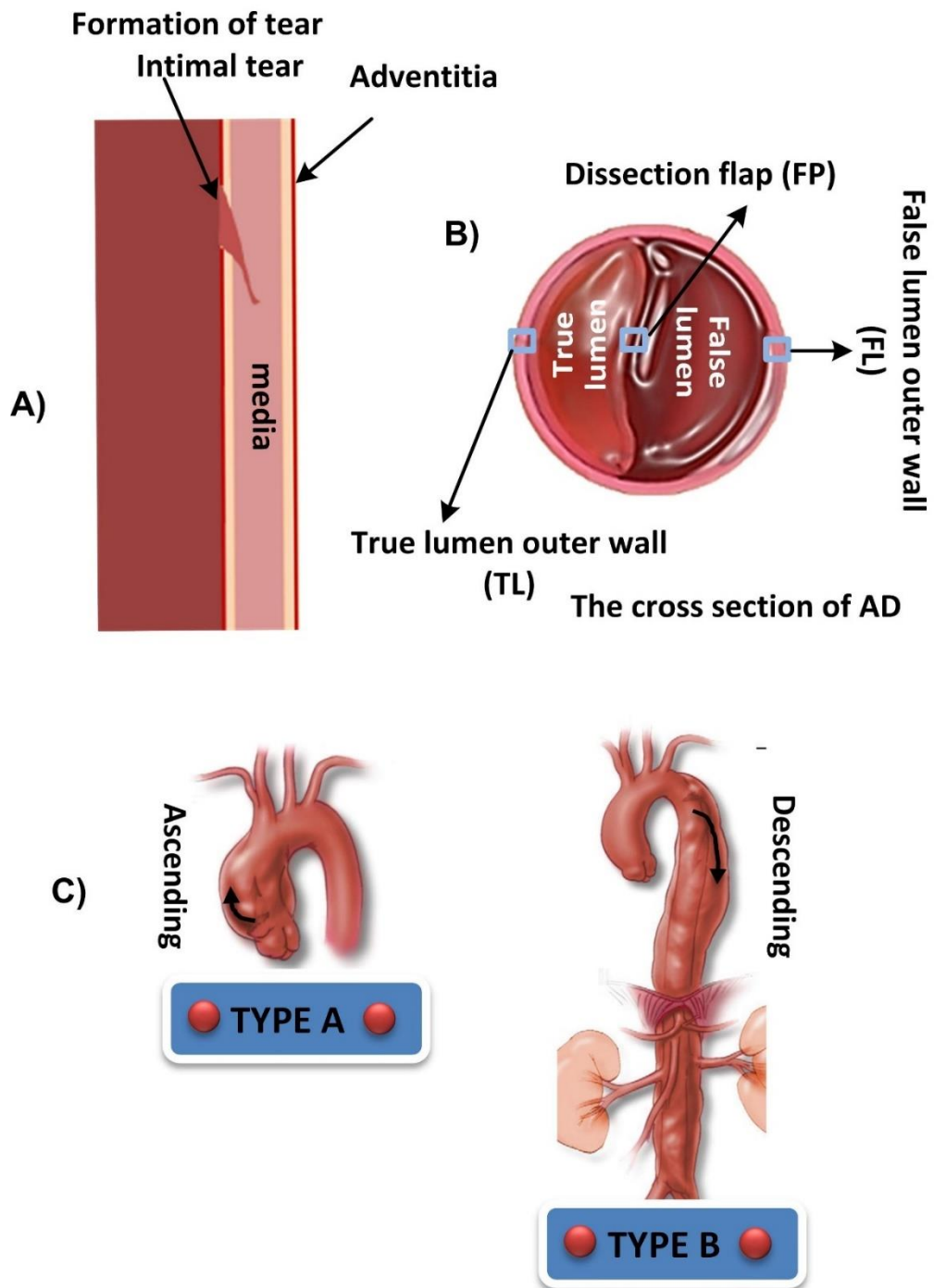


Figure 1.1 Schematic representation of aortic dissection: (A) The formation of the tear occurs in the intimal layer. (B) The cross section of aortic dissection with false lumen outer wall (FL), true lumen outer wall (TL) and dissection flap (FP) marked. (C) The Stanford classification.

The mortality rate for patients with type A AD without surgical intervention reaches 50% during the first 48 hours after onset, with an average mortality of up to 1% per hour (McClure et al., 2017). Type B AD is less dangerous than Type A AD because Type A outcome is almost always death without surgery. Patients with Type B AD without medical therapy have a mortality rate more than 50% due to severe complications such as rupture or malperfusion requiring thoracic endovascular aortic repair (TEVAR), while the mortality rate with medical therapy is reported to be approximately 10% (Luebke and Brunkwall, 2014).

AD can be classified as acute or chronic depending on the initial occurrence of dissection. If this duration is <14 days, the AD is classified as acute dissection. The International Registry of Aortic Dissection (IRAD) investigators have divided this into 4 main phases based on time frame: hyperacute (symptom onset to 24 hours), acute (2-7 days), subacute (between 8 days to 30 days), and chronic (more than 30 days) (Booher et al., 2013). Stanford Type A rarely becomes chronic as it is operated on or the patient dies prior to operation, whereas Type B is routinely chronic (Sherifova and Holzapfel, 2019).

The classic definition of acute dissection is based on scrutinising patient autopsies to determine whether the patient had Type A or Type B AD. It is reported that 74% of deaths with complicated cases of dissection occur within 14 days (Schepens, 2018). The complicated cases are defined as rapid rupture, intractable pain, persistent and uncontrollable hypertension. This definition is utilised in trials and in everyday medical practice (Schepens, 2018). However there is a suggestion from some studies that a significant proportion of patients presenting with acute complicated AD need

endovascular intervention between 15 to 85 days after the onset symptoms (Steuer et al., 2013) with clinical data presented indicating that it may take longer than 2 weeks for a dissection to stabilise (Steuer et al., 2011). Therefore, this demonstrates that there is a subacute, unstable phase which occurs between 14 and 90 days in the transitional period from acute to chronic dissection where life-threatening complications may occur which questions the relevance of the current definition (Schepens, 2018).

1.1.1 Biomechanics of Aortic Dissection

The underlying mechanisms of AD remain unclear. It is noticed that the aortic wall loses its structural integrity, leading to altered biomechanical properties (Sommer et al., 2016). Therefore, characterizing the biomechanical behaviour of the aorta is essential to understanding the progression of aortic diseases and for risk evaluation of aortic pathologies (Duprey et al., 2010, Khanafer, Schlicht and Berguer, 2013).

Conventionally, *in vitro* biomechanical testing of the aorta utilises macro-scale testing techniques such as tensile or biaxial testing techniques (Khanafer et al., 2011, 2013). However, the aorta is a complex, multi-layer structure and it is important to understand its mechanical properties in relation to the extracellular matrix (ECM) architecture and also specific structural components (Akhtar et al., 2009). These are organised at the micro-scale and mechanical testing at this length scale may provide greater insight into aortic disease.

Therefore, the motivation of this thesis is to characterise localised micromechanical properties and associated biochemical changes in chronic dissected aortic tissue. In

this thesis nanoindentation and ball indentation have been used to characterise the micromechanical properties and time-dependent deformation (creep) of chronic dissected aortic biopsies (dissection flap (FP), true outer wall (TL) and false lumen outer wall (FL)). The nanoindentation data are supported with established biochemical assays to quantify ECM component concentrations and Fourier transform infrared (FTIR) spectroscopy to map ECM distribution in the tissues. Initially an animal model (ovine) was utilised to validate methods prior to utilising precious human biopsy samples.

1.2 Aims and Objectives

The overall aim of this study is to quantify and define the biomechanics and biochemistry of the dissection flap, true lumen outer wall and false lumen outer wall in chronic dissection (Figure 1.1B). This aim will be achieved through the following objectives:

The first objective of this thesis was to explore the utility of oscillatory nanoindentation to investigate localised micromechanical properties of ovine tissue across the aortic tree, and to relate these data to biochemical changes. The ovine aorta was used as a model of human aorta for tissue structure and micromechanical changes.

The second objective was to apply the nanoindentation technique to aortic biopsy samples from chronic dissection patients to characterise the micromechanical properties of dissection flap, true lumen outer wall and false lumen outer wall and correlate these properties with biochemical properties and histological data.

The final objective was to characterise how the behaviour of dissection flap, true lumen outer wall and false lumen outer wall changes with time-dependent deformation (creep).

References

- Akhtar, R., Schwarzer, N., Sherratt, M., et al. (2009) 'Nanoindentation of histological specimens: mapping the elastic properties of soft tissues', *J.Mater.Res.*, 24 (3), pp.638-46.
- Bashir, M., Harky, A., Fok, M., et al. (2017) 'Acute type A aortic dissection in the United Kingdom: Surgeon volume-outcome relation', *J.Thorac.Cardiovasc.Surg.*, 154 (2), pp.398,406. e1.
- Booher, A. M., Isselbacher, E. M., Nienaber, C. A., et al. (2013) 'The IRAD classification system for characterizing survival after aortic dissection', *Am.J.Med.*, 126 (8), pp.730. e19,730. e24.
- Duprey, A., Khanafer, K., Schlicht, M., Avril, S., Williams, D. and Berguer, R. (2010) 'In vitro characterisation of physiological and maximum elastic modulus of ascending thoracic aortic aneurysms using uniaxial tensile testing', *Eur. J. Vasc. Endovasc. Surg.*, 39 (6), pp.700-7.
- Erbel, R., Aboyans, V., Boileau, C., et al. (2014) '2014 ESC Guidelines on the diagnosis and treatment of aortic diseases: Document covering acute and chronic aortic diseases of the thoracic and abdominal aorta of the adult. The Task Force for the Diagnosis and Treatment of Aortic Diseases of the European Society of Cardiology (ESC)', *Eur.Heart J.*, 35 (41), pp.2873-926.

Khanafer, K., Duprey, A., Zainal, M., Schlicht, M., Williams, D. and Berguer, R. (2011)

'Determination of the elastic modulus of ascending thoracic aortic aneurysm at different ranges of pressure using uniaxial tensile testing',

J.Thorac.Cardiovasc.Surg., 142 (3), pp.682-6.

Khanafer, K., Schlicht, M. S. and Berguer, R. (2013) 'How should we measure and

report elasticity in aortic tissue?', *Eur. J. Vasc. Endovasc. Surg.*, 45 (4), pp.332-9.

Luebke, T. and Brunkwall, J. (2014) 'Type B Aortic Dissection: A Review of Prognostic

Factors and Meta-analysis of Treatment Options', *Aorta (Stamford)*, 2 (6), pp.265-78.

McClure, R. S., Ouzounian, M., Boodhwani, M., et al. (2017) 'Cause of Death Following

Surgery for Acute Type A Dissection: Evidence from the Canadian Thoracic Aortic Collaborative', *Aorta (Stamford)*, 5 (2), pp.33-41.

Olsson, C., Thelin, S., Stahle, E., Ekbom, A. and Granath, F. (2006) 'Thoracic aortic

aneurysm and dissection: increasing prevalence and improved outcomes reported in a nationwide population-based study of more than 14,000 cases from 1987 to 2002', *Circulation*, 114 (24), pp.2611-8.

Peterss, S., Mansour, A. M., Ross, J. A., et al. (2016) 'Changing Pathology of the Thoracic

Aorta From Acute to Chronic Dissection: Literature Review and Insights',

J.Am.Coll.Cardiol., 68 (10), pp.1054-65.

Sampson, U. K. A., Norman, P. E., Fowkes, F. G. R., et al. (2014) 'Global and Regional

Burden of Aortic Dissection and Aneurysms: Mortality Trends in 21 World

Regions, 1990 to 2010', *Global Heart*, 9 (1), pp.171,180.e10.

Schepens, M. A. A. M. (2018) 'Type B aortic dissection: new perspectives', *J.Vis.Surg.*, 4

pp.75.

Sherifova, S. and Holzapfel, G. A. (2019) 'Biomechanics of aortic wall failure with a

focus on dissection and aneurysm: A review', *Acta Biomater.*,

Sommer, G., Sherifova, S., Oberwalder, P. J., et al. (2016) 'Mechanical strength of

aneurysmatic and dissected human thoracic aortas at different shear loading

modes', *J.Biomech.*, 49 (12), pp.2374-82.

Steuer, J., Björck, M., Mayer, D., et al. (2013) 'Distinction between acute and chronic

type B aortic dissection: is there a sub-acute phase?', *European Journal of*

Vascular and Endovascular Surgery, 45 (6), pp.627-31.

Steuer, J., Eriksson, M. -, Nyman, R., Björck, M., Wanhainen, A. and etc. (2011) 'Early

and Long-term Outcome after Thoracic Endovascular Aortic Repair (TEVAR) for

Acute Complicated Type B Aortic Dissection', *European Journal of Vascular and*

Endovascular Surgery, 41 (3), pp.318-23.

Chapter 2

Background and Literature Review

The chapter provides an overview of the background to the project and a comprehensive literature on all of the relevant topics within this thesis. Section 2.1 briefly introduces aortic anatomy, structure, and components of the aorta. Section 2.2 focuses on the definition and classification system of aortic dissection. Section 2.2 highlights how dissection flap morphology changes from the acute to the chronic phase. Section 2.4 covers biomechanical properties of the aortic wall. *In vitro* biomechanical testing of the aorta from the macroscopic to the microscopic length scales is presented in Section 2.5. Finally, Section 2.6 reviews the biomechanical and biochemical properties of the dissected aorta.

2.1 The Aorta: Anatomy, Structure and Composition

2.1.1 Aortic anatomy

The aorta is the largest blood conduit in the human body which transports oxygen-rich blood from the heart to other sections of the human body. It originates from the left ventricle, curves over the heart and extends down to the abdominal region. It is clinically separated into two main anatomic sections by the diaphragm: the thoracic and abdominal aorta.

The thoracic aorta can be divided into four main anatomic segments: 1) the aortic root, 2) ascending aorta, 3) aortic arch, and 4) the descending aorta. The abdominal aorta is divided into suprarenal abdominal aorta and infrarenal abdominal aorta, separated by the renal arteries (Erbel et al., 2014). The different regions of the aorta are shown in Figure 2.1.

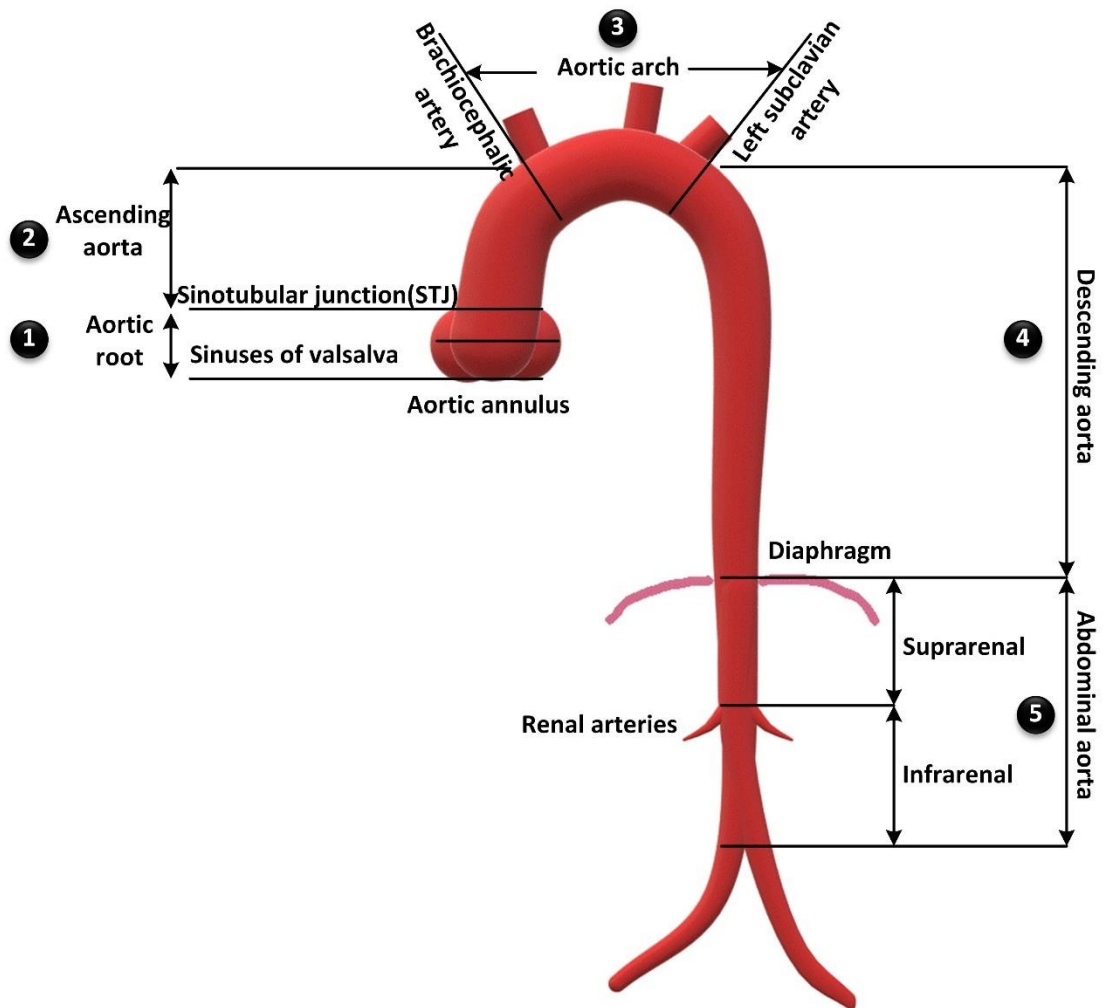


Figure 2.1 Sketch of anatomical aorta in different sections: 1) aortic root, 2) ascending, 3) aortic arch 4) descending thoracic 5) abdominal aorta.

2.1.1.1 The aortic root

The aortic root refers to the first section of the aorta close to the heart and aortic valve annulus. The top of the aortic root is the sinotubular junction (STJ), separating the aortic root and ascending region. Anatomically, its main structure contains the whole aortic valves, aortic cusps, inter-leaflet and the three sinuses of Valsava (Figure 2.2) (Hiratzka et al., 2010).

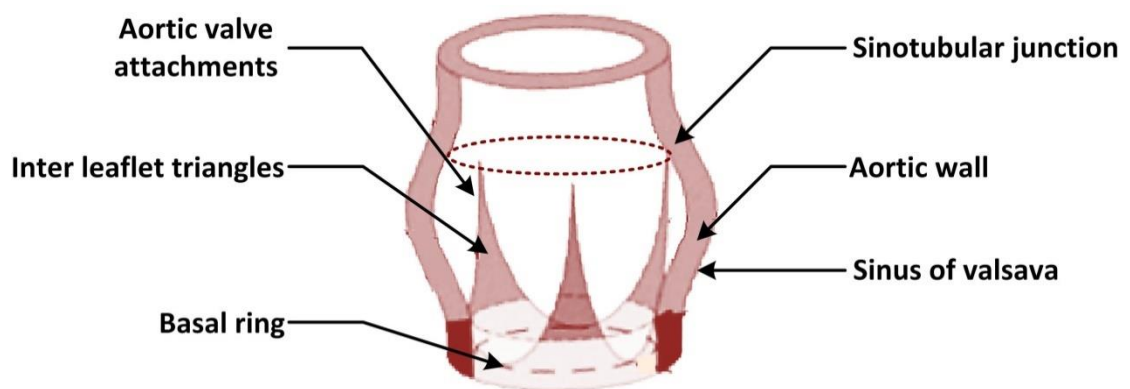


Figure 2.2 The normal anatomy of the aortic root. Adapted from Kırali and Günay (2017).

2.1.1.2 The ascending aorta

The ascending aorta is the second segment of the aorta. It begins from the STJ and extends upward to the start point of the brachiocephalic artery (Figure 2.1).

2.1.1.3 Aortic arch

The aortic arch is defined as the segment between the ascending and descending aorta. It travels backward on the left side of the human trachea (Figure 2.3). There are three main branches of arteries within the arch:

1. Brachiocephalic artery is within the proximal portion of the arching aorta. It is further divided into two small branches: the right subclavian artery and right common carotid artery. The right subclavian artery carries blood to the right arm whereas the right common carotid artery supplies blood to the right side of the head, and neck.
2. Left common carotid artery is in the central portion of the arch between the brachiocephalic artery and the left subclavian. It carries blood to the left side of the head and neck.
3. Left subclavian artery is in the distal portion of the arching aorta. It works with the left common carotid for supplying blood to the left side of the body (Hiratzka et al., 2010, Hapugoda and Gaillard, 2017).

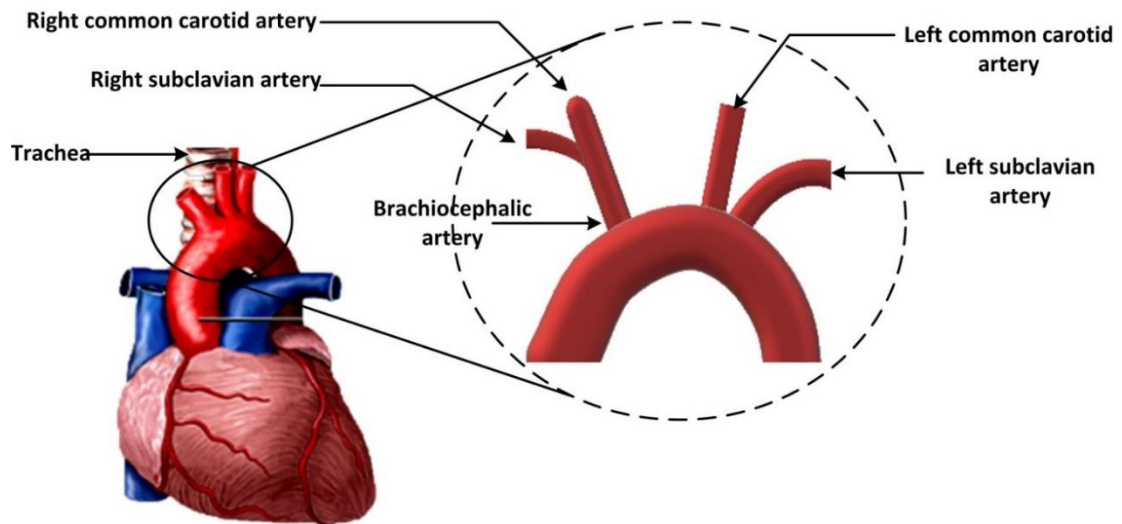


Figure 2.3 The aortic arch. Figure adapted from Drake et al. (2009).

2.3.1.4 The descending aorta

Anatomically, the descending aorta begins following the left subclavian artery at the fourth thoracic vertebrae (T4). It continually lies down in front of the spinal cord to end at the midline of the T12 vertebrae (Figure 2.4A) (Jacob, 2007).

2.3.1.5 The abdominal aorta

The abdominal aorta continues from the descending aorta beginning at the diaphragm (T12 vertebrae) and ending at the fourth lumbar vertebrae of the spinal cord. At this point it branches into the right and left iliac arteries that provide blood to the lower body (Figure 2.4 B) (Allan, Baxter and Weston, 2011).

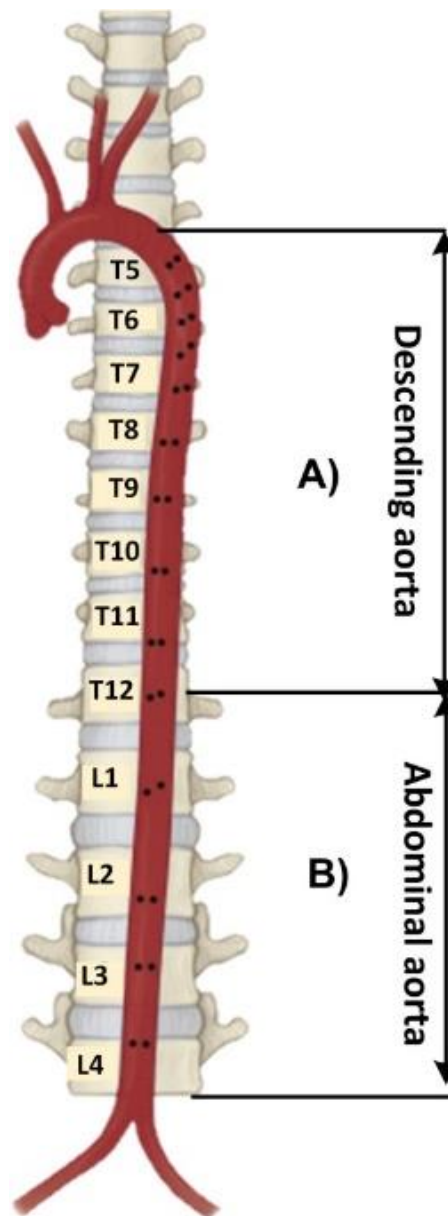


Figure 2.4 The anatomy of descending aorta along the spine cord: (A) The descending aorta spans from the fifth and twelfth thoracic vertebra (T5–T12) and (B) The abdominal aorta begins the first to fourth lumbar vertebra (L1-4). Figure adapted from Richardson et al. (2019).

2.1.2 The structure of the aortic wall

The normal aortic wall consists of three morphologically distinct layers, which from the inner to outer part of the wall are: intima, media and adventitial layer as shown in Figure 2.5 (Holzapfel, 2008, Emmott et al., 2016).

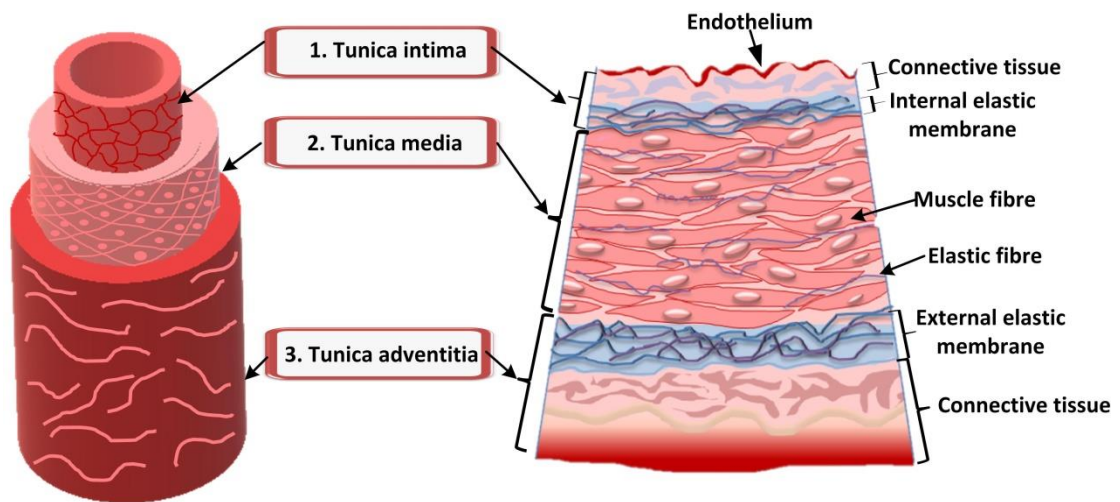


Figure 2.5 The layers and major components of the normal aortic wall: tunica intima, tunica media and tunica adventitia layer. Figure drawn by the author based on Britannica (2010).

2.1.2.1 Intima layer

The tunica intima layer is the inner layer of the aortic wall that interfaces with the blood flow. It consists of a monolayer of endothelial cells (ECs) which are attached to a basement membrane and supported by a sub-endothelial layer consisting of elastin fibres, collagen fibres, smooth muscle cells (SMCs) and some fibroblasts (Fung, 2013).

Collagen Type I and Type III are found scattered within the intima along with Type IV and V, whereas elastin is present in the form of a three-dimensional microstructural

network of elastic fibres (Shekhonin et al., 1985, Howard and Macarak, 1989, Fratzl, 2008, Stecco, 2014). The ECs play crucial functions in regulating arteriolar tone and structure, haemostatic barrier, blood coagulation, including vascular inflammation (Ziganshin and Elefteriades, 2019). The intima layer is adhered to a supporting membrane called the internal elastic membrane. This internal elastic membrane lies between the intima and media layers. The intima is a thin layer compared to the media and adventitia; however, it has an important role (Akyildiz, Speelman and Gijzen, 2014). The ECs act as mechanotransduction signalling pathways between haemodynamic forces and the vascular SMCs (Tarbell et al., 2014).

2.1.2.2 Media layer

The tunica media is the middle and largest layer of the aortic wall. This layer is composed of multiple medial lamellar units (MLU) which are the fundamental structural and functional unit of the aortic wall (Akhtar et al., 2011). The medial lamellar unit consists of about 43% of SMCs, 30% of collagen, 23% of elastin and 4% of glycosaminoglycans (GAGs) and proteoglycans (PGs) by dry weight (Roccabianca, Ateshian and Humphrey, 2014). The normal MLU is comprised of a pair of elastic laminae, which are embedded with SMCs, along with a network of elastin and collagen, fibronectin and GAGs (Figure 2.6) (Humphrey, 2013b).

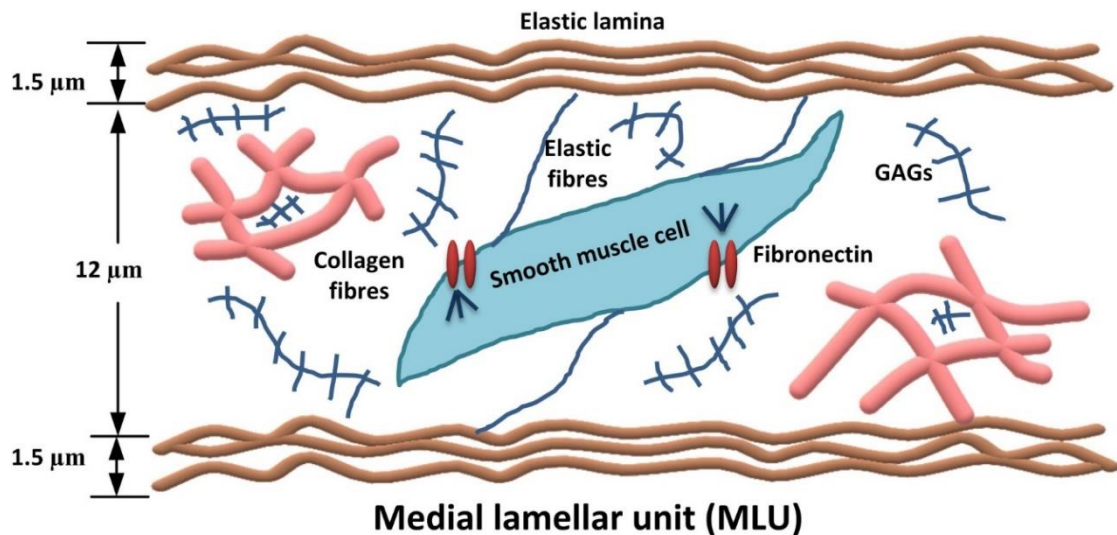


Figure 2.6 Schematic drawing of a medial lamellar unit (MLU) composed of paired elastic laminae with an embedded SMC, collagen and elastin fibres, as well as GAGs. Figure drawn by the author based on Humphrey (2013).

Previous studies have found that collagen (Types I and III), elastic fibres and SMCs are circumferentially oriented. The advantage of this alignment is so that the aortic wall can withstand the high force of loading in this direction (Canham et al., 1989, Holzapfel, Gasser and Ogden, 2000, Holzapfel, 2008).

2.1.2.3 Adventitial layer

The adventitia is the outermost layer and is separated from the media by the external elastic membrane. Its main constituents are fibroblast and fibrocytes, ground substance and bundles of collagen (Fratzl, 2008). It is also surrounded by loose connective tissue. The orientation of the collagen fibres in the adventitia is randomly dispersed, with the collagen fibres more tightly packed in the inner side than the outer side of the adventitia (Fratzl, 2008).

2.1.3 The components of the aorta

The previous sections highlighted that the main components of the aortic wall are ECM components which includes the structural proteins elastin and collagen, along with PGs. These components and SMCs are primarily responsible for the load-bearing functionality and maintaining the structure in the aortic wall. This section reviews collagen, elastin and PGs in more detail.

2.1.3.1 Collagen

Collagen is a family of natural proteins, with 28 different proteins known as collagens (Fratzl, 2008). Collagen molecules are formed by three alpha-polypeptide chains. They are grouped into 8 sub-families, among which fibrillar collagen is of the most attention from the biomechanical point of view which is characterised by a repeat banding pattern, referred to as D-period (Fratzl, 2008) (Figure 2.7).

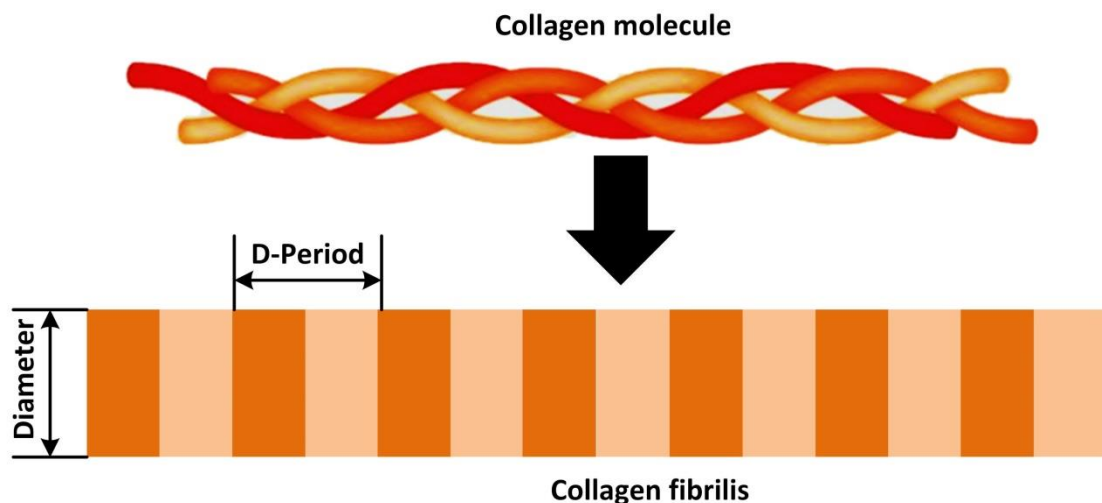


Figure 2.7 Collagen fibrils present a repeating banding pattern known as the D-period (~ 67 nm) which is formed by staggered parallel aligned collagen molecules (length = 300nm; diameter = 1.5 nm). Figure adapted from Sherman et al. (2015).

The aortic wall contains many fibrillar collagen Types: Type I, III, IV, V, VI and VII. However, the predominant collagens in the aortic wall are Type I and III, accounting for 80-90 percent of the total collagen, contributing to aortic wall stiffness, strength, and toughness. Collagen in the aortic wall has been investigated by a number of different methods including with hydroxyproline assays for extracting collagen concentration (Bannister and Burns, 1970), histological studies for image analysis of collagen content (Sokolis, Boudoulas and Karayannacos, 2008, Tonar et al., 2015), with the use of spectroscopy methods, polarized or optical coherence microscopy or nonlinear imaging analysis for examining collagen fibre morphology and orientation (Schriebl et al., 2012, 2013). Various studies have previously assessed differences in composition along the different regions of the aorta (Harkness et al., 1957, Grant, 1967, Sokolis, 2007, 2008).

Changes in the amount of total collagen may be involved with the alteration of biomechanical properties of the aortic wall. Collagen content is higher in the distal region than the proximal regions of the aorta (Harkness et al., 1957, Grant, 1967). Higher collagen in the abdominal aorta is associated with higher stiffness than the ascending aorta (Sokolis, 2007, 2008).

In the adventitial layer the orientation of the collagen fibres has a wide dispersion in contrast to the medial layer where a unimodal distribution was observed (Holzapfel, 2008, Schriebl et al., 2012). However, there were no organisational differences between proximal and distal vessels (Canham et al., 1989).

2.1.3.2 Elastin

Elastin is a highly polymerized insoluble protein in the ECM, and elastic laminae. It is found in elastic fibres which may comprise greater than 50% of the aortic wall (Rosenbloom, Abrams and Mecham, 1993). Elastic fibres are assembled with an inner core of amorphous crosslinked elastin and an outer fibrillin microfibrillar mantle which plays a significant role as the scaffold for elastin deposition (Figure 2.8).

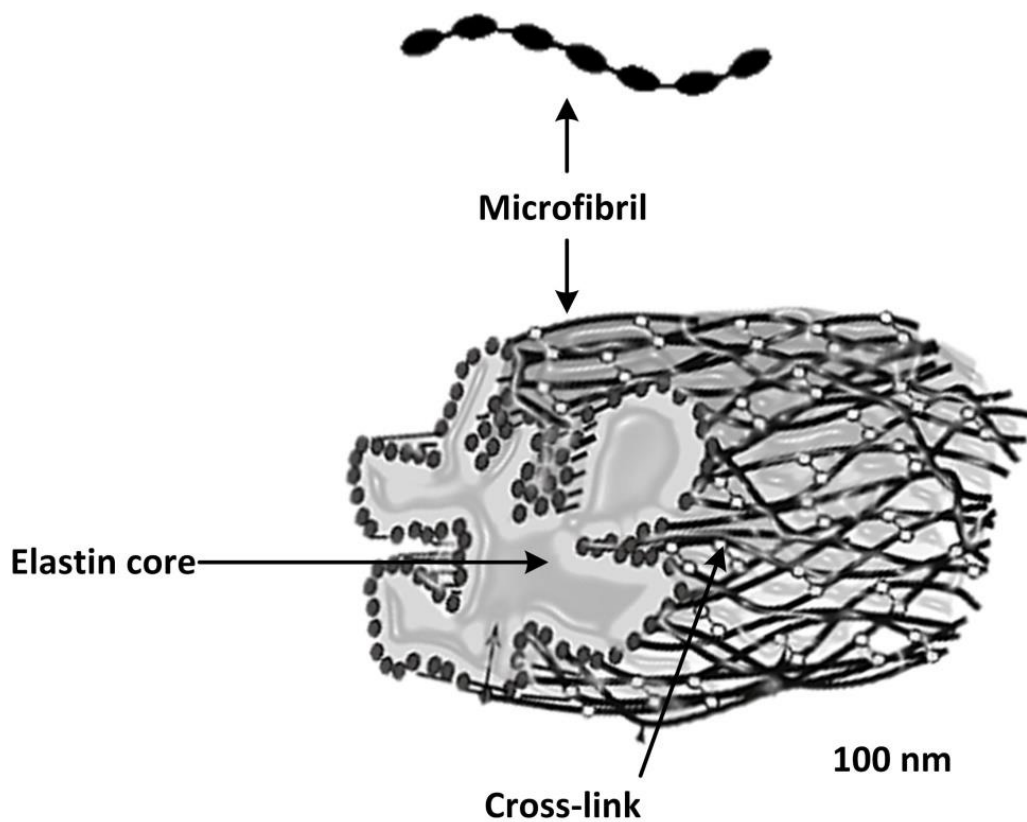


Figure 2.8 Schematic diagram of an elastic fibre assembled by the outer fibrillin microfibrillar mantle with characteristic repeating structures and inner amorphous crosslinked elastin. Adapted from Gasser (2017).

The main function of elastin is to provide elasticity and resilience to the aortic wall. It performs these functions as a partnership with collagen. The coordination and interaction between both provides load-bearing functionality allowing the aorta to extend and recoil back to its original shape during the cardiac cycle. Elastin performs a rubber-like role to bear the entire loading at low strain while collagen bears the load at high pressure following straightening of the fibres (Gasser, 2017). Elastin variability across the vascular tree has been exhibited in animal models from different species including canine and porcine tissue (Harkness et al., 1957, Grant, 1967). Elastin content in the abdominal region is lower than the proximal regions (Harkness et al., 1957, Grant, 1967, Sokolis, 2007, 2008). This is attributed to the observed biomechanical behaviours that show higher stiffness in distal regions due to decreasing elastin content (Sokolis, 2007, 2008, Dinardo et al., 2014). Due to the longevity and extremely low turnover rate of elastin, age-related fragmentation, calcification, and matrix metalloproteinases (MMP) degradation in elastin can be accumulated. As elastin fibres decay, they lose functionality and shift load bearing to collagen fibrils, which directly contribute to an increase in arterial stiffness (Schlatmann and Becker, 1977, Kohn et al., 2015).

Loss of elastin can induce stiffness in aortic walls, leading to high blood pressure and increasing the risk of cardiovascular diseases (Kristensen et al., 2019). Elastin degradation is involved with various diseases such as atherosclerosis (Smith et al., 2012), thoracic aortic aneurysms (Chim et al., 2019), Marfan syndrome (Tsamis, Krawiec and Vorp, 2013) and abdominal aortic aneurysms (Campa, Greenhalgh and Powell, 1987).

2.1.3.3 Smooth muscle cells

SMCs are layered within the MLU and intertwine throughout the interlamellar elastin network (Figure 2.6). The alignment of SMCs is in the circumferential direction with about 20° radial inclinations of SMCs nuclei (O'Connell et al., 2008, Gasser, 2017). They perform structural support and regulate vessel tone and diameter (Wang and Patterson, 2015). SMCs maintain vessel tone and regulate blood flow through contraction and dilation, thus ensuring intravascular pressure and tissue perfusion is maintained (Stegemann, Hong and Nerem, 2005). However, unlike collagen and elastin, SMCs of the media do not contribute to the elastic properties of the vessel wall (Berry, Greenwald and Rivett, 1975).

Under abnormal conditions, SMCs play a key role in the formation and progression of atherosclerosis and vascular lesions by proliferation and migration (Tarbell et al., 2014). Vascular lesion development may also be caused by the accumulation of SMCs within the intima (Dzau, Braun-Dullaeus and Sedding, 2002).

2.1.3.4 Proteoglycans and glycosaminoglycans

PGs are complex high molecular weight macromolecules in the ECM consisting of a core protein with one or more covalently bound various sized GAG as well as oligosaccharides (Figure 2.9). PGs are present on the cell surface of SMCs and within the ECM and are involved in diverse biological activities. In the matrix, PGs perform to control solute diffusion by virtue of polyanionic GAGs, leading to provide elasticity and mechanical support and influencing tissue permeability.

It is also accepted that PGs can directly and indirectly influence cell behaviour as well as participating in tissue structure, organisation and function (Fiedler, 2007). GAGs, previously called mucopolysaccharides are long linear polysaccharides made up of repeating heterogeneous disaccharide units, including heparin and heparin sulphate (Hep and HS), chondroitin sulphate (CS), dermatan sulphate (DS), keratan sulphate (KS), and hyaluronic acid (HA) (Zhang et al., 2019). Of these, CS, DS, and HA are commonly found in the aortic wall (Wigh, 2008, Humphrey, 2013b). Even though there is only a small fraction of PGs and their constituent GAG in normal aortic wall (2-5% dry weight), they are thought to play a significant role in maintaining the structure of the aortic wall, supporting mechanosensing functions and influencing collagen fibrillogenesis as well as correlating with aortic pathogenesis such as aortic aneurysm and dissection (Wight, 1989, Cherchi et al., 1990, Schriebl et al., 2015).

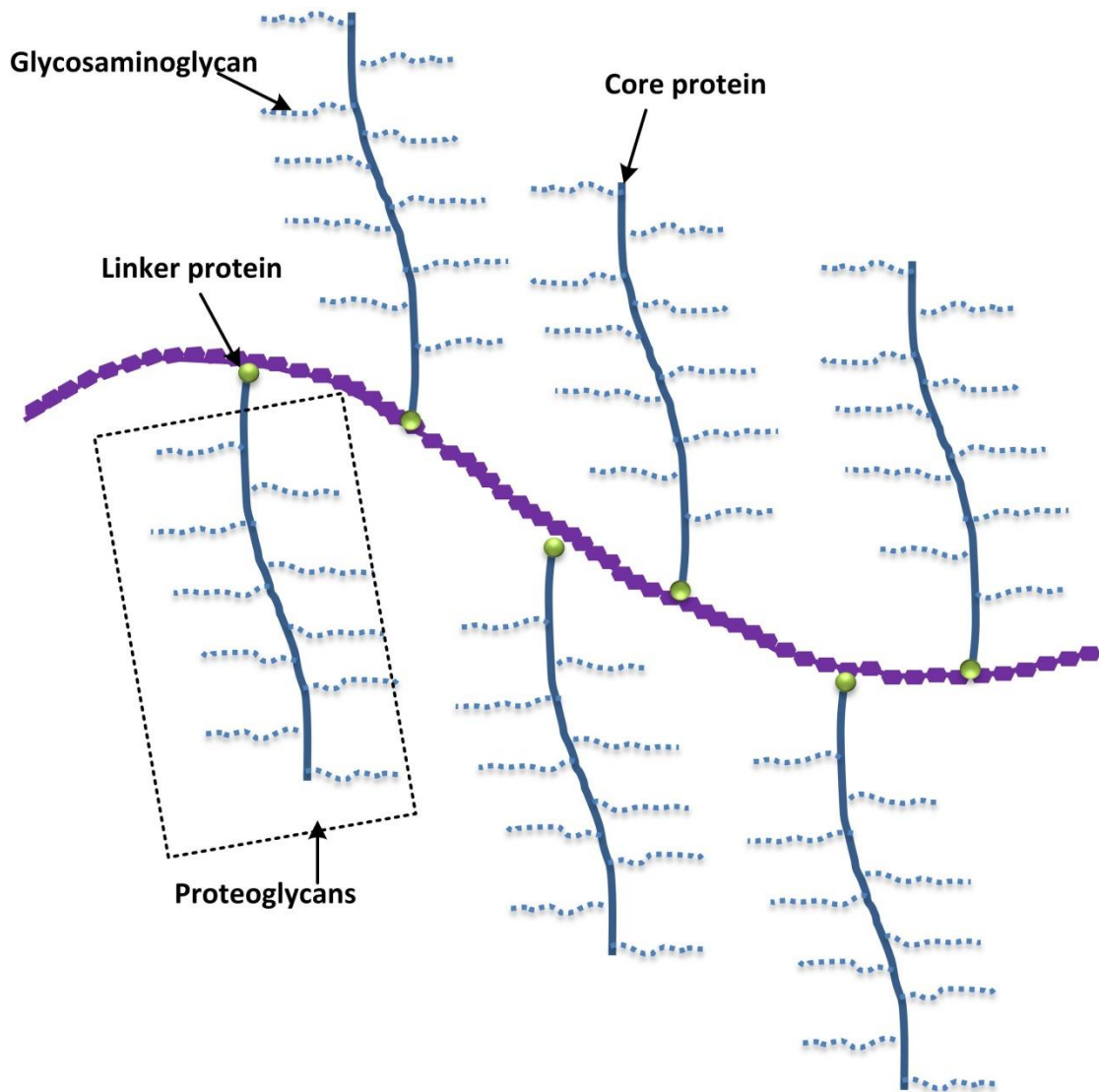


Figure 2.9 A schematic model of the proposed structure of a collection of proteoglycans. A typical proteoglycan monomer consists of a core protein which is attached to a variable number of glycosaminoglycans side chains. Glycosaminoglycans influence viscoelasticity and residual stress, which plays a significant role in arterial homeostasis and in correlation with aortic pathogenesis such as aortic aneurysm and dissection (Wight, 1989, Cherchi et al., 1990, Schriefl et al., 2015).

2.2 The definition of Aortic dissection

Aortic dissection (AD) is a rare, life-threatening disease associated with high morbidity and mortality. It is defined as a rupture within the medial layer of the aortic wall, with the propagation of continuous bleeding through the wall, leading to a split of the aortic layers within the aortic wall. Subsequently, a false lumen (FL) is created and is separated from the true lumen (TL) referring to the original lumen of aorta with a septum or dissection flap (FP) (Figure 2.10A).

In around 90 % of AD cases, a small tear occurs in the intima, resulting in the blood entering the tear and propagating the dissection within the medial layer of the aorta (Figure 2.10B). The remaining cases are a breakdown in the media, or a localised leakage of blood found without an intimal disruption. This can lead to rupture through the adventitial layer or the re-penetration into the true lumen through a second intimal tear generating the false lumen (Figure 2.10C) (Hiratzka et al., 2010, Erbel et al., 2015). Formation of a false lumen results in a reduction in the diameter of the true lumen (Hiratzka et al., 2010, Erbel et al., 2015).

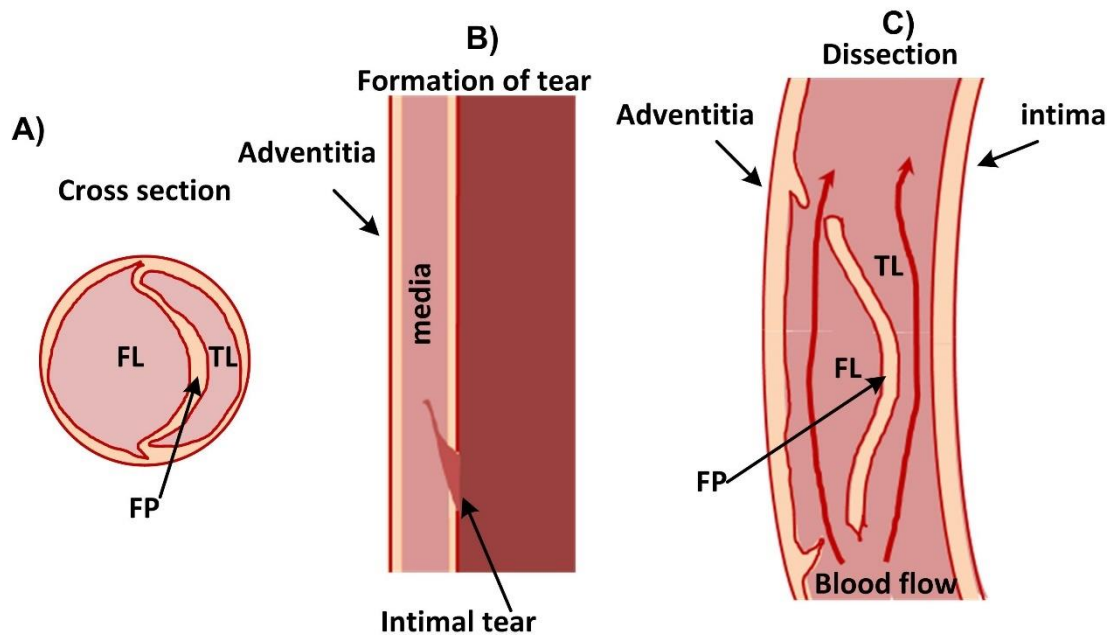


Figure 2.10 Schematic representation of aortic dissection: (A) The cross section of aortic dissection with FL, TL and FP marked. (B) The formation of tear occurs in the intimal layer in the majority of AD cases. (C) In some cases, blood enters the tear, flows through the dissection and re-enters the true lumen.

It is crucial to determine the position, size, and number of intimal tears in the aortic wall for surgical planning (Quint et al., 2003).

2.2.1 The classification systems for aortic dissection

Classification of AD aid risk evaluation and support surgical treatment. There are different ways to classify AD. Clinically, the commonly utilized ways to classify depend on the anatomical position of the dissection and the time from onset of symptoms of AD (Erbel et al., 2001, 2015, Carroll, Maron and O’Gara, 2019).

According to the anatomic location of originating of aortic dissection there are two classification systems which are (1) DeBakey classification and (2) Stanford classification (Hiratzka et al., 2010, Erbel et al., 2015, Maron and O'Gara, 2013).

2.2.1.1 DeBakey classification system

The DeBakey classification system has been used to categorise AD based on the originating location of the intimal tear and the extension of dissection. It is divided into three Types: Type I, Type II and Type III(a) and (b) (Figure 2.11). DeBakey Type I is defined as the tear or the split generally begins in the proximal ascending aorta. The expansion of dissection is along the aortic arch and frequently propagates to the distal aorta. For DeBakey Type II, the original tear and the propagation of dissection are within the ascending aorta. Type III(a) is the intimal tear originates within the descending aorta and extends to the thoracic aorta while Type III(b) extends to the abdominal aorta and iliac vessel (Maron and O'Gara, 2013).

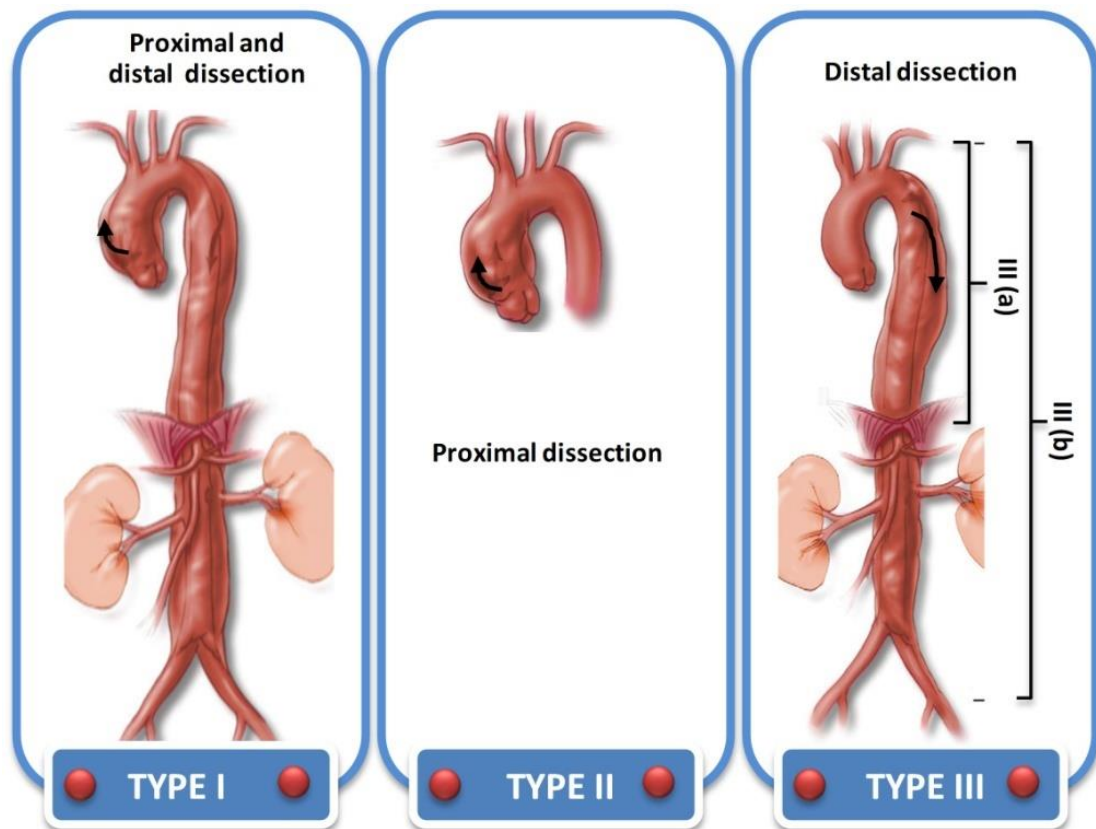


Figure 2.11 The DeBakey classification localisation. Adapted from Huh et al. (2013).

2.2.1.2 Stanford classification system

In this system, the dissection classification is split into two main groups: Type A and Type B (Figure 2.12). Stanford Type A refers to a dissection where a small tear originates at the ascending aorta. Its propagation can expand to the aortic arch or the descending aorta in some cases. On the other hand, Stanford Type B does not involve the ascending aorta, the tear only occurs within the descending aorta.

In terms of the correlation between DeBakey classification and Stanford classification, Stanford Type A consists of the DeBakey Type I and Type II, whereas Stanford Type B includes DeBakey Type III (a) and (b) without retrograde expansion into the ascending aorta. Stanford Type A dissections rarely progress to the chronic stage while Stanford Type B dissection (involving only the descending thoracic aorta) commonly progress to the chronic stage.

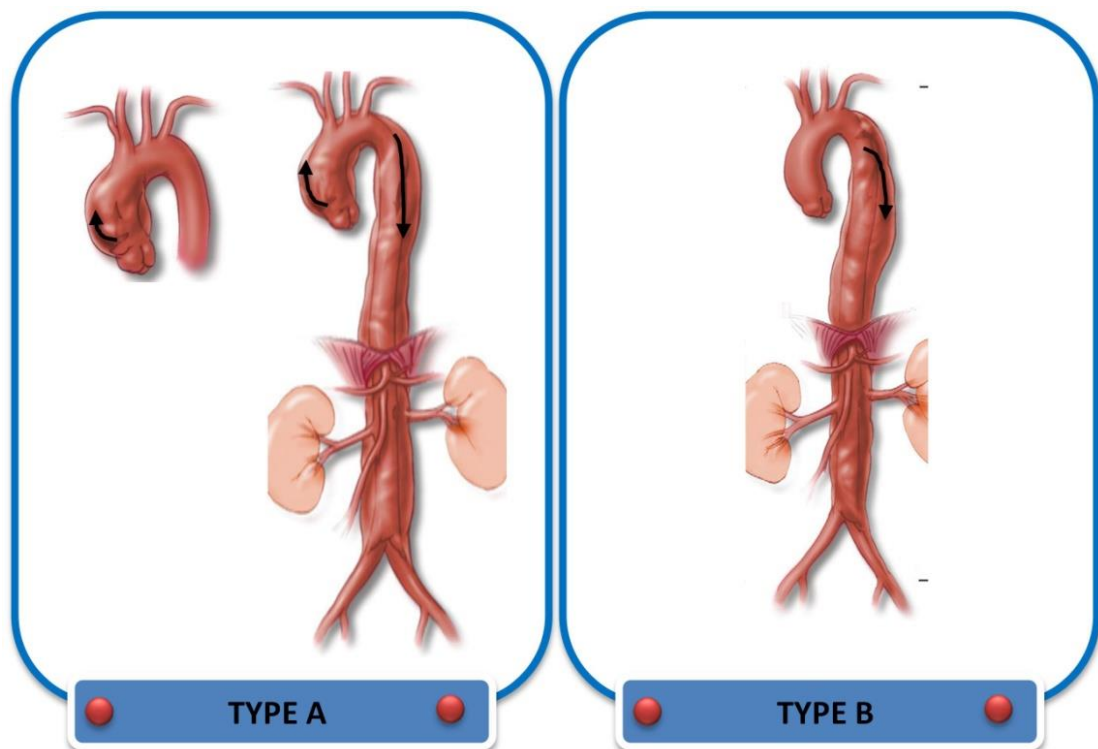


Figure 2.12 The Stanford classification. Adapted from Huh et al. (2013).

2.1.1.3 The classification system with aortic dissection staging

This classification studied the stage of signs of evolving dissections or dissection subtypes (Figure 2.13)(Svensson et al., 1999, Erbel et al., 2001). All classes of dissection can be seen in their acute and chronic stages.

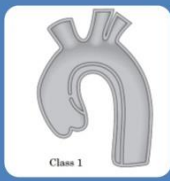


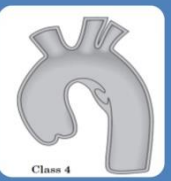
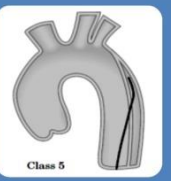
				
Class 1	Class 2	Class 3	Class 4	Class 5
Type	The common features			
Class 1	Classical AD with an intimal flap between TL and FL			
Class 2	The rupture of media with forming of intramural haematoma (IMH). IMH is an a typical form of aortic dissection due to bleeding into the wall from the vasa vasorum without an intimal tear.			
Class 3	Discrete/subtle dissection with bulging of aortic wall at tear site			
Class 4	Plaque rupture leading to aortic ulceration			
Class 5	Traumatic AD occurs during cardiac catheterization which is a procedure used to diagnose and treat certain cardiovascular conditions. During cardiac catheterization, a long thin tube called a catheter is inserted in an artery or vein			

Figure 2.13 The classification systems of AD with signs of evolving dissections from classes 1-5. Class 1: classic AD with TL and FL without communicating between two lumina; class 2: intramural haemorrhage; class 3: ulceration of aortic plaque following plaque rupture; class 4: subtle or discrete AD with bulging of the aortic wall; class 5: traumatic AD. Figure adapted from Erbel et al. (2001).

2.3 Dissection Flap

The structure of the septum separating the false lumen and the true lumen is referred to as the dissection flap. Clinically, it is generally accepted that there is a lack of mobility of the flap with disease state (Karmonik et al., 2012, Peterss et al., 2016). The flap can be visualised via Magnetic Resonance Imaging (MRI) and computerised tomography (CT). In the acute phase, the aortic intimal dissection flap usually has some curvature whereas, in the chronic phase, this structure becomes thick, straight, and less mobile as assessed via CT in Figure 2.14 (Cherry, Kenneth and Michael, 2009, Peterss et al., 2016). However, there is still a lack of quantitative information in the literature regarding this or the mechanical properties of the flap before rupture. It would be expected that the behaviours of the aortic flap may depend on its composition (e.g., the behaviour and quantification of elastic and collagen fibres) and biochemical changes (e.g. elastin and collagen content). Although a number of studies have illustrated that AD is associated with an increase in medial deterioration (Nakashima et al., 1990, Peng et al., 2007, Bode-Jänisch et al., 2012, Peterss et al., 2016), the alteration of the dissection flap in term of flap mobility, biomechanics, biochemistry and histology are still poorly understood. A better understanding how the properties of the dissection flap alter with the transitional phase of AD could lead to the development of numerical models to assist with predicting AD progression and in turn better management of medical treatment.

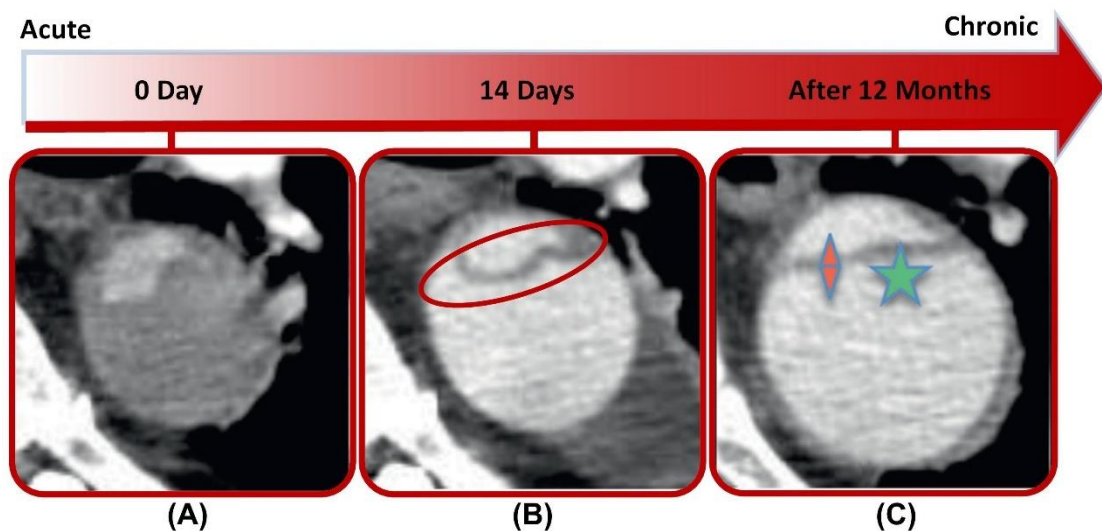


Figure 2.14 CT image demonstrating the morphological change during the transition from acute to chronic dissection (a, b) Curly flaps are observed in acute phase (0-14 days) compared with (c) straight flap in chronic phase (after 12 months). Decreased flap motion over time is presented by two orange triangle head and flap straightening over time is represented by a green star. Adapted from Peterss et al. (2016).

2.4 Treatment of Aortic Dissection

A consensus has evolved regarding acceptable treatment of patients with acute AD; however, despite recent advances in medical, surgical, and endovascular treatments, this disease remains a formidable clinical challenge (Dake et al., 1999). For patients with acute Stanford type A AD involving the ascending aorta, surgical intervention is generally necessary to avoid the high risk of death because of various complications, including cardiac tamponade, aortic regurgitation, and myocardial infarction while the preferred treatment for Stanford type B AD involving the descending is blood pressure control and a regular monitoring with repeat CT scanning. The dissection will mature and form scar tissue, requiring long term follow-up and possibly surgery.

2.5 Biomechanical properties of the aortic wall

In order to deal with the challenging task of providing variable amounts of oxygenated blood and nutrients to various human organs, the blood circulation through the small arteries needs to be regulated. The aorta acts as a reservoir to store a portion of ejected blood with each systolic contraction of the heart and then generates blood flow into small arteries during diastole (Safar and Lévy, 2007, Derby and Akhtar, 2015).

The blood pressure within the aorta leads to wall stress and strain. Blood pressure is translated into tension-dominated biomechanical wall stress. The main dominating stresses in the aortic wall are circumferential and axial stresses (Figure 2.15) (Bäck et al., 2013).

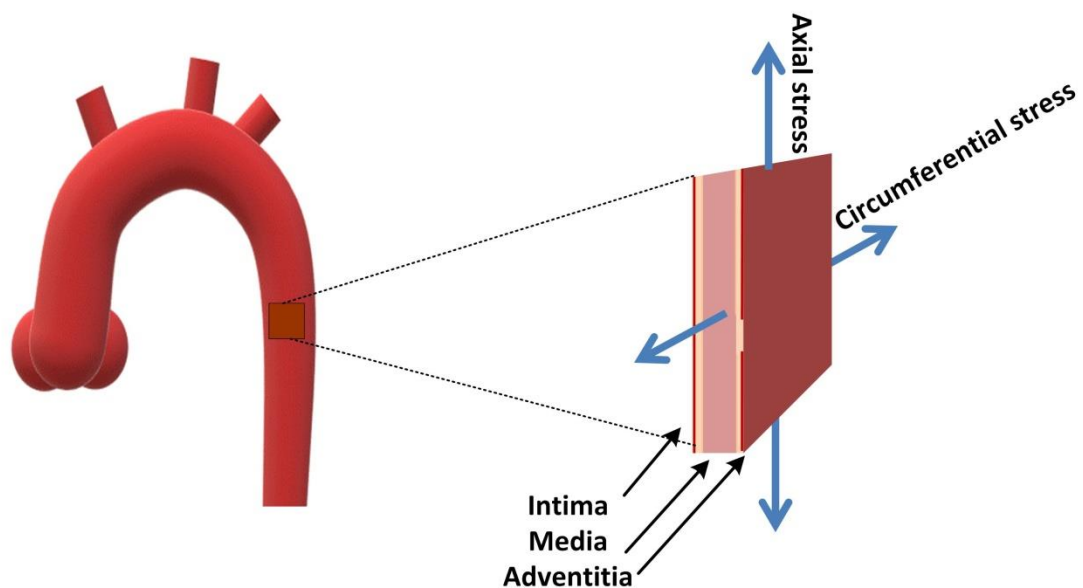


Figure 2.15 A schematic model of the main dominating stresses in the aortic wall: circumferential and axial stresses.

Due to aortic expansion during each systolic contraction, the aortic wall needs to deform isochorically to store a portion of the stroke volume for maintaining the blood volume. Consequently, stretching of the aortic wall in the circumferential and axial directions can also result in thinning of the wall.

Generally, the aortic wall is highly deformable and behaves in a non-linear fashion over finite strain. The aorta, like other soft biological tissues, shows unique biomechanical behaviour which is characterised by J-curve behaviour, as shown in Figure 2.16.

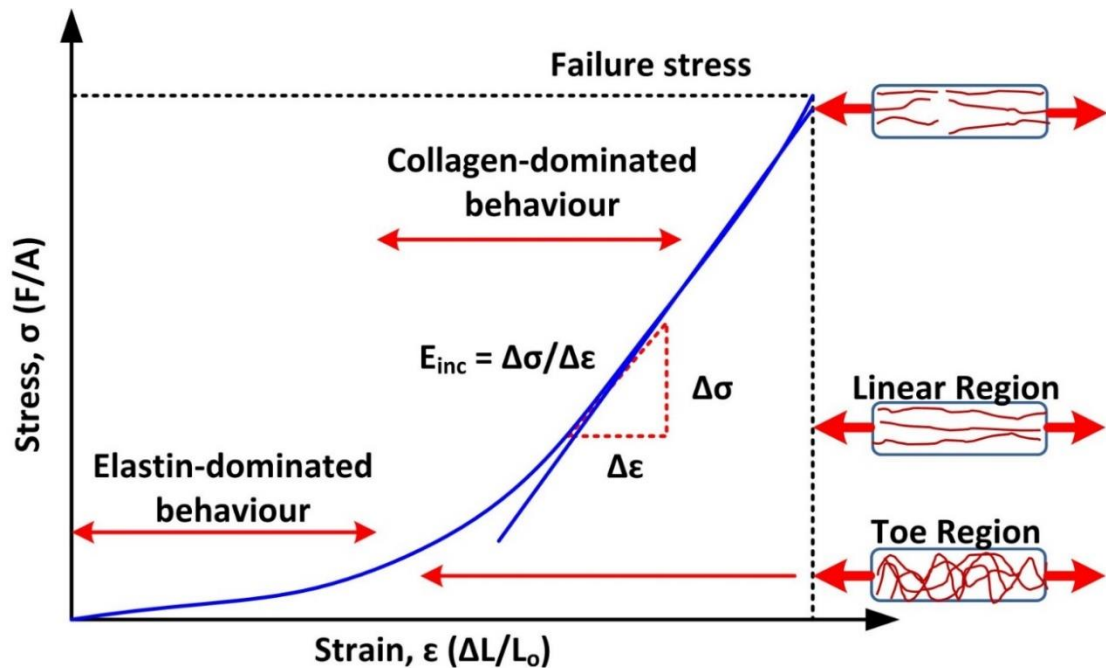


Figure 2.16 Typical stress-stretch curve for the aortic wall with key points marked. The incremental elastic modulus (E_{inc}) is defined as the ratio between the change of applied force ($\Delta\sigma$) and the change in the elongation ($\Delta\epsilon$). The stress (σ) is the force applied (F) to tissue, divided by the cross-sectional area of tissue (A) and the strain (ϵ) is the ratio between the specimen stretch (ΔL) divided by the original length (L_0).

The J-curve behaviour is characterised by an initial flat response (toe region) where there is a large change in strain for low levels of applied stress, followed by rapid stiffening at the higher levels of stress. The biomechanical properties of the aorta are mainly derived by the quantity and structure of collagen, elastin and SMCs and their organisation. At the lower levels of stress, the biomechanical behaviour is dominated by the compliant elastin fibres, whereas at larger extensions, the collagen fibres uncoil by stretching of the fibres leading to an increase of stiffness. This stage represents a relatively linear response.

The microstructure and biomechanical behaviour of the aorta varies with species, age, disease, and location along the vascular tree (Humphrey, 2013a). Increased stiffness of the aortic wall has been previously studied and associated with ageing, smoking and aortic disease (Lakatta and Levy, 2003, Lakatta, 2013). The increased stiffening with age is reported to be higher in males than females (Sonesson et al., 1993, Gasser, 2017, Mozos et al., 2017). Several lines of evidence show that the stiffness is highest at the distal region compared with the proximal region (Guo and Kassab, 2003, Peña et al., 2018).

Given the heterogeneous nature of aortic tissue, the biomechanical properties of the tissue are closely linked to its structural properties and organisation. Insight into aortic tissue mechanical behaviour can be obtained by considering different length scales. This is discussed in Section 2.6.

2.6 Biomechanical testing *in vitro* across the length scale

This section will provide the principles of *in vitro* techniques that are commonly used to investigate the biomechanical properties of the aortic wall, focussing on macroscopic length scale testing techniques through to the microscopic length scale. Relevant literature on aortic diseases gleaned from these techniques is reviewed.

2.6.1 Uniaxial tensile testing

2.6.1.1 Principles

Uniaxial tensile technique has been prevalently used to quantify the biomechanical properties of aortic tissues (He and Roach, 1994, Duprey et al., 2010, Khanafer et al., 2011, Sokolis et al., 2006, Shah et al., 2014, Avanzini et al., 2014, Ferrara et al., 2016). Testing is conducted on tissue in the form of a rectangle or a dumb-bell shaped specimen (dog-bone shaped specimens) which is clamped for uniaxial tensile testing (Figure 2.17). These tissues are pulled with gradually increasing tensile force. This technique is an easy way to perform biomechanical tests and yields the non-linear stress-strain relation of aortic tissues, outlined in Section 2.5.

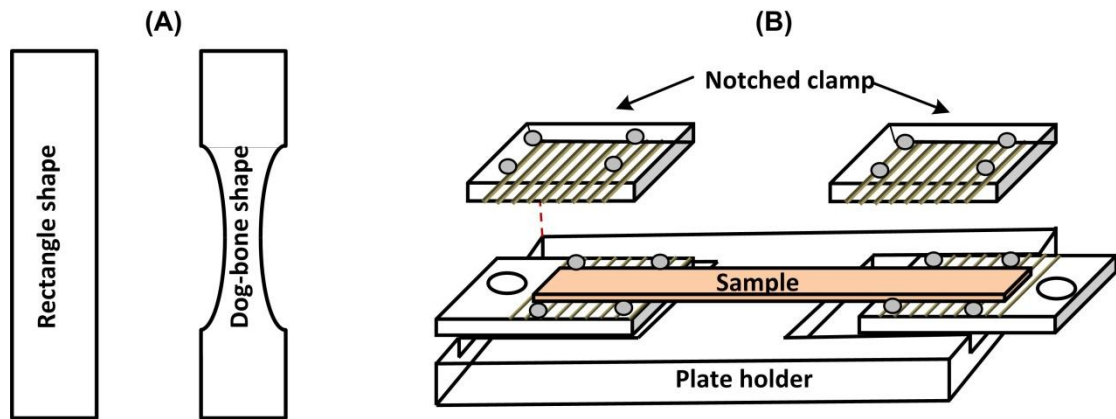


Figure 2.17 A schematic diagram showing (A) Typical tensile test specimen in the form of a rectangular strip or a dumb-bell or dog-bone shaped specimen and (B) Typical sample set up for uniaxial tensile testing. Samples are typically connected to notched mechanical clamps to protect against slipping of the sample.

In the literature, calculation of aortic mechanical properties from uniaxial tensile testing data varies depending on the definitions of both stress and strain that are utilised. Engineering stress and strain are commonly employed in some engineering applications where there are no changes in the sample cross section area and the length of the samples during applied force (Akhtar, 2014). The engineering stress (σ_E) is the ratio between the applied force (F) and the original cross-section area of specimen (A_0) (Equation 2.1).

$$\sigma_E = \frac{F}{A_0} \quad (2.1)$$

The Engineering strain (ϵ_E) is calculated from the specimen stretch (ΔL) divided by the original length (L_0) before applying the force:

$$\varepsilon_E = \frac{\Delta L}{L_0} \quad (2.2)$$

Khanafer et al. (2013) described that the definitions of engineering stress and strain are only appropriate for small strains and displacements. For biological soft tissues, during testing there is an alteration of the cross-sectional area and the length of the samples. Therefore, it is not a valid way to analyse the tissue biomechanical properties. Hence, true stress-strain has been used because it provides more precise assessment of the biomechanical behaviour (Khanafer, Schlicht and Berguer, 2013).

The true stress (σ_T) is defined as the applied load acting on the current cross-sectional area (A). Due to the tissue being considered an incompressible material (Khanafer, Schlicht and Berguer, 2013), we can imply that there is no change in volume ($V = AL$),

therefore:

$$A L = A_0 L_0 \quad (2.3)$$

$$A = \frac{A_0 L_0}{L} \quad (2.4)$$

where L is the current length of the aortic tissue

and $L = L_0 + \Delta L$

then,

$$\sigma_T = \frac{F}{A} = \frac{F}{\frac{A_0 L_0}{L}} = \frac{F L}{A_0 L_0} = \frac{F}{A_0} \frac{(L_0 + \Delta L)}{L_0} = \sigma_E (1 + \varepsilon_E) \quad (2.5)$$

The true strain (ε_T) can be defined as the instantaneous stretch per unit of the current length of the aortic specimen. Considering the increment of strain:

$$\delta\varepsilon_T = \frac{\delta L}{L} \quad (2.6)$$

$$\int \delta\varepsilon_T = \int_{L_0}^L \frac{\delta L}{L} = \ln \frac{L}{L_0} = \ln \frac{L_0 + \Delta L}{L_0} = \ln (1 + \varepsilon_E) \quad (2.7)$$

Therefore, true strain is

$$\varepsilon_T = \ln (1 + \varepsilon_E) \quad (2.8)$$

2.6.1.2 Application to the aorta

A focus of uniaxial testing on the aorta has been considering the region across the vascular tree and layer-dependence. A seminal study in the regional differences is the work of Sokolis (2007); he performed uniaxial tests on nine segments across the vascular tree of porcine aorta. He showed that the distal segments of the porcine aorta were significantly stiffer than the proximal regions both at physiologic and higher stresses. Although most tensile testing is conducted on full thickness aortic tissue, the technique has also been used to test specific layers of the aortic wall (Holzapfel et al., 2005). The layer-specific differences of the intima, media, and adventitia from uniaxial testing of human healthy arterial walls were documented by Holzapfel et al. (2005). They used macroscopic inspection of histological images to separate the layers and they found that the intima is the stiffest layer. Where “stiffness” is the ratio of the Cauchy stress to the associated extension ratio (Holzapfel et al., 2005).

For aortic diseased tissue a significant volume of literature has focused on tensile testing. Vorp and co-workers have studied the changes in biomechanical behaviour between aneurysmal and non-aneurysmal ascending thoracic aorta by using uniaxial tensile testing. They indicated that aneurysmal aortic tissues have a higher maximum tangential stiffness than non-aneurysmal aortic tissues (Vorp et al., 2003). The aortic tissues are anisotropic in nature and tissue stiffness has been found to be higher in the circumferential than in the longitudinal direction via uniaxial tensile testing (Iliopoulos et al., 2009, Ferrara et al., 2016). However, for aneurysmal tissue from the thoracic aorta it has been reported that there is no significant difference in stiffness between circumferential and longitudinal direction tested samples (Vorp et al., 2003). In terms of regional variations in the biomechanical behaviours of aneurysmal tissue, Iliopoulos et al. (2009) examined the behaviours across four different regions of the ascending thoracic aortic aneurysms: anterior, posterior, right and left lateral. They showed that the stiffness and strength of aneurysmal tissues have no regional differences in the circumferential direction, while in the longitudinal direction the anterior part was the weakest with lowest stiffness (Iliopoulos et al., 2009). This is consistent with clinical observation that bulging of the aortic wall for the ascending thoracic aortic aneurysms most frequently occurs in the anterior wall. The layer-specific difference properties from uniaxial data of the aortic diseased tissue were presented by Sokolis et al. (2012) who examined the mechanical properties of ascending thoracic aortic aneurysms. They disclosed that failure stress in the medial and adventitial layer is higher in the circumferential direction than the longitudinal direction (Sokolis, Kritharis and Iliopoulos, 2012).

2.6.2 Biaxial tensile testing

2.6.2.1 Principles

Data from uniaxial tensile testing is not enough for the investigation of multiaxial stress states of mechanical behaviours for aortic tissue (Geest, Sacks and Vorp, 2004). This is because uniaxial tensile testing treats the aortic wall as an isotropic material instead of investigating the anisotropic behaviour of the aortic wall comprehensively. To evaluate the anisotropic nature of aortic tissue, biaxial testing method is necessary for quantification of the physiologically relevant, multiaxial mechanical behaviour of aortic tissues. The detailed coverage of this method is beyond the scope of this thesis, but some studies are summarised below.

2.5.2.2 Application to the aorta

For variation in biomechanical properties across the aorta, biaxial testing was used to assess the behaviour of the porcine aorta in three regions: ascending, descending and abdominal region (Peña et al., 2018). They showed that the aorta was stiffer in the distal region than the ascending region.

Kamenskiy et al. measured the biomechanical properties of human aortic tissues in the longitudinal and circumferential directions using biaxial testing. They indicated that the aortic tissues became stiffer with the distance from the heart. Moreover, they perform anisotropy and nonlinear deformations. The aortic tissues at the proximal region were stiffer in the longitudinal direction, while renal regions were stiffer in the circumferential direction (Kamenskiy et al., 2014).

Regional variation in biomechanical properties of dilated human ascending aortas has been investigated with biaxial testing (Choudhury et al., 2009). It was found that the outer curvature has high stiffness, associating with the clinical observation of preferential dissection on the lateral region. Increasing stiffness for the lateral wall may make it more likely to reach its ultimate stress first.

2.6.3 Nanoindentation Testing

2.6.3.1 Principles

As described in Section 2.3.3, the aorta is a multi-layered composite structure. It is possible that biomechanical degradation of aortic wall starts at the cellular state and progresses to the higher levels of tissue structure (Akhtar, 2014). Investigation of the localised biomechanical properties of aortic tissues is necessary to fully understand the structure-function relationship across different length scales in aortic disease.

Nanoindentation is a depth-sensing indentation technique that is used to characterise localised mechanical properties of materials (Ebenstein and Pruitt, 2006). The main advantage of this technique over conventional techniques such as tensile testing is that it is able to test small volumes of samples or inhomogeneous samples with high spatial resolution (Akhtar et al., 2016).

The main target of nanoindentation testing is the extraction of mechanical properties in materials which are the elasticity and hardness of materials from measuring controlled load (P) and displacement (h) (Fischer-Cripps, 2002, Ebenstein and Pruitt, 2006). During a typical load-displacement cycle in quasi-static nanoindentation, the indenter is brought into contact with the sample under controlled load and then the

indenter is retracted. Loading and displacement are monitored and recorded during the cycle of loading and unloading (Figure 2.18).

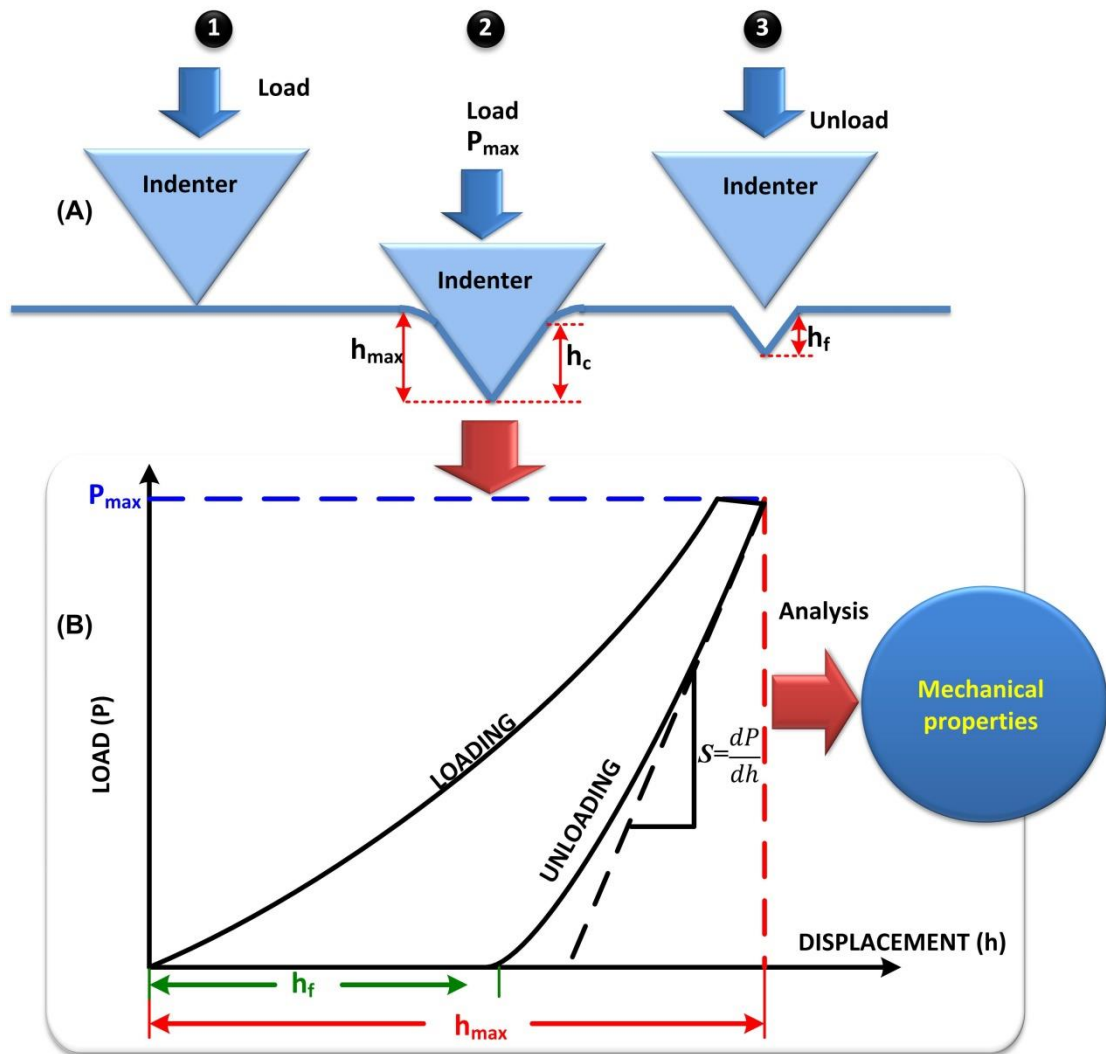


Figure 2.18 Schematic demonstrating showing: (A) the process of nanoindentation testing and (B) a typical nanoindentation load-displacement curve. Load is applied while the load displacement and displacement-time are recorded. h_{max} is indentation depth; h_c is contact depth, h_f is final depth and S is the contact stiffness calculated from change in load (P) and displacement (h) as shown.

This technique has been widely used to measure the mechanical properties of microstructural features for hard biological tissue such as bone (Rho, Tsui and Pharr,

1997, Bushby, Ferguson and Boyde, 2004) and teeth (Poolthong, Mori and Swain, 2001, Angker, Swain and Kilpatrick, 2003), and more recently for soft biological tissues: vascular tissue (Akhtar et al., 2009, Chim et al., 2019), brain (MacManus et al., 2015) and cartilage (Ebenstein et al., 2004).

The selection of the geometric indenter is important and should be considered before nanoindentation testing because it determines the modes of deformation. Very sharp tips such as the three-sided pyramidal Berkovich tip are used for hard tissues (Figure 2.19); however larger radius tips are typically used for soft tissues. A spherical tip (Figure 2.19) is commonly used to minimise plastic deformation and stress concentrations to avoid damaging the sample (Field and Swain, 1993). Cylindrical flat punch tips have been utilised to investigate the viscoelastic behaviour of soft tissue and hydrogels (Ebenstein and Pruitt, 2004, Odegard, Gates and Herring, 2005, Guglielmi et al., 2015, Wang and Niu, 2015, Akhtar et al., 2016). The cylindrical flat punch has the advantage of a constant, known contact area as a function of depth, however it can create a high stress at the contact circumference, which can allow for some error (Ebenstein and Pruitt, 2006).

Along with tip geometry, the contact area of the indenter is also significant for investigating mechanical properties of soft tissues. If the aim of testing is to investigate the overall mechanical behaviour of the tissue rather than individual components, the diameter of the indenter should be more than 50 μm to ensure the projected contact area will be larger than the diameter of individual cells (about 8 μm) or fibres and prevent any damage to the tissues as shown in Figure 2.19 (Ebenstein and Pruitt, 2004, 2006).

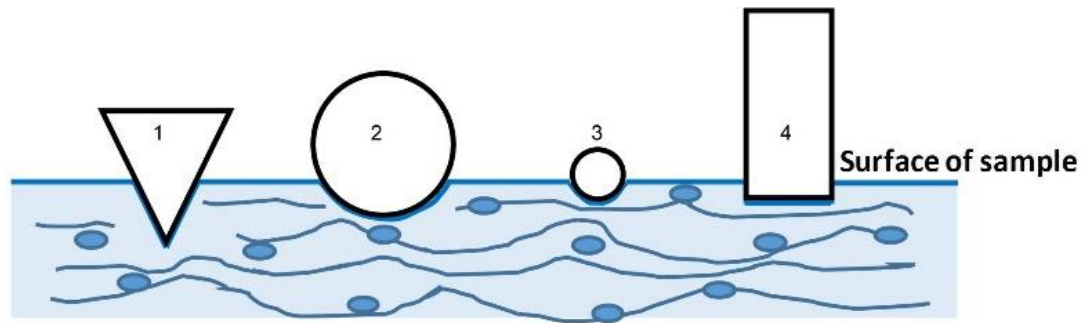


Figure 2.19 Schematic presenting indenter tips for nanoindentation of specimens: (1) Berkovich, (2) a large diameter spherical tip, (3) a small diameter spherical tip and (4) flat punch. The selection of the geometric indenter is significant for determining the modes of deformation.

To continuously control and monitor the indentation testing, the dynamic mechanical analysis (DMA) method was developed through applying oscillatory stress either as tension, compression, or torsion on the specimens and measuring the resulting oscillatory strain (Hayes, Goruppa and Jones, 2004, Hay, 2015). The outcome of a DMA testing can be expressed in terms of the storage modulus (G') which defines the specimen's capability to store energy elastically, and the loss modulus (G'') which identifies the specimen's capability to dissipate energy as heat. Phasor analysis of DMA mechanics shows that G' and G'' are concisely correlated through the loss factor (δ) which is the tangent of the phase angle, δ , by which the strain lags the stress (Akhtar et al., 2016, 2018).

In practice, G' , G'' , and $\tan \delta$ are measured by DMA as a function of frequency and temperature. When the specimen is too small to be tested by DMA, analogous measurements can be made by means of an oscillatory indentation method. As the indenter is pressed into the specimen, an oscillating force is imposed on the sample

through the indenter, and the resulting displacement oscillation is measured. By presuming the same kind of constitutive form which DMA uses, and by interpreting the indentation data in light of established contact models, one can measure equivalent values of G' and G'' by oscillatory indentation (Hay, 2015).

The advantages of the oscillatory nanoindentation over the traditional DMA are: 1) only a small amount of sample is needed and sample preparation is minimal whereas the DMA need to test with thick specimens; 2) the moving mass of the oscillatory indenter tip is much smaller than the moving mass of a traditional DMA method, which means that the oscillatory indenter can be used to make the oscillation at much higher frequencies, leading to be a more useful method for testing at a larger frequency than traditional DMA.

2.6.2.2 Application to the aorta

In terms of the application to the aortic wall, a custom-made indenter has been developed by (Levental et al., 2010). Their devices using a 255 μm tip were applied to characterise the stiffness of the mouse aorta in three main regions: arch, thoracic and abdominal region. They demonstrated that of these regions, the highest storage modulus is in the abdominal aorta, about 0.2 kPa followed by abdominal aorta (0.17 kPa) and then the aortic arch (0.08 kPa).

Previous studies have also demonstrated that a custom-made nanoindentation test setup using smaller tips can extract the localised mechanical properties of porcine aorta. Hemmasizadeh and co-workers conducted testing on porcine thoracic aorta in the axial orientation with a 10 μm conical tip (Hemmasizadeh, Autieri and Darvish,

2012). In that study, they revealed a high elastic modulus at the inferior artery as compared to the subclavian artery. In addition, they showed a difference in the elastic modulus between the inner half and outer half of the aortic wall, implying that the outer half had higher stiffness and showed less relaxation.

Kermani and co-workers have attempted to use a custom-made nanoindentation test setup for examining the inhomogeneous and anisotropic biomechanical properties of porcine aorta in axial, circumferential, and radial orientations with a 100 μm indenter. They reported that the distal regions were stiffer than the proximal regions in both axial (approximately 118-132 kPa) and circumferential directions (about 121-142 kPa). Across the thickness of the wall there were significant differences in the mechanical behaviour. In the medial region of porcine aortic wall, stiffness was lower than the innermost region of the aorta in the axial direction (Kermani et al., 2017).

Despite the importance of nanoindentation testing, in the literature there remains a paucity of evidence on the micromechanical properties of the human aorta or human aortic diseases that have been acquired from nanoindentation testing. To the best of the author's knowledge, the first study using nanoindentation testing on human abdominal aortic aneurysm (AAA) tissues was conducted by Meekel et al. and highlighted the importance of microscopic stiffness changes within the different layers of the AAA wall (Meekel et al., 2019). They revealed that AAA tissue has a lower stiffness than healthy aortic wall (non-pathologic aorta) in the media-to-intima direction. They summarized that decreased elastic modulus and altered wall composition warrant further microscopic stiffness investigation to potentially clarify AAA pathophysiology. Chim and co-workers (2019) conducted nanoindentation

method on human aortic disease. They examined the biomechanical, biochemical, and microstructural properties between bicuspid aortic valve aneurysm (BAV-A) and tricuspid aortic valve idiopathic degenerative aneurysm (DA), compared with normal aortic tissues. They found that the BAV-A tissue was stiffer than control and DA, and that elastin within the medial layer of BAV-A was more tightly packed. They were able to correlate the micromechanical, biochemical and histology for the same specimen due to nanoindentation method allowing localized, high-resolution measurements of tissue stiffness, non-destructively. They hypothesised that localised alterations in aortic microstructure occur in dissection and aortic rupture (Chim et al., 2019).

2.7 The biomechanical and biochemical behaviours of aortic dissection

2.7.1 The biomechanical behaviours of aortic dissection

The biomechanical behaviour of diseased tissues such as aneurysmal or aortic dissection tissues are different from that of healthy aorta, with changes in compliance or wall stiffness. Several studies have explored the behaviour of healthy aortic tissues (Geest, Sacks and Vorp, 2006, Holzapfel et al., 2007, Weisbecker et al., 2012), ascending thoracic aortic aneurysm (ATAA) (Chim et al., 2019) and AAA tissues (Sokolis et al., 2012, Martin et al., 2013, Azadani et al., 2013), however there are few studies that have investigated the biomechanical behaviours from AD cases (Babu et al., 2015, Manopoulos et al., 2018, Deplano et al., 2019). (Babu et al., 2015) studied the macroscopic biomechanical properties of ascending thoracic aortic dissection (ATAD) tissues. They showed that the dissected tissues have significantly stiffer

behaviour compared to control aorta without arterial disease, confirmed by the study of (Deplano et al., 2019). They also indicated that there was no correlation between an increase in stiffness of dissected aorta and greater diameter of aorta and age. However, for dilated human ascending tissues, both circumferential and radial stress increased with age (Pasta et al., 2012).

Failure stress, defined as the maximum stress before the failure of the tissue has been reported to be higher in the circumferential direction than in the longitudinal direction for ATAD. It was also significantly higher for the outer media than for the inner media (Manopoulos et al., 2018). However, the study of Deplano and colleagues stated that the stiffness of the ascending aorta in acute Type A dissection tissues longitudinally was greater than that circumferentially (Deplano et al., 2019).

The normal aortic wall has three layers, each with its own functionality. However, these layers behave differently after formation of an AD due to the damage in their structure. As described in Section 2.1, due to a split of aortic layers within the aortic wall, FL consists of the media and adventitia layer whereas FP is partly made up of intima and media layer. Most of the wall of the TL has similar structure to a healthy aorta, except the region that forms the FP. Consequently, one could expect that the TL would be more stable than the FL. Although most of our knowledge are from studies of the layer-specific biomechanical properties of ATAA that may lead to dissection, few studies have examined the layer-specific biomechanic properties of tissue following Type A aortic dissection and there is very little information about biomechanics of Type B descending aortic dissection tissue.

Manopoulos et al. applied tensile load until failure to ATAD and measured the biomechanical properties of these tissues. They presented that there was a significantly lower failure stress of intima-media than the media-adventitia, with both layers showing lower failure stress in the longitudinal than the circumferential direction. They suggested that this is the reason why dissections occur in the inner layers with circumferential tear (Manopoulos et al., 2018). *In vitro* biaxial testing of all types of tissues (healthy, dissected and FP) for Type A ascending aortic dissection presented anisotropic behaviour. The FP of acute Type A aortic dissection illustrated a linear mechanical behaviour whereas healthy and dissected ascending aortic tissues presented non-linear behaviour. They also found that the dissected tissues were higher stiffness than healthy ascending tissues (Deplano et al., 2019).

To gain insight into AD it is important to understand the biomechanical properties at the micro-scale. Although the previous study conducted nanoindentation method to investigate the micromechanical properties of aneurysm (Meekel et al., 2019, Chim et al., 2019), to the best of our knowledge no studies to date report micromechanical properties of AD.

2.7.2 The biochemical behaviours of aortic dissection

From a biochemical point of view, medial degeneration of the aorta is a key histopathologic feature of aneurysm disease and aortic dissection as originally presented by Erdheim (Erdheim, 1929). Medial degeneration is characterized by SMCs depletion, ECM degradation (Wu *et al.*, 2013), elastin fragmentation (Bode-Jänisch et al., 2012) and pooling of PGs/GAGs within areas of the medial layer (Roccabianca,

Ateshian and Humphrey, 2014, Roccabianca, Bellini and Humphrey, 2014, Cikach et al., 2018).

Histopathologic studies revealed that tissues with thoracic aortic aneurysm (TAA) and thoracic aortic dissection (TAD) presented loss of SMCs and elastic fibres in the media (He et al., 2006). Apoptosis (cell death) of SMCs can contribute to medial expansion, increased elastic lamina breaks and abnormal matrix deposition suggesting this might lead to aortic dissection (Clarke et al., 2008).

With the characterisation and quantification of elastin and collagen, and changes in their fibrous architecture within the wall of aortic dissection, it is essential to understand that both the terms content and concentration are utilised for quantification. These terms do not always imply the same thing. A change in content has been defined as the actual amount of the fibre of interest is altered, but a change in concentration means that the amount of the fibre of interest is altered or the amount of surrounding components (collagen, elastin and sugars) are altered while the fibre of interest is maintained constant.

One study by Cattell et al. (1993) indicated in dissecting aneurysms of the thoracic aorta, the elastin content slightly increased whereas the elastin concentration gradually decreased compared with control (non-dissected). There was also a slight decrease in the concentration of elastin cross-links compared with non-dissected tissue (Cattell, Hasleton and Anderson, 1993). In another study by Wang et al. (2005), the elastin content and fibulin-5 within the aortic wall of TAD at the proximal region (ascending or transverse arch) was lower than the control group (non-aortic disease) (Wang et al., 2005). Decreased fibulin-5 expression strongly correlated with decreased

amounts and fragmentation of elastin in aortic samples from patients with TAD. Fibulin-5 is a recently recognized extracellular protein widely expressed in the basement membrane of blood vessels. In addition, there was no difference in elastin content between acute and chronic dissections in TAD tissue. They also implied that the decreased expression of fibulin-5 may impair the assembly of elastin fibres within the aortic wall of ATA tissue, which could contribute to the aortic wall susceptibility to dissection. Localized elastin fragmentation was also seen in the media layer and basement membrane of ATAD tissues accompanied by cystic medial degeneration (CMD) and medionecrosis (Sariola, Viljanen and Luosto, 1986).

Collagen is another crucial component within the aortic wall and can contribute to the structural and functional properties of the aorta. Collagen content and fibrosis were histologically investigated in the ascending thoracic aortic wall of AD. Collagen content decreases in aortic dissections and aneurysms of ascending aorta involved with a weakness of the aortic wall was presented (de Figueiredo Borges et al., 2008). In contrast, collagen content increased in the medial layer of AD tissues compared with control (non-aortic disease) (Wang et al., 2005, 2006, 2012). Increased fibrosis was also seen in the wall of dissected tissues (Wang et al., 2005, 2006, 2012). They showed that TAD patients presented significantly increased expression of aortic collagen types I and III (Wang et al., 2006). Collagen Type I and III are the predominant fibre-forming types in the arterial wall, which in general fulfil the biomechanical function of imparting tensile strength and elastic resilience. Collagen Type I may impart arterial stiffness, while collagen Type III is involved with extensibility of the aortic wall. The increased collagen in the aortic wall might induce the observed increase in aortic

stiffness. Consequently, this can enhance the aortic wall's affectability to dissection or rupture (Sariola, Viljanen and Luosto, 1986).

Increased GAG and PG levels in aortic tissues are proposed to be involved with degeneration of the medial layer in TAD (Manley, 1964, Wu et al., 2013). PGs are the most abundant glycoproteins seen in the aortic wall and can be categorised into two classes by their relative sizes: large proteoglycans (such as aggrecan and versican) and small leucine rich proteoglycans (SLRPs) (such as decorin, biglycan, lumican and mimican) (Wu et al., 2013). Versican is an abundant PG in the arterial wall that is increased after arterial injury and accumulates in advanced atherosclerotic plaques (Kenagy, Plaas and Wight, 2006). In normal aortas, most of the versican is observed in the intima and media layer, while in AD, versican degradation is more prominent in the external half of the media where the dissection commonly occurs (Gutierrez et al., 1998). Hence, versican degradation may influence the aortic wall to dissection. The role of aggrecan in the aortic wall is unclear. SLRPS bind to collagen, tropoelastin, fibronectin, and microfibrils and may also play a role in TAD formation (Wu et al., 2013). Aortic tissues obtained from patients with acute AD revealed downregulation of decorin (Mohamed et al., 2009). In mice it found that biglycan inadequacy causes spontaneous aortic dissection and rupture (Heegaard et al., 2007).

2.8 Summary

In summary, the literature review, encompassing a wide range of disciplines, presents an overview of information that is relevant to this thesis. The author introduced the

importance of studying aortic dissection tissue (FP, TL and FL) and has briefly presented the structure and components of the aortic wall. *In vitro* biomechanical testing methods across the length scale have been emphasised to address the significance of developing nanoindentation techniques for biomechanical investigation of soft tissues and structures. This technique will be used to characterise the alteration of biomechanical properties of chronic dissection throughout the thesis. Finally, the author summarised what is known about the changes in biomechanical and biochemical behaviours that occur in AD. The alteration of matrix composition such as elastin, collagen and GAG is likely to change the biomechanical properties, possibly increasing the tendency to rupture.

Therefore, a combination and correlation of biomechanical, biochemical and microstructural characterisation of chronic aortic tissues is important to enhance understanding of the mechanisms of AD. There is still a gap in the literature in terms of micromechanical behaviour on AD especially the behaviour of flap, true lumen outer wall and false lumen outer wall. To the best of the author's knowledge, no study to date has addressed this gap and examined the structure or micromechanical properties of FP, TL and FL in parallel with biochemical measurements on the same tissues.

References

- Akhtar, R. (2014) 'In vitro characterisation of arterial stiffening: From the macro-to the nano-scale', *Artery Research*, 8 (1), pp.1-8.
- Akhtar, R., Draper, E. R., Adams, D. J. and Hay, J. (2018) 'Oscillatory nanoindentation of highly compliant hydrogels: A critical comparative analysis with rheometry', *J.Mater.Res.*, 33 (8), pp.873-83.
- Akhtar, R., Draper, E., Adams, D. and Pfaff, H. (2016) 'Complex shear modulus of hydrogels using a dynamic nanoindentation method', Anonymous *Mechanics of Biological Systems and Materials, Volume 6*, 6 Springer. pp.141-5.
- Akhtar, R., Schwarzer, N., Sherratt, M., et al. (2009) 'Nanoindentation of histological specimens: mapping the elastic properties of soft tissues', *J.Mater.Res.*, 24 (3), pp.638-46.
- Akhtar, R., Sherratt, M. J., Cruickshank, J. K. and Derby, B. (2011) 'Characterizing the elastic properties of tissues', *Materials Today*, 14 (3), pp.96-105.
- Akyildiz, A. C., Speelman, L. and Gijzen, F. J. (2014) 'Mechanical properties of human atherosclerotic intima tissue', *J.Biomech.*, 47 (4), pp.773-83.
- Allan, P. L., Baxter, G. M. and Weston, M. J. (2011) *Clinical Ultrasound, 2-Volume Set E-Book: Expert Consult: Online and Print*. Elsevier Health Sciences.

- Angker, L., Swain, M. V. and Kilpatrick, N. (2003) 'Micro-mechanical characterisation of the properties of primary tooth dentine', *J.Dent.*, 31 (4), pp.261-7.
- Avanzini, A., Battini, D., Bagozzi, L. and Bisleri, G. (2014) 'Biomechanical evaluation of ascending aortic aneurysms', *Biomed.Res.Int.*, 2014 pp.820385.
- Azadani, A. N., Chitsaz, S., Mannion, A., et al. (2013) 'Biomechanical properties of human ascending thoracic aortic aneurysms', *Ann.Thorac.Surg.*, 96 (1), pp.50-8.
- Babu, A. R., Byju, A. G., Gundiah, N. and etc. (2015) 'Biomechanical properties of human ascending thoracic aortic dissections', *J.Biomech.Eng.*, 137 (8),
- Bäck, M., Gasser, T. C., Michel, J. and Caligiuri, G. (2013) 'Biomechanical factors in the biology of aortic wall and aortic valve diseases', *Cardiovasc.Res.*, 99 (2), pp.232-41.
- Bannister and Burns. (1970) 'Adaptation of the Bergman and Loxley technique for hydroxyproline determination to the autoanalyzer and its use in determining plasma hydroxyproline in the domestic fowl', *Analyst*, 95 (1131), pp.596-600.
- Berry, C., Greenwald, S. and Rivett, J. (1975) 'Static mechanical properties of the developing and mature rat aorta', *Cardiovasc.Res.*, 9 (5), pp.669-78.
- Bode-Jänisch, S., Schmidt, A., Günther, D., Stuhmann, M. and Fieguth, A. (2012) 'Aortic dissecting aneurysms—Histopathological findings', *Forensic Sci.Int.*, 214 (1-3), pp.13-7.

Britannica, E. (2010) *Britannica Book of the Year 2010*. Encyclopaedia Britannica, Inc.

Bushby, A., Ferguson, V. and Boyde, A. (2004) 'Nanoindentation of bone: Comparison of specimens tested in liquid and embedded in polymethylmethacrylate', *J.Mater.Res.*, 19 (01), pp.249-59.

Campa, J., Greenhalgh, R. and Powell, J. T. (1987) 'Elastin degradation in abdominal aortic aneurysms', *Atherosclerosis*, 65 (1-2), pp.13-21.

Canham, P. B., Finlay, H. M., Dixon, J. G., Boughner, D. R. and Chen, A. (1989) 'Measurements from light and polarised light microscopy of human coronary arteries fixed at distending pressure', *Cardiovasc.Res.*, 23 (11), pp.973-82.

Carroll, B. J., Maron, B. A. and O'Gara, P. T. (2019) 'Pathophysiology, Clinical Evaluation, and Medical Management of Aortic Dissection', *Vascular Medicine: A Companion to Braunwald's Heart Disease E-Book*, pp.415.

Cattell, M. A., Hasleton, P. S. and Anderson, J. C. (1993) 'Increased elastin content and decreased elastin concentration may be predisposing factors in dissecting aneurysms of human thoracic aorta', *Cardiovasc.Res.*, 27 (2), pp.176-81.

Cherchi, G., Coinu, R., Demuro, P., et al. (1990) 'Structural and functional modifications of human aorta proteoglycans in atherosclerosis', *Matrix*, 10 (6), pp.362-72.

- Cherry, J., Kenneth, J. and Michael, D. (2009) 'chapter 31 - Aortic Dissection'. In:
Anonymous (ed.). Comprehensive Vascular and Endovascular Surgery (Second Edition). Philadelphia: Mosby. pp.517-31.
- Chim, Y. H., Davies, H. A., Mason, D., et al. (2019) 'Bicuspid valve aortopathy is associated with distinct patterns of matrix degradation',
J.Thorac.Cardiovasc.Surg.,
- Choudhury, N., Bouchot, O., Rouleau, L., et al. (2009) 'Local mechanical and structural properties of healthy and diseased human ascending aorta tissue',
Cardiovascular Pathology, 18 (2), pp.83-91.
- Cikach, F. S., Koch, C. D., Mead, T. J., et al. (2018) 'Massive aggrecan and versican accumulation in thoracic aortic aneurysm and dissection', *JCI Insight*, 3 (5),
pp.10.1172/jci.insight.97167.
- Clarke, M. C., Littlewood, T. D., Figg, N., et al. (2008) 'Chronic apoptosis of vascular smooth muscle cells accelerates atherosclerosis and promotes calcification and medial degeneration', *Circ.Res.*, 102 (12), pp.1529-38.
- Dake, M. D., Kato, N., Mitchell, R. S., et al. (1999) 'Endovascular stent-graft placement for the treatment of acute aortic dissection', *N.Engl.J.Med.*, 340 (20), pp.1546-52.

de Figueiredo Borges, L., Jaldin, R. G., Dias, R. R., Stolf, N. A. G., Michel, J. and Gutierrez,

P. S. (2008) 'Collagen is reduced and disrupted in human aneurysms and

dissections of ascending aorta', *Hum.Pathol.*, 39 (3), pp.437-43.

Deplano, V., Boufi, M., Gariboldi, V., et al. (2019) 'Mechanical characterisation of

human ascending aorta dissection', *J.Biomech.*, 94 pp.138-46.

Derby, B. and Akhtar, R. (2015) *Mechanical properties of aging soft tissues*. Springer.

Dinardo, C. L., Venturini, G., Zhou, E. H., et al. (2014) 'Variation of mechanical

properties and quantitative proteomics of VSMC along the arterial tree', *Am J*

Physiol Heart Circ Physiol, 306 (4), pp.H505-16.

Duprey, A., Khanafer, K., Schlicht, M., Avril, S., Williams, D. and Berguer, R. (2010) 'In

vitro characterisation of physiological and maximum elastic modulus of

ascending thoracic aortic aneurysms using uniaxial tensile testing', *Eur.J. Vasc.*

Endovasc. Surg., 39 (6), pp.700-7.

Dzau, V. J., Braun-Dullaeus, R. C. and Sedding, D. G. (2002) 'Vascular proliferation and

atherosclerosis: new perspectives and therapeutic strategies', *Nat.Med.*, 8 (11),

pp.1249-56.

Ebenstein, Kuo, Rodrigo, et al. (2004) 'A nanoindentation technique for functional

evaluation of cartilage repair tissue', *J.Mater.Res.*, 19 (1), pp.273-81.

- Ebenstein and Pruitt. (2004) 'Nanoindentation of soft hydrated materials for application to vascular tissues', *Journal of Biomedical Materials Research Part A*, 69 (2), pp.222-32.
- Ebenstein and Pruitt. (2006) 'Nanoindentation of biological materials', *Nano Today*, 1 (3), pp.26-33.
- Emmott, A., Garcia, J., Chung, J., et al. (2016) 'Biomechanics of the ascending thoracic aorta: a clinical perspective on engineering data', *Can.J.Cardiol.*, 32 (1), pp.35-47.
- Erbel, R., Aboyans, V., Boileau, C., et al. (2015) '2014 ESC guidelines on the diagnosis and treatment of aortic diseases', *Revista Española de Cardiología*, 68 (3), pp.242.
- Erbel, R., Alfonso, F., Boileau, C., et al. (2001) 'Diagnosis and management of aortic dissection: task force on aortic dissection, European society of cardiology', *Eur.Heart J.*, 22 (18), pp.1642-81.
- Erbel, R., Aboyans, V., Boileau, C., et al. (2014) '2014 ESC Guidelines on the diagnosis and treatment of aortic diseases: Document covering acute and chronic aortic diseases of the thoracic and abdominal aorta of the adult. The Task Force for the Diagnosis and Treatment of Aortic Diseases of the European Society of Cardiology (ESC)', *Eur.Heart J.*, 35 (41), pp.2873-926.

- Erdheim, J. (1929) 'Medionecrosis aortae idiopathica', *Virchows Archiv für pathologische Anatomie und Physiologie und für klinische Medizin*, 273 (2), pp.454-79.
- Ferrara, A., Morganti, S., Totaro, P., Mazzola, A. and Auricchio, F. (2016) 'Human dilated ascending aorta: mechanical characterization via uniaxial tensile tests', *J Mech Behav Biomed Mater*, 53 pp.257-71.
- Fiedler, L. (2007) *Role of decorin in control of endothelial cell behaviour*. Cardiff University (United Kingdom).
- Field, J. and Swain, M. (1993) 'A simple predictive model for spherical indentation', *J.Mater.Res.*, 8 (2), pp.297-306.
- Fischer-Cripps, A. C. (2002) 'Mechanical Engineering Series',
- Fratzl, P. (2008) 'Collagen: structure and mechanics, an introduction'. In: Anonymous (ed.). *Collagen*. Springer. pp.1-13.
- Fung, Y. (2013) *Biomechanics: mechanical properties of living tissues*. Springer Science & Business Media.
- Gasser, T. C. (2017) 'Aorta'. In: Anonymous (ed.). *Biomechanics of Living Organs*. Elsevier. pp.169-91.

- Geest, J. P. V., Sacks, M. S. and Vorp, D. A. (2004) 'Age dependency of the biaxial biomechanical behavior of human abdominal aorta', *J.Biomech.Eng.*, 126 (6), pp.815-22.
- Geest, J. P. V., Sacks, M. S. and Vorp, D. A. (2006) 'The effects of aneurysm on the biaxial mechanical behavior of human abdominal aorta', *J.Biomech.*, 39 (7), pp.1324-34.
- Grant. (1967) 'Content and distribution of aortic collagen, elastin and carbohydrate in different species', *J.Atheroscler.Res.*, 7 (4), pp.463-72.
- Guglielmi, P., Herbert, E., Tartivel, L., et al. (2015) 'Mechanical characterization of oligo (ethylene glycol)-based hydrogels by dynamic nanoindentation experiments', *J Mech Behav Biomed Mater*, 46 pp.1-10.
- Guo and Kassab. (2003) 'Variation of mechanical properties along the length of the aorta in C57bl/6 mice', *Am J Physiol Heart Circ Physiol*, 285 (6), pp.H2614-22.
- Gutierrez, P., Reis, M., Higuchi, M., Aiello, V., Stolf, N. and Lopes, E. (1998) 'Distribution of hyaluronan and dermatan/chondroitin sulfate proteoglycans in human aortic dissection', *Connect.Tissue Res.*, 37 (3-4), pp.151-61.
- Hapugoda, S. and Gaillard, F. (2017) *Aortic arch [Online]*
<https://radiopaedia.org/articles/aortic-arch>

- Harkness, M. L., Harkness, R. D., McDonald, D. A. and etc. (1957) 'The collagen and elastin content of the arterial wall in the dog', *Proc.R.Soc.Lond.B.Biol.Sci.*, 146 (925), pp.541-51.
- Hay, J. (2015) '*Dynamic Mechanical Analysis (DMA) of Polymers by Oscillatory Indentation*', *google*. KLA-Tencor Company:
- Hayes, S., Goruppa, A. and Jones, F. (2004) 'Dynamic nanoindentation as a tool for the examination of polymeric materials', *J.Mater.Res.*, 19 (11), pp.3298-306.
- He and Roach. (1994) 'The composition and mechanical properties of abdominal aortic aneurysms', *J Vasc Surg*, 20 (1), pp.6-13.
- He, R., Guo, D., Estrera, A. L., et al. (2006) 'Characterization of the inflammatory and apoptotic cells in the aortas of patients with ascending thoracic aortic aneurysms and dissections', *J.Thorac.Cardiovasc.Surg.*, 131 (3), pp.671,678. e2.
- Heegaard, A. M., Corsi, A., Danielsen, C. C., et al. (2007) 'Biglycan deficiency causes spontaneous aortic dissection and rupture in mice', *Circulation*, 115 (21), pp.2731-8.
- Hemmasizadeh, A., Autieri, M. and Darvish, K. (2012) 'Multilayer material properties of aorta determined from nanoindentation tests', *J Mech Behav Biomed Mater*, 15 pp.199-207.

Hiratzka, L. F., Bakris, G. L., Beckman, J. A., et al. (2010) '2010

ACCF/AHA/AATS/ACR/ASA/SCA/SCAI/SIR/STS/SVM Guidelines for the Diagnosis and Management of Patients With Thoracic Aortic Disease', *J.Am.Coll.Cardiol.*, 55 (14), pp.e27-e129.

Holzapfel, G. A. (2008) 'Collagen in arterial walls: biomechanical aspects'. In:

Anonymous (ed.). *Collagen*. Springer. pp.285-324.

Holzapfel, G. A., Gasser, T. C. and Ogden, R. W. (2000) 'A new constitutive framework

for arterial wall mechanics and a comparative study of material models', *Journal of elasticity and the physical science of solids*, 61 (1-3), pp.1-48.

Holzapfel, G. A., Sommer, G., Auer, M., Regitnig, P. and Ogden, R. W. (2007) 'Layer-

specific 3D residual deformations of human aortas with non-atherosclerotic intimal thickening', *Ann.Biomed.Eng.*, 35 (4), pp.530-45.

Holzapfel, G. A., Sommer, G., Gasser, C. T. and Regitnig, P. (2005) 'Determination of

layer-specific mechanical properties of human coronary arteries with nonatherosclerotic intimal thickening and related constitutive modeling', *Am J Physiol Heart Circ Physiol*, 289 (5), pp.H2048-58.

Howard and Macarak. (1989) 'Localization of collagen types in regional segments of

the fetal bovine aorta', *Lab.Invest.*, 61 (5), pp.548-55.

Huh, J., Coselli, J. S. and LeMaire, S. A. (2013) 'Chapter 35 - Surgical Therapy for Aortic Dissection' *ScienceDirect*. ID: 283145. Philadelphia: W.B. Saunders. pp.433-46.

Humphrey, J. (2013a) *Cardiovascular solid mechanics: cells, tissues, and organs*. Springer Science & Business Media.

Humphrey, J. (2013b) 'Possible mechanical roles of glycosaminoglycans in thoracic aortic dissection and associations with dysregulated transforming growth factor-beta', *J.Vasc.Res.*, 50 (1), pp.1-10.

Iliopoulos, D. C., Kritharis, E. P., Giagini, A. T., Papadodima, S. A. and Sokolis, D. P. (2009) 'Ascending thoracic aortic aneurysms are associated with compositional remodeling and vessel stiffening but not weakening in age-matched subjects', *J.Thorac.Cardiovasc.Surg.*, 137 (1), pp.101-9.

Jacob, S. (2007) *Human anatomy: a clinically-orientated approach*. Elsevier Health Sciences.

Kamenskiy, A. V., Dzenis, Y. A., Kazmi, S. A. J., et al. (2014) 'Biaxial mechanical properties of the human thoracic and abdominal aorta, common carotid, subclavian, renal and common iliac arteries', *Biomech. Model. Mechanobiol.*, 13 (6), pp.1341-59.

Karmonik, C., Duran, C., Shah, D. J., et al. (2012) 'Preliminary findings in quantification of changes in septal motion during follow-up of type B aortic dissections', *J Vasc Surg*, 55 (5), pp.1419,1426. e1.

- Kenagy, R. D., Plaas, A. H. and Wight, T. N. (2006) 'Versican degradation and vascular disease', *Trends Cardiovasc.Med.*, 16 (6), pp.209-15.
- Kermani, G., Hemmasizadeh, A., Assari, S., Autieri, M. and Darvish, K. (2017) 'Investigation of inhomogeneous and anisotropic material behavior of porcine thoracic aorta using nano-indentation tests', *J Mech Behav Biomed Mater*, 69 pp.50-6.
- Khanafer, K., Duprey, A., Zainal, M., Schlicht, M., Williams, D. and Berguer, R. (2011) 'Determination of the elastic modulus of ascending thoracic aortic aneurysm at different ranges of pressure using uniaxial tensile testing', *J.Thorac.Cardiovasc.Surg.*, 142 (3), pp.682-6.
- Khanafer, K., Schlicht, M. S. and Berguer, R. (2013) 'How should we measure and report elasticity in aortic tissue?', *Eur. J. Vasc. Endovasc. Surg.*, 45 (4), pp.332-9.
- Kirali, K. and Günay, D. (2017) 'Isolated Aortic Root Aneurysms'. In: Anonymous (ed.). *Aortic Aneurysm*. InTech.
- Kohn, J. C., Lampi, M. C., Reinhart-King, C. A. and etc. (2015) 'Age-related vascular stiffening: causes and consequences', *Front.Genet.*, 6 pp.112.
- Kristensen, J. H., Thorlacius-Ussing, J., Rønnow, S. R. and Karsdal, M. A. (2019) 'Chapter 30 - Elastin'. In: Anonymous (ed.). *Biochemistry of Collagens, Laminins and Elastin (Second Edition)*. Academic Press. [ScienceDirect]. pp.265-73.

Lakatta. (2013) 'The reality of aging viewed from the arterial wall', *Artery Res.*, 7 (2), pp.73-80.

Lakatta and Levy. (2003) 'Arterial and cardiac aging: major shareholders in cardiovascular disease enterprises: Part I: aging arteries: a “set up” for vascular disease', *Circulation*, 107 (1), pp.139-46.

Levental, I., Levental, K., Klein, E., et al. (2010) 'A simple indentation device for measuring micrometer-scale tissue stiffness', *Journal of Physics: Condensed Matter*, 22 (19), pp.194120.

MacManus, D., Pierrat, B., Murphy, J. G. and Gilchrist, M. (2015) 'Dynamic mechanical properties of murine brain tissue using micro-indentation', *J.Biomech.*, 48 (12), pp.3213-8.

Manley, G. (1964) 'Histology of the Aortic Media in Dissecting Aneurysms', *J.Clin.Pathol.*, 17 pp.220-4.

Manopoulos, C., Karathanasis, I., Kouerinis, I., et al. (2018) 'Identification of regional/layer differences in failure properties and thickness as important biomechanical factors responsible for the initiation of aortic dissections', *J.Biomech.*, 80 pp.102-10.

Maron, B. A. and O'Gara, P. T. (2013) 'Chapter 34 - Pathophysiology, Clinical Evaluation, and Medical Management of Aortic Dissection'. In: Anonymous (ed.). *Vascular*

Medicine: A Companion to Braunwald's Heart Disease (Second Edition).

Philadelphia: W.B. Saunders. pp.419-32.

Martin, C., Sun, W., Pham, T. and Elefteriades, J. (2013) 'Predictive biomechanical analysis of ascending aortic aneurysm rupture potential', *Acta Biomater*, 9 (12), pp.9392-400.

Meekel, J. P., Mattei, G., Costache, V. S., Balm, R., Blankensteijn, J. D. and Yeung, K. K. (2019) 'A multilayer micromechanical elastic modulus measuring method in ex vivo human aneurysmal abdominal aortas', *Acta Biomater*, 96 pp.345-53.

Mohamed, S. A., Sievers, H. H., Hanke, T., et al. (2009) 'Pathway analysis of differentially expressed genes in patients with acute aortic dissection', *Biomarker insights*, 4 pp.BMI. S2530.

Mozos, I., Maidana, J. P., Stoian, D. and Stehlik, M. (2017) 'Gender differences of arterial stiffness and arterial age in smokers', *International journal of environmental research and public health*, 14 (6), pp.565.

Nakashima, Y., Kurozumi, T., Sueishi, K. and Tanaka, K. (1990) 'Dissecting aneurysm: A clinicopathologic and histopathologic study of 111 autopsied cases', *Human Pathology*, 21 (3), pp.291-6.

- O'Connell, M. K., Murthy, S., Phan, S., et al. (2008) 'The three-dimensional micro-and nanostructure of the aortic medial lamellar unit measured using 3D confocal and electron microscopy imaging', *Matrix Biology*, 27 (3), pp.171-81.
- Odegard, G., Gates, T. and Herring, H. (2005) 'Characterization of viscoelastic properties of polymeric materials through nanoindentation', *Exp.Mech.*, 45 (2), pp.130-6.
- Pasta, S., Phillippi, J. A., Gleason, T. G. and Vorp, D. A. (2012) 'Effect of aneurysm on the mechanical dissection properties of the human ascending thoracic aorta', *J.Thorac.Cardiovasc.Surg.*, 143 (2), pp.460-7.
- Peña, J. A., Corral, V., Martínez, M. A. and Peña, E. (2018) 'Over length quantification of the multiaxial mechanical properties of the ascending, descending and abdominal aorta using Digital Image Correlation', *J Mech Behav Biomed Mater*, 77 pp.434-45.
- Peng, S., Larsson, A., Wassberg, E., et al. (2007) 'Role of aggregated medin in the pathogenesis of thoracic aortic aneurysm and dissection', *Laboratory Investigation*, 87 (12), pp.1195-205.
- Peterss, S., Mansour, A. M., Ross, J. A., et al. (2016) 'Changing Pathology of the Thoracic Aorta From Acute to Chronic Dissection: Literature Review and Insights', *J.Am.Coll.Cardiol.*, 68 (10), pp.1054-65.

- Poolthong, S., Mori, T. and Swain, M. V. (2001) 'Determination of elastic modulus of dentin by small spherical diamond indenters', *Dent.Mater.J.*, 20 (3), pp.227-36.
- Quint, L. E., Platt, J. F., Sonnad, S. S., Deeb, G. M. and Williams, D. M. (2003) 'Aortic intimal tears: detection with spiral computed tomography', *Journal of Endovascular Therapy*, 10 (3), pp.505-10.
- Rho, J., Tsui, T. Y. and Pharr, G. M. (1997) 'Elastic properties of human cortical and trabecular lamellar bone measured by nanoindentation', *Biomaterials*, 18 (20), pp.1325-30.
- Richardon, A. M., Manzano, G. and Levi, A. D. (2019) '4 - Relevant Surgical Anatomy of the Lateral and Anterior Lumbar Spine' *ScienceDirect*. Elsevier. pp.27-35.
- Roccabianca, S., Ateshian, G. and Humphrey, J. (2014) 'Biomechanical roles of medial pooling of glycosaminoglycans in thoracic aortic dissection', *Biomech. Model. Mechanobiol.*, 13 (1), pp.13-25.
- Roccabianca, S., Bellini, C. and Humphrey, J. (2014) 'Computational modelling suggests good, bad and ugly roles of glycosaminoglycans in arterial wall mechanics and mechanobiology', *J. R. Soc. Interface*, 11 (97), pp.20140397.
- Rosenbloom, J., Abrams, W. R. and Mecham, R. (1993) 'Extracellular matrix 4: the elastic fiber', *FASEB J.*, 7 (13), pp.1208-18.

- Safar, M. E. and Lévy, B. I. (2007) 'Chapter 13 - Resistance Vessels in Hypertension'
ScienceDirect. Philadelphia: Mosby. pp.145-50.
- Sariola, H., Viljanen, T. and Luosto, R. (1986) 'Histological pattern and changes in extracellular matrix in aortic dissections', *J.Clin.Pathol.*, 39 (10), pp.1074-81.
- Schlatmann, T. J. and Becker, A. E. (1977) 'Histologic changes in the normal aging aorta: implications for dissecting aortic aneurysm', *Am.J.Cardiol.*, 39 (1), pp.13-20.
- Schriefl, A. J., Schmidt, T., Balzani, D., Sommer, G. and Holzapfel, G. A. (2015) 'Selective enzymatic removal of elastin and collagen from human abdominal aortas: Uniaxial mechanical response and constitutive modeling', *Acta Biomater.*, 17 pp.125-36.
- Schriefl, A. J., Wolinski, H., Regitnig, P., Kohlwein, S. D. and Holzapfel, G. A. (2013) 'An automated approach for three-dimensional quantification of fibrillar structures in optically cleared soft biological tissues', *J. R. Soc. Interface*, 10 (80), pp.20120760.
- Schriefl, A. J., Zeindlinger, G., Pierce, D. M., Regitnig, P. and Holzapfel, G. A. (2012) 'Determination of the layer-specific distributed collagen fibre orientations in human thoracic and abdominal aortas and common iliac arteries', *J. R. Soc. Interface*, 9 (71), pp.1275-86.

- Shah, S. B., Witzenburg, C., Hadi, M. F., et al. (2014) 'Prefailure and failure mechanics of the porcine ascending thoracic aorta: experiments and a multiscale model', *J.Biomech.Eng.*, 136 (2),
- Shekhonin, B. V., Domogatsky, S. P., Muzykantov, V. R., Idelson, G. L. and Rukosuev, V. S. (1985) 'Distribution of type I, III, IV and V collagen in normal and atherosclerotic human arterial wall: immunomorphological characteristics', *Coll.Relat.Res.*, 5 (4), pp.355-68.
- Sherman, V. R., Yang, W. and Meyers, M. A. (2015) 'The materials science of collagen', *J Mech Behav Biomed Mater*, 52 pp.22-50.
- Smith, E. R., Tomlinson, L. A., Ford, M. L., McMahon, L. P., Rajkumar, C. and Holt, S. G. (2012) 'Elastin degradation is associated with progressive aortic stiffening and all-cause mortality in predialysis chronic kidney disease', *Hypertension*, 59 (5), pp.973-8.
- Sokolis, D. P. (2007) 'Passive mechanical properties and structure of the aorta: segmental analysis', *Acta physiologica*, 190 (4), pp.277-89.
- Sokolis, D. P., Boudoulas, H. and Karayannacos, P. E. (2008) 'Segmental differences of aortic function and composition: clinical implications', *Hellenic J Cardiol*, 49 (3), pp.145-54.

- Sokolis, D. P., Kefaloyannis, E. M., Kouloukoussa, M., Marinos, E., Boudoulas, H. and Karayannacos, P. E. (2006) 'A structural basis for the aortic stress-strain relation in uniaxial tension', *J.Biomech.*, 39 (9), pp.1651-62.
- Sokolis, D. P., Kritharis, E. P. and Iliopoulos, D. C. (2012) 'Effect of layer heterogeneity on the biomechanical properties of ascending thoracic aortic aneurysms', *Med.Biol.Eng.Comput.*, 50 (12), pp.1227-37.
- Sokolis, D. P., Kritharis, E. P., Giagini, A. T., Lampropoulos, K. M., Papadodima, S. A. and Iliopoulos, D. C. (2012) 'Biomechanical response of ascending thoracic aortic aneurysms: association with structural remodelling', *Comput.Methods Biomech.Biomed.Engin.*, 15 (3), pp.231-48.
- Sonesson, B., Hansen, F., Stale, H. and Länne, T. (1993) 'Compliance and diameter in the human abdominal aorta—the influence of age and sex', *Eur.J.Vasc.Surg.*, 7 (6), pp.690-7.
- Stecco, C. (2014) *Functional Atlas of the Human Fascial System E-Book*. Elsevier Health Sciences.
- Stegemann, J. P., Hong, H. and Nerem, R. M. (2005) 'Mechanical, biochemical, and extracellular matrix effects on vascular smooth muscle cell phenotype', *J.Appl.Physiol.*, 98 (6), pp.2321-7.

- Svensson, L. G., Labib, S. B., Eisenhauer, A. C. and Butterly, J. R. (1999) 'Intimal tear without hematoma: an important variant of aortic dissection that can elude current imaging techniques', *Circulation*, 99 (10), pp.1331-6.
- Tarbell, J. M., Shi, Z., Dunn, J. and Jo, H. (2014) 'Fluid mechanics, arterial disease, and gene expression', *Annu.Rev.Fluid Mech.*, 46
- Tonar, Z., Kubíková, T., Prior, C., et al. (2015) 'Segmental and age differences in the elastin network, collagen, and smooth muscle phenotype in the tunica media of the porcine aorta', *Annals of Anatomy-Anatomischer Anzeiger*, 201 pp.79-90.
- Tsamis, A., Krawiec, J. T. and Vorp, D. A. (2013) 'Elastin and collagen fibre microstructure of the human aorta in ageing and disease: a review', *J.R.Soc.Interface*, 10 (83), pp.20121004.
- Vorp, D. A., Schiro, B. J., Ehrlich, M. P., Juvonen, T. S., Ergin, M. A. and Griffith, B. P. (2003) 'Effect of aneurysm on the tensile strength and biomechanical behavior of the ascending thoracic aorta', *Ann.Thorac.Surg.*, 75 (4), pp.1210-4.
- Wang, LeMaire, S. A., Chen, L., et al. (2006) 'Increased collagen deposition and elevated expression of connective tissue growth factor in human thoracic aortic dissection', *Circulation*, 114 (1_supplement), pp.I,200-I-205.
- Wang, LeMaire, S., Chen, L., et al. (2005) 'Decreased expression of fibulin-5 correlates with reduced elastin in thoracic aortic dissection', *Surgery*, 138 (2), pp.352-9.

- Wang and Niu. (2015) 'Nanoindentation of soft solids by a flat punch', *Acta Mechanica Sinica*, 31 (4), pp.531-5.
- Wang and Patterson. (2015) *Atherosclerosis: risks, mechanisms, and therapies*. John Wiley & Sons.
- Wang, Zhang, J., Fu, W., et al. (2012) 'Association of smooth muscle cell phenotypes with extracellular matrix disorders in thoracic aortic dissection', *J Vasc Surg*, 56 (6), pp.1698,1709. e1.
- Weisbecker, H., Pierce, D. M., Regitnig, P. and Holzapfel, G. A. (2012) 'Layer-specific damage experiments and modeling of human thoracic and abdominal aortas with non-atherosclerotic intimal thickening', *J Mech Behav Biomed Mater*, 12 pp.93-106.
- Wigh. (2008) 'Arterial remodeling in vascular disease: a key role for hyaluronan and versican', *Front.Biosci.*, 13 (4), pp.933-7.
- Wight. (1989) 'Cell biology of arterial proteoglycans', *Arteriosclerosis*, 9 (1), pp.1-20.
- Wu, D., Shen, Y. H., Russell, L., Coselli, J. S. and LeMaire, S. A. (2013) 'Molecular mechanisms of thoracic aortic dissection', *J.Surg.Res.*, 184 (2), pp.907-24.
- Zhang, T., Zhang, R., Lv, Y., et al. (2019) 'Glycosaminoglycans in biological samples–towards identification of novel biomarkers', *TrAC Trends in Analytical Chemistry*, pp.115732.

Ziganshin, B. A. and Elefteriades, J. A. (2019) 'Mechanics of the Thoracic Aortic Wall'. In:

Anonymous (ed.). *Surgical Management of Aortic Pathology*. Springer. pp.149-62.

Chapter 3

Materials and Methods

To characterise micromechanical properties and associated biochemical changes in chronic dissected aortic tissue, initially ovine aortic tissue was utilised to validate methods prior to utilising precious human biopsy samples. This chapter details all the materials and methods relevant to the work presented in Chapters 4 and 5. Sample preparation for the ovine and human chronic tissues are described in the Materials section. Following this, detailed description experimental methods of nanoindentation testing, creep testing (time-dependent deformation), biochemical analysis to quantify ECM components and FTIR to map ECM distribution in the tissues are presented.

3.1 Materials

3.1.1 Ovine aortic tissue preparation

Six fresh ovine aortas (*Ovis aries*, 6-8 months, males) were obtained from a local butcher on the day of slaughter and immediately transferred to the laboratory for testing. Three of the aortas were used for nanoindentation testing and three for uniaxial tensile testing. Any excess connective tissue and adipose tissue was removed from the aortic surface and Full methodological details have been presented elsewhere (Chim et al., 2019). All aortic specimens were snap frozen for storage at a temperature of -80°C and thawed at room temperature prior to testing.

Figure 3.1 summarises the tissue preparation and testing method that was conducted for nanoindentation, tensile testing, FTIR analysis and creep testing.

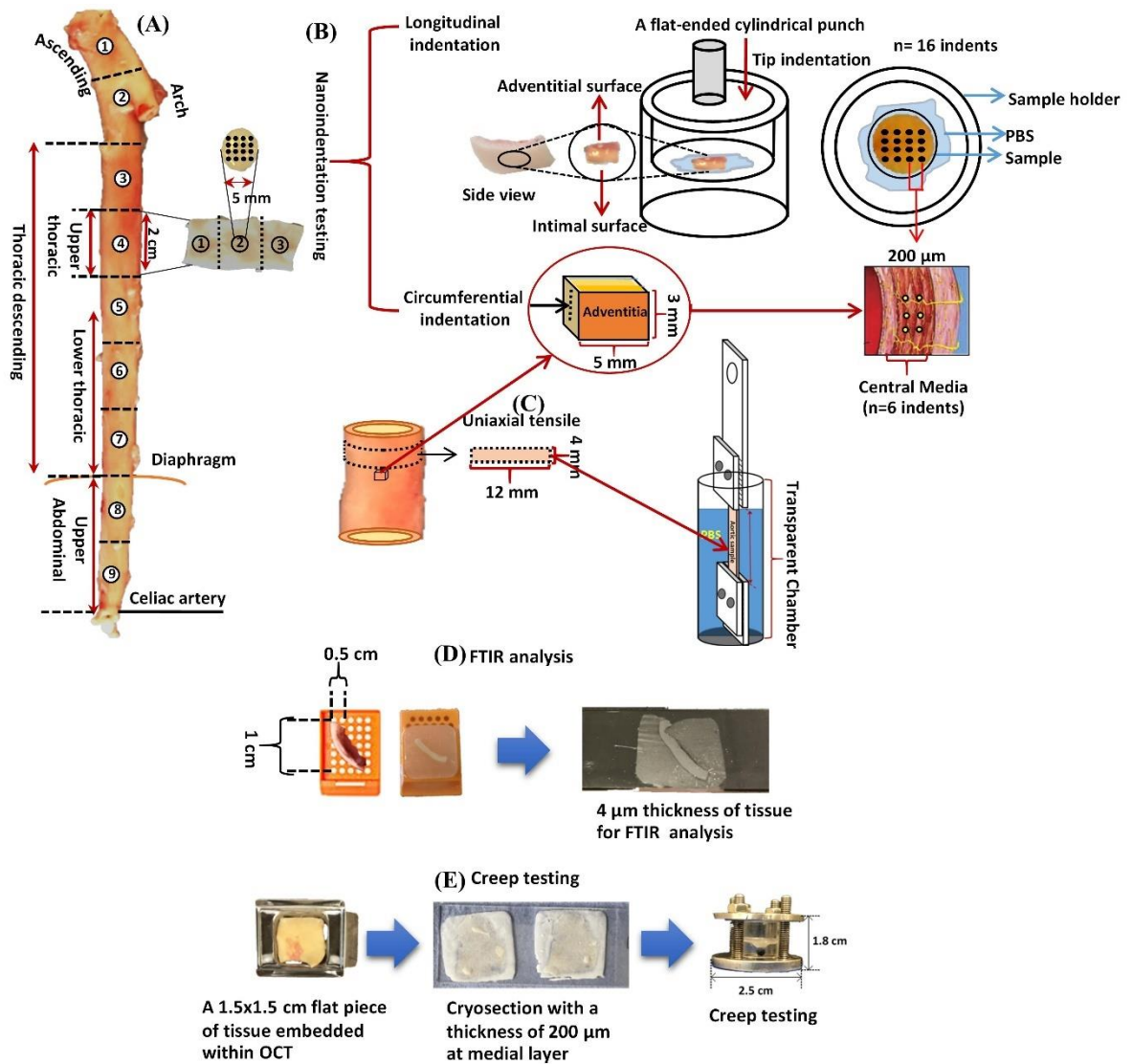


Figure 3.1 Schematic representation of the experimental approach for ovine model: (A) The aortic locations where the tissue was taken from for nanoindentation testing. Samples were extracted from aortic root through to the celiac artery. (B) Schematic representation of longitudinal indentation of side view of aortic biopsy specimen with adventitial and intimal faces marked and circumferential indentation of aortic sections for nanoindentation testing. The specimen holder and the orientation of the flat-ended cylindrical punch are also shown. (C) Schematic representation of tensile set up using mechanical clamps and sample for testing hydrated with phosphate buffered saline (PBS) in the liquid cell. (D) Schematic representation of tissue preparation for FTIR analysis. (E) Schematic representation of tissue preparation and an assembled specimen holder for creep behaviour testing.

For nanoindentation, testing was conducted in three orientations: longitudinal (adventitial and intimal face) and circumferential (central media layer). For the longitudinal orientation, the entire aorta was split into nine sections, separated by 2 cm in length from the aortic root to the celiac artery region. Each of these sections was used to create three 5 mm circular biopsy punches (3 biopsies per section, a total of 81 biopsies) (Figure 3.1A, B). For the circumferential orientation, the aorta was subdivided into three main parts: the ascending aorta, upper thoracic aorta and upper abdominal aorta, matching the uniaxial testing. Three samples were tested at the central medial layer for each location.

For uniaxial testing, aorta samples were collected from the following three regions: the ascending, upper thoracic aorta and upper abdominal regions. Three circumferential strips were prepared per region which had a width of 4 mm and were cut using a double-bladed tool. In total, there were 27 aortic strips. Each strip had a testing length of 12 mm after clamping (Figure 3.1C).

For FTIR analysis, the aortic tissues were collected from the same ovine ascending region and cut into a slim strip with a length of approximately 0.5 cm and placed into a cassette. This was then formalin-fixed and paraffin embedded. 4 μm thickness of tissue were sectioned consecutively and placed on Low-e microscope slides (Kevley Technologies, Chesterland) for FTIR analysis and placed on glass slides (Lavender X-tra Slides, Leica, Milton Keynes, U.K.) for histological staining (Figure 3.1D).

For creep testing, the ovine aortic tissues were collected from ascending and descending regions. A 1.5x1.5 cm flat piece of tissue was cut and any excess connective and adipose tissue removed. A small amount of OCT (optimal cutting

temperature) embedding medium (Cellpath™ OCT Embedding Matrix) was put into a mould. The flat piece of aorta was then embedded within OCT and immediately snap-frozen using dry ice and super-cooled isopentane for cryosectioning. Cryosections with a thickness of 200 µm were cut using a Thermo Scientific™ Microm HM525 NX Cryostat (Fisher Scientific UK Ltd, Loughborough) and adhered onto the glass slide (Figure 3.1E). All cryosectioned tissues were kept in the -80°C freezer until testing. Before creep deformation measurements, the sectioned tissue was thawed at room temperature for 5 minutes and then washed to remove any excess OCT compound with distilled water.

3.2.1 Human chronic AD tissue harvest and sample preparation

All study protocol was approved by the Liverpool Bio-Innovation Hub (LBIH) biobank (project approval references 15-06 and 19-09). The LBIH Biobank confers ethical approval for the use of samples through their ethical approval as a Research Tissue Bank (REC reference 14/NW/1212, NRES Committee North West–Haydock). A segment of fresh aortic wall was excised from resection surgery obtained from patients undergoing elective surgical repair for chronic dissected aneurysm at the Liverpool Heart Chest Hospital (LHCH). The chronic aortic tissues were collected from 16 consented patients. The collected tissues were grouped into three main sample types: FP (n=10 specimens), TL (n=9 specimens) and FL (n=5 specimens). The aortic tissues were cut and any excess connective tissue and adipose tissue was removed from the surface of the aortas (Chim et al., 2019). They were immediately snap-frozen using dry ice and super-cooled isopentane and were stored in a -80°C freezer until testing. A list of available chronic AD tissues for each experiment was presented in Table 3.1.

Table 3.1 A list of chronic AD was used for each experiment.

Patient ID	Age, Year	Gender	Syndromic (Marfan)	Hypertension	Cholesterol	Family history aneurysm	Tissue type	Nanoindentation	Ball indentation	Biochemical analysis	%elastin, %collagen content	Elastin fragmentation	Alcian blue staining	FTIR Analysis	CT scan Image
894-15	65	M	N	Y	Y	N	TL	✓	X	✓	✓	✓	X	X	X
05-00001-16	45	M	Y	N	N	N	FP	✓	✓	✓	✓	✓	X	X	X
05-00020-16	49	M	N	N	N	N	FP	✓	✓	✓	✓	✓	X	X	X
							TL	✓	✓	✓	✓	✓	X	X	X
05-00023-16	37	M	N	Y	N	Y	TL	✓	X	✓	✓	✓	X	X	X
05-00027-16	66	M	N	Y	Y	N	TL	✓	✓	✓	✓	✓	✓	X	X
05-00045-16	68	M	N	Y	Y	N	FP	✓	✓	✓	✓	✓	✓	X	X
05-00060-16	77	M	N	N	Y	N	TL	✓	✓	✓	✓	✓	X	X	X
05-00064-16	54	M	Y	N	N	N	FP	✓	✓	✓	✓	✓	✓	X	X
05-00070-16	62	M	N	N	N	N	FP	✓	✓	✓	✓	✓	✓	X	X
							TL	✓	X	✓	✓	✓	✓	X	X
05-00020-17	77	M	N	Y	Y	N	FP	✓	✓	✓	✓	✓	X	X	X
05-00061-17	70	F	N	Y	Y	N	FL	✓	✓	✓	✓	✓	X	X	X
05-00070-17	50	M	Y	N	N	N	FL	✓	✓	✓	✓	✓	X	X	X
05-00003-18	40	M	N	N	Y	N	FP	✓	✓	✓	✓	✓	✓	X	X
							TL	✓	✓	✓	X	X	X	X	X
							FL	✓	✓	✓	✓	✓	X	X	X
05-00040-18	60	M	N	Y	Y	N	FP	✓	✓	✓	✓	✓	X	X	X
05-00064-18	39	M	Y	Y	N	Y	FP	✓	✓	✓	✓	✓	✓	✓	✓
							TL	✓	✓	✓	✓	✓	✓	✓	✓
							FL	✓	✓	✓	✓	✓	✓	✓	✓
05-00017-19	67	M	N	Y	Y	N	FP	✓	✓	✓	✓	✓	X	✓	✓
							TL	✓	✓	✓	✓	✓	X	✓	✓
							FL	✓	✓	✓	✓	✓	✓	✓	✓

M, male; *F*, Female; *Y*, Yes; *N*, No.

3.2 Methods

3.2.1 Biomechanical testing

3.1.2.1 Uniaxial tensile testing

Uniaxial tensile was performed on an Instron 3366 series instrument (Instron, Norwood, MA, USA). The machine was set up using a 10 N load cell with a specified accuracy of 0.025 N. The thickness of the extracted specimens was measured using a digital Vernier calliper with 10 μm accuracy and average values were obtained from five measurements along the length of each strip. The strip was held between two mechanical clamps with a notched surface (Figure 3.2A). To prevent slippage, sandpaper was used between the specimen and clamps. Following this, the clamped aortic strip was immersed in a phosphate buffered saline (PBS) bath to maintain hydration of the tissue during testing (Figure 3.2B). Ten cycles were used to obtain repeatable stress–strain curves at a rate of 10 mm/min. The rate was selected based on a previous study (Khanafer et al., 2011). Subsequently, the aortic strip was loaded until failure at the same rate of 10 mm/min.

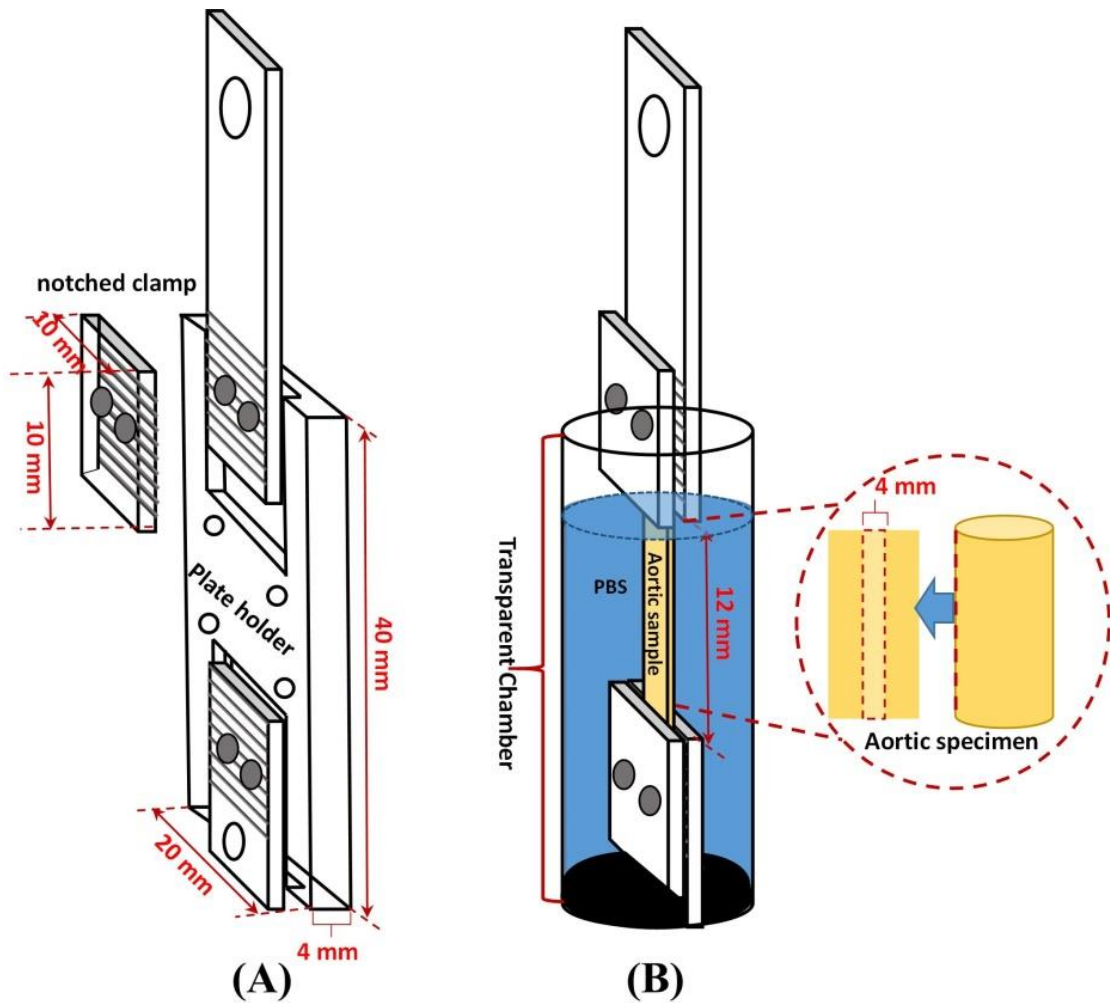


Figure 3. 2 Schematic diagram of the tensile set up: (A) The mechanical clamps: the upper clamp was moved whilst the lower clamp remained fixed in position. (B) Sample for testing hydrated with PBS in the liquid cell.

Applied force and elongation were recorded for each test. The true stress and true strain were determined using the approach presented in the literature, with the assumption that the tissue is incompressible (Carew et al., 1968, Khanafer et al., 2011). The following parameters were derived from the data: physiological elastic modulus (PE), tangent modulus (TM) at 0.5 strain, the maximum elastic modulus (ME) and failure stress.

To calculate the PE, we have assumed that the aortic pressure range in ovine is 60-90 kPa, based on literature (Pagani et al., 1979, Segers et al., 2001). Laplace's law was used to compute circumferential stress based on this pressure range. The PE was defined as the slope of the stress-strain curve within this pressure range. The TM at 0.5 strain was obtained from the gradient of the stress-strain curve at this strain value. ME was obtained from each true stress-strain curve as the maximum slope before pre-failure stress (Figure 3.3).

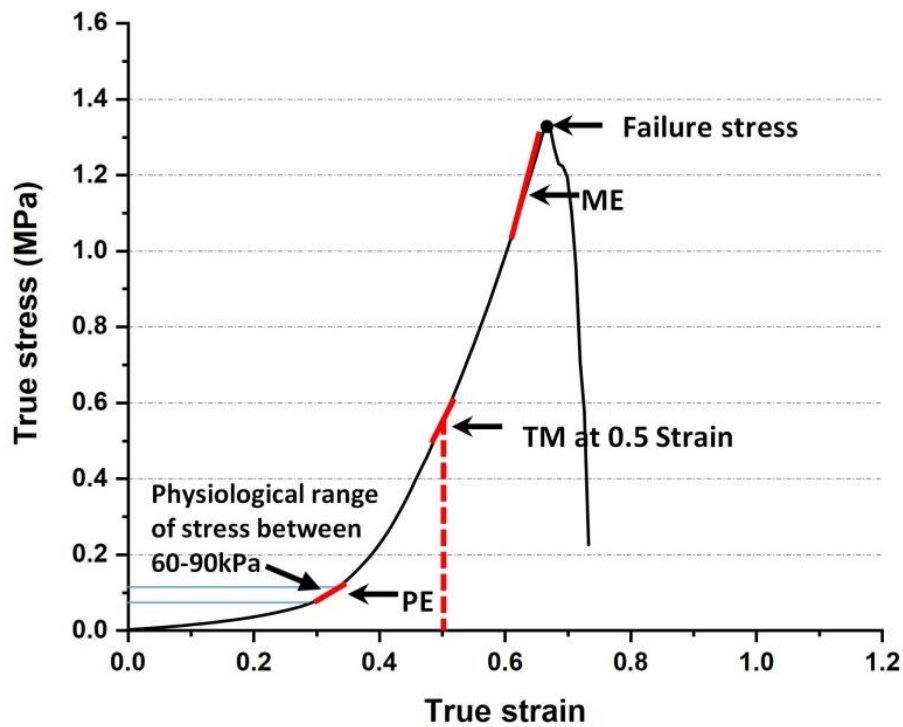


Figure 3.3 Typical stress-strain relationship showing the points on the curve which were used to calculate physiological elastic modulus (PE), tangent modulus (TM) at 0.5 strain, maximum elastic modulus (ME) and failure stress.

3.1.2.2 Nanoindentation

Oscillatory nanoindentation was performed with a KLA-Tencor Nanoindenter G200 system equipped with a DCM-II head (California, USA) to characterise the micromechanical properties of aortic tissues. The nanoindentation system and methodology used in our experiment was similar to that presented in detail previously (Akhtar et al., 2018) using a 100 μm diameter flat-ended cylindrical punch (Synton-MDP Ltd, Nidau, Switzerland) mounted on the DCM II head (Akhtar et al., 2018). An aortic sample was placed on a liquid cell that was designed with appropriate depth able to hold the specimen hydrated with PBS. A pre-test compression of 8 μm was used with all tests conducted at the resonant frequency of the indenter (110 Hz) and with a 500 nm amplitude vibration. Following each indentation, the tip was cleaned by driving it into double-sided Scotch tape (3M, MN, USA) to avoid any contamination on the subsequent indent location. The tape was mounted on an adjacent sample puck.

Principles of oscillatory nanoindentation

Oscillatory nanoindentation was conducted to determine the shear storage (G') and shear loss modulus (G'') as well as the loss factor ($\tan \delta = \frac{G''}{G'}$). A Poisson's ratio of 0.5 was assumed (Hemmasizadeh, Autieri and Darvish, 2012). The underlying theory has been described in detail in Chapter 2 and summarised here.

The complex shear modulus (G^*) exhibits real elastic element (G') and imaginary viscous element (G'') is shown in Equation 3.1:

$$G^* = G' + G'' \quad (3.1)$$

The shear storage modulus (G') is calculated using Sneddon's analysis (Sneddon, 1965):

$$G' = \frac{S(1 - \nu)}{(2D)} \quad (3.2)$$

where S is the stiffness of the contact, and D is the diameter of contact and Poisson's ratio (ν).

The shear loss modulus (G'') depends on contact damping (C_w) and can be given by:

$$G'' = \frac{C_w(1 - \nu)}{(2D)} \quad (3.3)$$

The elastic modulus (E) can be calculated using the following relationship:

$$G' = \frac{E}{2(1 + \nu)} \quad (3.4)$$

Nanoindentation testing for ovine aortic tissues.

16 oscillatory indentations were applied to the surface of both sides for the same sample: the inner (intima layer) and outer side of the tissue (adventitial layer). For the first biological replicate, the intimal face was tested first followed by the adventitial face. For the second replicate, the adventitial face was tested first followed by the intimal face. Finally, for the third biological replicate, the intimal face was tested first followed by the adventitial face (Figure 3.1B). For the circumferential direction, 6 indents were made at the central media.

Nanoindentation testing for human chronic AD tissues.

Oscillatory nanoindentation was conducted to determine the localised tissue compliance of human chronic aortic tissue. Before measurement, the sample tissues were cut into three 5 mm circle biopsy punches and thawed at room temperature. Three biopsies per type groups (FP, TL and FL) were tested to determine the micromechanical properties. 16 indents with 200 μm spacing were applied in the longitudinal orientation to the surface of both sides of the vessel (inner and outer), as shown in Figure 3.4.

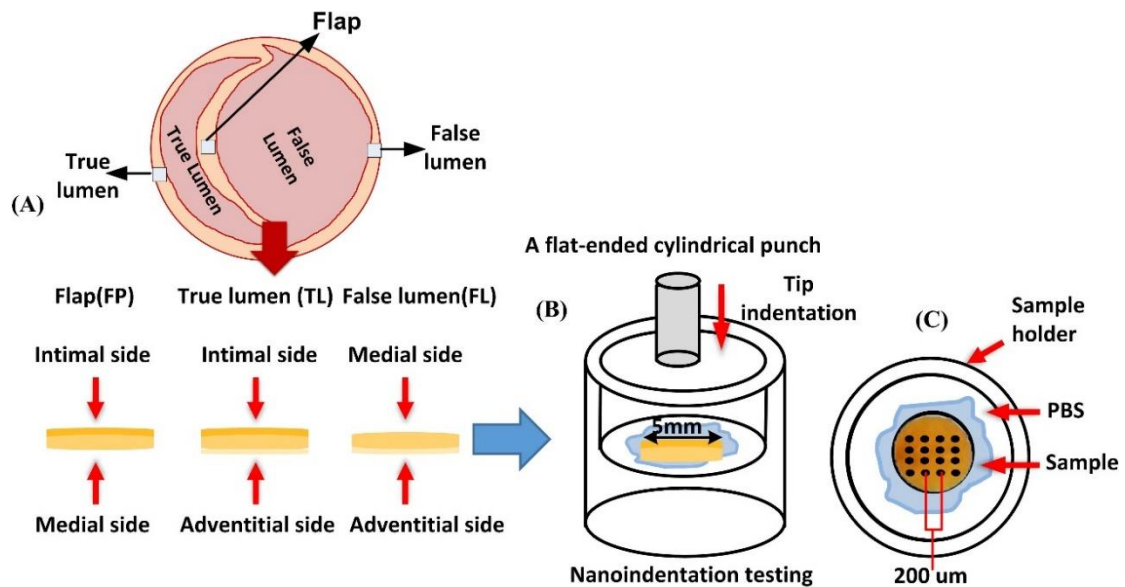


Figure 3.4 Schematic representation of the experimental approach for nanoindentation in human chronic AD: (A) The dissection tissue types used for nanoindentation testing: flap (inner:intima, outer:medial face); true lumen outer wall (inner:intimal, outer:adventitial face) and false lumen outer wall (inner:medial, outer:adventitial face). Samples were tested on both sides (the inner and outer side of the tissue). (B) Schematic representation of the side view of specimen holder with a flat-ended cylindrical punch showing tip direction, (C) The top view of 16 indentations with 200 μm of spacing on the adventitia surface and partial submersion of the samples in PBS.

3.1.2.3 Creep testing (time-dependent deformation)

The creep behaviour and elastic modulus of the aortic tissues were investigated using a non-destructive ball indentation method based on a pre-established device by other researchers (Ahearne et al., 2005, Weli et al., 2017). These measurements were carried out using two ovine aortas from two different regions: ascending and descending. The creep set-up is composed of two main parts: 1) a sample holder with a specific design includes two transparent plastic circle rings clamped together with stainless steel plates (Figure 3.5A and B) and 2) an image acquisition and processing system (Figure 3.5C). The aortic section was clamped between two transparent rings

and then placed on the stainless-steel plate above the transparent ring and screwed to it. Deformation of the tissues was achieved using a constant stainless-steel ball of weight 0.079 g and diameter 2.4 mm which was placed on the central portion of the tissues. The whole assembly of the sample holder were placed in a moist square petri dish and incubated at 37°C and 5% CO₂. The side view of the tissue deformation was imaged and recorded with the acquisition system which was composed of a long focal distance microscope (Edmund Optics, Barrington, USA) connected to a CCD video camera (Sony CCD XC-ST50CE Video Camera Module, Japan). The software module employed in this work for displaying and recording the images was developed in LabView (National Instruments Corporation (U.K.) Ltd., Berkshire). Creep deformation of the tissue was recorded over 5 hours.

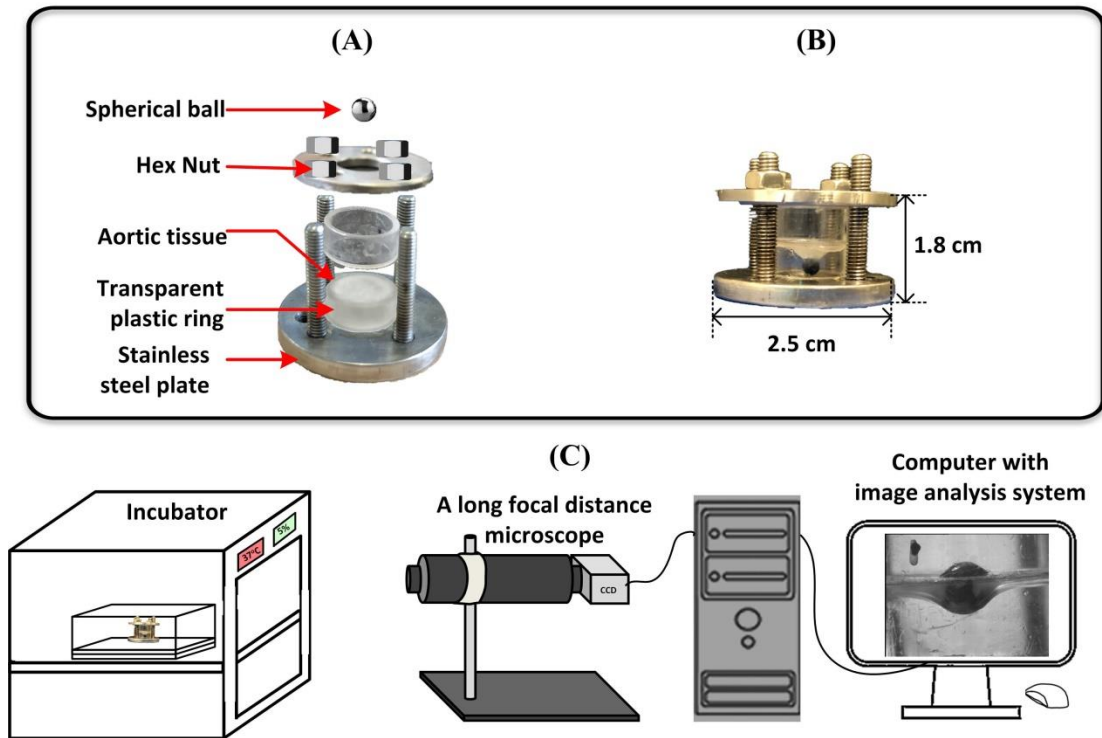


Figure 3.5 Schematic representation of the experimental approach for creep behaviour testing: (A) The disassembled specimen holder and spherical ball, (B) Completely assembled specimen holder and (C) Instrument system consisted of incubator; long focal distance microscope connected with CCD video camera and image analysis system.

The elastic modulus was determined with Equation 3.5. This equation has been used to calculate the elastic modulus of intact vaginal tissue (Weli et al., 2017) and hydrogels (Ahearne et al., 2005).

$$E = \frac{6w}{hR} * \frac{1}{0.075\left(\frac{\delta}{R}\right)^2 + 0.78\left(\frac{\delta}{R}\right)} \quad (3.5)$$

where w is the weight of the spherical ball, h is the thickness of the aortic tissues, R is the radius of spherical ball, a is the radius of the membrane and δ represents the initial displacement caused by the weight of the spherical ball (Figure 3.6).

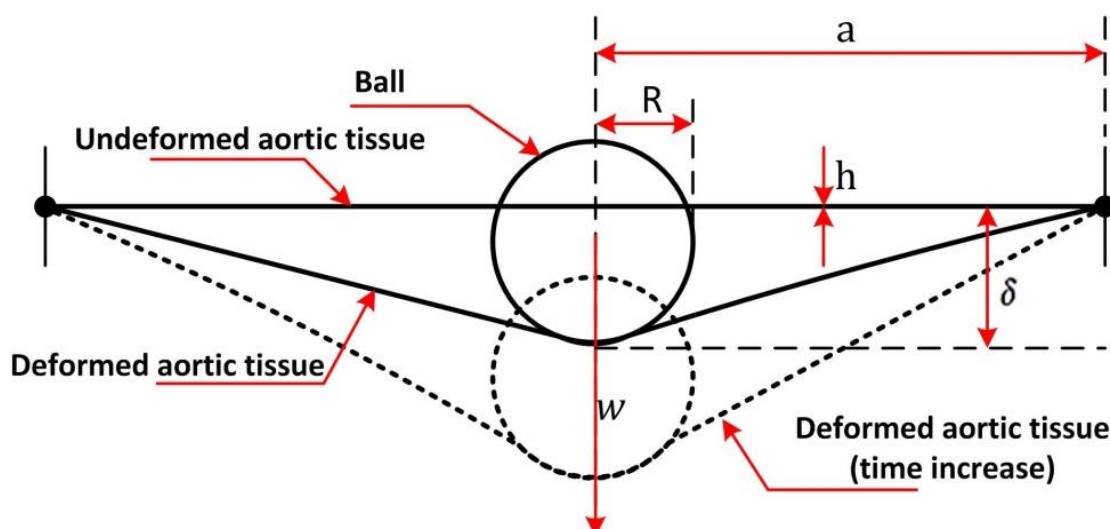


Figure 3.6 Schematic representation of indentation of the aortic tissue by the weight of spherical ball. All parameters are used to calculate the elastic modulus of aortic tissue.

3.2.2 Biochemical analysis

Following nanoindentation measurements the same pieces of tissue were used for biochemical analysis. Wet tissues weighing 7.5 mg were used to determine elastin levels and the remaining tissue was weighed, finely chopped and digested with papain to quantify the collagen and GAG levels. Collagen, elastin, and GAG level were expressed as $\mu\text{g}/\text{mg}$ of wet aortic tissue weight.

3.2.2.1 Elastin quantification

750 μl of 0.25 M oxalic acid was added to 7.5 mg of tissue and heated at 100 °C for 1 h. Samples were allowed to cool and centrifuged at 21,000 $\times g$ for 10 min. The supernatant was removed and digestion repeated a further 4 times with fresh oxalic acid. 200 μl from each digestion was pooled (total 1 ml). The Fastin™ Elastin Assay kit (Biocolor Ltd., County Antrim, UK) was used to quantify elastin using 200 μl of pooled

oxalic acid digests in duplicates from each biopsy (a total of 81 biopsies from 3 ovine aorta and 6 testing/3 biopsies for human chronic AD tissues each FP, TL and FL tissue type).

3.2.2.2 Collagen quantification

Hydroxyproline concentration was measured to represent the collagen content of the tissue (Bergman and Loxley, 1963, Bannister and Burns, 1970). All remaining tissue was digested with papain (P4762: Sigma-Aldrich Co. LLC, USA) at 10 units/ml in 0.1 M sodium acetate, 2.4 mM EDTA, 5 mM L-cysteine, pH 5.8 at 60 °C overnight (50 mg tissue in 500 µl). Following digestion, 100 µl of 12 M HCl was added to 100 µl of papain digested tissue and autoclaved. Samples were then lyophilised and re-dissolved in 2 ml ddH₂O.

50 µl of sample was added to 200 µl ddH₂O prior to addition of 250 µl of diluent (2:1 propan-2-ol:ddH₂O). 250 µl of oxidant (0.42 g chloroamine T, 5 ml ddH₂O, 25 ml of stock buffer containing (6.87 g sodium acetate, 7.5 g trisodium citrate.2H₂O, 1.1 g citric acid, 80 ml propan-2-ol made up to 200 ml with ddH₂O)) was added and left for 20 mins at room temperature. 250 µl of colour reagent (3 g 1,3-Dimethylbutylamine (DMBA), 4.5 ml 70% perchloric acid, 25 ml propan-2-ol) was added and left for 14 mins at room temperature followed by heating at 70 °C for 20 mins. Samples were left to cool for 10 mins before reading the absorbance at 550 nm. Hydroxyproline is present in collagen at 14 %; this value was used to calculate the collagen content of the tissue compared to a standard curve of L-hydroxyproline. Samples were analysed in triplicate for each biopsy (a total of 81 biopsies from 3 ovine aortas and 9 testing/3 biopsies for human chronic AD tissues each flap, true and false tissue type).

3.2.2.3 GAG quantification

Papain digested samples were diluted 1 in 10 with ddH₂O and added to a 96 well flat-bottomed transparent plate in a volume of 40 µl. 250 µl of dimethyl methylene blue (DMMB) dye (16 mg 1-9 dimethyl methylene blue, 2 g sodium formate, 2 ml formic acid, in 1 litre water, pH 3.5) was added and absorbance at 570 nm read immediately compared to a standard curve of Chondroitin Sulphate C (Farndale et al., 1982). Samples were analysed in triplicate for each biopsy (a total of 81 biopsies from 3 ovine aortas and 9 testing/3 biopsies for human chronic AD tissues each flap, true and false tissue type).

3.2.3 FTIR analysis

FTIR spectral images were obtained in transflection mode using an Agilent 680-IR FTIR spectrometer coupled to an Agilent 620-IR FTIR imaging microscope fitted with a liquid nitrogen cooled 64x64 mercury–cadmium–telluride focal plane array detector (FPA). Overview and transverse FTIR images of one ovine aorta section covering an area of ~4.9 mm x 11.2 mm with a spatial resolution of ~52 µm and ~1.4 mm x 4.9 mm with a spatial resolution of ~13 µm respectively were measured in the wavenumber region of 950-3800 cm⁻¹. The FTIR data was conducted by Dr Kerstin Mader, Materials and Engineering Research Institute, Sheffield Hallam University and it was pre-processed using the following strategy. Firstly, a second derivative transformation (Savitzky–Golay: filter order 3, filter length 15) was applied to the spectra using the ISys 5.0.0.14 software (Malvern Instruments Limited, Malvern, Worcestershire, UK). Secondly, pixels within the FTIR image showing only the presence of paraffin or substrate were identified and masked using spectral statistics (histogram at 1554 cm⁻¹, masked at 0).

Masked pixels were then assigned a value of 0. Haematoxylin and eosin stain (H&E) equivalent distribution images were generated by peak integration of the Amide I peak (integration limits: 1616-1704 cm^{-1})(Mader et al., 2016).

The data sets were analysed using Multivariate curve resolution-alternating least squares (MCR-ALS) is described in detail by (Wang et al., 2003). The basic method of the MCR-ALS algorithm comprised the transformation of abstract factors deduced from non-linear iterative partial least squares (NIPALS) decomposition into chemical and concentration information by applying a modified iterative alternating least square optimisation.

MCR-ALS was carried out on overview and transverse FTIR imaging data sets spanning the spectral region of 950-1600 cm^{-1} using the software application MCR (MCRv1.6[®], Unilever, Leatherhead, UK). Chemical identities were assigned to extracted MCR-ALS factors by a comparison of the spectral profiles to 2nd derivative reference spectral profiles of collagen and elastin and the distribution maps to histologically stained sections. Full methodological information has been reported by Mader et al. (Mader et al., 2016) and is beyond the scope of this thesis.

To validate the generated FTIR distribution maps they were compared to histologically stained (H&E, Picrosirius red (PSR) and Verhoeff-Van Gieson (VVG) stain) consecutive sections of the aorta.

3.2.4 Histological analysis

For histological stain, sections were deparaffinised, dehydrated and subjected to H&E, PSR, alcian blue and VVG staining using standard kits according to manufacturer's

protocols. Histology was conducted by Angela Platt-Higgins, Faculty of Health and Life Sciences, University of Liverpool. Images were generated using an Axio slide scanner at 20x resolution, by Mandy Prior, Faculty of Health and Life Sciences, University of Liverpool.

3.2.4.1 Aortic fibrillar collagen and elastic fibre content

The analysis of the relative areas of elastic fibre content and aortic fibrillar collagen in the VVG stain images and PSR stain images, respectively was achieved using image analysis software, Image SXM (Barrett, 2020). The details of image analysis to quantify the percentage of collagen and elastin content was developed and conducted by Dr Steve Barrett, Department of Physics, University of Liverpool. Four random rectangle images from the medial layer were taken for image analysis for each tissue section. The VVG stained image (Figure 3.7A) was used to create a binary mask using the contrast of the blue channel of the RGB colour image between chronic AD tissue and background. The bright field image was thresholded to define the pixels that are part of the tissues. Only pixels that are within the tissue mask were considered to calculate the amount of elastin. For elastin, the binary image can manifest as results from grey to black pixels of elastin fibres (Figure 3.7B). The amount of elastin pixels detected in each image were expressed as a percentage of total tissue section area.

Collagen percentage was determined using a similar approach. Collagen in PSR stained images can present as a range of colours from light pink to red (Figure 3.7C). A binary black and white image was created to present the location of collagen in the aortic tissue sample. The amount of collagen pixels was expressed as a percentage of entire tissue section (Figure 3.7D). All calculations of percentage area are the ratios of the

pixel counts for the collagen or elastin divided by the pixel count in the tissue mask, meaning that spatial calibration of the images is not required.

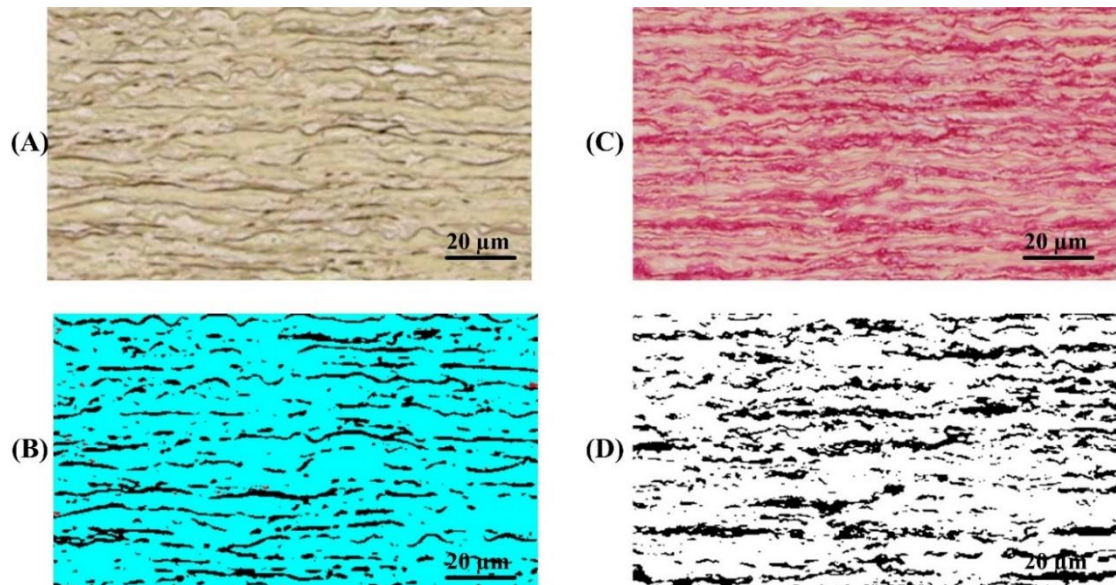


Figure 3.7 Image processing procedure to obtain percentage of elastin and collagen: (A) VVG stained image for elastin (B) RGB binary image of chronic AD (C) PSR stained image for collagen (D) Binary black and white image. Scale bar indicates 20 μm .

3.2.4.2 Elastin fragmentation

As used for quantification measurements above, four random rectangle images at the medial layer were taken per tissue, from VVG stained images for grading of elastin fragmentation. Elastin fragmentation is defined as focal fragmentation of elastin. The grades were determined based on the worst region observed in each rectangle region. The criteria for the histologic grading were modified from (Schlatmann and Becker, 1977) and are summarized as following:

Grade I: up to five foci of elastic fragmentation of two to four neighbouring elastic lamellae in one microscopic field of 100 X magnification.

Grade II: more than five foci of elastic fragmentation of two to four neighbouring elastic lamellae.

Grade III: more than five foci of elastic fragmentation with disarray of smooth muscle cells.

An example of each grade is shown in Figure 3.8. The classification of elastin fragmentation was conducted by the author and co-supervisor Dr Jill Madine independently.

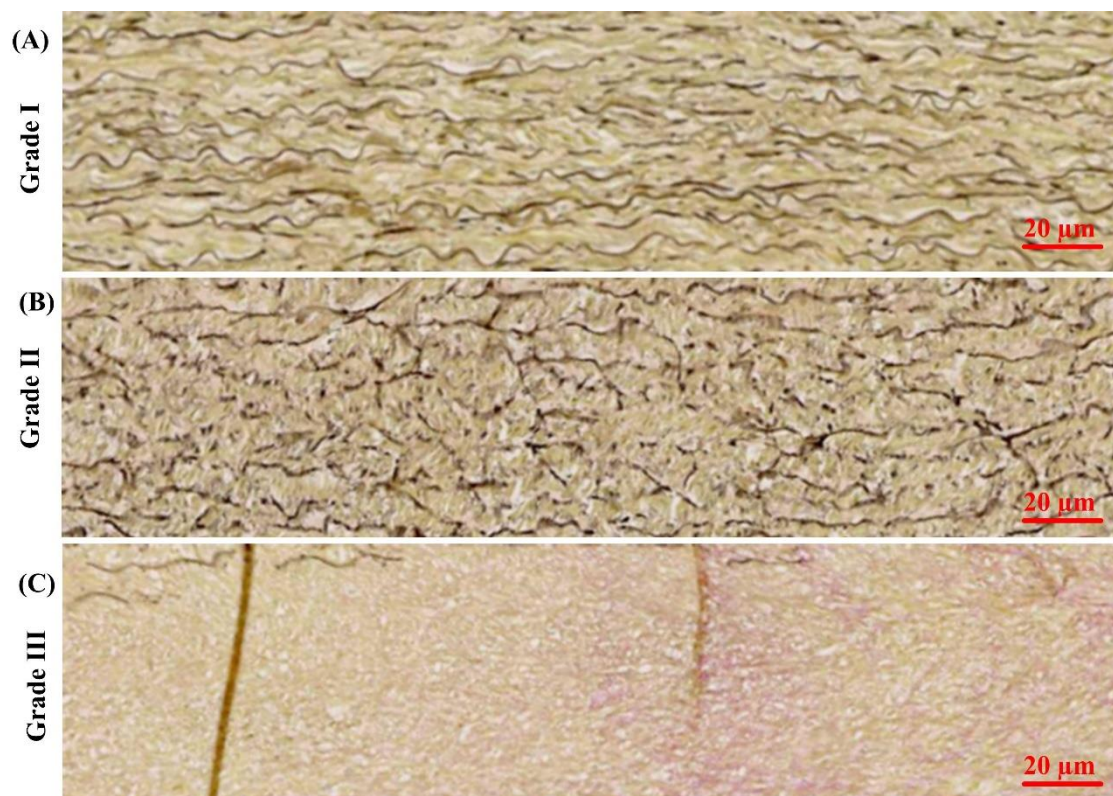


Figure 3.8 Example of the three grades of elastin fragmentation: (A), (B) and (C) demonstrates grades I, II and III, respectively.

3.2.5 Statistical analysis

Statistical analysis was performed using OriginPro version 9 (OriginLab, Northampton, MA, USA). All data for ovine tissues are presented as mean values \pm standard deviation (SD). One-way ANOVA with post-hoc Bonferroni was used to analyse the statistical variation between the ascending region, upper thoracic region, and upper abdominal region (uniaxial testing). Following this, One-way ANOVA with post-hoc Bonferroni was also performed to examine intra-group variability both for biomechanical properties (G' , G'' and $\tan \delta$) and biochemical properties (collagen, GAG and elastin) and inter-group variation (for the distance from heart). Bivariate correlation with Pearson product-moment correlation coefficients were calculated with simple linear regression analyses. This was performed to define the relationship between biomechanical properties from nanoindentation (G' , G'' and $\tan \delta$) and biochemical properties (collagen, GAG and elastin level) with distance from the heart, as well as correlation between biomechanical properties and biochemical properties. A p-value below 0.05 was considered as statistically significant. For human chronic AD the biomechanical properties (G' , G'' and $\tan \delta$) and biochemical properties (collagen, GAG and elastin level) for each group: FP (intimal and medial face), TL (intimal and adventitial face) and FL (medial and adventitial face) are presented using box plots with 5th and 95th percentile as whiskers. For all comparisons between each group, the Man-Whitney test was performed at a significance level of 0.05. Bivariate correlation with Spearman product-moment correlation coefficients were calculated. This was performed to define the relationship between micromechanical aortic elastic modulus from nanoindentation technique, ball indentation techniques, biochemical

properties (collagen, GAG elastin and collagen/elastin ratio level) and histological data with clinical data (interval of index event to operation (IIEO) and the growth rate). A p-value below 0.05 was considered as statistically significant.

References

- Ahearne, M., Yang, Y., El Haj, A. J., Then, K. Y. and Liu, K. K. (2005) 'Characterizing the viscoelastic properties of thin hydrogel-based constructs for tissue engineering applications', *J.R.Soc.Interface*, 2 (5), pp.455-63.
- Akhtar, R., Draper, E. R., Adams, D. J. and Hay, J. (2018) 'Oscillatory nanoindentation of highly compliant hydrogels: A critical comparative analysis with rheometry', *J.Mater.Res.*, 33 (8), pp.873-83.
- Bannister and Burns. (1970) 'Adaptation of the Bergman and Loxley technique for hydroxyproline determination to the autoanalyzer and its use in determining plasma hydroxyproline in the domestic fowl', *Analyst*, 95 (1131), pp.596-600.
- Barrett, S. (2020) *Image SXM [Online]*
<https://www.liverpool.ac.uk/~sdb/ImageSXM/#how>
- Bergman and Loxley. (1963) 'Two improved and simplified methods for the spectrophotometric determination of hydroxyproline.', *Anal.Chem.*, 35 (12), pp.1961-5.
- Carew, T. E., Vaishnav, R. N., Patel, D. J. and etc. (1968) 'Compressibility of the arterial wall', *Circ.Res.*, 23 (1), pp.61-8.
- Chim, Y. H., Davies, H. A., Mason, D., et al. (2019) 'Bicuspid valve aortopathy is associated with distinct patterns of matrix degradation',
J.Thorac.Cardiovasc.Surg.,

- Farndale, R. W., Sayers, C. A., Barrett, A. J. and etc. (1982) 'A direct spectrophotometric microassay for sulfated glycosaminoglycans in cartilage cultures', *Connect.Tissue Res.*, 9 (4), pp.247-8.
- Hemmasizadeh, A., Autieri, M. and Darvish, K. (2012) 'Multilayer material properties of aorta determined from nanoindentation tests', *J Mech Behav Biomed Mater*, 15 pp.199-207.
- Khanafer, K., Duprey, A., Zainal, M., Schlicht, M., Williams, D. and Berguer, R. (2011) 'Determination of the elastic modulus of ascending thoracic aortic aneurysm at different ranges of pressure using uniaxial tensile testing', *J.Thorac.Cardiovasc.Surg.*, 142 (3), pp.682-6.
- Mader, K. T., Peeters, M., Detiger, S. E., et al. (2016) 'Investigation of intervertebral disc degeneration using multivariate FTIR spectroscopic imaging', *Faraday Discuss.*, 187 pp.393-414.
- Pagani, M., Mirsky, I., Baig, H., Manders, W. T., Kerkhof, P. and Vatner, S. F. (1979) 'Effects of age on aortic pressure-diameter and elastic stiffness-stress relationships in unanesthetized sheep', *Circ.Res.*, 44 (3), pp.420-9.
- Schlatmann, T. J. and Becker, A. E. (1977) 'Histologic changes in the normal aging aorta: implications for dissecting aortic aneurysm', *Am.J.Cardiol.*, 39 (1), pp.13-20.

- Segers, P., Steendijk, P., Stergiopoulos, N. and Westerhof, N. (2001) 'Predicting systolic and diastolic aortic blood pressure and stroke volume in the intact sheep', *J.Biomech.*, 34 (1), pp.41-50.
- Sneddon, I. N. (1965) 'The relation between load and penetration in the axisymmetric Boussinesq problem for a punch of arbitrary profile', *Int.J.Eng.Sci.*, 3 (1), pp.47-57.
- Wang, J., Hopke, P. K., Hancewicz, T. M. and Zhang, S. L. (2003) 'Application of modified alternating least squares regression to spectroscopic image analysis', *Anal.Chim.Acta*, 476 (1), pp.93-109.
- Weli, H. K., Akhtar, R., Chang, Z., Li, W., Cooper, J. and Yang, Y. (2017) 'Advanced glycation products' levels and mechanical properties of vaginal tissue in pregnancy', *Eur. J. Obstet. Gynecol.*, 214 pp.78-85.

Chapter 4

Macro- and micro mechanical properties of the ovine aorta: Correlation with regional variations in collagen, elastin and glycosaminoglycan Levels.

This chapter focusses on development of methods. It includes applying the nanoindentation and ball indentation technique to characterise biomechanical properties and time-dependent deformation (creep) of ovine aortic tissues, respectively. In parallel, biochemical properties (collagen, GAG and elastin levels) were also measured using established biochemical assays. Using multivariate FTIR method to obtain the image distribution maps of chemical species is also introduced.

4.1 Introduction

Aortic diseases manifest in different ways across the vascular tree, for example, with Type A dissection being caused by a tear in the ascending aorta and Type B dissection occurring in the descending aorta. The abdominal aorta is more prone to aneurysm development than the thoracic aorta and it has been reported that around 75% of abdominal aortic aneurysms (AAAs) occur in the infrarenal region (Drury et al., 2005). Given this clinical relevance, a number of studies have previously studied differences in composition and mechanical properties in different regions of the aorta. Early studies have demonstrated that elastin and collagen content varies along the length of the aorta. By combining biomechanical and biochemical or microstructural evaluation of the same tissue, several studies have attempted to correlate the variation in mechanical properties with the composition in different regions of the aorta. Haskett et al. (2010) combined biaxial testing with microstructural imaging via small angle light scattering in the human aorta and found a progressive reduction in aortic compliance from the proximal to the distal aorta, with the difference being more pronounced with age. Overall, they reported statistically significant regional differences both in terms of its microstructure and biomechanical response. Sokolis et al. (2007) used tensile testing and histological quantification of collagen and elastin to examine regional variations in the porcine aorta. They found that there were good correlations between the elastic modulus and either elastin or collagen across the different regions.

There is still a gap in the literature in terms of understanding micromechanical behaviour across different regions of the aorta. Although alterations in the

macroscopic biomechanical behaviour correlate well with regional microstructural changes as shown in previous studies (Sokolis, 2007, Haskett et al., 2010), to the best of our knowledge, no previous study has combined micromechanical properties of aortic tissue with regional differences in biochemical composition. Further, while most previous work considers regional variation of elastin and collagen, GAG distribution across the aorta has not previously been measured. The important role of GAGs has been presented in the literature in arterial stiffening (Tovar et al., 1998), as well as in thoracic aortic aneurysms and dissections (Humphrey, 2013).

Due to lack of availability in obtaining human aortas across the vascular tree, this study was conducted on ovine aortas to develop techniques that were subsequently applied to human dissected tissues. The aims of study in the ovine model were to map the mechanical properties across the entire length of the ovine aorta at the macro- and micro-scale. Most of the published work on aneurysm and dissected human tissues has used tensile testing, therefore micromechanical data collected with oscillatory nanoindentation was compared with conventional uniaxial tensile testing data. To characterise the time-dependent properties of ovine aortic wall a ball indentation method was presented. The mechanical property data are then compared with collagen, elastin and GAG levels measured across the different regions. Moreover, FTIR spectroscopy with MCR-ALS analysis is utilised to develop distribution maps matching histological stains for collagen, and elastin for the ovine aortic wall.

4.2 Results

4.2.1 Regional variations in the uniaxial behaviour of the ovine aorta

Three regions of three ovine aortas: the ascending, upper thoracic aorta and upper abdominal regions were used to investigate the macromechanical properties. True stress-strain data for the three regions are shown in Figure 4.1. The expected non-linear behaviour is clearly visible with increasing strain. There was a clear difference in the curves for each region with the upper abdominal aorta exhibiting the stiffest behaviour at the higher strains.

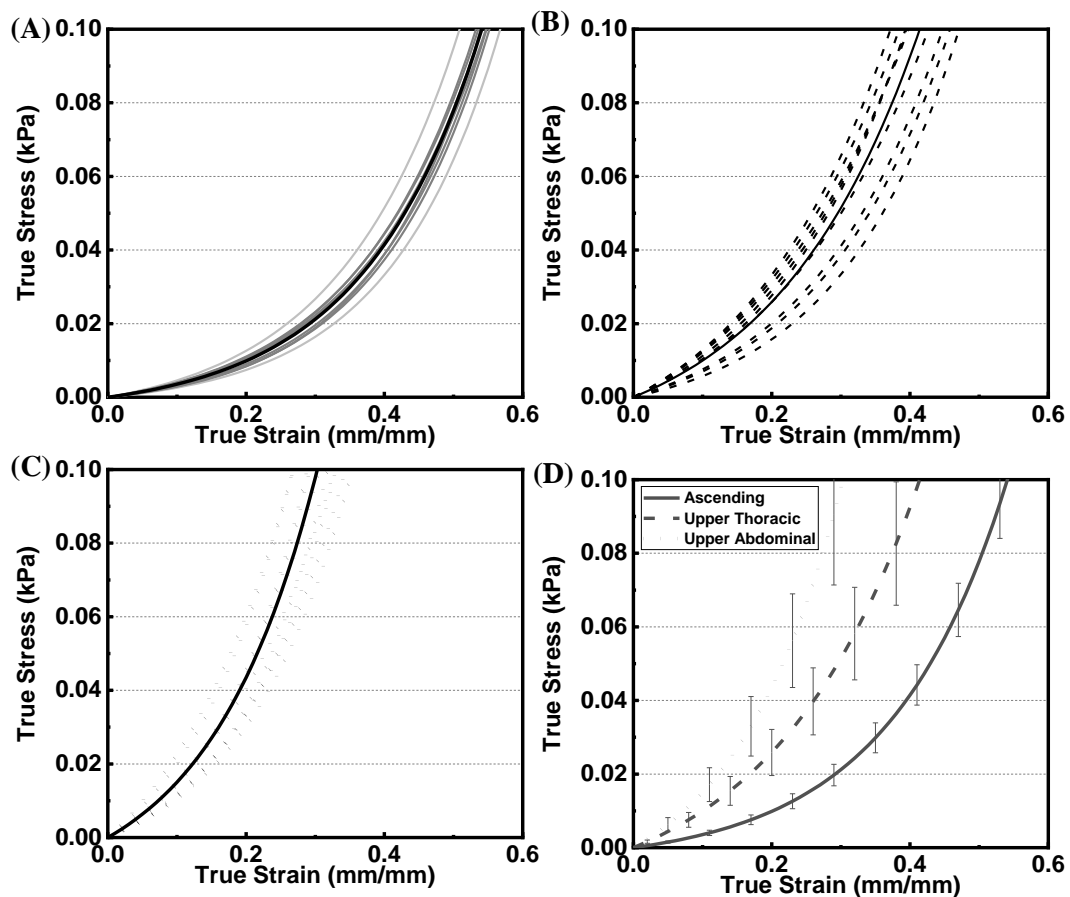


Figure 4.1 The true stress–strain relationship extracted from: (A) ascending, (B) upper thoracic region, (C) upper abdominal region and (D) comparison of average stress–strain behaviour for the three main regions ($n = 9$ samples per region).

There were no statistically significant differences in PE when comparing the ascending and upper thoracic regions ($p=0.2$), however significant differences were observed between the ascending and upper abdominal regions ($p=7.6\times 10^{-11}$) and the upper thoracic and upper abdominal regions ($p=2.7\times 10^{-9}$) (Figure 4.2A). For the TM at 0.5 strain, there was a significant difference between the ascending and upper thoracic regions ($p=0.04$), ascending and upper abdominal ($p=4.5\times 10^{-13}$), as well as upper thoracic and upper abdominal regions ($p=3.0\times 10^{-11}$) (Figure 4.2B).

The differences in ME were also statistically significant across the regions for ascending and upper thoracic region ($p=1.1\times 10^{-5}$), upper thoracic and upper abdominal regions ($p=0.01$) and for ascending and upper abdominal regions ($p=8.2\times 10^{-9}$) (Figure 4.2C). The failure stress in different regions also showed a significant difference between the ascending, upper thoracic and upper abdominal regions ($p<0.0001$) (Figure 4.2D), with the upper abdominal region exhibiting the highest values.

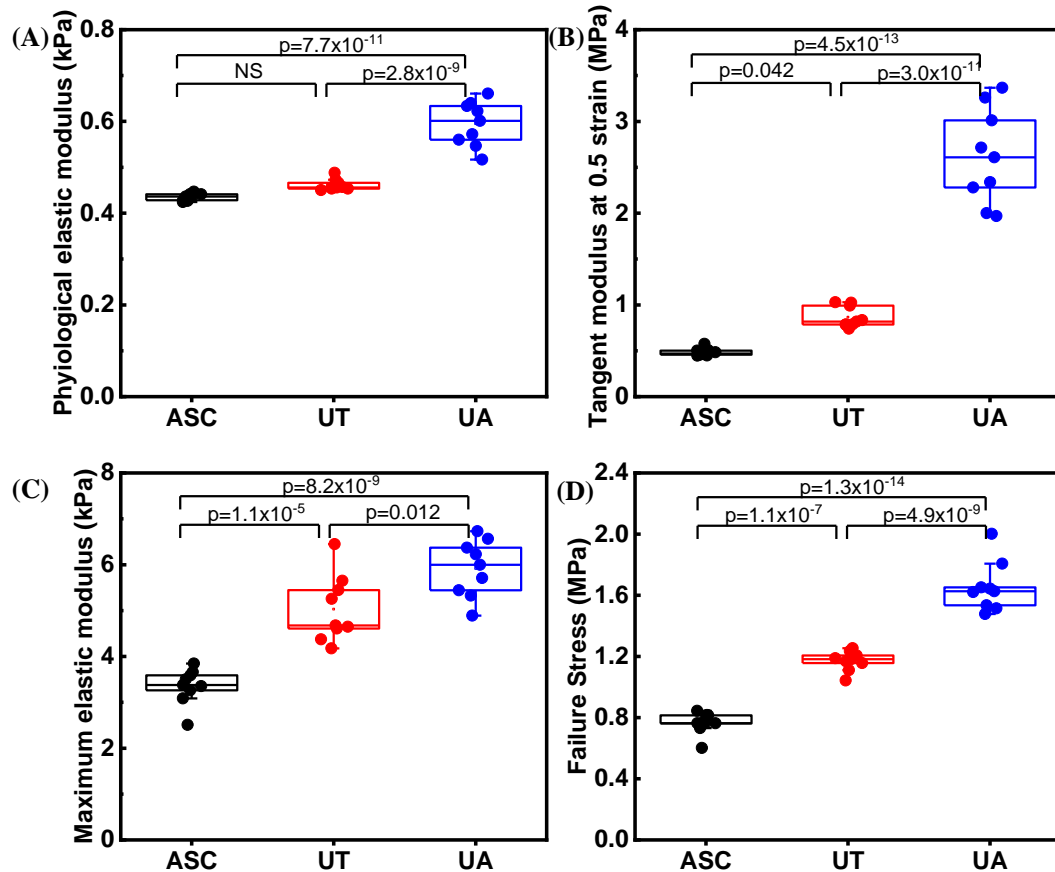


Figure 4.2 Box-whisker plots presented for the macro-mechanical data for the 3 aortic regions (the ascending (ASC), upper thoracic (UT) and upper abdominal aorta (UA)) that were tested (n=9 samples/region): A) PE (B) Tangent modulus at 0.5 strain (C) ME (D) Failure stress. All values are shown with boxes representing the 25th and 75th percentiles of data. Whiskers represent the 5th and 95th percentiles of data. NS = Not significant.

4.2.2 Micromechanical behaviour of ovine aortic tissue

G' , G'' and $\tan(\delta)$ were measured using nanoindentation to determine the micromechanical properties, for both the circumferential and longitudinal direction.

4.2.2.1 Circumferential direction

Six oscillatory indentations were performed on the medial layer in the circumferential direction (the tissue cross-section). In order to compare to the uniaxial data, testing was conducted for samples taken from the same regions as for the uniaxial tests, namely the ascending aorta, upper thoracic aorta and upper abdominal aorta. Overall, the mean values for G' and G'' (at the medial layer), increased from the ascending to the upper abdominal aorta. G' and G'' for the upper abdominal aorta were higher than the ascending aorta by 220.8%, and 219.7% respectively. G' and G'' for the upper abdominal aorta were 148.95% and 167.6% higher than the upper thoracic aorta respectively. As shown in Figure 4.3, there were statistically significant differences for both G' and G'' when comparing the ascending, upper thoracic regions and upper abdominal aorta.

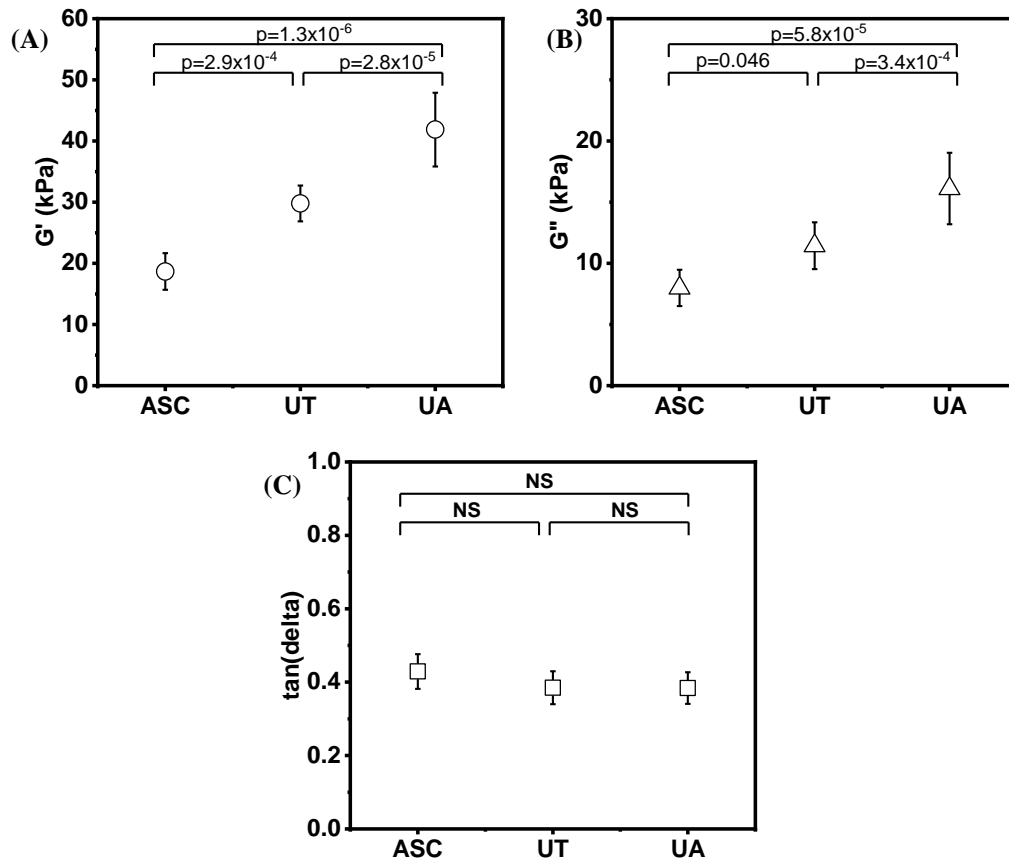


Figure 4.3 Micromechanical properties of the medial layer (circumferential orientation), shown for the ascending (ASC), upper thoracic (UT) and upper abdominal aorta (UA): (A) G' (B) G'' and (C) $\tan(\delta)$. Symbols represent the mean values and error bars represent the standard deviation.

4.2.2.2 Longitudinal orientation

Longitudinal properties were mapped for both the adventitial face and intimal face of the aortic wall. G' and G'' increased with distance from the heart for both the adventitial face and intimal faces (Figures 4.4A and 4.4B). For the adventitial face, G' increased from 14.9 ± 1.4 kPa (2 cm from aortic root) to 30.4 ± 2.5 kPa (14 cm from aortic root).

For the intimal face, G' increased from 21.1 ± 1.6 kPa (2 cm from aortic root) to 36.9 ± 2.4 kPa (14 cm from aortic root). Similar trends were found for G'' . For the adventitial face, G'' increased from 5.4 ± 0.5 kPa (2 cm from aortic root) to 10.2 ± 1.3 kPa. For the intimal face, G'' increased from 7.6 ± 1.1 kPa (2 cm from aortic root) to 13.4 ± 2.9 kPa. As shown in Figures 4.4A and 4.4B, G' and G'' were both found to be higher when the intimal face was tested, across all regions.

A significant positive correlation was observed with distance from the heart to the celiac artery region for G' for the adventitial face ($R^2=0.95$, $R=0.97$, $p=0.000028$) and intimal face ($R^2=0.94$, $R=0.97$, $p=0.000016$). Similar, correlations were found for G'' ; adventitial face ($R^2=0.90$, $R=0.95$, $p=0.00089$) and for the intimal face ($R^2=0.88$, $R=0.94$, $p=0.00035$). $\tan(\delta)$ was found to be relatively consistent, typically around 0.35-0.40 for both the adventitial and intimal face (Figure 4.4C).

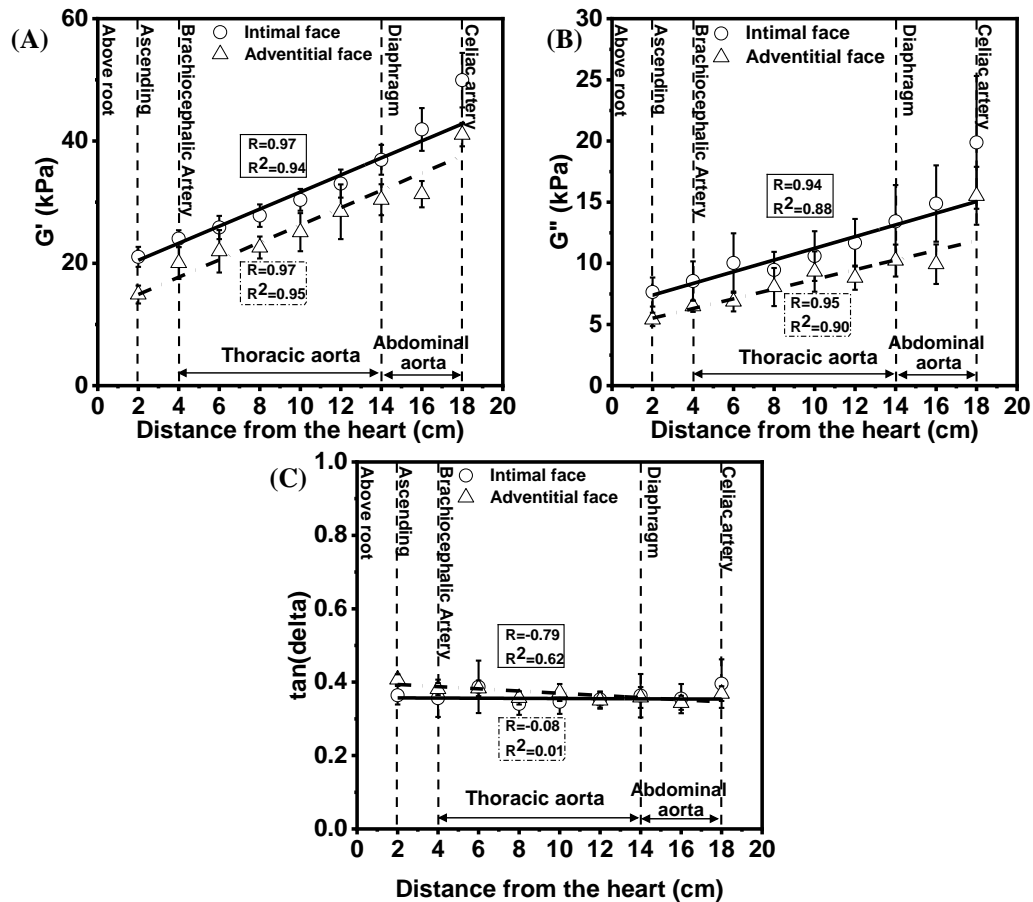


Figure 4.4 Longitudinal micromechanical properties across the ovine aorta as a function of distance from the aortic root to celiac region (A) G' -distance (B) G'' -distance were found to have a high positive correlation (Pearson correlation coefficient, G' -distance: $R = 0.97$, $p=0.000028$ and $R=0.97$, $p=0.000016$ for adventitia and intima, respectively. G'' -distance: $R = 0.95$, $p=0.00089$ for adventitia and $R=0.94$, $p=0.00035$ for intima) (C) the relationship between $\tan(\delta)$ and distance. The data are averaged from 81 samples ($n=9/\text{region}$ with 3 samples/animal) shown as mean \pm SD.

4.2.3 Comparison of micromechanical and macromechanical behaviour

A comparison was made of the mechanical property data obtained via uniaxial tensile testing and oscillatory nanoindentation. The most appropriate comparison was the mean elastic modulus obtained from the circumferential tests (medial layer) via nanoindentation with the PE obtained via tensile testing. Although the testing approach, testing scale and rates differed with the two methods, and as a result the

absolute values differed, it was found that the overall trends from the ascending to the upper abdominal aorta were similar (as shown in Figure 4.5).

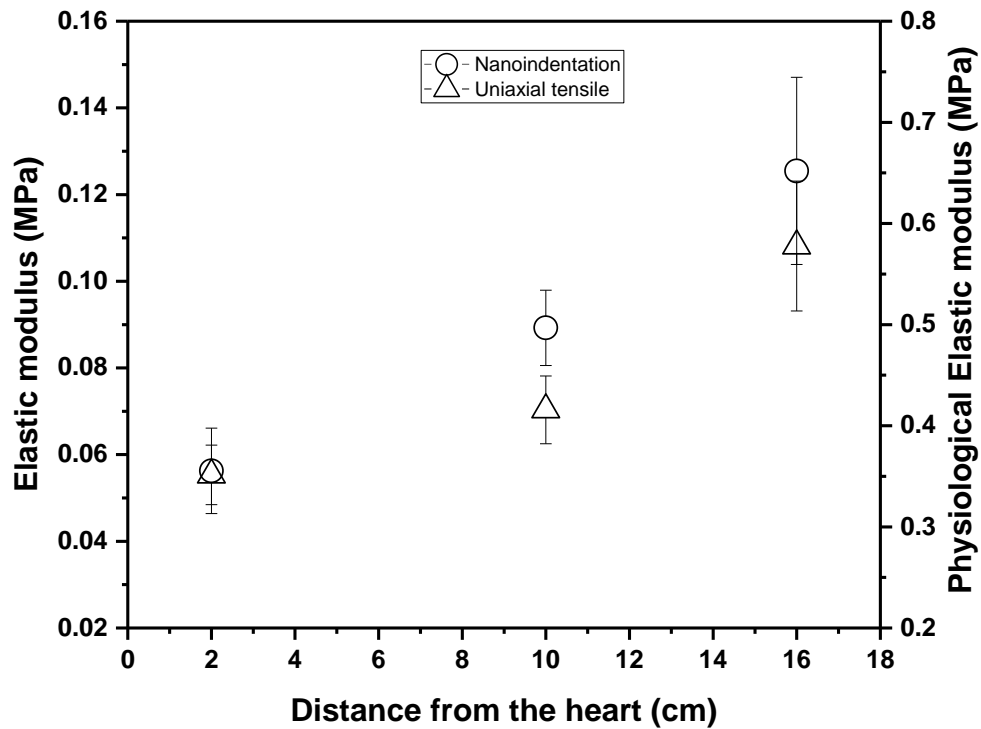


Figure 4.5 Comparison of trends obtained via circumferential testing of the medial layer using oscillatory nanoindentation (elastic modulus) with PE values obtained via uniaxial tensile testing, for the ascending, upper thoracic and upper abdominal aorta, shown as a function of distance (length) from the heart.

In terms of the absolute values, with nanoindentation, the elastic modulus was in the range of 0.05-0.12 MPa and from uniaxial tensile testing at PE the range was 0.4-0.6 MPa. Hence, the bulk measurements were 5-8 times higher than the micromechanical measurements.

4.2.4 Creep behaviour (time-dependent deformation)

Using the ball indentation method, aortic tissues were deformed over five hours (300 minutes) with a constant force (stainless steel ball of weight 0.079 g). A side view of the deformed aortic tissue by the microscope system is shown in Figure 4.6. It can be seen that high resolution images of the tissue deformation were obtained. The displacement of central deformation and the thickness of ovine aortic tissue was observed and measured from the images acquired by using a long focal distance microscope connected to CCD camera and computer.

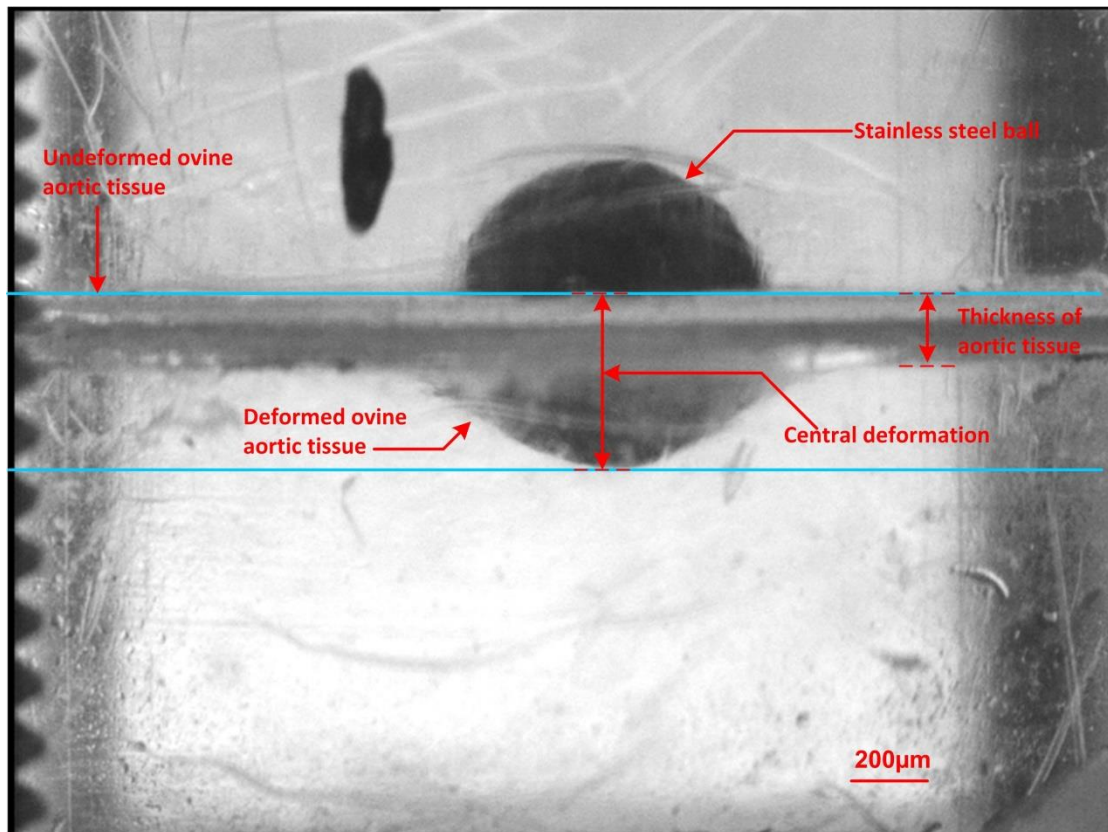


Figure 4.6 Side view of the deformed aortic tissue with the ball indentation method. Image was acquired using a long focal distance microscope. Scale bar is 200µm.

Figure 4.6 shows an example of the ovine aorta tissue section prior to indentation, indentation at 0 minutes and 300 minutes in different locations (ascending and descending). It is apparent that after 300 minutes the displacement of the central deformation increased (Figure 4.7).

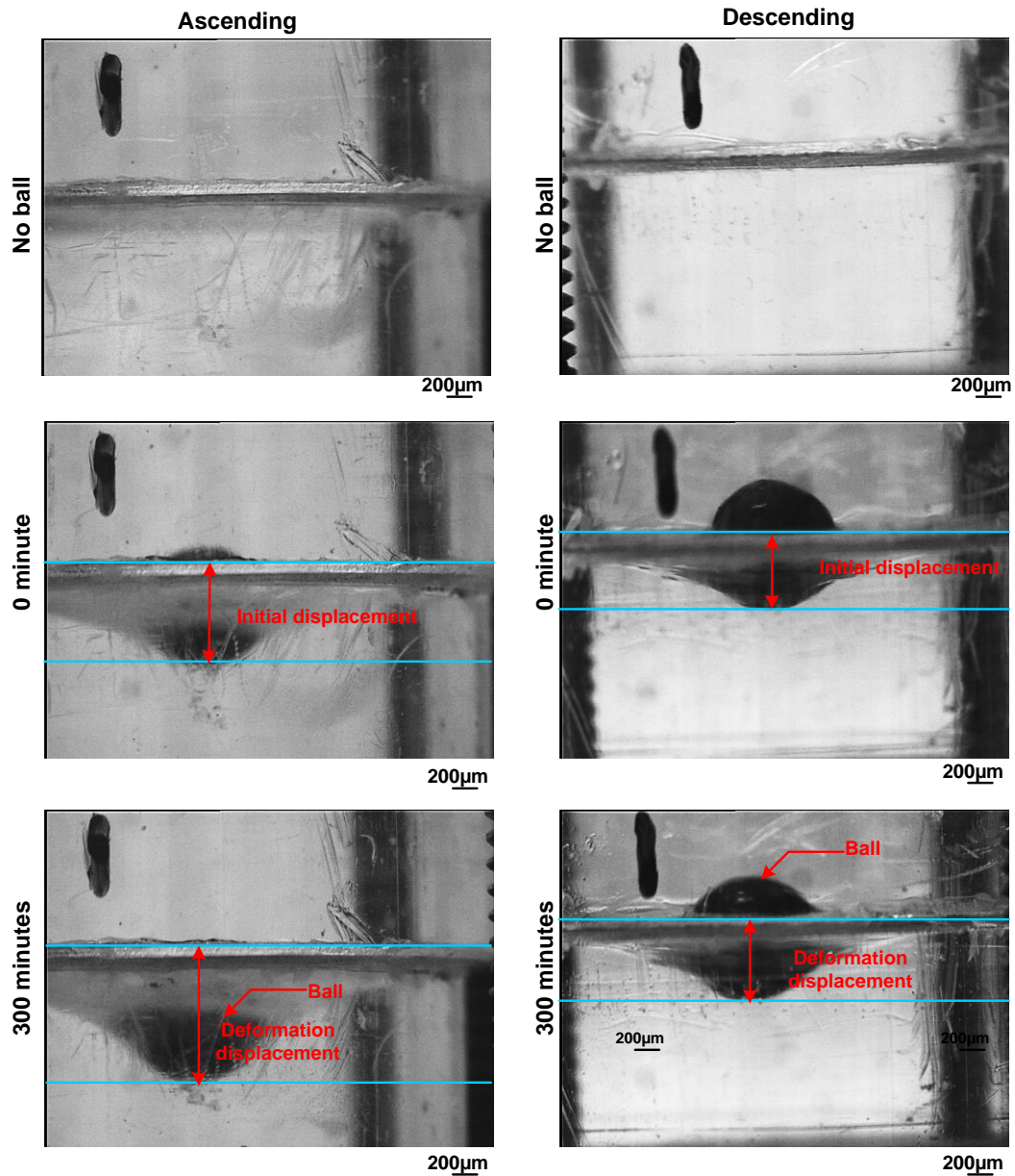


Figure 4.7 Optical images showing central deformation of the ovine aorta over five hours in the ascending and descending regions. Scale bar is 200µm.

A typical curve of the average central deformation over time is shown in Figure 4.8.

The central deformation slowed down over time until the displacement reached a plateau. The ascending aortic wall exhibited the highest deformation over time.

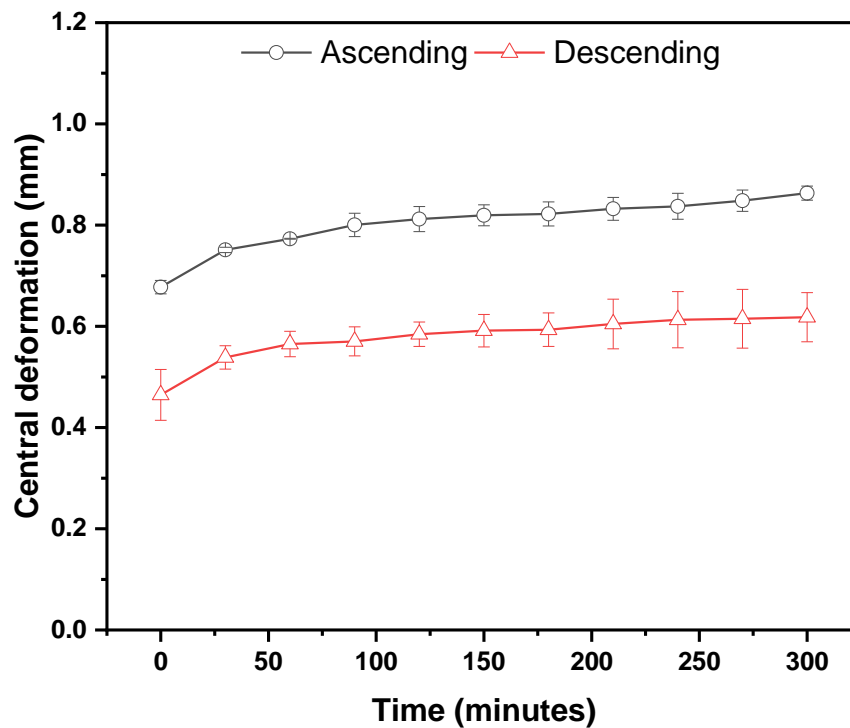


Figure 4.8 Time-dependent deformation (creep behaviour) of the ovine aortic wall for the ascending and descending regions over five hours.

Using Equation 3.5 (Chapter 3), the elastic modulus was determined utilising the initial displacement measured at 0 seconds. The elastic modulus of both ascending and descending are presented (Figure 4.9). Significantly lower elastic modulus was observed in the ascending region ($p=0.02173$) as compared with the descending region. The data trends were consistent with the elastic modulus obtained from nanoindentation technique.

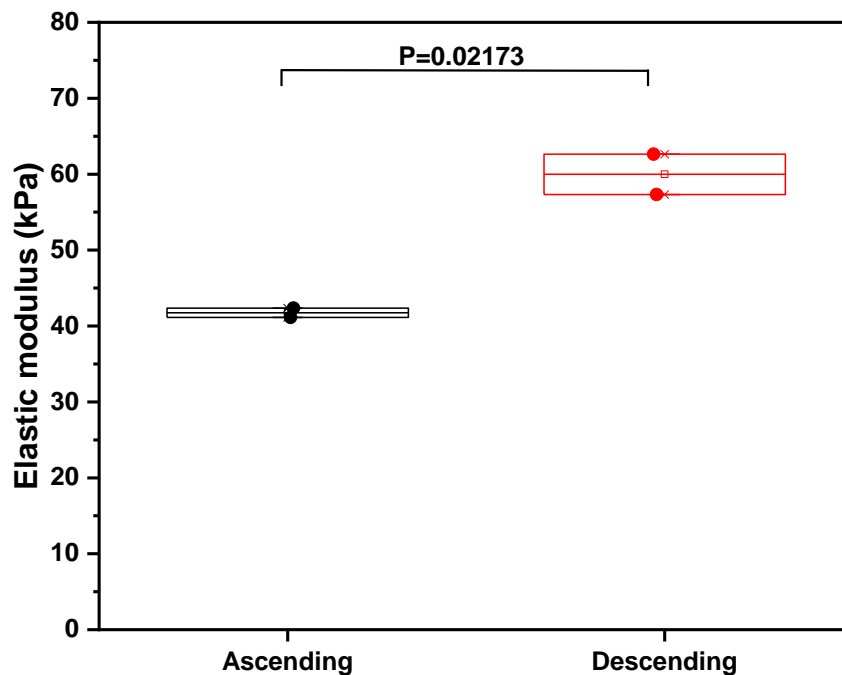


Figure 4.9 Box-whisker plots presented for the elastic modulus determined with the ball-indentation technique for the ascending and descending (n=2 samples/region). All values are shown with boxes representing the 25th and 75th percentiles of data. Whiskers represent the 5th and 95th percentiles of data. There was significant difference with a 95% confidence interval, determined by one way ANOVA with a Bonferroni test.

4.2.5 Biochemical analysis

Clear trends were visible for all biochemical measurements as the distance from the aortic root increased for each of the extracellular matrix components analysed (collagen, GAG and elastin) (Figure 4.10). As shown in Figure 4.10A, the collagen level was lowest at the first point of measurement (closest to the root, $27.3 \pm 7.0 \mu\text{g}/\text{mg}$) and steadily increased with distance to the celiac artery, reaching a maximum of approximately $40.1 \pm 8.8 \mu\text{g}/\text{mg}$. In contrast, GAG ($4.2 \pm 0.9 \mu\text{g}/\text{mg}$) and elastin ($102.5 \pm 24.5 \mu\text{g}/\text{mg}$) decreased along the length of the aorta approximately to 3.5 ± 0.4

$\mu\text{g}/\text{mg}$ and $80.2 \pm 11.0 \mu\text{g}/\text{mg}$ for GAG and elastin, respectively (Figures 4.10B and 4.10C). Pearson's correlation and R-square values demonstrated a strong positive correlation between collagen level and distance from aortic root ($R=0.88$ and $R^2=0.78$). In contrast, there was a strong negative relationship between GAG ($R=-0.84$ and $R^2=0.74$) and elastin levels ($R=-0.89$ and $R^2=0.80$) with distance from the aortic root. The mean values of collagen, GAG and elastin levels for the three ovine aortas are presented in Table A1 (Appendix A).

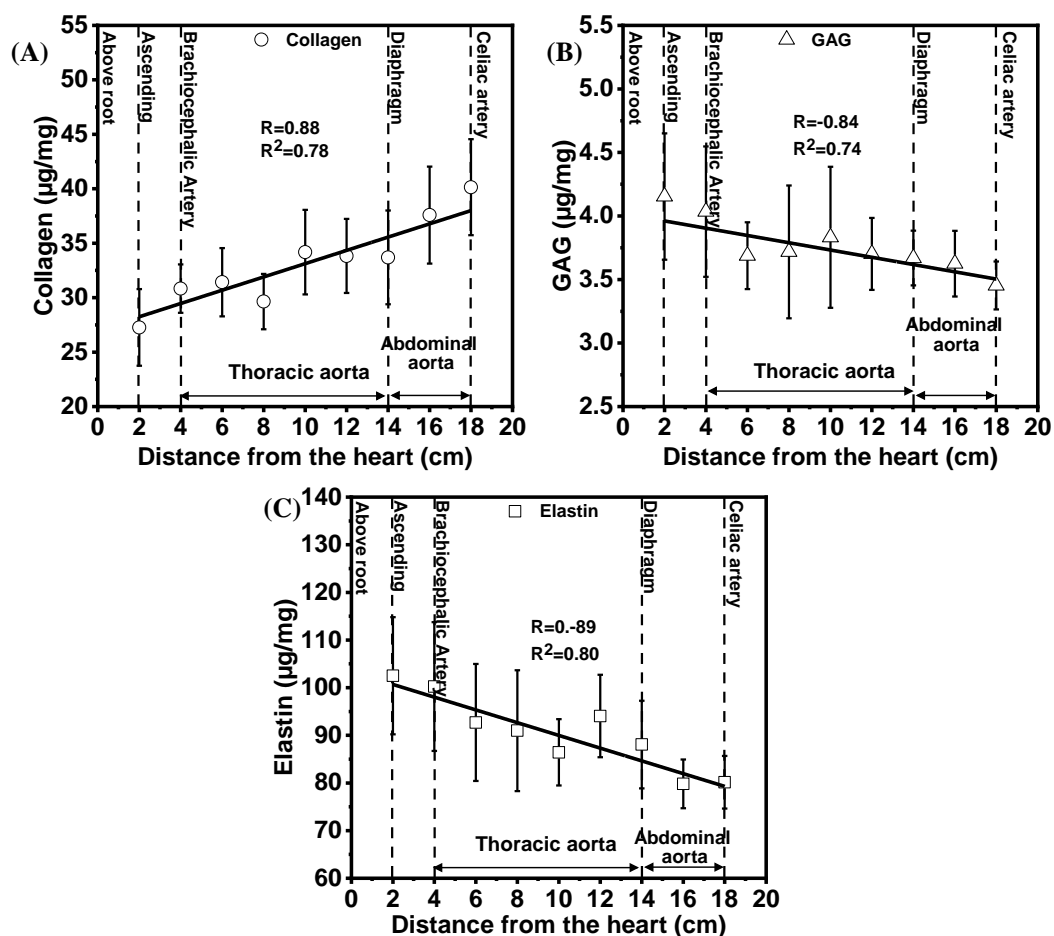


Figure 4.10 Biochemical properties across the ovine aorta as a function of distance from the aortic root (A) Collagen levels were found to be positively correlated with distance (Pearson correlation coefficient, $R=0.88$, $p=0.00187$) (B) GAG levels and (C) Elastin levels showed a negative relationship with distance (Pearson correlation coefficient, GAG level-distance: $R=-0.84$, $p=0.0043$ and elastin level-distance: $R=-0.89$, $p=0.001$). All biochemical data are expressed as $\mu\text{g}/\text{mg}$ of wet tissue weight from 81 samples ($n=9/\text{region}$ with 3 samples/animal) shown as mean \pm SD.

We found a positive correlation between collagen and E (collagen- E: $R = 0.91$, $R^2=0.83$ and $P=0.0006$) whereas for GAG (GAG- E: $R=-0.89$ $R^2=0.79$ and $P=0.00126$) and elastin (elastin- E: $R=-0.80$ $R^2=0.65$ and $P=0.0097$) there was a negative correlation.

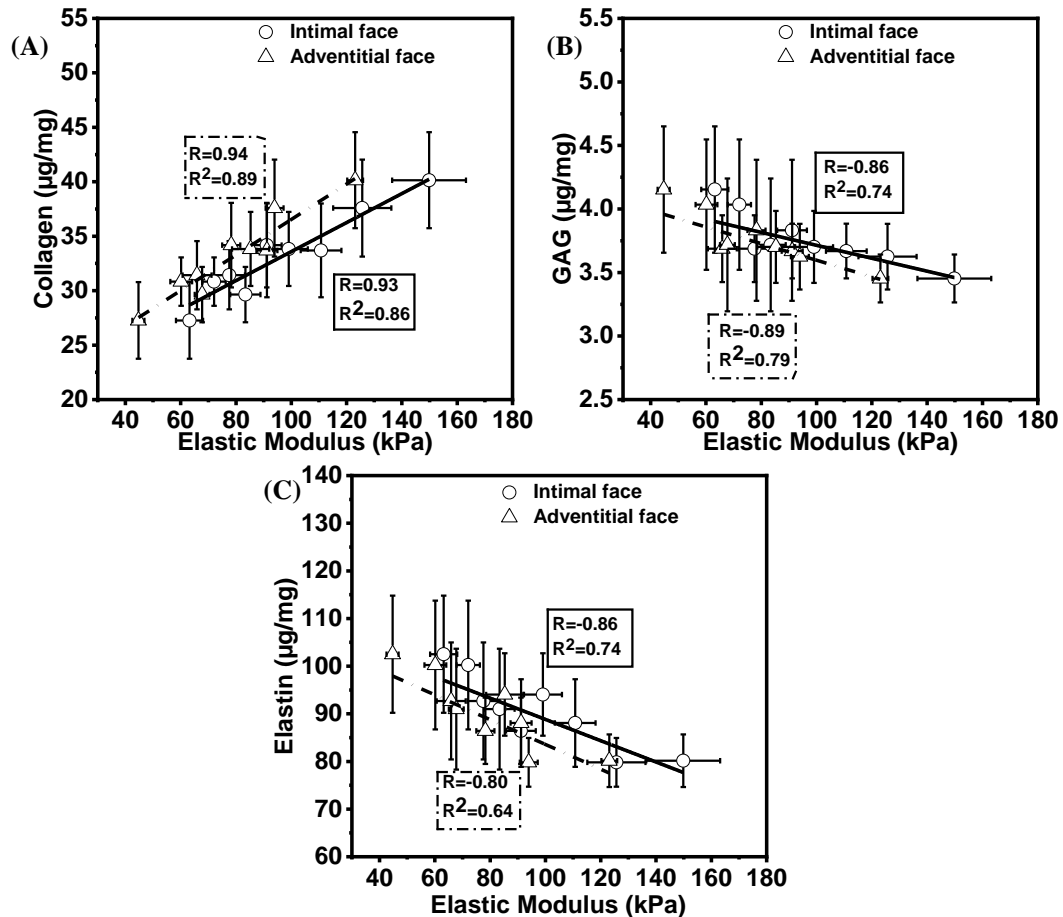


Figure 4.11 Comparison between biochemical properties (collagen, GAG and elastin levels) and elastic modulus determined with nanoindentation in the longitudinal orientation (A) Collagen (B) GAG and (C) elastin. Data are shown as mean±SD

Intra-group variability both for biomechanical properties (G' , G'' and $\tan \delta$) and biochemical properties (collagen, GAG and elastin) and inter-group variation (for the distance from heart) was examined and presented in Tables A2-A7 (Appendix A).

4.2.6 FTIR analysis

The underlying description on MCR-ALS theory has been provided in detail elsewhere (Mader et al., 2016). Theoretically, MCR-ALS analysis yields spectra of single/pure components. In order to assist with assignment of the biochemical identity of the extracted factors, the spectral profiles were compared to the reference spectral profile. MCR-ALS deconvolution was carried out without any input of the spectral or distribution characteristics of the aortic wall. For the investigated ovine aorta images the analytical strategy previously reported for tissue of intervertebral discs was adapted and a wavenumber region of 950-1600 cm^{-1} was chosen for MCR-ALS deconvolution (Mader et al., 2016). Finding the optimum number of factors for the MCR-ALS model is important as using not enough factors (under modelling) leads to an unstable model, which does not give reproducible results. On the other hand, using too many factors (over-modelling) adds noise rather than chemical meaningful information. In this work the optimum number of factors was estimated firstly based on the percentage variance assigned to principal component analysis (PCA) factors. Secondly, MCR-ALS analysis was carried out using a range of factors around the optimum number of factors estimated by PCA analysis. The optimum number of factors for MCR-ALS analysis was then determined based on a comparison of MCR-ALS results to reference spectra and histological stains of target tissue components. Details of all MCR-ALS results derived from the spectral regions 950–1600 cm^{-1} modelled using 4 to 6 factors can be found in Appendix A (Figures A1-4).

Due to the PCA result six and five modelled factors were chosen as the optimum number of factors for the MCR-ALS analysis for overview and transverse FTIR imaging

data sets, respectively. From the extracted factors, the estimated spectral profiles were correlated to the reference spectral profile of elastin and collagen as they are the predominant components of aortic wall that will contribute to the FTIR signature (Figure 4.12A). Ideally all of the factors represent different sample components however in reality some represent changes in the signal intensity due to changes in the sample surface or instrumental/measurements artefacts (Table. 4.1 and 4.2).

Table 4.1 The representative factor index after MCR-ALS analysis in the spectral region 950-1600 cm⁻¹ for the overview FTIR imaging data sets.

No. of factors used for model	Factor index after MCR	Component
6	F1	Collagen
6	F2	reflective artefacts (gradual change in surface structure or reflective index change)
6	F3	collagen+instrumental artefact (e.g. different illumination across the field of view)
6	F4	Elastin
6	F5	collagen+instrumental artefact (e.g. different illumination across the field of view)
6	F6	Elastin+instrumental artefact (e.g. different illumination across the field of view)

Table 4.1 presented the factor index after MCR-ALS analysis for the overview FTIR imaging data sets. It was found that factor 1 and factor 4 corresponded to collagen and elastin, respectively (Figure 4.12B). For image distribution, an overview section of paraffin embedded ovine aortic wall was measured and a tissue distribution map of the aortic wall was generated. Overall, the average intensity is similar across the aortic layer (Figure 4.12C). MCR-ALS distribution maps of factor 1 (collagen) and 4 (elastin) are presented in Figure 4.12D and E, respectively. It reveals that for factor 1 (collagen) the average intensity shows a gradual decrease from the outer to inner layer of the aortic wall, whereas local higher intensity of factor 4 (elastin) can be observed in the inner layer of the aortic wall.

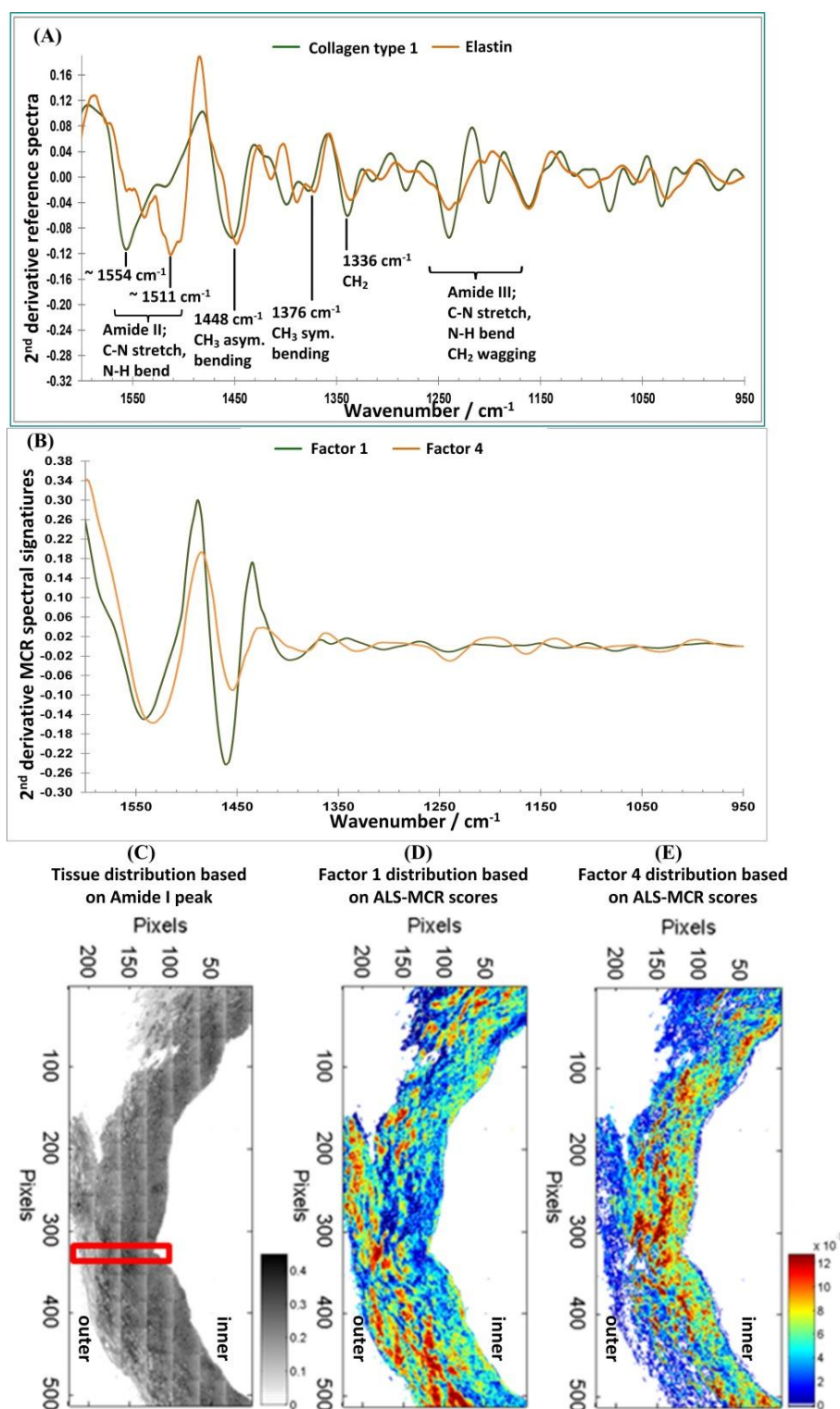


Figure 4.12 (A) Comparison of spectral profiles of 2nd derivative reference of collagen and elastin with (B) extracted spectral signatures from MCR-ALS analysis. Overview FTIR image of a sheep aorta section showing from (C) overall distribution map of tissue section, (D) MCR-ALS factor 1 refers to collagen (E) MCR-ALS factor 4 refers to elastin. Red rectangle represents transverse image that was used to more analyse for FTIR across the layer of aortic wall.

The highlighted area shown within the red box in Figure 4.12, was analyzed in more detail. The correlation between the reference spectral profiles (Figure 4.13A) and extracted spectral profiles (Figure 4.13B) highlighted that the best correlation was factor 1 and factor 2 corresponding to collagen and elastin, respectively (Table 4.2).

Table 4.2 Representative factor index after MCR-ALS analysis in the spectral region 950-1600 cm⁻¹ for the transverse FTIR imaging data sets.

No. of factors used for model	Factor index after MCR		Component
5	F1	Collagen	
5	F2	Elastin	
5	F3	Other type of collagen	
5	F4	Reflective artefacts (gradual change in surface structure)	
5	F5	Reflective artefacts (gradual change in surface structure)	

For a comparison between histological stains and the MCR-ALS imaging distribution maps, the 2nd derivative peak integration map of amide II spectral region is proposed to visualize the overall aortic tissue distribution and is determined by matching with H&E stained tissue section. It found that the distribution maps of general tissue and H&E stained tissues section is similar (Figure 4.13C). Like the H&E tissue section, the distribution map can show the overall structure of aortic wall. The section presented a densely packed inner layer (at the top) whereas a less dense outer layer (at the

bottom). This finding is consistent with that of Witter and co-workers (Witter et al., 2017). They characterised the histological morphology of animal arteries (porcine, canine and feline) in different regions analysed using light microscopy and found that the outer layer of arteries was a loose layer. The distribution map of MCR-ALS factor 1 for collagen illustrates a high intensity at the adventitial region, in agreement with Picrosirius red stain (Figure 4.13D). The distribution map of MCR-ALS factor 2 for elastin shows a decrease in intensity from intima toward adventitial region (at the top to the bottom) that matches with the black areas of VVG stain section corresponding to elastin staining (Figure 4.13E).

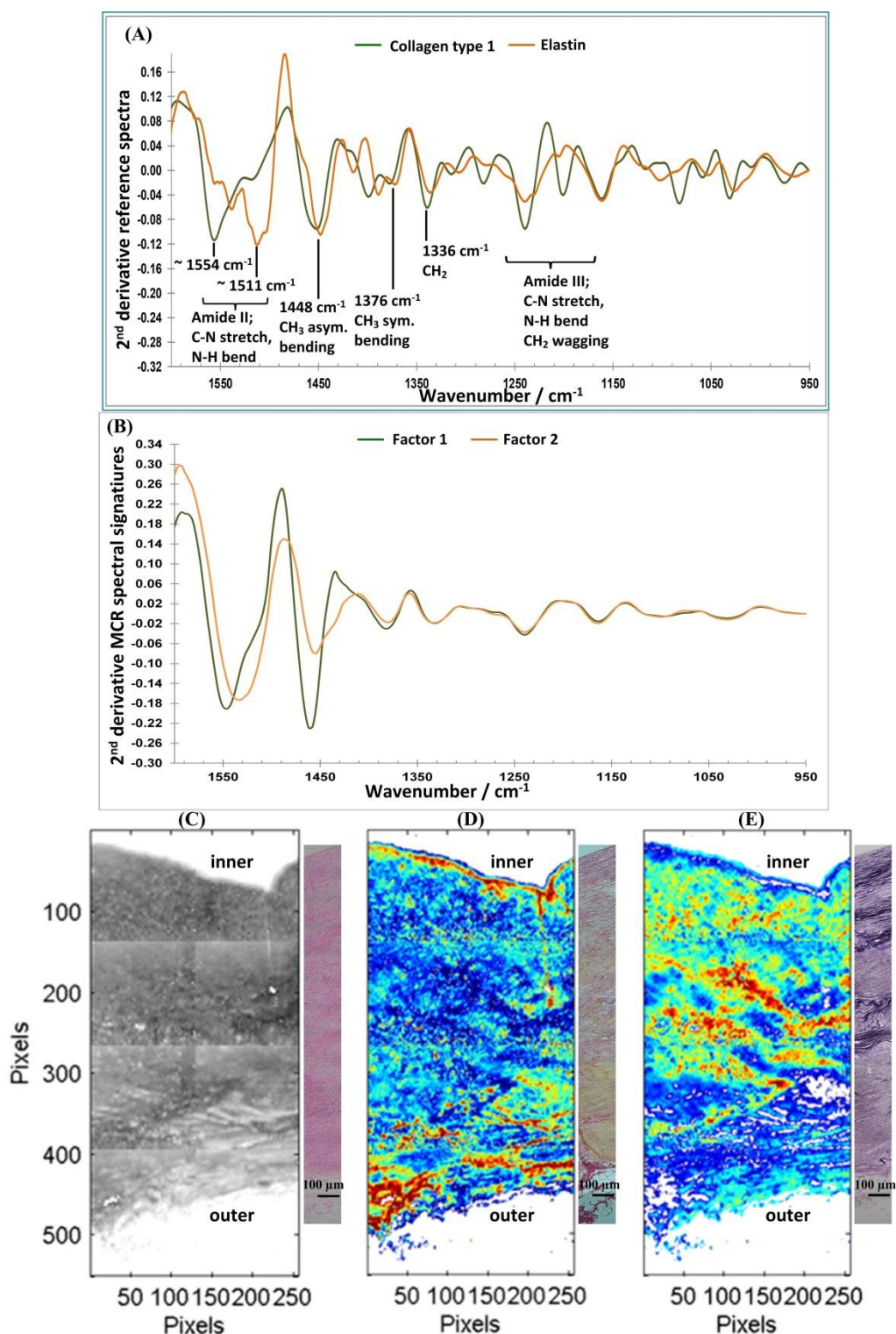


Figure 4.13 (A) Comparison of spectral profiles of 2nd derivative reference spectra of Collagen and Elastin with (B) extracted spectral signatures from MCR-ALS analysis. Transverse FTIR image across the aortic wall of the same ovine aorta section shown in Figure 3.13 (highlighted in red box) showing (C) distribution maps of the tissue overall and H & E stain, (D) MCR-ALS factor 1 and Picrosirius red stain and (E) MCR-ALS factor 2 and VVG stain (Scale bar = 100 μm).

4.3. Discussion

Aortic diseases such as aneurysms and dissections are location dependent (Isselbacher, 2012). For example, 60% of thoracic aortic aneurysms occur in the ascending aorta (Isselbacher, 2012). Hence, it is important to understand the mechanical and biochemical properties of the aorta across different regions. This is not only important for understanding aortopathies and surgical planning but also for designing stent grafts (Khanafer et al., 2011). In this chapter, the macro, micro-mechanical and biochemical properties of the ovine aorta have been comprehensively mapped across the vascular tree. The methodologies used will be employed in later chapters in this thesis for human tissue biopsies from patients with chronic aortic dissections.

The main novelty of the work presented in this chapter is, through the application of oscillatory nanoindentation, the determination of regional variation of biomechanical properties, which are directly related to the biochemical variation in collagen, elastin and GAG levels. In addition, orientation-dependent nanoindentation properties along with macroscopic uniaxial testing were presented to provide a comprehensive picture of the variation of properties across the aorta. In addition, the application of oscillatory nanoindentation allowed the mechanical properties to be determined with a much higher spatial resolution than is possible with uniaxial testing. By presenting both uniaxial and nanoindentation data, it was possible to compare the data collected with other studies and also correlate the novel nanoindentation method with more conventional, established mechanical testing methods. These data may serve as a useful reference given the increase in use of indentation-based techniques for aortic

biomechanical analysis (Meekel et al., 2019, Kermani et al., 2017, Akhtar et al., 2016, Grant and Twigg, 2012).

The advantages of nanoindentation over uniaxial tensile testing are that the technique is non-destructive, requires small samples and the spatial resolution is in line with the microstructural organisation of the fibres. The oscillatory nanoindentation method provided the viscoelastic behaviour for the longitudinal orientation (both intimal and adventitial face) and circumferential measurements on the media. These were correlated with the biochemical composition, across the different regions. As the technique is non-destructive, the same samples could be used for subsequent biochemical testing.

The nanoindentation data collected in this chapter follow the trends reported by (Kermani et al., 2017) who examined the mechanical properties of porcine aorta with a custom-made nanoindentation test setup. They reported that the distal regions of the aorta were stiffer than the proximal regions. The trends are also in agreement with another nanoindentation study on the porcine aorta which showed that the elastic modulus is higher at the inferior artery as compared to the subclavian artery (Hemmasizadeh, Autieri and Darvish, 2012). Whilst the absolute values differ when comparing our nanoindentation data with the uniaxial testing data, the trends are similar as shown in Figure 4.5. While the elastic behaviour of the aorta has been previously investigated (Peña et al., 2018, Haskett et al., 2010, Sokolis, Boudoulas and Karayannacos, 2008, Sokolis et al., 2006, Guo and Kassab, 2003), time-dependent behaviour have yet to be quantified. To understand how the behaviour of ovine aortic wall with time-dependent deformation (creep), the ball indentation method was

introduced to measure the central deformation between for ascending and descending over time. The ascending aortic wall appeared to more compliant to deformation over time relative to descending region. The elastic modulus is lower in ascending relative to descending region matching the data obtained from nanoindentation. This technique offers potential for assessing chronic dissected human tissues and will be utilised in Chapter 5.

Sokolis (2007) has previously examined regional differences in the porcine aorta by determining the mechanical properties under uniaxial tension along with elastin and collagen content as measured by histological analysis. They split the aortas into nine segments in one study (Sokolis, 2007) and seven segments in a later study (Sokolis, Boudoulas and Karayannacos, 2008). The overall trends in the biomechanical properties that have been reported in this chapter match those of Sokolis et al. The novelty in our work is the determination of collagen, elastin and GAG levels for the same samples that were used for mechanical testing. Unlike previous work in the literature, there was no need to rely on semi-quantitative assessment of collagen and elastin content from histology images. Furthermore, the author is not aware of any other studies that have reported GAG variations across the aorta.

The matrix fibres (collagen and elastin), and GAGs together govern the mechanical behaviour of the aorta. Alteration in these components within the aortic wall can lead to detrimental changes in the biomechanical properties and function of the aorta (He and Roach, 1994). A better understanding of the distribution of collagen, elastin and GAGs in relation to aortic biomechanics may help better elucidate the physiopathology of aortic disease in specific locations. One key finding in this chapter

is that there is a significant correlation with an increase in G' and collagen with distance from the aortic root whilst elastin and GAG levels significantly decreased. The negative relationship between GAG content and distance from aortic root to celiac artery region is of particular interest. It was found that GAG content decreased by 83.1% from the ascending region to the abdominal aortic region, accompanied by 220.8% increase in the circumferential elastic modulus. GAG pooling has been implicated in the development of thoracic aortic aneurysm and dissection (Roccabianca, Ateshian and Humphrey, 2014, Roccabianca, Bellini and Humphrey, 2014). The data also presented in this chapter suggests that given the differences in ECM content in the ascending vs. abdominal aorta, different degradation pathways may be implicated in aneurysm formation in different regions, initiating dissection and in the propagation. GAGs play a significant role in maintaining the structure of the aortic wall, supporting mechanosensing functions and influencing collagen fibrillogenesis and are altered with aortic pathogenesis (Wight, 1989, Schriebl et al., 2015, Cherchi et al., 1990). The role of GAGs in the proximal aorta requires further analysis especially given the increased prevalence of type A dissection at the proximal aorta as compared to type B dissection at the distal aorta. Hence, these data have potential to support mechanistic insight into aortic aneurysms and dissection development in different regions of the aorta.

In this study, the author has also investigated the potential of multivariate FTIR methods to identify chemical species within the ovine aortic wall. The FTIR spectral images of overview and transverse tissues of the ovine aorta were collected in transflection mode. The presented results show that this method allows the resolution

of the 2nd derivative FTIR microscopic imaging spectra of paraffin embedded aortic wall sections. Important biochemical matrix components (collagen and elastin) can be identified and their distribution visualised from a single piece of aortic tissue at the same time. By comparing both overview and transverse tissues of the ovine aorta, the extracted spectral signatures from MCR-ALS analysis presented the same trend for collagen and elastin. Furthermore, the observations of ovine aortic wall highlights the distribution map of elastin and reveals a gradual decrease in intensity from the inner layer to outer layer of the aortic wall, whereas collagen presented a high intensity in the outer layer (adventitia). The observed distribution map data follow the trends reported by Graham et al., 2011 who analyzed the collagen and elastin of female sheep aorta by semi-quantitative histological methods. They illustrated that the intensity of elastin decreases with distance from the intimal surface. Using the multivariate FTIR method it is possible to measure spatially resolved quantitative biochemical information of collagen and elastin.

4.4. Limitations

Ovine aortic tissue was used in this chapter to develop techniques and examine regional differences in the tissue structure and properties. However, there are differences between ovine and human aortas e.g., in terms of haemodynamic. Further, the work in this chapter did not serve as a model for aortic dissection, which is the main focus of this thesis. The macroscopic mechanical property measurements were conducted in uniaxial test conditions. In order to fully capture the anisotropic properties of the aortic wall, biaxial testing should also be considered. GAG work could be followed up by quantifying the presence of specific proteoglycans in the tissue.

4.5. Conclusions

To conclude, in this chapter, ovine aorta served as a readily accessible model for studying biomechanical and biochemical properties of the aorta across the different regions. It demonstrates how collagen, elastin and GAG levels relate to the biomechanical properties of different regions of the aorta. A significant trend of increasing stiffness both at the macroscopic and at the micromechanical scale was observed from the ascending aorta to the abdominal aorta. These changes in the mechanical properties were correlated with increased collagen, decreased elastin and GAGs as the distance from the heart increases. With time-dependent deformation (creep) of aortic tissues, the ball indentation method as the key technique for understanding how the behaviour of aortic tissues was optimised in terms of its sample preparation and testing procedures. Furthermore, using multivariate FTIR method chemical species information was obtained from a single piece of tissue to

correlate distribution information instead of needing to do multiple stains. It is a promising tool which allows extensive investigations to be performed on limited tissue samples such as chronic aortic dissection tissues used in our next study. All the technique development work in this chapter paves the way to explore biomechanical and biochemical changes in human chronic aortic dissections in the following chapters.

References

- Akhtar, R., Graham, H., Derby, B., et al. (2016) 'Frequency-modulated atomic force microscopy localises viscoelastic remodelling in the ageing sheep aorta', *J Mech Behav Biomed Mater*, 64 pp.10-7.
- Cherchi, G., Coinu, R., Demuro, P., et al. (1990) 'Structural and functional modifications of human aorta proteoglycans in atherosclerosis', *Matrix*, 10 (6), pp.362-72.
- Drury, D., Michaels, J., Jones, L. and Ayiku, L. (2005) 'Systematic review of recent evidence for the safety and efficacy of elective endovascular repair in the management of infrarenal abdominal aortic aneurysm', *Br J Surg*, 92 (8), pp.937-46.
- Grant and Twigg. (2012) 'Pseudostatic and dynamic nanomechanics of the tunica adventitia in elastic arteries using atomic force microscopy', *ACS nano*, 7 (1), pp.456-64.
- Guo and Kassab. (2003) 'Variation of mechanical properties along the length of the aorta in C57bl/6 mice', *Am J Physiol Heart Circ Physiol*, 285 (6), pp.H2614-22.
- Harkness, M. L., Harkness, R. D., McDonald, D. A. and etc. (1957) 'The collagen and elastin content of the arterial wall in the dog', *Proc.R.Soc.Lond.B.Biol.Sci.*, 146 (925), pp.541-51.

- Haskett, D., Johnson, G., Zhou, A., Utzinger, U. and Geest, J. V. (2010) 'Microstructural and biomechanical alterations of the human aorta as a function of age and location', *Biomech. Model. Mechanobiol.*, 9 (6), pp.725-36.
- He and Roach. (1994) 'The composition and mechanical properties of abdominal aortic aneurysms', *J Vasc Surg*, 20 (1), pp.6-13.
- Hemmasizadeh, A., Autieri, M. and Darvish, K. (2012) 'Multilayer material properties of aorta determined from nanoindentation tests', *J Mech Behav Biomed Mater*, 15 pp.199-207.
- Hickson, S. S., Butlin, M., Graves, M., et al. (2010) 'The relationship of age with regional aortic stiffness and diameter', *JACC: Cardiovascular Imaging*, 3 (12), pp.1247-55.
- Humphrey, J. (2013) 'Possible mechanical roles of glycosaminoglycans in thoracic aortic dissection and associations with dysregulated transforming growth factor-beta', *J.Vasc.Res.*, 50 (1), pp.1-10.
- Isselbacher, E. M. (2012) '78 - Diseases of the Aorta'. In: Anonymous (ed.). *Goldman's Cecil Medicine (Twenty-Fourth Edition)*. Philadelphia: W.B. Saunders. pp.482-6.
- Kermani, G., Hemmasizadeh, A., Assari, S., Autieri, M. and Darvish, K. (2017) 'Investigation of inhomogeneous and anisotropic material behavior of porcine thoracic aorta using nano-indentation tests', *J Mech Behav Biomed Mater*, 69 pp.50-6.

Khanafer, K., Duprey, A., Zainal, M., Schlicht, M., Williams, D. and Berguer, R. (2011)

'Determination of the elastic modulus of ascending thoracic aortic aneurysm at different ranges of pressure using uniaxial tensile testing',

J.Thorac.Cardiovasc.Surg., 142 (3), pp.682-6.

Mader, K. T., Peeters, M., Detiger, S. E., et al. (2016) 'Investigation of intervertebral disc

degeneration using multivariate FTIR spectroscopic imaging', *Faraday Discuss.*,

187 pp.393-414.

Meekel, J. P., Mattei, G., Costache, V. S., Balm, R., Blankensteijn, J. D. and Yeung, K. K.

(2019) 'A multilayer micromechanical elastic modulus measuring method in ex

vivo human aneurysmal abdominal aortas', *Acta Biomater.*, 96 pp.345-53.

Peña, J. A., Corral, V., Martínez, M. A. and Peña, E. (2018) 'Over length quantification of

the multiaxial mechanical properties of the ascending, descending and

abdominal aorta using Digital Image Correlation', *J Mech Behav Biomed Mater.*,

77 pp.434-45.

Roccabianca, S., Ateshian, G. and Humphrey, J. (2014) 'Biomechanical roles of medial

pooling of glycosaminoglycans in thoracic aortic dissection', *Biomech. Model.*

Mechanobiol., 13 (1), pp.13-25.

Roccabianca, S., Bellini, C. and Humphrey, J. (2014) 'Computational modelling suggests

good, bad and ugly roles of glycosaminoglycans in arterial wall mechanics and

mechanobiology', *J. R. Soc. Interface*, 11 (97), pp.20140397.

- Schriebl, A. J., Schmidt, T., Balzani, D., Sommer, G. and Holzapfel, G. A. (2015) 'Selective enzymatic removal of elastin and collagen from human abdominal aortas: Uniaxial mechanical response and constitutive modeling', *Acta Biomater*, 17 pp.125-36.
- Sokolis, D. P. (2007) 'Passive mechanical properties and structure of the aorta: segmental analysis', *Acta physiologica*, 190 (4), pp.277-89.
- Sokolis, D. P., Boudoulas, H. and Karayannacos, P. E. (2008) 'Segmental differences of aortic function and composition: clinical implications', *Hellenic J Cardiol*, 49 (3), pp.145-54.
- Sokolis, D. P., Kefaloyannis, E. M., Kouloukoussa, M., Marinos, E., Boudoulas, H. and Karayannacos, P. E. (2006) 'A structural basis for the aortic stress-strain relation in uniaxial tension', *J.Biomech.*, 39 (9), pp.1651-62.
- Tovar, A. M., Cesar, D. C., Leta, G. C. and Mourao, P. A. (1998) 'Age-related changes in populations of aortic glycosaminoglycans: species with low affinity for plasma low-density lipoproteins, and not species with high affinity, are preferentially affected', *Arterioscler.Thromb.Vasc.Biol.*, 18 (4), pp.604-14.
- Wight. (1989) 'Cell biology of arterial proteoglycans', *Arteriosclerosis*, 9 (1), pp.1-20.

Witter, K., Tonar, Z., Schöpper, H. and etc. (2017) 'How many layers has the adventitia?–Structure of the arterial tunica externa revisited',
Anat.Histol.Embryol., 46 (2), pp.110-20.

Chapter 5

Micromechanical properties, time-dependent deformation and biochemical properties of chronic aortic dissection tissues

This chapter focusses on structural and biomechanical changes in chronic AD tissues: FP, TL and FL. Oscillatory nanoindentation and ball indentation techniques that were comprehensively assessed and optimised in Chapter 4 (ovine aortic tissues) are applied to chronic AD tissues for characterising localised micromechanical properties and time-dependent deformation of the FP, TL and FL tissues. Post-nanoindentation, the same tissue samples were used for biochemical analysis of collagen, elastin and GAG. Histological analysis was also conducted to quantify elastin and collagen percentage per tissue section area. FTIR analysis was also used to co-locate elastin, collagen and GAG distributions in the tissues. Finally, the micromechanical properties and biochemical properties are compared with clinical data.

5.1 Introduction

Chronic AD is generally defined as the presence of dissection after more than 30 days following the initial occurrence (Booher *et al.*, 2013). Chronic AD tends to be associated with a weakened aortic wall. Eventually the degenerated, weakened aortic wall can lead to rupture. Another important complication of a chronic dissection is the gradual loss of distal perfusion which can eventually lead to ischemic syndromes (Beebejaun, Malec and Gupta, 2013). Stanford Type A aortic dissections affecting the ascending region rarely become chronic, while Stanford Type B aortic dissections affecting the descending thoracic region only, are routinely chronic with a thickened, straightened intimal flap which loses its mobility because of remodelling (Peterss *et al.*, 2016, Sherifova and Holzapfel, 2019). Stanford Type A aortic dissections typically require surgical intervention whereas Type B aortic dissections are more often typically treated medically with blood pressure control in the acute state and surgically in the chronic state (Safi *et al.*, 1998, Blount and Hagspiel, 2009, Sherifova and Holzapfel, 2019). A report from IRAD revealed an in-hospital surgical mortality rate of 30% in patients with Type A AD and 13% in Type B AD (Hagan *et al.*, 2000, Suzuki *et al.*, 2003, Li *et al.*, 2016). Long-term survival of surgically treated patients with type B AD after hospital discharge was estimated to range from 50% to 80% at five years and 30% to 60% at 10 years (Tsai *et al.*, 2006, Luebke and Brunkwall, 2014, Li *et al.*, 2016). Clinicians consider several indicators including maximum diameter, expansion rate, genetic risk factors and family history. Current guidance recommends treatment for patients at reasonable surgical risk with chronic aortic dissection complicated by

aneurysmal degeneration with a thoracic aortic diameter over 55mm (Riambau et al., 2017).

Descending thoracic aortic aneurysms (DTA) and thoracoabdominal aortic aneurysms (TAAA) with a diameter 60 mm or greater were associated with a 19% yearly rate of rupture, dissection, or death. Median size at acute type B AD was 41 mm. Some 80% of dissections occurred below 50 mm, whereas 93% of ruptures occurred above 50 mm (Zafar et al., 2019). To prevent aortic rupture the dilated AD is treated with surgical operation if the diameter is more than 50 mm. Lower thresholds can be considered in patients with a connective tissue disorder such as Marfan syndrome. However, the aneurysms can rupture at any diameter (Pape et al., 2007, 2015, Sherifova and Holzapfel, 2019). In the case of Marfan syndrome, open-heart surgery is preferred over TEVAR due to concerns that the aortic wall may be weakened due to dissection (Nollen et al., 2004). There is no evidence supporting any use of TEVAR in patients with connective tissue disease, except emergency situations in order to get initial stabilization as a bridge to definitive surgical therapy (Parisi et al., 2015). Previous literature shows that the ECM composition changes during the progression of AD (Sherifova and Holzapfel, 2019). A key structural change in AD termed medial degeneration is associated with SMC loss, elastic fibre fragmentation, and an accumulation of proteoglycans (Bode-Jänisch et al., 2012, Humphrey, 2013, Sherifova and Holzapfel, 2019). To gain a more in-depth understanding of the underlying mechanism for chronic AD there is a need to study the micromechanical and biochemical characterisation, comparing FP, TL and FL tissues. The nanoindentation technique is suitable for investigating the mechanical properties of soft tissues at the

micro-scale. A few studies have begun using the nanoindentation for examining the mechanical properties in human aortic pathology at micro-scale (Chim et al., 2019, Meekel et al., 2019). However, information about micromechanical properties of chronic AD tissues is largely unknown and there have been no previous studies investigating the behaviour of chronic AD tissues with regards to time-dependent deformation. It is widely known that the change in ECM microstructure and components in the aortic wall occur together with changes in their mechanical behaviour (Humphrey and Holzapfel, 2012), which are likely to contribute to the development of AD.

This chapter aims to apply the nanoindentation technique and ball indentation method that were used to successfully determine micromechanical properties and time-dependent behaviours of the ovine aorta, respectively across different anatomical regions (Chapter 4) to aortic biopsy samples from chronic dissection patients to characterise the micromechanical properties of FP, TL and FL alongside biochemical measurements on the same samples. Subsequently, fibrillar collagen and elastic fibres were characterised by histological analysis. This chapter further highlights how the changes in localised mechanical properties, biochemical data and histological data are associated with the IIEO and the growth rate, to increase understanding of the underlying mechanisms for chronic AD, leading to improved surgical planning and clinical care.

Example CT scans for two patients with chronic type B dissection from whom tissue was sampled are shown in Figure 5.1 and 5.2. These are the only 2 patients with availability of all three tissue types (FP, TL and FL) (Table 3.1, Chapter 3). The CT scan

images were all provided by Mr. Mark Field (Liverpool Heart and Chest Hospital). The images are axial and 3D reconstructions in the coronal and sagittal planes. They demonstrate the nature of a chronic dissection with FL, TL and FP. In addition, the images show aneurysmal formation with tortuosity.

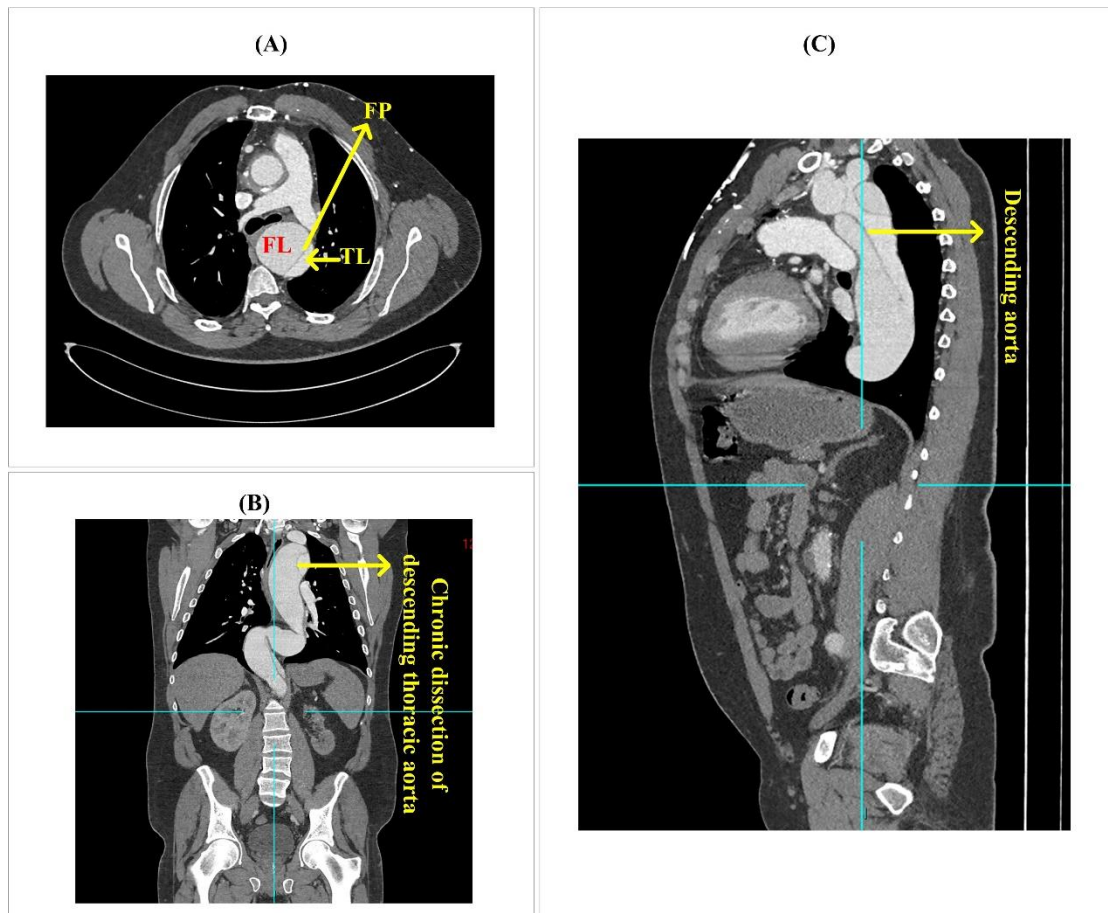


Figure 5.1 Contrast-enhanced computed tomography images demonstrating the morphology of patient ID:05-00064-18 with chronic type B dissection in (A) axial plane, (B) coronal plane and (C) sagittal plane.

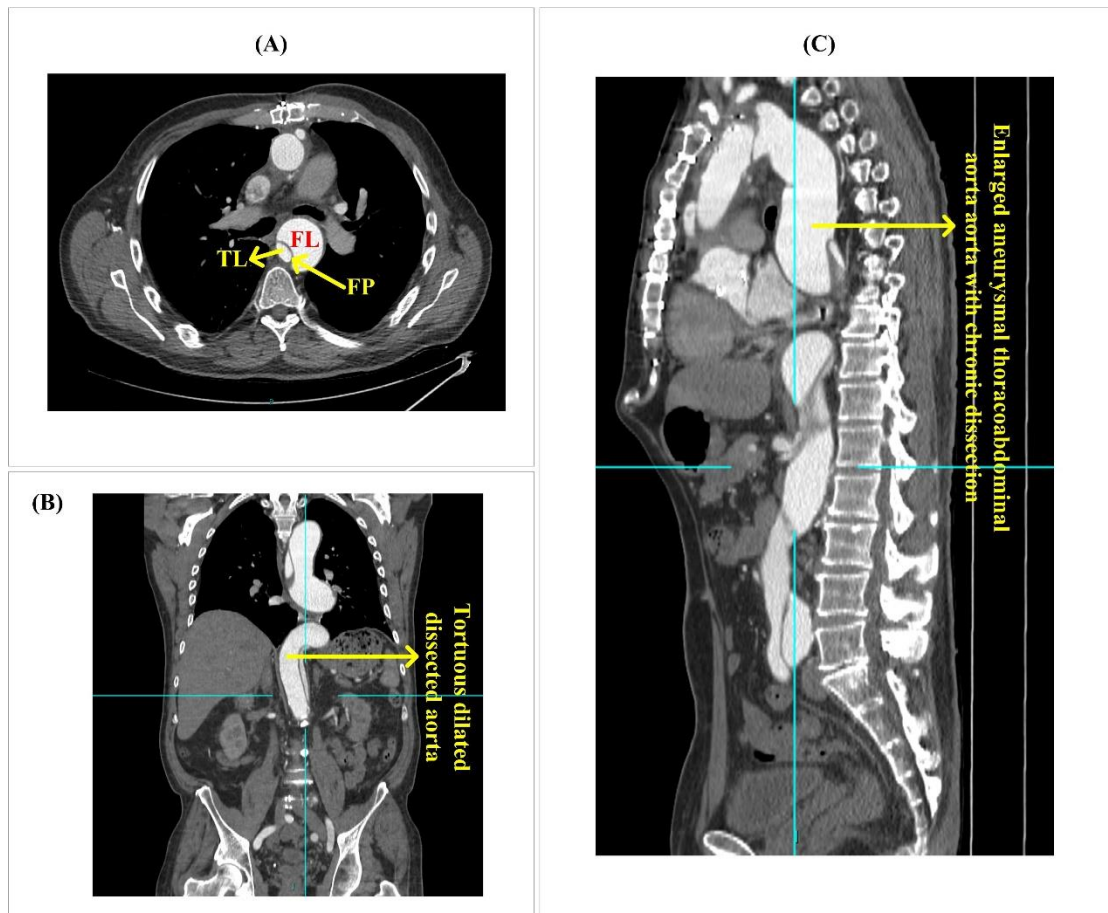


Figure 5.2 Contrast-enhanced computed tomography images demonstrating the morphology of patient ID:05-00017-19 with chronic type B dissection in (A) axial plane, (B) coronal plane and (C) sagittal plane.

5.2 Results

5.2.1 Patients and demographics

16 patients, including 15 males (93.8%) and 1 female (6.2%) were available, with ages ranging from 39 to 77 years (mean \pm SD; 57.3 \pm 13.5 years). 4 of the 16 patients were clinically characterised as having a syndromic disorder, Marfan syndrome. The remaining 11 were classified as non-syndromic. The chronic AD tissues were resected in two main regions; ascending (n=3 patients) and descending regions (n=13 patients). Table 5.1 presents clinical characteristics for all patients divided into tissue types available. There are no differences between FP, TL and FL in age and preoperative aortic diameter ($P>0.05$). The percentage split among the groups for the categorical data were as follows: male, 100% (FP and TL), 80% (FL); family history aneurysm, 10% (FP), 22.2% (TL) and 20% (FL); hypertension, 50% (FP), 66.7% (TL) and 60% (FL); cholesterol, 50% (FP), 55.6% (TL) and 40% (FL).

Table 5. 1 Clinical characteristics for the chronic patients, grouped by tissue type. Data are displayed as Mean \pm Standard deviation and *n* represents number of patients. FP, flap tissues; TL, true lumen outer wall tissues; FL, false lumen outer wall tissues.

	FP (n=10)	TL (n=9)	FL (n=5)	P-value
Age	56.0 \pm 12.7	55.7 \pm 14.6	53.0 \pm 14.4	0.92
Gender				0.001
Male, n	10 (100%)	9 (100%)	4 (80%)	
Female, n	0	0	1 (20%)	
Location				0.17
Ascending	1 (10%)	1 (11.1%)	3 (60%)	
Descending	9 (90%)	8 (88.9%)	2 (40%)	
Preoperative aortic diameter (cm)	6.2 \pm 0.4	6.2 \pm 1.1	6.5 \pm 2.1	0.86
Aetiology				0.47
Syndromic (Marfan)	3 (30%)	2 (22.2%)	2 (40%)	
Non syndromic (Unknown)	7 (70%)	7 (77.8%)	3 (60%)	
Family history aneurysm				0.89
Yes, n	1 (10%)	2 (22.2%)	1 (20%)	
No, n	9 (90%)	7	4 (80%)	
Hypertension				0.86
Yes, n	5 (50%)	5 (55.6%)	2 (40%)	
No, n	5 (50%)	4 (44.4%)	3 (60%)	
Cholesterol				0.86
Yes, n	5 (50%)	5 (55.6%)	2 (40%)	
No, n	5 (50%)	4 (44.4%)	3 (60%)	

5.2.2 Biomechanical findings

5.2.2.1 Micromechanical properties of chronic aortic dissection tissues (FP, TL and FL) determined by nanoindentation

Micromechanical properties (G' , G'' and $\tan(\delta)$) in the longitudinal direction were measured using nanoindentation. 16 oscillatory indentations were performed on the face of both sides (inner and outer) of chronic aortic tissues: FP, intimal and medial face; TL, intimal and adventitial face and FL, medial and adventitial face. G' , G'' and $\tan(\delta)$ are presented as Boxplots in Figure 5.3.

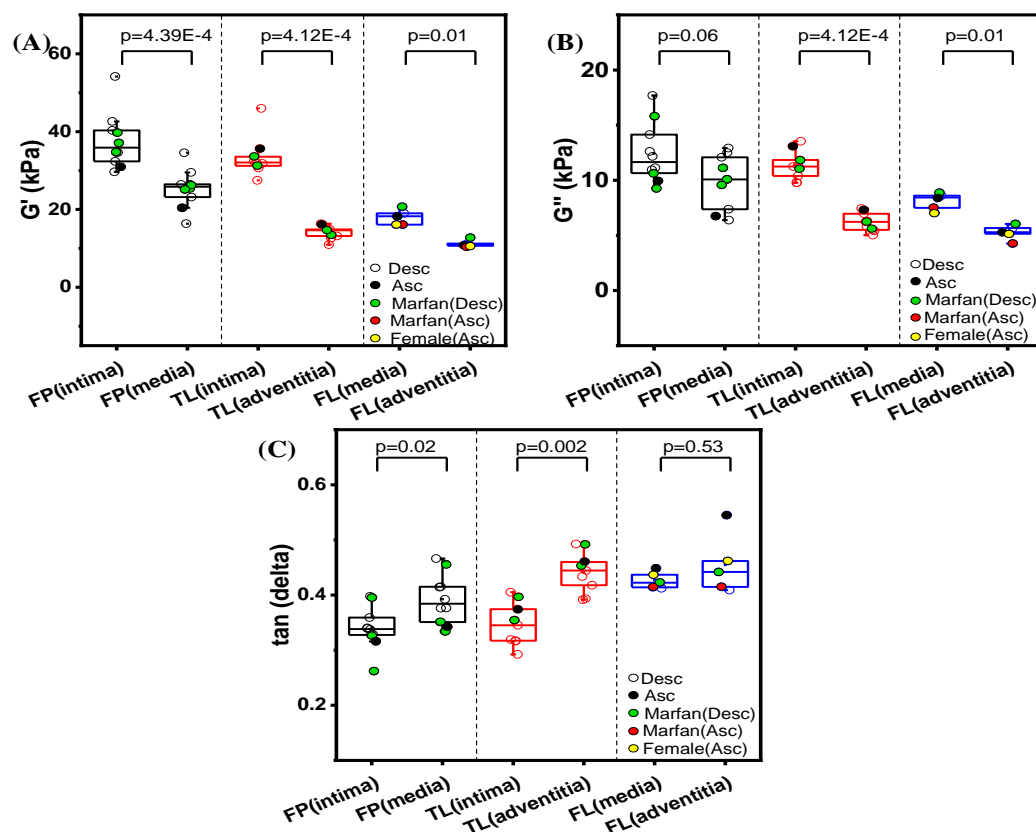


Figure 5.3 Micromechanical properties for the adventitial and intimal face for FP, TL and FL in longitudinal orientation: (A) G' (B) G'' and (C) $\tan(\delta)$. All values are shown with boxes representing the 25th and 75th percentiles of data. Whiskers represent the 5th and 95th percentiles of data and the middle horizontal lines represent the median value. Each point within the plot represents an individual patient for the variable specified. A p-value below 0.05 was considered as statistically significant.

Analysis of the longitudinal properties showed a significant difference in both sides of the wall for each tissue type. As shown in Figure 5.3A G' for FP in intimal face (median 36.8 kPa) was significantly higher than the medial face (26.0 kPa) ($p=0.001$). There was also a higher G' in intimal face (32.1 kPa) than adventitial face of TL (14.6 kPa) ($p=4.1E-4$). Similarly, G' for FL in adventitial face (11.2 kPa) was less than the medial face (19.0 kPa) ($p=0.012$). Overall, G' for FP group was highest relative to the TL and FL group. In addition, trends for G'' were similar to G' (Figure 5.3B). $\tan(\delta)$ was found to be relatively consistent, typically around 0.34-0.44 for FP, TL and FL group for both faces (Figure 5.3C). $\tan(\delta)$ for FL in intimal face (0.34) was significantly lower than the medial face (0.38) ($p=0.02$). There was also a lower $\tan(\delta)$ in intimal face (0.35) than adventitial face of TL (0.44) ($p=0.002$).

5.2.2.2 Central deformation of chronic aortic dissection tissues (FP, TL and FL).

Deformation of the chronic aortic tissues over time was obtained by using a ball indentation method as presented in ovine model (Chapter 4). The ball indentation experiment was conducted with a constant force over 300 minutes. A side view of the deformed chronic aortic dissection tissues was captured by a long focal microscope as shown in Figure 5.4.

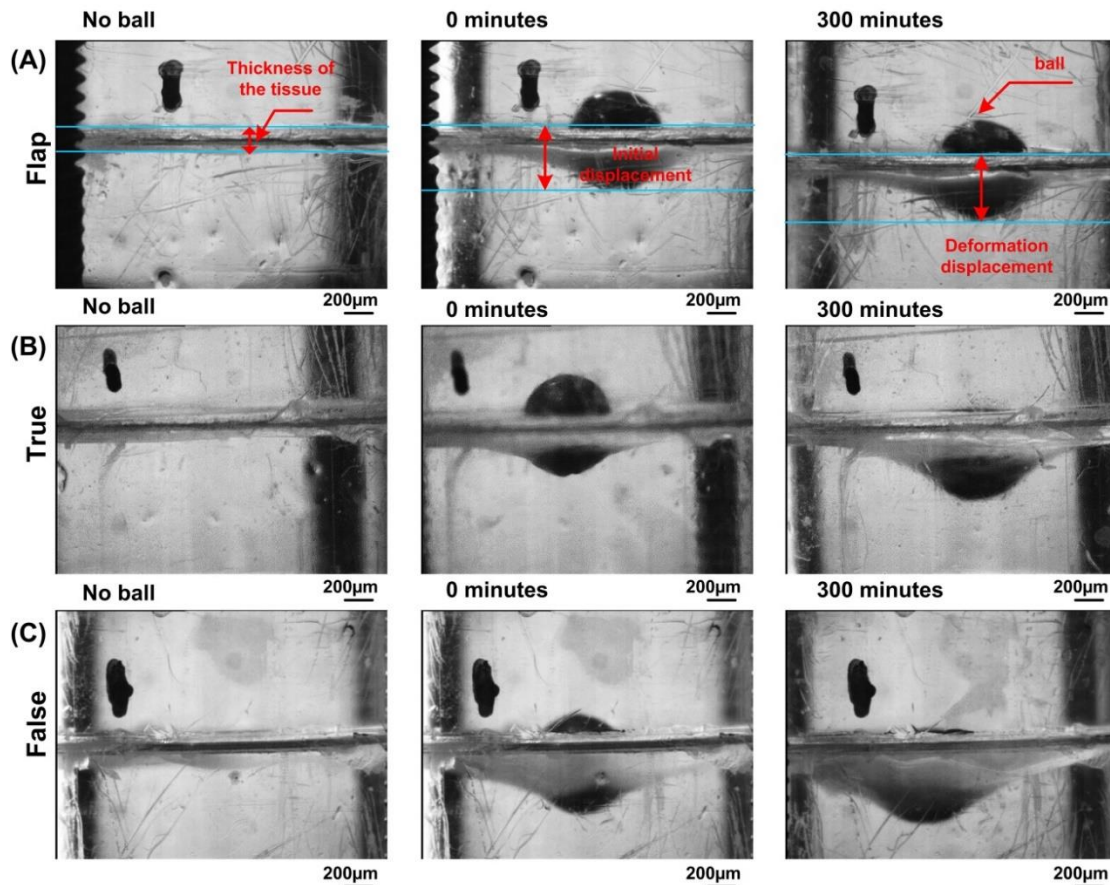


Figure 5.4 Images showing deformation for chronic aortic dissection tissues with no ball, under ball at 0 minute and 300 minutes: (A) FP, (B) TL and (c) FL. Scale bar represents 200 µm.

One measurement per tissue sample was performed on the medial layer in three different types of chronic aortic dissection tissues: FP, TL and FL. The actual curves for central displacement over time are shown in Figure 5.5. The central displacement for these chronic aortic dissection tissues increased owing to creep behaviour. There was a clear difference in the curves for each tissue type with FL showing the greatest deformation relative to FP which was more resistant to creep.

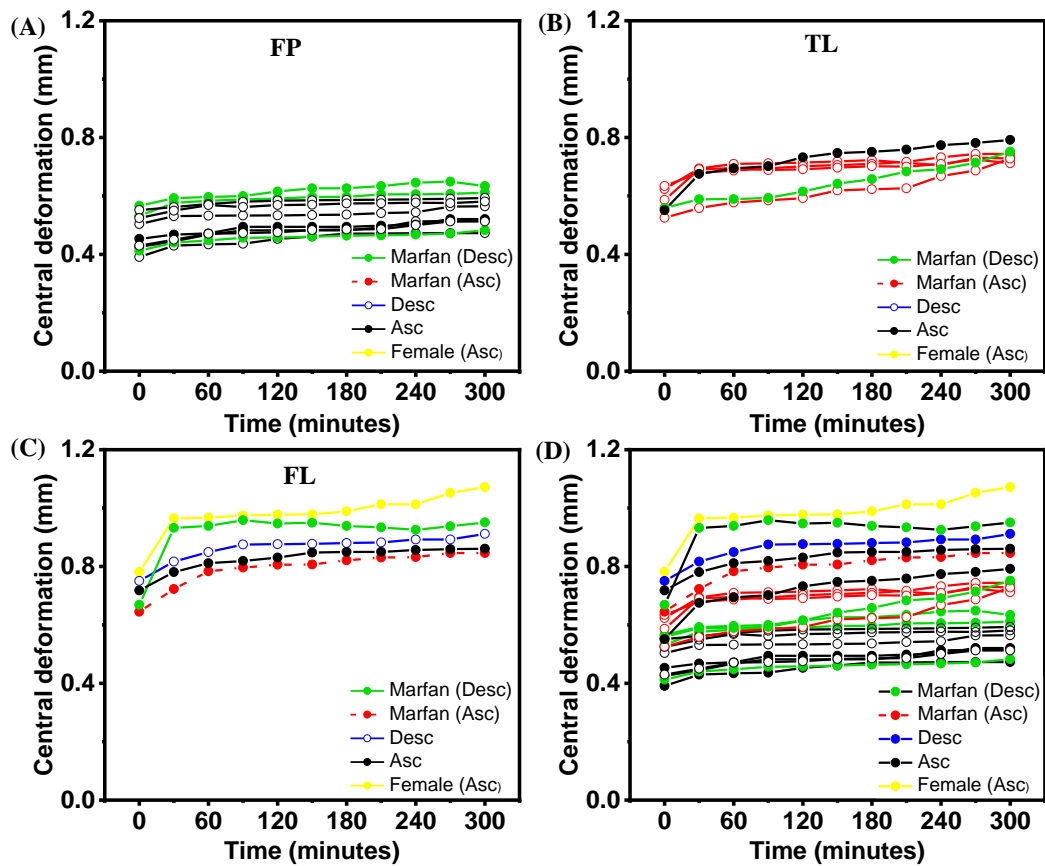


Figure 5.5 Central displacement deformation–time relationship extracted from: (A) FP (n=10), (B) TL (n=6), (c) FL (n=5) and (D) all FP, TL, FL in one graph. One measurement per tissue sample.

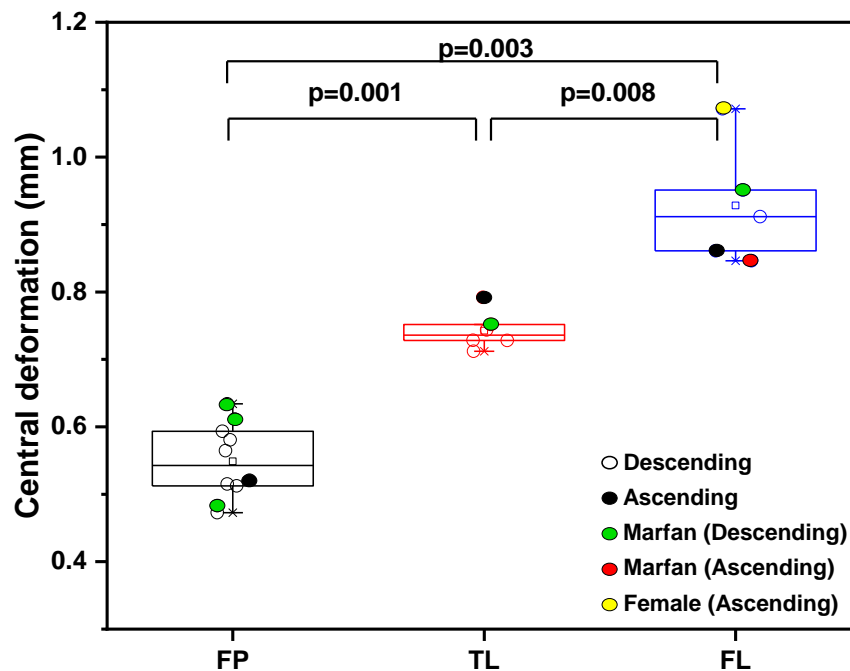


Figure 5.6 Box-whisker plots presented for the central deformation of chronic aortic dissection tissues between the three tissue types: FP (n=10), TL (n=6) and FL (n=5). The tissues were collected from ascending FP, TL (n=1) and FL (n=3) and descending sections FP (n=9), TL (n=5) and FL (n=2) from 14 patients. The Marfan syndromes were grouped by tissues type: FP (n=3), TL (n=1), and FL (n=2). All values are shown with boxes representing the 25th and 75th percentiles of data. Whiskers represent the 5th and 95th percentiles of data and the middle horizontal line represents the median. Each point within the plot represents a patient sample for the variable specified.

As shown in Figure 5.6, there were statistically significant differences for the time-dependent measurement over 300 minutes of the central displacement deformation when comparing FP and TL ($p=0.00138$), FP and FL ($p=0.00269$), as well as TL and FL ($p=0.00811$). It was noticed that the central displacement deformation for FP was significantly lowest relative to TL and FL.

5.2.2.3 The elastic modulus of chronic aortic dissection tissues (FP, TL and FL) from the ball indentation

The initial displacement measured with ball indentation at 0 minute was used to obtain the elastic modulus. The elastic modulus for FP, TL and FL is presented in Figure 5.7. Overall, significantly greater elastic modulus (tissue stiffness) was observed in FP as compared with TL and FL ($p=0.01081$ and $p=0.00269$, respectively). The elastic modulus was significantly lower in FL relative to TL ($p=0.00811$).

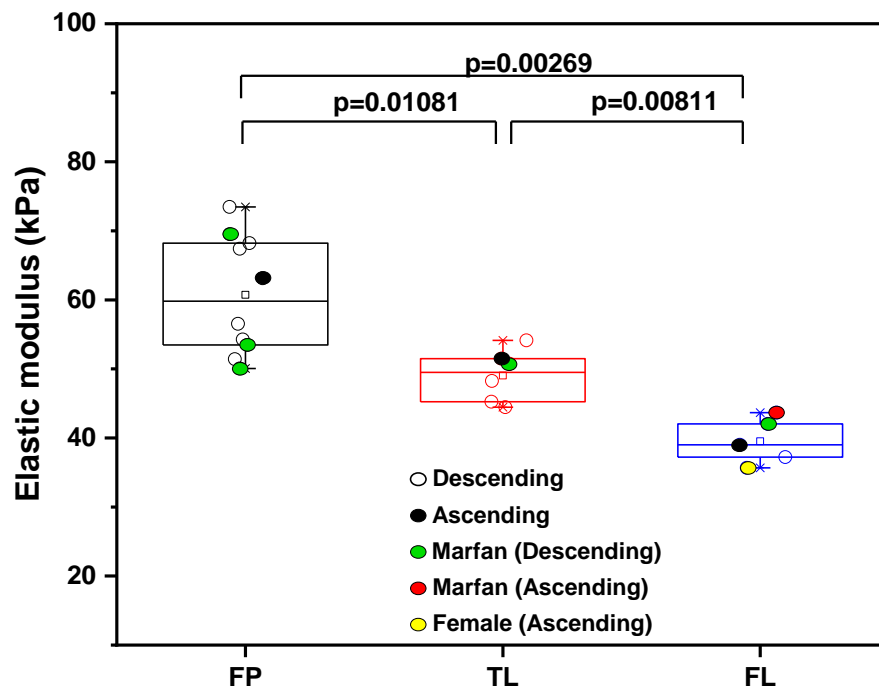


Figure 5.7 Box-whisker plots presented for elastic modulus for FP (n=10), TL (n=6) and FL (n=5). The tissues were collected from ascending FP, TL (n=1) and FL (n=3) and descending sections FP (n=9), TL (n=5) and FL (n=2) for 14 patients. Patients with Marfan syndrome are marked FP (n=3), TL (n=1), and FL (n=2). All values are shown with boxes representing the 25th and 75th percentiles of data. Whiskers represent the 5th and 95th percentiles of data and the middle horizontal line represents the median. Each point within the plot represents a patient sample for the variable specified.

Despite the small numbers, the difference between other factors such as anatomical location (ascending and descending), genetic disorders (syndromic Marfan and non-syndromic unknown), and sex differences (males or females) were minimal. It was found that the elastic modulus and central deformation between these variables did not differ. All of the values were within the range of the box-whisker plots.

5.2.2.4 Comparison of the elastic modulus obtained with nanoindentation and non-destructive ball indentation methods.

Both nanoindentation and the ball indentation test method utilised for the work presented in this chapter enable the elastic modulus of the tissue to be determined with the main difference being the length scale. A 100 μm diameter flat-ended cylindrical punch was used for nanoindentation method whereas a 2.4 mm stainless sphere ball was used for ball indentation method. The most appropriate comparison was the mean elastic modulus obtained via nanoindentation testing at the medial layer with the elastic modulus acquired from non-destructive ball technique. Given the testing approach and scale of testing differed with the two methods, the absolute values differed, however, it showed that overall trends of elastic modulus obtained from non-destructive ball is higher in the FP tissue relative to FL matching the nanoindentation data (as shown in Figure 5.8)

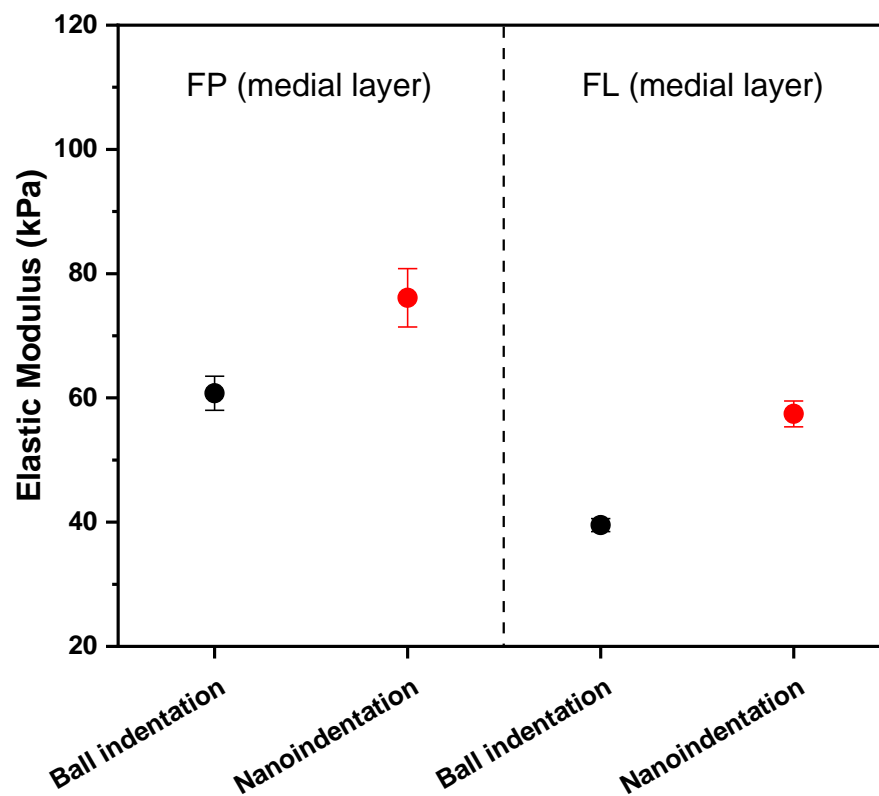


Figure 5.8 Comparison of trends of elastic modulus obtained via nanoindentation testing at the medial layer with elastic modulus values obtained via non-destructive ball testing for FP and FL.

In terms of the absolute values, with nanoindentation, the elastic modulus at medial surface was in the range of 49-104 kPa for FP, and 48-65 kPa for FL and from the non-destructive ball indentation method at medial membrane the range was 50-73 kPa and 36-44 for FP and FL, respectively. Therefore, the nanoindentation measurements were 1.0-1.4 times for FP and 1.3-1.5 times for FL higher than ball indentation measurements.

5.2.3 Biochemical analysis

Collagen, elastin and GAG levels were quantified from the same samples of tissue used for nanoindentation testing. All biochemical data are presented in Figure 5.9. It can be seen from Figure 5.9A that the collagen level was significantly higher in FL (66.0 $\mu\text{g}/\text{mg}$) as compared with TL (59.1 $\mu\text{g}/\text{mg}$, $p=0.032$) and FP (40.1 $\mu\text{g}/\text{mg}$, $p=0.003$) whereas GAG level for FL (2.2 $\mu\text{g}/\text{mg}$) was significantly lower relative to TL (2.8 $\mu\text{g}/\text{mg}$, $p=0.016$) and FP (3.7 $\mu\text{g}/\text{mg}$, $p=0.003$) (Figure 5.9B). Elastin levels were marginally greater in TL (82.9 $\mu\text{g}/\text{mg}$) relative to FP (81.7 $\mu\text{g}/\text{mg}$, $p=0.270$) but not significantly. The lowest elastin level and narrow distribution were noticed in FL (49.3 $\mu\text{g}/\text{mg}$) as compared with FP and TL (Figure 5.9C). Collagen/elastin ratio was lowest in FP (0.4 $\mu\text{g}/\text{mg}$) relative to TL (0.6 $\mu\text{g}/\text{mg}$, $p=0.006$) and FL (1.4 $\mu\text{g}/\text{mg}$, $p=0.003$) (Figure 5.8D).

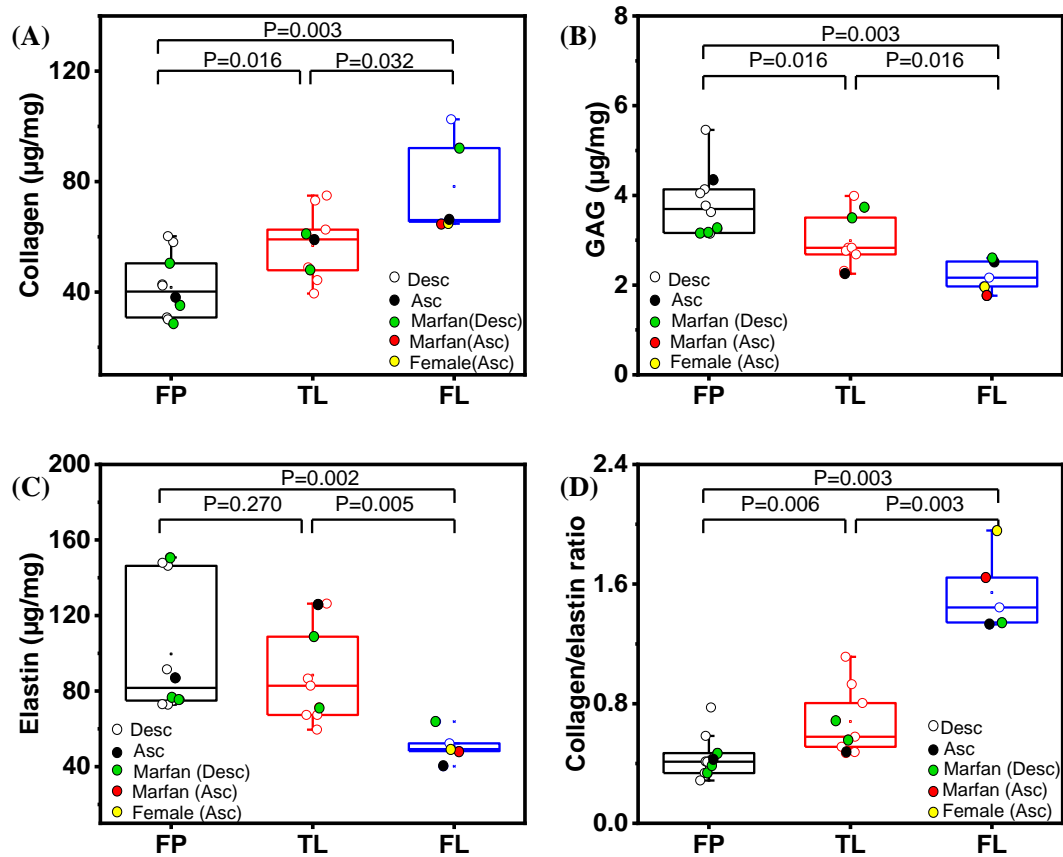


Figure 5.9 Boxplots of biochemical data between the three tissue types: FP (n=10), TL (n=9) and FL (n=5). These tissue types were collected from ascending FP, TL (n=1) and FL (n=3) and descending sections FP (n=9), TL (n=8) and FL (n=2) during replacement surgery from 16 patients. Marfan patients were grouped by tissue type: FP (n=3), TL (n=2), and FL (n=2). All data are represented as box plots representing the 25th and 75th percentiles of data. Whiskers represent the 5th and 95th percentiles of data and the middle horizontal lines represent the median value. Each point within the plot represents an individual patient for the variable specified. Variables acquired from the specimens were: (A) collagen levels (B) GAG level (C) elastin levels and (D) collagen/elastin ratio levels. The non-parametric Mann-Whitney analyses were performed to determine whether they were significantly different between groups.

5.2.4 Histological analysis

5.2.4.1 Aortic fibrillar collagen and elastic fibre content

The aortic fibrillar collagen and elastic fibre content were measured by analysis of Picrosirius red and VVG stained images respectively, for all groups (FP, TL and FL) at medial layer. The percentage of aortic fibrillar collagen per tissue section area was greater in FL (34.4%) relative to the FP (12.1%, $p=0.113$) and TL (16.6%, $p=0.536$) but not significantly (Figure 5.10A). In contrast the percentage of elastic fibre content for FL (0.04%) was significantly lowest as compared with TL (8.2%, $p=0.016$) and FP (7.0%, $p=0.027$) (Figure 5.10B). Overall trends of percentage collagen and percentage elastin per tissue section area obtained from histological analysis is similar trend obtained from biochemical analysis. The percentage collagen per tissue section area and collagen content are highest in the FL tissue whereas the percentage elastin and elastin content are lowest FL tissue relative to FP, TL.

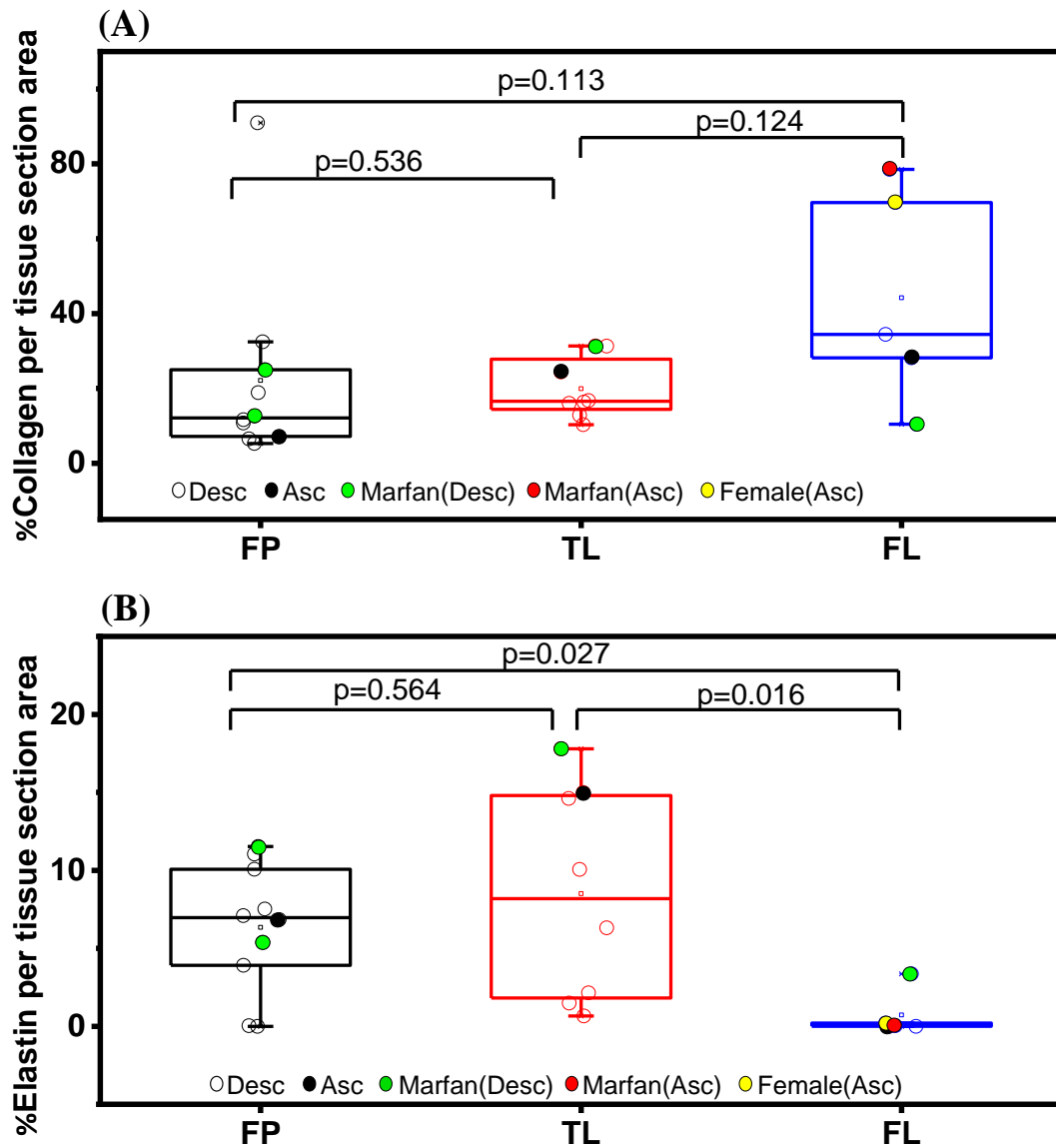


Figure 5.10 Box-whisker plots presented for: (A) Percentage of collagen per tissue section area and (B) Percentage of elastin per tissue section between the three tissue types: FP (n=10), TL (n=8) and FL (n=5). All values are shown with boxes representing the 25th and 75th percentiles of data. Whiskers represent the 5th and 95th percentiles of data and the middle horizontal line represents the median. Each point within the plot represents an individual patient for the variable specified.

5.2.4.2 Elastin fragmentation

Representative VVG stained sections of chronic AD tissues for TL, FP and FL groups are illustrated in Figure 5.11. The TL and FP tissues had highly compact, long, aligned elastic fibres compared with FL tissues. Elastin fragmentation was graded as shown in section 3.2.4.2. In the most cases for TL (Figure 5.11B) Grade I (71%) was seen while Grade II (70%) and Grade III (20%) were classified in FP group (Figure 5.11A) and Grade III (100%) for FL (Figure 5.11C).

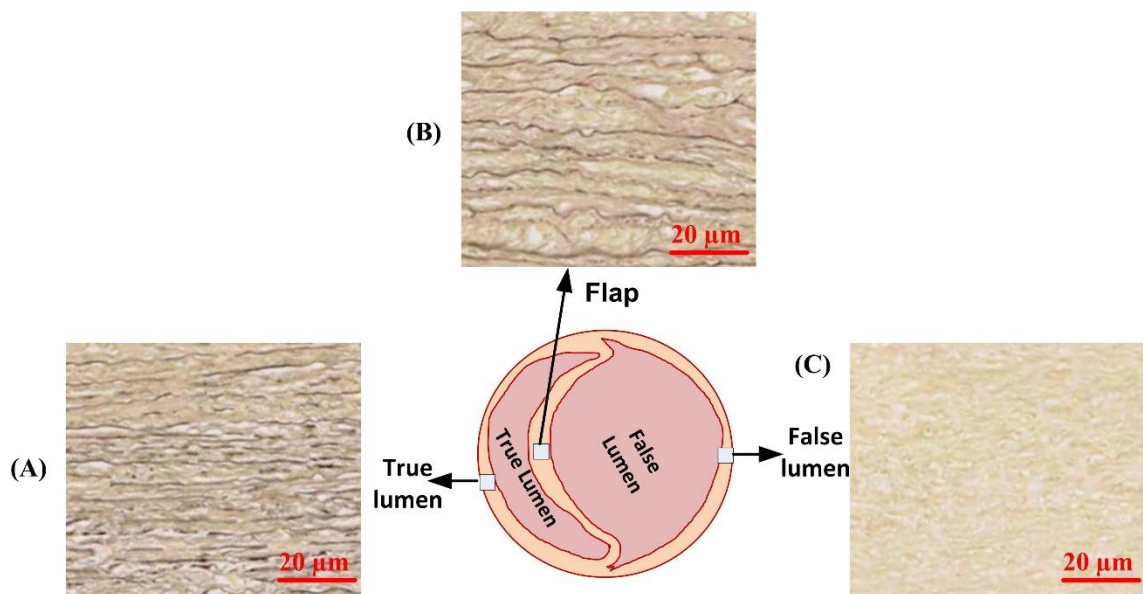


Figure 5.11 Example elastin fragmentation for chronic AD tissues: (A), (B) and (C) demonstrates TL, FP and FL, respectively. Scale bar is 20μm.

Given that elastin fragmentation occurs in the aortic wall with increasing age (Schlatmann and Becker, 1977) and this information is important. The graded images were also classified by age as shown in Figure 5.12.

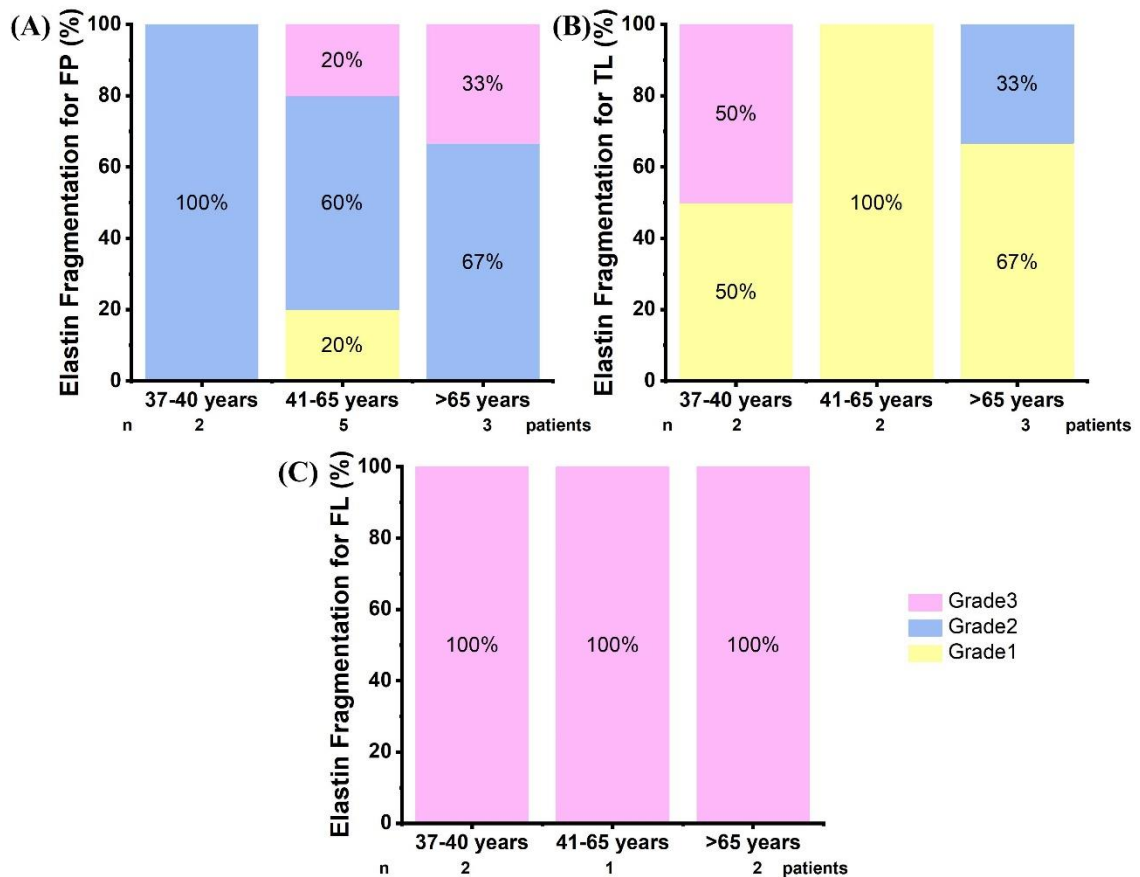


Figure 5.12 Percentage of elastin fragmentation graded by age for: (A) flap (FP), (B) true lumen outer wall (TL) and (C) false lumen outer wall (FL).

5.2.3.3 Alcian blue staining for quantifying GAG

Alcian blue staining was used to detect GAG. GAG (identified as dark blue in the images) was predominantly present across the FP tissue in contrast to TL and FL where layer specific staining was observed (Figure 5.13). These results are consistent with GAG level data measured by biochemical assay.

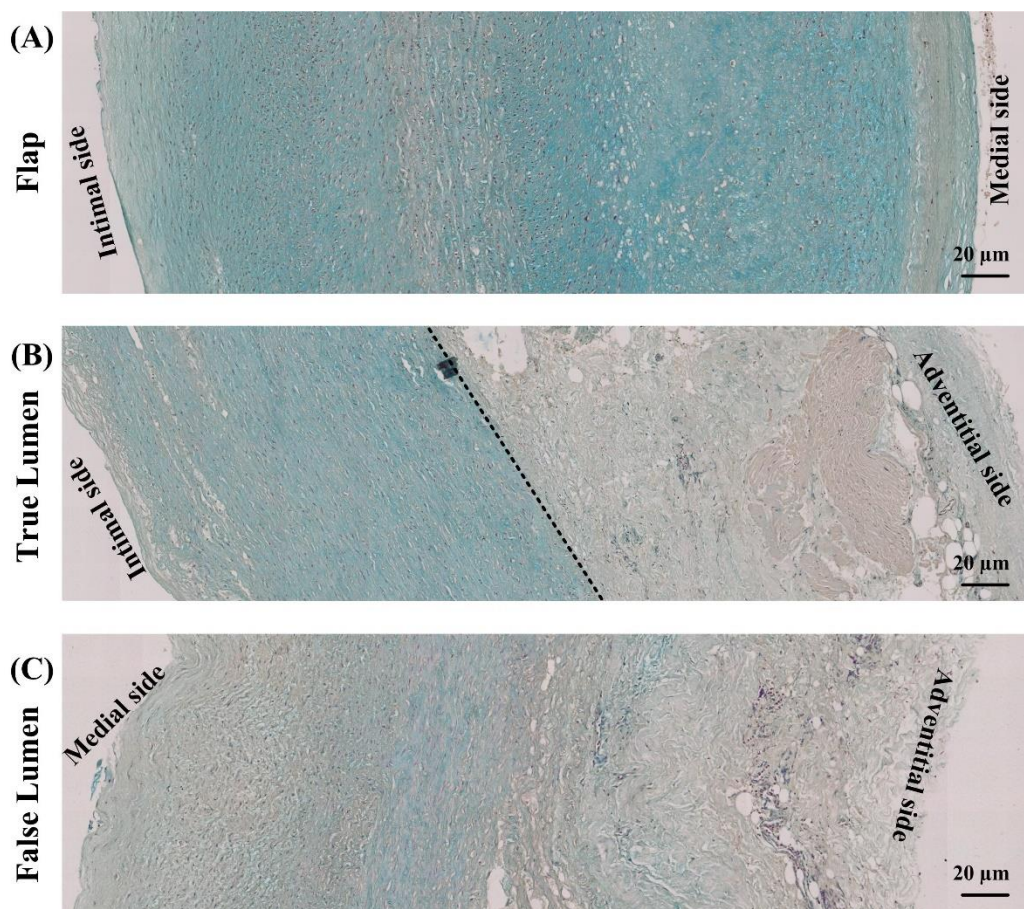


Figure 5.13 Representative histology sections stained to reveal GAG (Blue) for: (A) flap (FP), (B) true lumen outer wall (TL) and (C) false lumen outer wall (FL). Scale bar 20μm.

5.2.5 FTIR analysis

MCR-ALS analysis can be used to present spectra of single/pure components from multi-component FTIR measurements. In this work two chronic AD patients (05-00064-18 and 05-00017-19) were chosen due to availability of all three tissue types for analysis and these patients are the same patients that CT scan images were shown in Figure 5.1 and 5.2, respectively. The analytical strategy previously reported for ovine aortic tissue was adapted, with a wavenumber region of 950-1600 cm^{-1} chosen for MCR-ALS deconvolution, as per Chapter 4 (Section 4.3.6). Based on a comparison of MCR-ALS results to reference spectra and histological stains of target tissue components, the optimum number of factors for MCR-ALS analysis is then established.

From the PCA result, four modelled factors were chosen as the optimum number of factors for the MCR-ALS analysis for both patients (05-00064-18 and 05-00017-19). The correlation between the reference spectral profiles (Figure 5.14A) and extracted spectral profiles for patient 05-00064-18 (Figure 5.14B) showed that the best correlation was factor 2 and factor 4 corresponding to elastin and collagen, respectively (Table B1 in Appendix B). Considering this correlation in patient 05-00017-19 (Figure 5.14C), it was found that factor 3 and factor 4 corresponded to collagen and elastin, respectively (Table B2 in Appendix B).

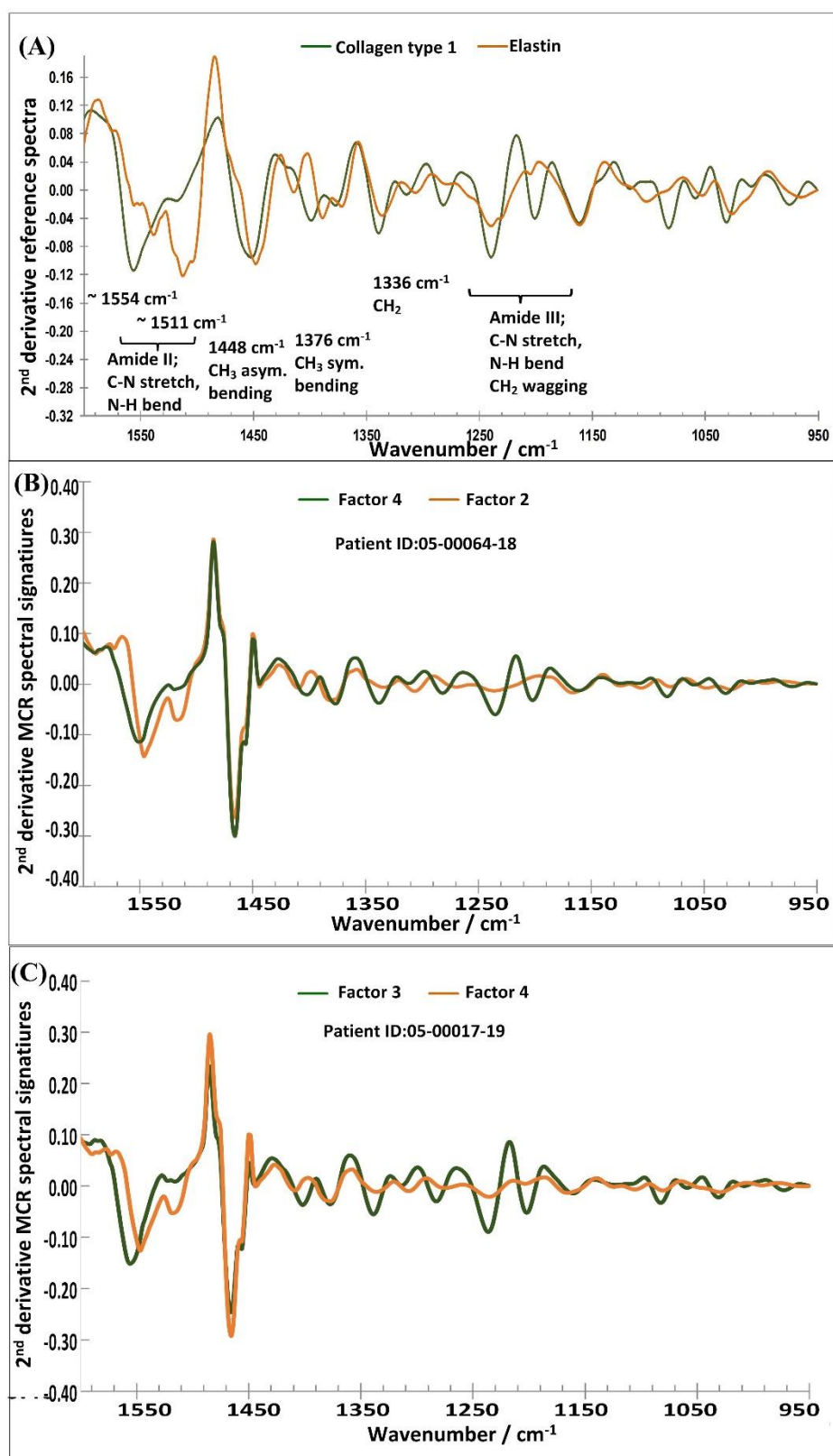


Figure 5.14 (A) Comparison of spectral profiles of 2nd derivative reference of collagen and elastin with (B) extracted spectral signatures from MCR-ALS analysis for patient 05-00064-18 (C) extracted spectral signatures from MCR-ALS analysis for patient 05-00017-19.

A comparison between the histological stains and the MCR-ALS imaging distribution maps were determined. For the visualization of overall chronic AD tissue distribution, the 2nd derivative peak integration map of amide II spectral region was considered and compared with H&E-stained tissue section for patient 05-00064-18 (Figure 5.15) and 05-00017-19 (Figure 5.15). It shows the distribution of overall tissue architecture, similar to that seen with the general H&E stain. A similar intensity was noted in the FTIR images and the stained sections for FP, TL and FL (Figure 5.15A, Figure 5.16A). The distribution map of MCR-ALS factor 2 (05-00064-18) and factor 4 (05-00017-19) for elastin had a high intensity in intima and media region as highlighted with a red arrow, in agreement with the black areas of VVG stain section (Figure 5.15B, 5.16B). The distribution map of MCR-ALS factor 4 (05-00064-18) and factor 3 (05-00017-19) for collagen showed the highest intensity in the adventitial region as highlighted by the blue arrow in Figure 5.15C and Figure 5.16C for FL and TL, matching the dark red areas of Picrosirius red stain corresponding to collagen staining whereas the highest intensity for FP was little seen as compared with FL. Although a limitation of the FTIR work presented in this chapter is the small sample size, it was found that the overall trends of intensity is the same for both case studies. The observed distribution map data follow the trends that obtained by histological analysis in this study and also support the collagen and elastin level data quantified by biochemical assay. Higher intensity for elastin was seen in TL relative to FP and FL whereas a high intensity for collagen was noticed at the adventitial layer for FL.

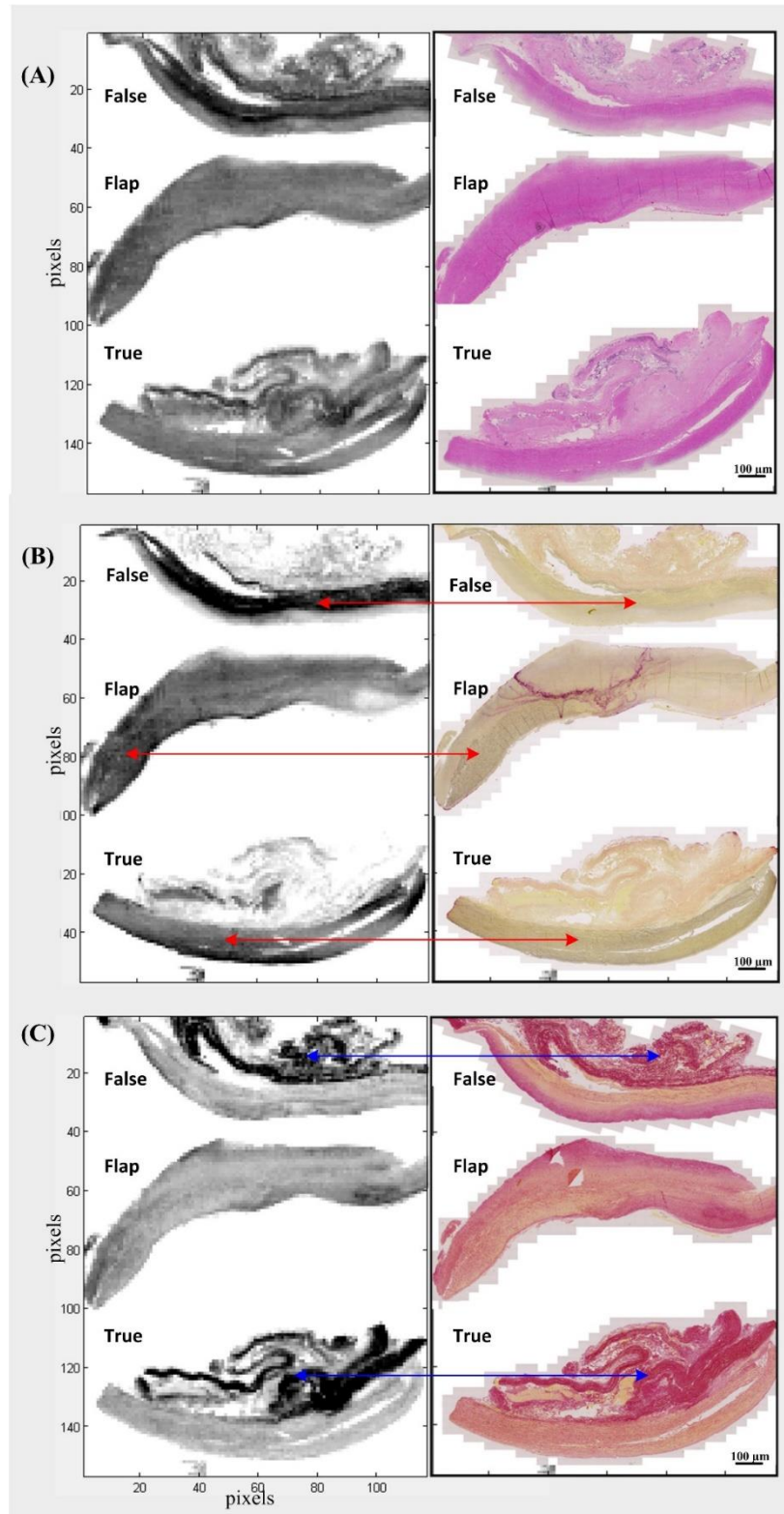


Figure 5.15 Overview FTIR images of the chronic aortic tissues (patient ID:05-00064-18): Flap, True and False Lumen outer wall showing (A) Overall distribution maps of the tissue sections shown alongside H & E stain, (B) MCR-ALS factor 2 and VVG stain and (C) MCR-ALS factor 4 and Picrosirius red stain (Scale bar = 100 µm).

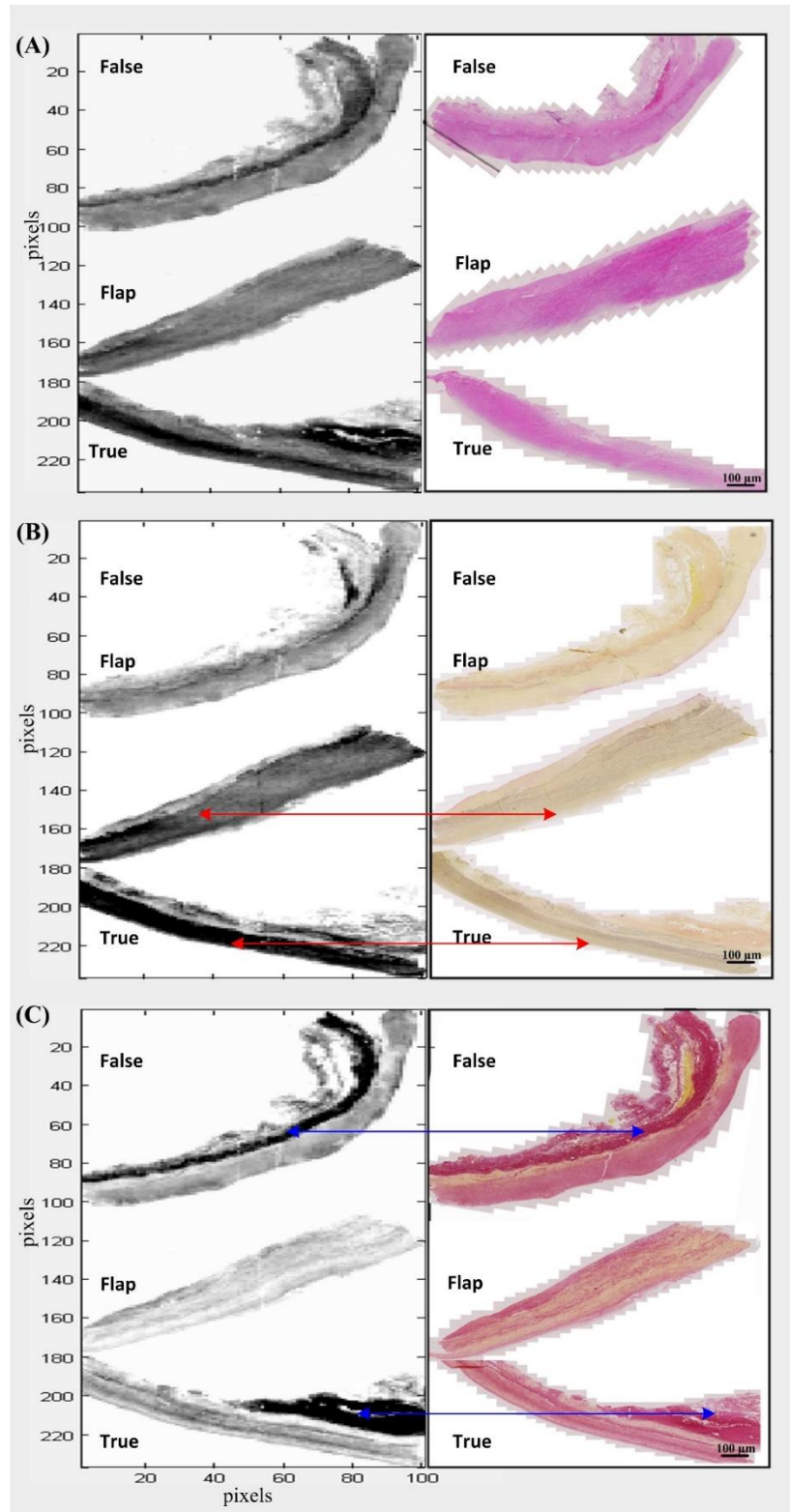


Figure 5.16 FTIR images of the chronic aortic tissues (patient ID 05-00017-19): Flap, True and False Lumen outer showing (A) distribution maps of general tissue and H & E stain, (B) MCR-ALS factor 4 and VVG stain and (C) MCR-ALS factor 3 and Picrosirius red stain (Scale bar = 100 μm).

5.2.6 Correlations of biomechanical data with clinical data

5.2.6.1 Relationship between elastic modulus and central deformation with interval of index event to operation

In clinical studies, it is suggested that the dissected tissues are altering in terms of stiffness and mobility over time (Peterss et al., 2016). Hence, the *in vitro* biomechanical data collected in this chapter was compared with the interval of index event to operation. A comparison was made of elastic modulus from both methods (nanoindentation and ball indentation) and central deformation obtained via the ball indentation method with IIEO, which is the time period from the diagnosis of dissection to operation. The overall mean of IIEO time was 4 years with minimum of 0.1 year and maximum of 15 years. Correlations between biomechanical properties with IIEO are shown for all groups of chronic AD (see Figure B1, B2 in Appendix B). Interestingly, spearman's correlation R_s presented a significantly positive correlation between elastic modulus from both techniques with IIEO for FP (Figure 5.17A, B and C), whereas it was found that there was a strong negative relationship between central deformation for FP tissues and IIEO ($R_s = -0.84$ and $p = 0.002$) (Figure 5.17D).

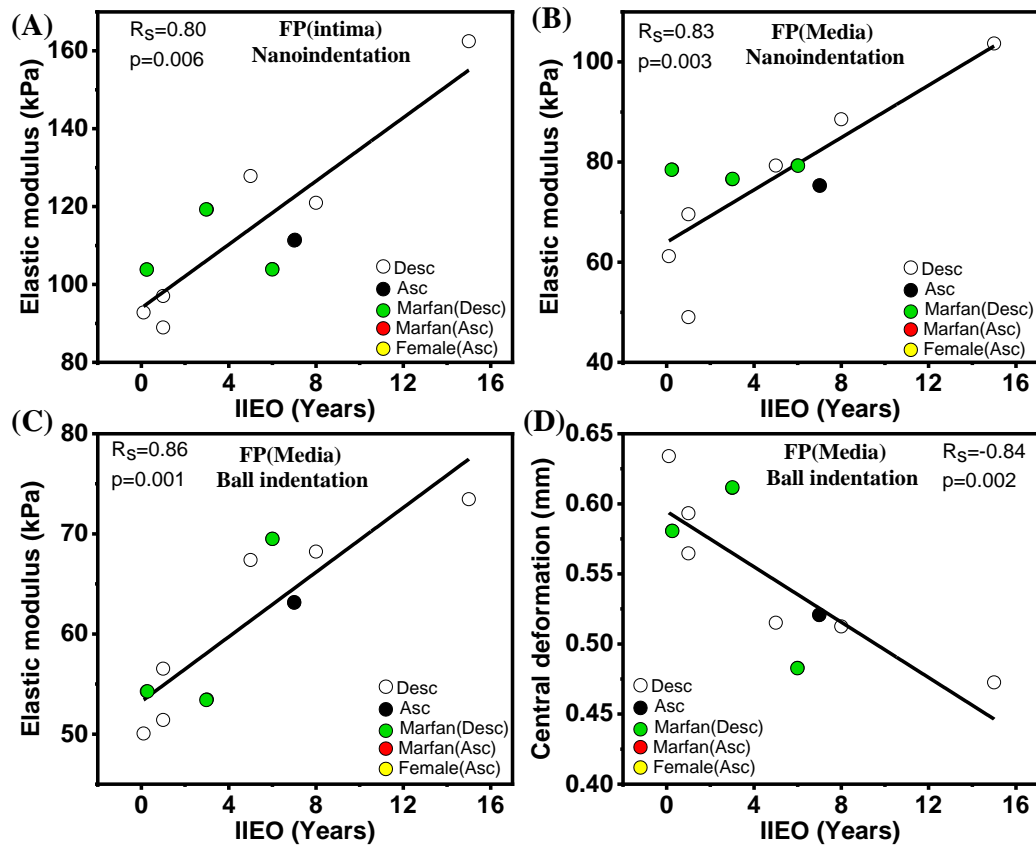


Figure 5.17 The correlation between elastic modulus obtained from both techniques, central deformation obtained from ball indentation with IIEO for FP (n=10 samples). A, B presented the correlation IIEO with intimal and media surface from nanoindentation technique (NI). C showed the correlation IIEO with elastic modulus obtained from the ball indentation (BI). D presented the relationship between central deformation with IIEO. This figure shows the most important correlations. Additional correlations are shown in Figure B1, B2 in Appendix B.

5.2.6.2 Relationship between elastic modulus and central deformation with growth rate

The growth rate of aortic dissection was measured by recording the cross-sectional diameter of the aorta from CT scans and thereby recording the growth rate data. The CT scan measurements and growth rate calculation were all conducted by Mr. Mark Field, Mr. Omar Nawaytou and Dr. Amer Ali Hasan Harky who are the part of the aortic surgery team at Liverpool Heart Chest Hospital (U.K.). For some patients, historical CT scans were not available. Hence, growth rate was calculated for 12 patients.

The results of the correlational analysis between biomechanical properties with the growth rate for all groups of chronic AD are shown (see Figure B3, B4 in Appendix B). The correlational analysis reveals that elastic modulus for FL significantly decreases with increasing growth rate ($R_s = 0.90$, $p = 0.037$) (Figure 5.18A). Moreover, although there was no significant correlation between central deformation with growth rate for FL and TL, positive and negative correlations were noted for FL ($R_s = 0.60$, $p = 0.284$) (Figure 5.18B) and FL ($R_s = -0.60$, $p = 0.208$) (Figure 5.18C), respectively.

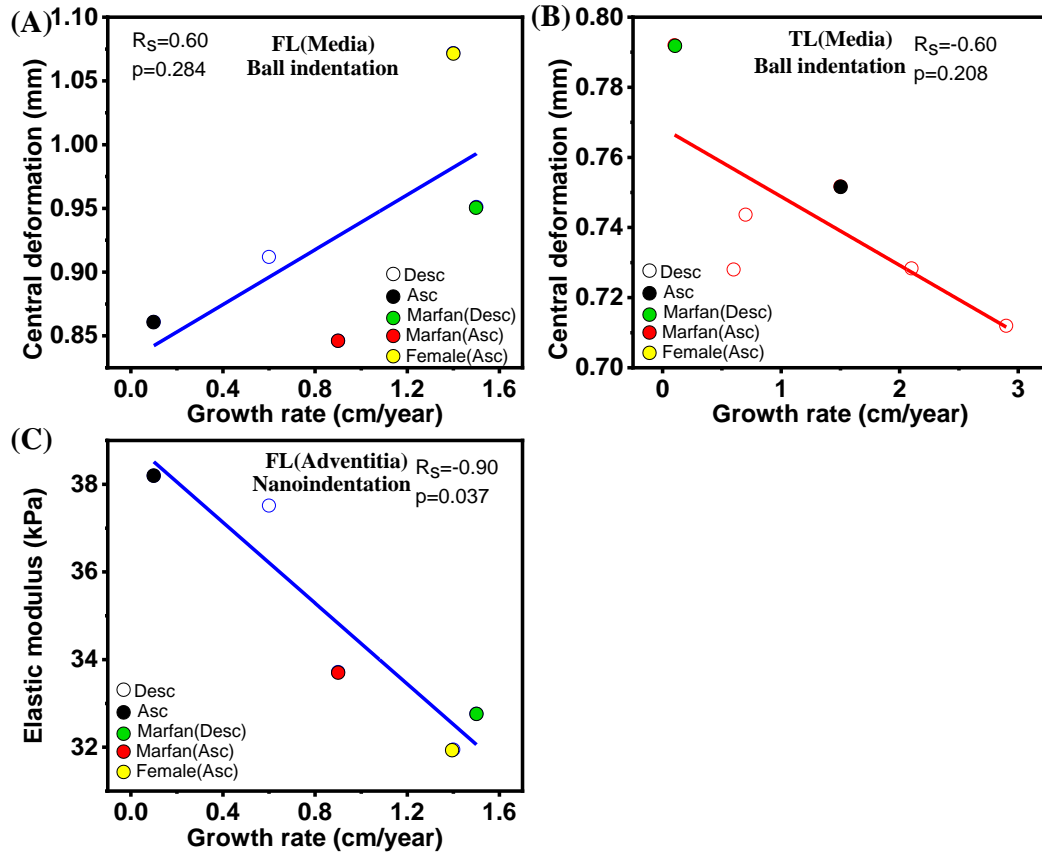


Figure 5.18 Correlation between mechanical findings with growth rate shown (A) central deformation obtained from ball indentation in FL (n=5 samples) and (B) central deformation obtained from ball indentation in TL (n=6 samples) and (C) elastic modulus from nanoindentation method in FL (n=5 samples). This figure shows the most important correlations. Additional correlations are shown in Figure B3, B4 in Appendix B.

5.2.7 Correlations of biochemical data, histological findings with clinical data

5.2.7.1 Relationship between biochemical data and histological findings with IIEO

Collagen, GAG, elastin and collagen/elastin ratio obtained from biochemical assays were compared to IIEO (see Figure B5 in Appendix B). The most surprising aspect of the relationship analysis is that collagen for FL ($R_s = 0.80$, $p=0.104$) (Figure 5.19A) and FP ($R_s = 0.62$, $p=0.055$) (Figure 5.19C) and collagen/elastin ratio for FL ($R_s = 0.95$, $p=0.013$) (Figure 5.19B) go up with increasing IIEO.

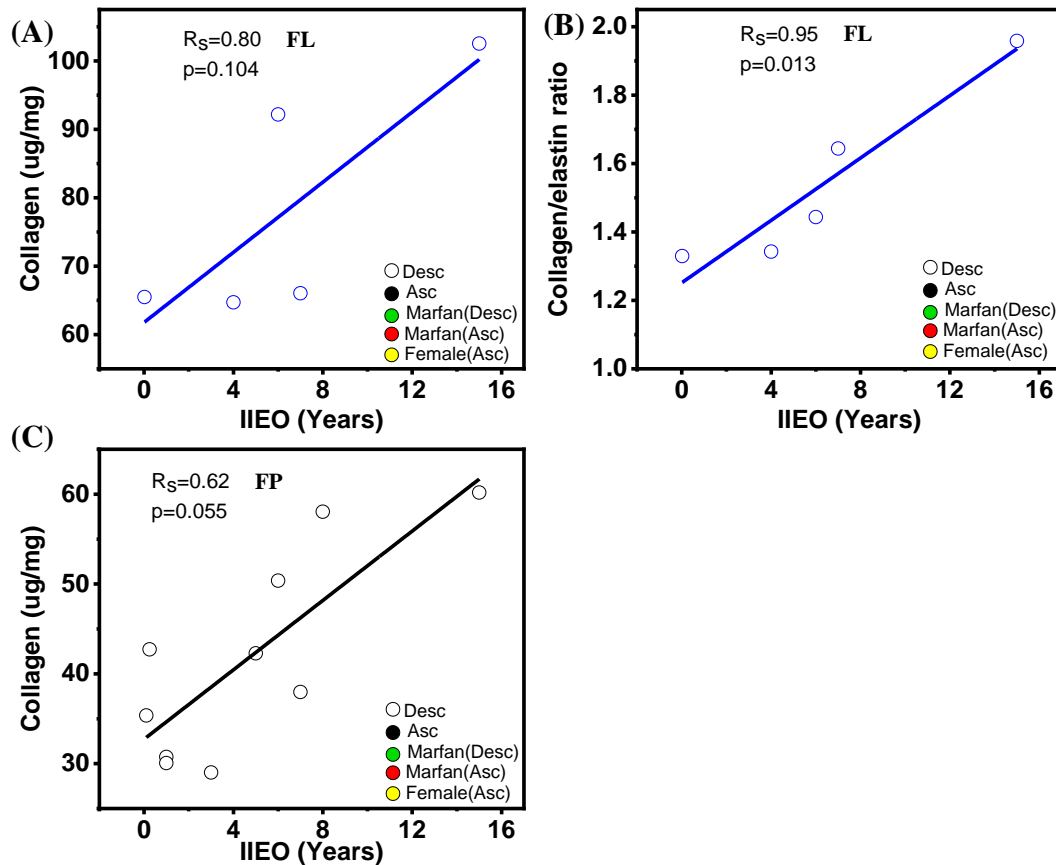


Figure 5.19 Relationships between biochemical findings with IIEO shown (A) collagen in FL (n=5 samples), (B) collagen/elastin ratio in FL (n=5 samples) and (C) collagen in FP (n=10 samples). This figure shows the most important correlations. Additional correlations are shown in Figure B5 in Appendix B.

5.2.7.2 Relationship between biochemical data, histological findings with the growth rate

Considering the correlation between biochemical data and growth rate for FP, TL and FL groups (see Figure B6 in Appendix B). Even though none of these correlations were statistically significant, a positive trend was noticed in FL for elastin ($R_s = 0.70$, $p=0.188$) (Figure 5.20A) and % elastin per tissue section area ($R_s = 0.90$, $p=0.037$) (Figure 5.20B).

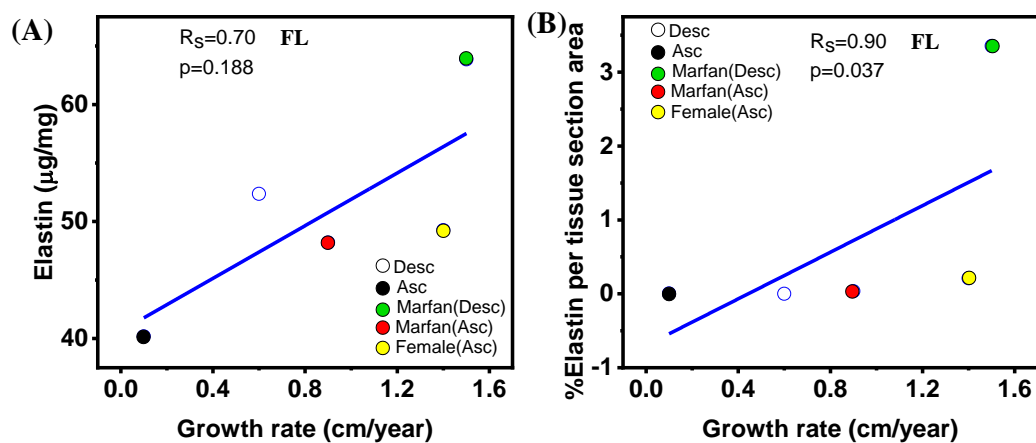


Figure 5.20 Relationships between biochemical and histological findings with growth rate shown (A) elastin in FL (n=5 samples) and (B) percentage elastin per tissue section area in FL (n=5 samples). This figure shows the most important correlations. Additional correlations are shown in Figure B6 in Appendix B.

5.3. Discussion

AD is a life-threatening event with high mortality rates despite improvements in treatment over the years (Sherifova and Holzapfel, 2019). The optimal treatment for patients with AD remains a matter of debate with different medical and surgical treatment strategies employed in different people (Sueyoshi et al., 2004). Although extensive studies have been carried out concerning the pathology of AD, the underlying mechanisms of chronic AD are not yet completely clear. There is a growing body of literature suggesting that AD is influenced by macro and micro-mechanical properties of the aortic wall. Hence, it is crucial to better understand the micromechanical and biochemical properties of chronic AD across different dissection tissues (FP, TL and FL). This is not only important for understanding aortopathies but also for current clinical treatment options. The main novelty of this chapter is the determination of localised mechanical properties in different tissue types (FP, TL and FL tissues) through the application of oscillatory nanoindentation and identification of the distribution of collagen, elastin and GAGs in the same tissues used to investigate the localised mechanical properties. In addition, determination of behaviour change with time-dependent deformation (creep) provides. Experimental data are directly correlated to the clinical data of IIEO and growth rate to gain new insights into the behaviour of each tissue type to help better elucidate the physiopathology of chronic AD.

The analyses found that the mechanical properties of chronic dissected tissues in the three groups (FP, TL and FL) are underlined by differences in the ECM microstructure (Figure 5.19) The key findings from this work, as highlighted in Figure 5.21, showed

that the FP was stiff and more resistant to deformation under constant load relative to the compliant FL which was characterised by a localised loss of the elastic fibres and a high degree of elastin fibre fragmentation. In contrast, the FP exhibited densely packed elastin fibres with little fragmentation.

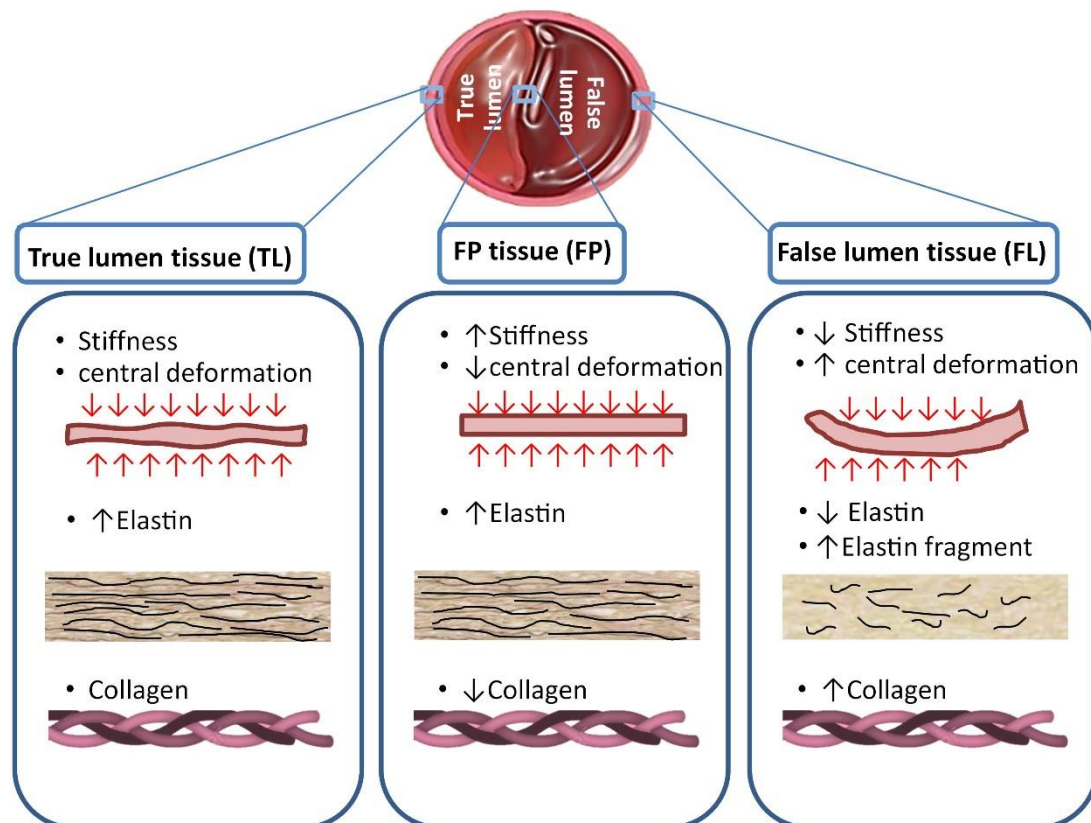


Figure 5.21 Summary schematic highlighting the biomechanical and biochemical properties between FP, TL and FL chronic AD tissues. Overall, FP and TL were stiffer with the arrangement of elastin fibres being highly compact, long, and aligned, whereas FL is more compliant with localized loss of the elastic fibres and increasing elastin fragmentation that correlates with time of illness.

The nanoindentation data collected in this chapter provide information about the localized, high-resolution measurements of tissue stiffness in the different faces of the tissue types: FP (intimal and medial face), TL (intimal and adventitial face) and FL (medial and adventitial face). The ball indentation method was used to examine the

elastic modulus of the central layer of the tissues along with characterisation of time-dependent mechanical behaviour. It was found that tissue stiffness was highest for FP relative to TL and FL tissues, whereas over time (5 hours) central deformation for the FP group was significantly lower than both the TL and FL groups. High elastic response values indicate that the tissue is extremely stiff. Therefore, the FP group presented the highest stiffness and less deformation over time as compared to TL and FL groups matching the data obtained from nanoindentation. FP is not affected by the growth rate however, the mechanical data from the FP group was found to be related to IIEO. In patients where the IIEO was less than five years, there was more deformation in the tissue under the fixed load over the 5 hours duration of the experiment. This means that the behaviours of these tissues are elastic and still responding to the load, whereas more than five years of IIEO the central deformation was minimal, with no deformation observed for tissue with IIEO of 15 years. While over 15 years of IIEO the elastic modulus (tissue stiffness) increased. To date there are limited studies in the literature on the behaviour of human dissected tissues, however our study supports evidence from previous clinical observation reported by Peterss et al. (2016). Their study focused on changing of flap dissection mobility from thoracic AD patients who transitioned into the chronic state without surgical or endovascular intervention assessed via CT and echocardiography. FP mobility is represented by the amplitude of the flap movement. They revealed that the structure of FP becomes straighter, with increased stiffness (immobility) as acute aortic dissection transitions over time to chronic aortic dissection (1 year) (Peterss et al., 2016).

A possible explanation for the stiffness for FP while FL is more compliant could be explained by understanding elastin distribution and architecture seen via histological images. The elastic fibres for TL and FP tissues were highly compact close to the intima layer, with long and aligned elastin fibres observed. This finding was supported by the study of Moriwaki and co-worker (2011). They revealed that the elastic modulus of the collagen-rich region was substantially lower than that of the elastin-rich region, despite collagen fibrils having a higher elastic modulus than elastin by 100 times (Moriwaki et al., 2011). This finding was also reported by Matsumoto et al., 2004. They found that of the high elastic modulus region of the porcine aortic wall is mainly composed of elastin and that the low elastic modulus region mostly comprises SMCs (Matsumoto et al., 2004). In this study it was also found that the FL is more compliant and explained with localized loss of the elastic fibres and increasing of elastin fragmentation. Moreover, regions of increased wall shear stress in the FL are involved with greater elastin degradation or elastin fragmentation observed by (Guzzardi et al., 2015). It was also noticed that the collagen for FL is the highest as compared with FP and TL. This result may be explained by the study of Wang et al., 2006, 2012. They determined the relevance of collagen to aortic dissection TAD patients. They indicate that increasing collagen within medial and adventitial layers of the aortic wall of TAD patients could be responsible for the expansion of the aortic wall and systemic compliance (Wang et al., 2006, 2012). Interestingly, the biomechanical data is independent of the aetiological type of tissues (Marfan syndrome or non-syndromic unknown), location (ascending or descending) or sex differences (males or females). Biomechanical changes in this study appear to be driven by the role elastic fibres alignment, architecture and degradation in aortic wall. These findings are, to

the best of our knowledge, the first report on local elastic modulus of the chronic AD wall. Based on our study, aortic wall composition and biomechanical aortic wall aspects play a role in the pathophysiology of chronic AD.

5.4. Limitations

This study provides valuable insight into the utility of oscillatory nanoindentation to investigate localised micromechanical properties of chronic AD (FP, TL and FL), however there are a number of limitations which should be addressed. Firstly, the micromechanical property measurements were conducted with the nanoindentation technique in longitudinal direction. In order to fully capture the anisotropic properties of the aortic wall the investigation of micromechanical properties in circumferential direction should also be considered. Secondly, for ball indentation it was not always possible to conduct replicate testing due to the small specimen size. Thirdly, biochemical methods used for investigation of collagen, GAG and elastin level do not discriminate across the layers. Layer-specific measurements for biochemical tests would be useful. Moreover, inflammatory reactions are likely involved in the development of AD and exhibit different time courses of their changes in acute-phase reactions and between acute and chronic AD, but detailed inflammation is beyond the scope of this chapter. Finally, there are limitations of FP tissues, in order to gain insight into the FP behaviour at the hinge points, the biomechanical properties of FP at the hinge points should be investigated.

5.5. Conclusions

This chapter probed the micromechanical properties and biochemical changes in chronic AD tissues (FP, TL and FL) and these were related with clinical data (IIEO and the growth rate). Results suggest a loss of tissue compliance in FP and TL relative to FL, with FP being the stiffest. Loss of tissue compliance in FP was related to the arrangement of elastin fibres (highly compact, long, and aligned elastic fibres) whereas FL is highly compliant with localised loss of the elastic fibres and high elastin fragmentation. This study contributes to understanding of how the structural properties of dissection tissues within the aortic wall alter with time. Interestingly, in terms of time for IIEO the FP increases in stiffness, whereas TL and FL show no correlation with IIEO. The FP seems to be a dynamic structure while FL is governed by haemodynamic effects over the time. This could be related to chronic inflammation or fibrosis. Moreover, data presented here suggests that the initial aetiology (Marfan syndrome or and non-syndromic unknown) of the dissection has no role to play in how the dynamics of the tissue properties react in the future. These findings can help to provide clarification and inform guidelines for surgical planning and clinical care. This study suggests that irrelevant as to the presence of connective tissues disorder or not, all dissections should be considered for the same treatment after post dissection.

References

- Beebeejaun, M. Y., Malec, A. and Gupta, R. (2013) 'Conservative management of chronic aortic dissection with underlying aortic aneurysm', *Int. Heart J.*, 8 (1), pp.hi. 2013. e4.
- Blount, K. J. and Hagspiel, K. D. (2009) 'Aortic diameter, true lumen, and false lumen growth rates in chronic type B aortic dissection', *Am.J.Roentgenol.*, 192 (5), pp.W222-9.
- Bode-Jänisch, S., Schmidt, A., Günther, D., Stuhmann, M. and Fieguth, A. (2012) 'Aortic dissecting aneurysms—Histopathological findings', *Forensic Sci.Int.*, 214 (1–3), pp.13-7.
- Booher, A. M., Isselbacher, E. M., Nienaber, C. A., et al. (2013) 'The IRAD classification system for characterizing survival after aortic dissection', *Am.J.Med.*, 126 (8), pp.730. e19,730. e24.
- Chim, Y. H., Davies, H. A., Mason, D., et al. (2019) 'Bicuspid valve aortopathy is associated with distinct patterns of matrix degradation', *J.Thorac.Cardiovasc.Surg.*,
- Guzzardi, D. G., Barker, A. J., Van Ooij, P., et al. (2015) 'Valve-related hemodynamics mediate human bicuspid aortopathy: insights from wall shear stress mapping', *J.Am.Coll.Cardiol.*, 66 (8), pp.892-900.

- Hagan, P. G., Nienaber, C. A., Isselbacher, E. M., et al. (2000) 'The International Registry of Acute Aortic Dissection (IRAD): new insights into an old disease', *JAMA*, 283 (7), pp.897-903.
- Humphrey, J. (2013) 'Possible mechanical roles of glycosaminoglycans in thoracic aortic dissection and associations with dysregulated transforming growth factor-beta', *J.Vasc.Res.*, 50 (1), pp.1-10.
- Humphrey, J. and Holzapfel, G. A. (2012) 'Mechanics, mechanobiology, and modeling of human abdominal aorta and aneurysms', *J.Biomech.*, 45 (5), pp.805-14.
- Kermani, G., Hemmasizadeh, A., Assari, S., Autieri, M. and Darvish, K. (2017) 'Investigation of inhomogeneous and anisotropic material behavior of porcine thoracic aorta using nano-indentation tests', *J Mech Behav Biomed Mater*, 69 pp.50-6.
- Li, D., Ye, L., He, Y., et al. (2016) 'False lumen status in patients with acute aortic dissection: a systematic review and meta-analysis', *Journal of the American Heart Association*, 5 (5), pp.e003172.
- Luebke, T. and Brunkwall, J. (2014) 'Type B Aortic Dissection: A Review of Prognostic Factors and Meta-analysis of Treatment Options', *Aorta (Stamford)*, 2 (6), pp.265-78.
- Matsumoto, T., Goto, T., Furukawa, T. and Sato, M. (2004) 'Residual stress and strain in the lamellar unit of the porcine aorta: experiment and analysis', *J.Biomech.*, 37 (6), pp.807-15.

Meekel, J. P., Mattei, G., Costache, V. S., Balm, R., Blankensteijn, J. D. and Yeung, K.

K. (2019) 'A multilayer micromechanical elastic modulus measuring method in ex vivo human aneurysmal abdominal aortas', *Acta Biomater*, 96 pp.345-53.

Moriwaki, T., Oie, T., Takamizawa, K., et al. (2011) 'Variations in local elastic modulus along the length of the aorta as observed by use of a scanning haptic microscope (SHM)', *Int J Artif Organs*, 14 (4), pp.276-83.

Nollen, G. J., Groenink, M., Tijssen, J. G., Van Der Wall, Ernst E and Mulder, B. J.

(2004) 'Aortic stiffness and diameter predict progressive aortic dilatation in patients with Marfan syndrome', *Eur.Heart J.*, 25 (13), pp.1146-52.

Pape, L. A., Awais, M., Woznicki, E. M., et al. (2015) 'Presentation, diagnosis, and

outcomes of acute aortic dissection: 17-year trends from the International Registry of Acute Aortic Dissection', *J.Am.Coll.Cardiol.*, 66 (4), pp.350-8.

Pape, L. A., Tsai, T. T., Isselbacher, E. M., et al. (2007) 'Aortic diameter \geq 5.5 cm is

not a good predictor of type A aortic dissection: observations from the International Registry of Acute Aortic Dissection (IRAD)', *Circulation*, 116 (10), pp.1120-7.

Parisi, R., Secco, G. G., Di Eusanio, M. and Fattori, R. (2015) 'Endovascular repair of

aortic dissection in Marfan syndrome: current status and future perspectives', *Diseases*, 3 (3), pp.159-66.

- Peterss, S., Mansour, A. M., Ross, J. A., et al. (2016) 'Changing Pathology of the Thoracic Aorta From Acute to Chronic Dissection: Literature Review and Insights', *J.Am.Coll.Cardiol.*, 68 (10), pp.1054-65.
- Riambau, V., Bockler, D., Brunkwall J FAU o,P., et al. (2017) 'Editor's Choice - Management of Descending Thoracic Aorta Diseases: Clinical Practice Guidelines of the European Society for Vascular Surgery (ESVS)', *Eur.J.Vasc.Endovasc.Surg.*, 53 (1), pp.4-52.
- Safi, H. J., Miller III, C. C., Reardon, M. J., et al. (1998) 'Operation for acute and chronic aortic dissection: recent outcome with regard to neurologic deficit and early death', *Ann.Thorac.Surg.*, 66 (2), pp.402-11.
- Schlatmann, T. J. and Becker, A. E. (1977) 'Histologic changes in the normal aging aorta: implications for dissecting aortic aneurysm', *Am.J.Cardiol.*, 39 (1), pp.13-20.
- Sherifova, S. and Holzapfel, G. A. (2019) 'Biomechanics of aortic wall failure with a focus on dissection and aneurysm: A review', *Acta Biomater.*
- Sueyoshi, E., Sakamoto, I., Hayashi, K., Yamaguchi, T. and Imada, T. (2004) 'Growth rate of aortic diameter in patients with type B aortic dissection during the chronic phase', *Circulation*, 110 (11_suppl_1), pp.II,256-II-261.
- Suzuki, T., Mehta, R. H., Ince, H., et al. (2003) 'Clinical profiles and outcomes of acute type B aortic dissection in the current era: lessons from the International

Registry of Aortic Dissection (IRAD)', *Circulation*, 108 (10_suppl_1), pp.II,312-II-317.

Tsai, T. T., Evangelista, A., Nienaber, C. A., et al. (2006) 'Long-term survival in patients presenting with type A acute aortic dissection: insights from the International Registry of Acute Aortic Dissection (IRAD)', *Circulation*, 114 (1_supplement), pp.I,350-I-356.

Wang, LeMaire, S. A., Chen, L., et al. (2006) 'Increased collagen deposition and elevated expression of connective tissue growth factor in human thoracic aortic dissection', *Circulation*, 114 (1_supplement), pp.I,200-I-205.

Wang, Zhang, J., Fu, W., et al. (2012) 'Association of smooth muscle cell phenotypes with extracellular matrix disorders in thoracic aortic dissection', *J Vasc Surg*, 56 (6), pp.1698,1709. e1.

Zafar, M. A., Chen, J. F., Wu, J., et al. (2019) 'Natural history of descending thoracic and thoracoabdominal aortic aneurysms', *J.Thorac.Cardiovasc.Surg.*,

Chapter 6

Summary of Findings, Conclusions and Future Work

This chapter summarises the key findings, and contributions of the research work. Additionally, suggestions for continuing the current work are also made.

6.1 Summary of findings

The aim of this thesis was to quantify and define the biomechanics and biochemistry of FP, TL and FL tissues in chronic dissection. This section highlights the key findings of each chapter and their significance.

Chapter 3 Materials and Methods

Chapter 3 provided the sample preparation of ovine model and human chronic AD tissues for investigating biomechanical properties and biochemical data. This chapter provided detailed descriptions of the oscillatory nanoindentation and creep testing methods that were utilised for characterisation of the mechanical properties of the aortic tissues. In addition, methodology was optimised for the biochemical analysis to quantify ECM component concentrations and FTIR to map ECM distribution in the tissues, along with conventional histology and image analysis methods that were carried out on the stained sections.

All sample preparation procedures and testing procedures used in ovine model (Chapter 4) were applied for the work on human chronic aortic dissection tissues. To the best of the author's knowledge, the creep methodology and the FTIR techniques had not been used for characterisation of aortic tissue prior to this study.

Chapter 4 Macro- and micro mechanical properties of the ovine aorta: Correlation with regional variations in collagen, elastin and glycosaminoglycan Levels

In Chapter 4, the biomechanical and biochemical properties of the ovine aorta have been comprehensively mapped across different regions of the ovine aorta (from the

ascending to the abdominal aorta). Tensile testing and the oscillatory nanoindentation technique were used to characterise the macro-mechanical properties and micro-mechanical properties, respectively. Additionally, the behaviour of ovine aortic wall with time-dependent deformation (creep) was tested by using the ball indentation method. The data presented in this chapter showed that there was an increasing trend of stiffness both at the macroscopic and at the micromechanical scale from the ascending aorta to the abdominal aorta. This was coupled with increased collagen, decreased elastin and GAGs as the distance from the heart increased. These findings may support future work on the mechanisms of aneurysm and dissection development in different regions of the aorta.

The work in this chapter was also important for technique development and validation. Each of the techniques were applied to the human tissue work presented in Chapter 5.

Chapter 5 Micromechanical, the behaviour changes with time-dependent deformation (creep) and biochemical properties of chronic aortic dissection tissues.

The oscillatory nanoindentation method and ball indentation are applied to chronic AD tissues for characterising localised micromechanical properties and the behaviour change with time-dependent deformation of the FP, TL and FL. Post-nanoindentation the same tissue samples were used for biochemical analysis (collagen, elastin and GAG). The histological analysis was also conducted to quantify percentage collagen and elastin per tissue section area. These micromechanical properties and biochemical properties were compared with clinical data (IIEO and the growth rate). The main results from this chapter were that a loss of tissue compliance in FP was

related to the arrangement of elastin fibres (highly compact, long, and aligned elastic fibres) whereas FL was highly compliant with localized loss of the elastic fibres and a high degree of elastin fibre fragmentation.

Importantly, it was found that there was no difference in behaviour of FP and FL over 300 minutes regardless of aetiology (Marfan syndrome or and non-syndromic unknown), location (ascending or descending) and sex differences (males or females) for patients who have already dissected or chronic dissections. The results from this study suggest that size-dependent indications for surgery in chronic aortic dissection may be independent of features such as: aetiology, dimensions, interval and anatomical segment.

6.2 Conclusions

To conclude, the first objective of this thesis was to explore the utility of oscillatory nanoindentation to investigate localised micromechanical properties of ovine tissue across the aortic tree, and to relate these data to biochemical changes. It found that the utility of oscillatory nanoindentation for ovine aorta was validated, which paved the way to probe human aorta and investigate the localised alterations in chronic AD structure *in vitro*.

The second objective was to apply the nanoindentation technique to aortic biopsy samples from chronic dissection patients to characterise the micromechanical properties of dissection flap, true and false lumen and correlate these properties with biochemical properties and histological data. It shows that FL was found to be highly compliant with localized loss of the elastic fibres and a high degree of elastin fibre fragmentation relative to the much stiffer FP tissue with highly compact, long, and aligned elastic fibres.

The final objective was to characterise how the behaviour of dissection flap, true and false lumen changes with time-dependent deformation (creep). It is noticed that 300 minutes the central deformation was minimal, with no deformation observed for tissue with IIEO of 15 years. The biomechanical change is independent of the aetiological type of tissues and location.

6.3 Future work

6.3.1 Micromechanical properties and biochemical properties across the layer of aortic wall

Oscillatory nanoindentation was utilised to assess micromechanical properties for each face of FP (intimal and medial layer), TL (intimal and adventitial layer) and FL (medial and adventitial layer). Therefore, for better modelling the disease-related changes, it is recommended to examine the micromechanical properties across the layers of the aortic wall. Moreover, since collagen, elastin and GAG are key components to biomechanical and structural properties of aortic wall, it would be useful to investigate the alterations in collagen, elastin and GAG content in different layers. This may help better understanding progressive of AD.

6.3.2 Characterisation of behaviours changes with time-dependent deformation at adventitial layer

The adventitia is in contact with and surrounds the media and is the interface between the aortic wall and its neighbouring tissues. It is associated with the vascular development and vascular disease (Majesky, 2015). Therefore, future work should investigate changes in the adventitial layer with time. It is possible to separate the chronic AD tissue layers by using reflected light microscopy to inspect the layer preparation process (Sommer et al., 2008).

6.3.3 Measurement of the specific of PGs/GAGs

Since PGs/GAGs play a significant role in maintaining the structure of the aortic wall and are involved with aortic pathogenesis such as aortic aneurysm and dissection (Wight, 1989, Cherchi et al., 1990, Schriebl et al., 2015), specific PGs/GAGs in chronic AD and their contribution towards tissue structure and mechanical properties should be considered for future investigations.

6.3.4 Development of FTIR to quantify more chemical species

FTIR method enabled identification of chemical species within the ovine aortic wall and was able to simultaneously provide information about collagen and elastin from a single tissue section. In this thesis the human work was an extension of the optimisation in sheep and now this is done. FTIR will be used in future study to generate additional information of distribution of PGs and correlation with collagen/elastin etc all within a single scan.

6.3.5. Quantifying of the inflammatory reactions and fibrosis

Recent clinical and basic study are shown that an inflammatory and fibrosis mechanism are involved in medial degeneration and its association with the clinical manifestations of aortic dissection (Luo et al., 2009, Wen et al., 2011). Analysis of the inflammatory and fibrosis mechanisms could provide more insight into the understanding of behaviours of chronic AD over time.

6.3.6 Characterisation of micromechanical behaviours and biochemical changes in patients with acute and sub-acute AD

To better understand the progressive process from an acute to a chronic dissection over time characterisation of micromechanical behaviours and biochemical changes in patients with acute and sub-acute AD should be characterised and compared. These processes have implications regarding clinical decisions.

6.3.7 Measurement of follow-up clinical data

To provide the data to guide current treatment strategies and future innovation, clinical data parameters need to measure and be compared with biomechanical and biochemical data such as the pulse wave velocity or the movement of FP recorded from MRI and CT scans before and after the occurrence of AD.

References

- Cherchi, G., Coinu, R., Demuro, P., et al. (1990) 'Structural and functional modifications of human aorta proteoglycans in atherosclerosis', *Matrix*, 10 (6), pp.362-72.
- Luo, F., Zhou, X., Li, J. and Hui, R. (2009) 'Inflammatory response is associated with aortic dissection', *Ageing research reviews*, 8 (1), pp.31-5.
- Majesky, M. W. (2015) 'Adventitia and perivascular cells', *Arterioscler.Thromb.Vasc.Biol.*, 35 (8), pp.e31-5.
- Schriebl, A. J., Schmidt, T., Balzani, D., Sommer, G. and Holzapfel, G. A. (2015) 'Selective enzymatic removal of elastin and collagen from human abdominal aortas: Uniaxial mechanical response and constitutive modeling', *Acta Biomater*, 17 pp.125-36.
- Sommer, G., Gasser, T. C., Regitnig, P., Auer, M. and Holzapfel, G. A. (2008) 'Dissection properties of the human aortic media: an experimental study', *J.Biomech.Eng.*, 130 (2), pp.021007.
- Wen, D., Zhou, X., Li, J. and Hui, R. (2011) 'Biomarkers in aortic dissection', *Clinica chimica acta*, 412 (9-10), pp.688-95.
- Wight. (1989) 'Cell biology of arterial proteoglycans', *Arteriosclerosis*, 9 (1), pp.1-20.

Appendix A

**Table A1 Mean and standard deviation (SD) of the collagen, GAG and elastin levels for aortas
(n = 27/ distance with three samples/animal)**

Distance (cm)	Collagen ($\mu\text{g}/\text{mg}$)	GAG ($\mu\text{g}/\text{mg}$)	Elastin ($\mu\text{g}/\text{mg}$)
2	27.26 \pm 7.03	4.15 \pm 0.89	102.50 \pm 24.58
4	30.84 \pm 4.44	4.03 \pm 1.03	100.24 \pm 27.03
6	31.42 \pm 6.27	3.69 \pm 0.53	92.69 \pm 24.56
8	29.64 \pm 5.08	3.71 \pm 0.95	90.98 \pm 25.37
10	34.17 \pm 7.75	3.83 \pm 0.56	86.42 \pm 13.91
12	33.83 \pm 6.78	3.70 \pm 0.43	94.06 \pm 17.30
14	33.69 \pm 8.61	3.67 \pm 0.43	88.07 \pm 18.40
16	37.58 \pm 8.89	3.62 \pm 0.51	79.81 \pm 10.24
18	40.14 \pm 8.81	3.45 \pm 0.37	80.15 \pm 11.01

Table A2 Statistical comparison within groups for each distance from heart (2 cm-18 cm) for G', G'' and tan (δ) on the intimal face, for each animal. NS is not significant at 0.05 level.

Intimal face	G' (kPa)		p-value	G'' (kPa)		p-value	tan (δ)		p-value
Group 1 (2 cm)	Ovine 1	Ovine2	NS	Ovine 1	Ovine2	NS	Ovine 1	Ovine2	NS
	Ovine 1	Ovine3	NS	Ovine 1	Ovine3	NS	Ovine 1	Ovine3	NS
	Ovine 2	Ovine 3	NS	Ovine 2	Ovine 3	NS	Ovine 2	Ovine 3	NS
Group 2 (4 cm)	Ovine 1	Ovine2	NS	Ovine 1	Ovine2	NS	Ovine 1	Ovine2	NS
	Ovine 1	Ovine3	NS	Ovine 1	Ovine3	NS	Ovine 1	Ovine3	NS
	Ovine 2	Ovine 3	NS	Ovine 2	Ovine 3	NS	Ovine 2	Ovine 3	NS
Group 3 (6 cm)	Ovine 1	Ovine2	NS	Ovine 1	Ovine2	NS	Ovine 1	Ovine2	NS
	Ovine 1	Ovine3	NS	Ovine 1	Ovine3	NS	Ovine 1	Ovine3	NS
	Ovine 2	Ovine 3	NS	Ovine 2	Ovine 3	NS	Ovine 2	Ovine 3	NS
Group 4 (8 cm)	Ovine 1	Ovine2	NS	Ovine 1	Ovine2	NS	Ovine 1	Ovine2	NS
	Ovine 1	Ovine3	NS	Ovine 1	Ovine3	NS	Ovine 1	Ovine3	NS
	Ovine 2	Ovine 3	NS	Ovine 2	Ovine 3	NS	Ovine 2	Ovine 3	NS
Group 5 (10 cm)	Ovine 1	Ovine2	9.2x10 ⁻⁴	Ovine 1	Ovine2	0.009	Ovine 1	Ovine2	NS
	Ovine 1	Ovine3	2.8x10 ⁻⁴	Ovine 1	Ovine3	NS	Ovine 1	Ovine3	NS
	Ovine 2	Ovine 3	NS	Ovine 2	Ovine 3	NS	Ovine 2	Ovine 3	NS
Group 6 (12 cm)	Ovine 1	Ovine2	NS	Ovine 1	Ovine2	NS	Ovine 1	Ovine2	NS
	Ovine 1	Ovine3	NS	Ovine 1	Ovine3	NS	Ovine 1	Ovine3	NS
	Ovine 2	Ovine 3	NS	Ovine 2	Ovine 3	NS	Ovine 2	Ovine 3	NS
Group 7 14 cm	Ovine 1	Ovine2	NS	Ovine 1	Ovine2	NS	Ovine 1	Ovine2	NS
	Ovine 1	Ovine3	NS	Ovine 1	Ovine3	NS	Ovine 1	Ovine3	NS
	Ovine 2	Ovine 3	NS	Ovine 2	Ovine 3	NS	Ovine 2	Ovine 3	NS
Group 8 (16 cm)	Ovine 1	Ovine2	NS	Ovine 1	Ovine2	NS	Ovine 1	Ovine2	NS
	Ovine 1	Ovine3	NS	Ovine 1	Ovine3	NS	Ovine 1	Ovine3	NS
	Ovine 2	Ovine 3	NS	Ovine 2	Ovine 3	NS	Ovine 2	Ovine 3	NS
Group 9 (18 cm)	Ovine 1	Ovine2	NS	Ovine 1	Ovine2	NS	Ovine 1	Ovine2	NS
	Ovine 1	Ovine3	NS	Ovine 1	Ovine3	NS	Ovine 1	Ovine3	NS
	Ovine 2	Ovine 3	NS	Ovine 2	Ovine 3	NS	Ovine 2	Ovine 3	NS

Table A3 Statistical comparison within groups for each distance from heart (2 cm-18 cm) between three ovines for G' , G'' and $\tan(\delta)$ on the adventitial face, for each animal. NS is not significant at 0.05 level.

Adventitial face	G' (kPa)		p-value	G'' (kPa)		p-value	$\tan(\delta)$		p-value
Group 1 (2 cm)	Ovine 1	Ovine2	NS	Ovine 1	Ovine2	NS	Ovine 1	Ovine2	NS
	Ovine 1	Ovine3	NS	Ovine 1	Ovine3	NS	Ovine 1	Ovine3	NS
	Ovine 2	Ovine 3	NS	Ovine 2	Ovine 3	NS	Ovine 2	Ovine 3	NS
Group 2 (4 cm)	Ovine 1	Ovine2	0.018	Ovine 1	Ovine2	NS	Ovine 1	Ovine2	NS
	Ovine 1	Ovine3	0.029	Ovine 1	Ovine3	0.02	Ovine 1	Ovine3	NS
	Ovine 2	Ovine 3	NS	Ovine 2	Ovine 3	NS	Ovine 2	Ovine 3	NS
Group 3 (6 cm)	Ovine 1	Ovine2	0.026	Ovine 1	Ovine2	NS	Ovine 1	Ovine2	NS
	Ovine 1	Ovine3	NS	Ovine 1	Ovine3	NS	Ovine 1	Ovine3	NS
	Ovine 2	Ovine 3	NS	Ovine 2	Ovine 3	NS	Ovine 2	Ovine 3	NS
Group 4 (8 cm)	Ovine 1	Ovine2	NS	Ovine 1	Ovine2	NS	Ovine 1	Ovine2	NS
	Ovine 1	Ovine3	NS	Ovine 1	Ovine3	NS	Ovine 1	Ovine3	NS
	Ovine 2	Ovine 3	NS	Ovine 2	Ovine 3	NS	Ovine 2	Ovine 3	NS
Group 5 (10 cm)	Ovine 1	Ovine2	0.019	Ovine 1	Ovine2	NS	Ovine 1	Ovine2	NS
	Ovine 1	Ovine3	NS	Ovine 1	Ovine3	NS	Ovine 1	Ovine3	NS
	Ovine 2	Ovine 3	NS	Ovine 2	Ovine 3	NS	Ovine 2	Ovine 3	NS
Group 6 (12 cm)	Ovine 1	Ovine2	NS	Ovine 1	Ovine2	NS	Ovine 1	Ovine2	NS
	Ovine 1	Ovine3	NS	Ovine 1	Ovine3	NS	Ovine 1	Ovine3	NS
	Ovine 2	Ovine 3	NS	Ovine 2	Ovine 3	NS	Ovine 2	Ovine 3	NS
Group 7 14 cm	Ovine 1	Ovine2	NS	Ovine 1	Ovine2	NS	Ovine 1	Ovine2	NS
	Ovine 1	Ovine3	NS	Ovine 1	Ovine3	NS	Ovine 1	Ovine3	NS
	Ovine 2	Ovine 3	NS	Ovine 2	Ovine 3	NS	Ovine 2	Ovine 3	NS
Group 8 (16 cm)	Ovine 1	Ovine2	NS	Ovine 1	Ovine2	NS	Ovine 1	Ovine2	NS
	Ovine 1	Ovine3	NS	Ovine 1	Ovine3	NS	Ovine 1	Ovine3	NS
	Ovine 2	Ovine 3	NS	Ovine 2	Ovine 3	NS	Ovine 2	Ovine 3	NS
Group 9 (18 cm)	Ovine 1	Ovine2	NS	Ovine 1	Ovine2	0.03	Ovine 1	Ovine2	NS
	Ovine 1	Ovine3	NS	Ovine 1	Ovine3	NS	Ovine 1	Ovine3	NS
	Ovine 2	Ovine 3	NS	Ovine 2	Ovine 3	NS	Ovine 2	Ovine 3	NS

Table A4 Statistical comparison between groups for each distance from heart (2 cm-18 cm) for G', G'' and tan (δ) on the intimal face. NS is not significant at 0.05 level.

Intimal face	G' (kPa)	p-value	G'' (kPa)		p-value	tan (δ)		p-value
G.1 (2 cm)	G.2 (4 cm)	NS	G.1 (2 cm)	G.2 (4 cm)	NS	G.1 (2 cm)	G.2 (4 cm)	NS
	G.3 (6 cm)	0.005		G.3 (6 cm)	NS		G.3 (6 cm)	NS
	G.4 (8 cm)	6.9×10^{-6}		G.4 (8 cm)	NS		G.4 (8 cm)	NS
	G.5 (10 cm)	3.2×10^{-4}		G.5 (10 cm)	NS		G.5 (10 cm)	NS
	G.6 (12 cm)	5.8×10^{-15}		G.6 (12 cm)	0.01		G.6 (12 cm)	NS
	G.7 (14 cm)	2.9×10^{-21}		G.7 (14 cm)	2.2×10^{-5}		G.7 (14 cm)	NS
	G.8 (16 cm)	3.4×10^{-28}		G.8 (16 cm)	4.0×10^{-8}		G.8 (16 cm)	NS
	G.9 (18 cm)	2.8×10^{-37}		G.9 (18 cm)	1.0×10^{-17}		G.9 (18 cm)	NS
G.2 (4 cm)	G.3 (6 cm)	NS	G.2 (4 cm)	G.3 (6 cm)	NS	G.2 (4 cm)	G.3 (6 cm)	NS
	G.4 (8 cm)	NS		G.4 (8 cm)	NS		G.4 (8 cm)	NS
	G.5 (10 cm)	NS		G.5 (10 cm)	NS		G.5 (10 cm)	NS
	G.6 (12 cm)	8.4×10^{-10}		G.6 (12 cm)	0.02		G.6 (12 cm)	NS
	G.7 (14 cm)	1.5×10^{-16}		G.7 (14 cm)	7.3×10^{-4}		G.7 (14 cm)	NS
	G.8 (16 cm)	3.3×10^{-24}		G.8 (16 cm)	2.0×10^{-6}		G.8 (16 cm)	NS
	G.9 (18 cm)	3.3×10^{-34}		G.9 (18 cm)	4.7×10^{-16}		G.9 (18 cm)	NS
G.3 (6 cm)	G.4 (8 cm)	NS	G.3 (6 cm)	G.4 (8 cm)	NS	G.3 (6 cm)	G.4 (8 cm)	NS
	G.5 (10 cm)	NS		G.5 (10 cm)	NS		G.5 (10 cm)	NS
	G.6 (12 cm)	1.2×10^{-6}		G.6 (12 cm)	NS		G.6 (12 cm)	NS
	G.7 (14 cm)	1.8×10^{-13}		G.7 (14 cm)	0.008		G.7 (14 cm)	NS
	G.8 (16 cm)	1.5×10^{-21}		G.8 (16 cm)	7.8×10^{-4}		G.8 (16 cm)	NS
	G.9 (18 cm)	3.5×10^{-32}		G.9 (18 cm)	3.0×10^{-13}		G.9 (18 cm)	NS
G.4 (8 cm)	G.5 (10 cm)	NS	G.4 (8 cm)	G.5 (10 cm)	NS	G.4 (8 cm)	G.5 (10 cm)	NS
	G.6 (12 cm)	0.001		G.6 (12 cm)	NS		G.6 (12 cm)	NS
	G.7 (14 cm)	5.1×10^{-10}		G.7 (14 cm)	0.0001		G.7 (14 cm)	NS
	G.8 (16 cm)	1.6×10^{-18}		G.8 (16 cm)	9.0×10^{-5}		G.8 (16 cm)	NS
	G.9 (18 cm)	7.5×10^{-30}		G.9 (18 cm)	2.4×10^{-14}		G.9 (18 cm)	NS
G.5 (10 cm)	G.6 (12 cm)	3.4×10^{-5}	G.5 (10 cm)	G.6 (12 cm)	NS	G.5 (10 cm)	G.6 (12 cm)	NS
	G.7 (14 cm)	6.6×10^{-12}		G.7 (14 cm)	0.005		G.7 (14 cm)	NS
	G.8 (16 cm)	3.4×10^{-20}		G.8 (16 cm)	2.2×10^{-5}		G.8 (16 cm)	NS
	G.9 (18 cm)	3.9×10^{-31}		G.9 (18 cm)	5.4×10^{-15}		G.9 (18 cm)	NS
G.6 (12 cm)	G.7 (14 cm)	NS	G.6 (12 cm)	G.7 (14 cm)	NS	G.6 (12 cm)	G.7 (14 cm)	NS
	G.8 (16 cm)	1.5×10^{-9}		G.8 (16 cm)	NS		G.8 (16 cm)	NS
	G.9 (18 cm)	7.8×10^{-23}		G.9 (18 cm)	5.1×10^{-10}		G.9 (18 cm)	NS
G.7 (14 cm)	G.8 (16 cm)	0.003	G.7 (14 cm)	G.8 (16 cm)	NS	G.7 (14 cm)	G.8 (16 cm)	NS
	G.9 (18 cm)	9.6×10^{-17}		G.9 (18 cm)	1.2×10^{-6}		G.9 (18 cm)	NS
G.8 (16 cm)	G.9 (18 cm)	3.9×10^{-8}	G.8 (16 cm)	G.9 (18 cm)	4.6×10^{-4}	G.8 (16 cm)	G.9 (18 cm)	NS

Table A5 Statistical comparison between groups for each distance from heart (2 cm-18 cm) for G', G'' and tan (δ) on the adventitial face. NS is not significant at 0.05 level.

Adventi tial face	G' (kPa)	p- valu e	G'' (kPa)		p-value	tan (δ)		p- value
G.1 (2 cm)	G.2 (4 cm)	0.03	G.1 (2 cm)	G.2 (4 cm)	NS	G.1 (2 cm)	G.2 (4 cm)	NS
	G.3 (6 cm)	3.5x		G.3 (6 cm)	0.02		G.3 (6 cm)	NS
	G.4 (8 cm)	7.3x		G.4 (8 cm)	0.01		G.4 (8 cm)	NS
	G.5 (10 cm)	7.3x		G.5 (10 cm)	6.6×10^{-6}		G.5 (10 cm)	NS
	G.6 (12 cm)	4.9x		G.6 (12 cm)	1.8×10^{-7}		G.6 (12 cm)	2.8×10^{-7}
	G.7 (14 cm)	1.7x		G.7 (14 cm)	3.9×10^{-11}		G.7 (14 cm)	0.02
	G.8 (16 cm)	7.6x		G.8 (16 cm)	1.2×10^{-9}		G.8 (16 cm)	8.1×10^{-9}
	G.9 (18 cm)	13.3		G.9 (18 cm)	4.1×10^{-21}		G.9 (18 cm)	3.1×10^{-21}
G.2 (4 cm)	G.3 (6 cm)	NS	G.2 (4 cm)	G.3 (6 cm)	NS	G.2 (4 cm)	G.3 (6 cm)	NS
	G.4 (8 cm)	NS		G.4 (8 cm)	NS		G.4 (8 cm)	NS
	G.5 (10 cm)	0.04		G.5 (10 cm)	NS		G.5 (10 cm)	NS
	G.6 (12 cm)	1.1x		G.6 (12 cm)	0.04		G.6 (12 cm)	0.001
	G.7 (14 cm)	4.8x		G.7 (14 cm)	3.6×10^{-5}		G.7 (14 cm)	NS
	G.8 (16 cm)	3.4x		G.8 (16 cm)	8.0×10^{-4}		G.8 (16 cm)	3.5×10^{-4}
	G.9 (18 cm)	7.2x		G.9 (18 cm)	1.6×10^{-15}		G.9 (18 cm)	0.01
G.3 (6 cm)	G.4 (8 cm)	NS	G.3 (6 cm)	G.4 (8 cm)	NS	G.3 (6 cm)	G.4 (8 cm)	NS
	G.5 (10 cm)	NS		G.5 (10 cm)	NS		G.5 (10 cm)	NS
	G.6 (12 cm)	0.00		G.6 (12 cm)	NS		G.6 (12 cm)	NS
	G.7 (14 cm)	1.0x		G.7 (14 cm)	1.1×10^{-4}		G.7 (14 cm)	NS
	G.8 (16 cm)	7.8x		G.8 (16 cm)	0.002		G.8 (16 cm)	NS
	G.9 (18 cm)	1.0x		G.9 (18 cm)	5.2×10^{-15}		G.9 (18 cm)	NS
G.4 (8 cm)	G.5 (10 cm)	NS	G.4 (8 cm)	G.5 (10 cm)	NS	G.4 (8 cm)	G.5 (10 cm)	NS
	G.6 (12 cm)	NS		G.6 (12 cm)	NS		G.6 (12 cm)	NS
	G.7 (14 cm)	5.1x		G.7 (14 cm)	2.8×10^{-4}		G.7 (14 cm)	NS
	G.8 (16 cm)	4.3x		G.8 (16 cm)	0.005		G.8 (16 cm)	NS
	G.9 (18 cm)	5.1x		G.9 (18 cm)	1.5×10^{-14}		G.9 (18 cm)	NS
G.5 (10 cm)	G.6 (12 cm)	NS	G.5 (10 cm)	G.6 (12 cm)	NS	G.5 (10 cm)	G.6 (12 cm)	NS
	G.7 (14 cm)	0.02		G.7 (14 cm)	NS		G.7 (14 cm)	NS
	G.8 (16 cm)	0.00		G.8 (16 cm)	NS		G.8 (16 cm)	NS
	G.9 (18 cm)	5.0x		G.9 (18 cm)	6.6×10^{-11}		G.9 (18 cm)	NS
G.6 (12 cm)	G.7 (14 cm)	NS	G.6 (12 cm)	G.7 (14 cm)	NS	G.6 (12 cm)	G.7 (14 cm)	NS
	G.8 (16 cm)	NS		G.8 (16 cm)	NS		G.8 (16 cm)	NS
	G.9 (18 cm)	6.8x		G.9 (18 cm)	2.7×10^{-9}		G.9 (18 cm)	NS
G.7 (14 cm)	G.8 (16 cm)	NS	G.7 (14 cm)	G.8 (16 cm)	NS	G.7 (14 cm)	G.8 (16 cm)	NS
	G.9 (18 cm)	2.0x		G.9 (18 cm)	1.0×10^{-5}		G.9 (18 cm)	NS
G.8 (16 cm)	G.9 (18 cm)	2.8x	G.8 (16 cm)	G.9 (18 cm)	3.8×10^{-7}	G.8 (16 cm)	G.9 (18 cm)	NS

Table A6 Statistical comparison within groups for each distance from heart (2 cm-18 cm) for collagen, GAG and elastin, for each animal. NS is not significant at 0.05 level.

	Collagen		p-	GAG		p-	Elastin		p-
	(µg/mg)		value	(µg/mg)		value	(µg/mg)		value
Group 1									
(2 cm)	Ovine 1	Ovine2	NS	Ovine 1	Ovine2	NS	Ovine 1	Ovine2	NS
	Ovine 1	Ovine3	NS	Ovine 1	Ovine3	NS	Ovine 1	Ovine3	NS
	Ovine 2	Ovine 3	NS	Ovine 2	Ovine 3	NS	Ovine 2	Ovine 3	NS
Group 2									
(4 cm)	Ovine 1	Ovine2	NS	Ovine 1	Ovine2	NS	Ovine 1	Ovine2	NS
	Ovine 1	Ovine3	NS	Ovine 1	Ovine3	NS	Ovine 1	Ovine3	NS
	Ovine 2	Ovine 3	NS	Ovine 2	Ovine 3	NS	Ovine 2	Ovine 3	NS
Group 3									
(6 cm)	Ovine 1	Ovine2	NS	Ovine 1	Ovine2	0.04	Ovine 1	Ovine2	NS
	Ovine 1	Ovine3	NS	Ovine 1	Ovine3	NS	Ovine 1	Ovine3	NS
	Ovine 2	Ovine 3	NS	Ovine 2	Ovine 3	NS	Ovine 2	Ovine 3	NS
Group 4									
(8 cm)	Ovine 1	Ovine2	NS	Ovine 1	Ovine2	NS	Ovine 1	Ovine2	NS
	Ovine 1	Ovine3	NS	Ovine 1	Ovine3	NS	Ovine 1	Ovine3	NS
	Ovine 2	Ovine 3	NS	Ovine 2	Ovine 3	NS	Ovine 2	Ovine 3	NS
Group 5									
(10 cm)	Ovine 1	Ovine2	NS	Ovine 1	Ovine2	0.04	Ovine 1	Ovine2	NS
	Ovine 1	Ovine3	NS	Ovine 1	Ovine3	NS	Ovine 1	Ovine3	NS
	Ovine 2	Ovine 3	NS	Ovine 2	Ovine 3	NS	Ovine 2	Ovine 3	NS
Group 6									
(12 cm)	Ovine 1	Ovine2	NS	Ovine 1	Ovine2	NS	Ovine 1	Ovine2	NS
	Ovine 1	Ovine3	NS	Ovine 1	Ovine3	NS	Ovine 1	Ovine3	NS
	Ovine 2	Ovine 3	NS	Ovine 2	Ovine 3	NS	Ovine 2	Ovine 3	NS
Group 7									
14 cm	Ovine 1	Ovine2	0.027	Ovine 1	Ovine2	NS	Ovine 1	Ovine2	NS
	Ovine 1	Ovine3	NS	Ovine 1	Ovine3	NS	Ovine 1	Ovine3	NS
	Ovine 2	Ovine 3	0.022	Ovine 2	Ovine 3	NS	Ovine 2	Ovine 3	0.025
Group 8									
(16 cm)	Ovine 1	Ovine2	NS	Ovine 1	Ovine2	NS	Ovine 1	Ovine2	NS
	Ovine 1	Ovine3	NS	Ovine 1	Ovine3	NS	Ovine 1	Ovine3	NS
	Ovine 2	Ovine 3	NS	Ovine 2	Ovine 3	NS	Ovine 2	Ovine 3	NS
Group 9									
(18 cm)	Ovine 1	Ovine2	0.004	Ovine 1	Ovine2	NS	Ovine 1	Ovine2	NS
	Ovine 1	Ovine3	NS	Ovine 1	Ovine3	NS	Ovine 1	Ovine3	NS
	Ovine 2	Ovine 3	0.002	Ovine 2	Ovine 3	NS	Ovine 2	Ovine 3	NS

Table A7 Statistical comparison between groups for each distance from heart (2 cm-18 cm) for collagen, GAG and Elastin. NS is not significant at 0.05 level.

G'		p-	G''		p-	tan (δ)		p-
(kPa)		value	(kPa)		value			value
G.1 (2 cm)	G.2 (4 cm)	NS	G.1 (2 cm)	G.2 (4 cm)	NS	G.1 (2 cm)	G.2 (4 cm)	NS
	G.3 (6 cm)	NS		G.3 (6 cm)	NS		G.3 (6 cm)	NS
	G.4 (8 cm)	NS		G.4 (8 cm)	NS		G.4 (8 cm)	NS
	G.5 (10 cm)	NS		G.5 (10 cm)	NS		G.5 (10 cm)	NS
	G.6 (12 cm)	NS		G.6 (12 cm)	NS		G.6 (12 cm)	NS
	G.7 (14 cm)	NS		G.7 (14 cm)	NS		G.7 (14 cm)	NS
	G.8 (16 cm)	NS		G.8 (16 cm)	NS		G.8 (16 cm)	NS
	G.9 (18 cm)	NS		G.9 (18 cm)	NS		G.9 (18 cm)	NS
G.2 (4 cm)	G.3 (6 cm)	NS	G.2 (4 cm)	G.3 (6 cm)	NS	G.2 (4 cm)	G.3 (6 cm)	NS
	G.4 (8 cm)	NS		G.4 (8 cm)	NS		G.4 (8 cm)	NS
	G.5 (10 cm)	NS		G.5 (10 cm)	NS		G.5 (10 cm)	NS
	G.6 (12 cm)	NS		G.6 (12 cm)	NS		G.6 (12 cm)	NS
	G.7 (14 cm)	NS		G.7 (14 cm)	NS		G.7 (14 cm)	NS
	G.8 (16 cm)	NS		G.8 (16 cm)	NS		G.8 (16 cm)	NS
G.3 (6 cm)	G.4 (8 cm)	NS	G.3 (6 cm)	G.4 (8 cm)	NS	G.3 (6 cm)	G.4 (8 cm)	NS
	G.5 (10 cm)	NS		G.5 (10 cm)	NS		G.5 (10 cm)	NS
	G.6 (12 cm)	NS		G.6 (12 cm)	NS		G.6 (12 cm)	NS
	G.7 (14 cm)	NS		G.7 (14 cm)	NS		G.7 (14 cm)	NS
	G.8 (16 cm)	NS		G.8 (16 cm)	NS		G.8 (16 cm)	NS
G.4 (8 cm)	G.5 (10 cm)	NS	G.4 (8 cm)	G.5 (10 cm)	NS	G.4 (8 cm)	G.5 (10 cm)	NS
	G.6 (12 cm)	NS		G.6 (12 cm)	NS		G.6 (12 cm)	NS
	G.7 (14 cm)	NS		G.7 (14 cm)	NS		G.7 (14 cm)	NS
	G.8 (16 cm)	NS		G.8 (16 cm)	NS		G.8 (16 cm)	NS
G.5 (10 cm)	G.6 (12 cm)	NS	G.5 (10 cm)	G.6 (12 cm)	NS	G.5 (10 cm)	G.6 (12 cm)	NS
	G.7 (14 cm)	NS		G.7 (14 cm)	NS		G.7 (14 cm)	NS
	G.8 (16 cm)	NS		G.8 (16 cm)	NS		G.8 (16 cm)	NS
G.6 (12 cm)	G.7 (14 cm)	NS	G.6 (12 cm)	G.7 (14 cm)	NS	G.6 (12 cm)	G.7 (14 cm)	NS
	G.8 (16 cm)	NS		G.8 (16 cm)	NS		G.8 (16 cm)	NS
G.7 (14 cm)	G.8 (16 cm)	NS	G.7 (14 cm)	G.8 (16 cm)	NS	G.7 (14 cm)	G.8 (16 cm)	NS
	G.9 (18 cm)	NS		G.9 (18 cm)	NS		G.9 (18 cm)	NS
G.8 (16 cm)	G.9 (18 cm)	NS	G.8 (16 cm)	G.9 (18 cm)	NS	G.8 (16 cm)	G.9 (18 cm)	NS

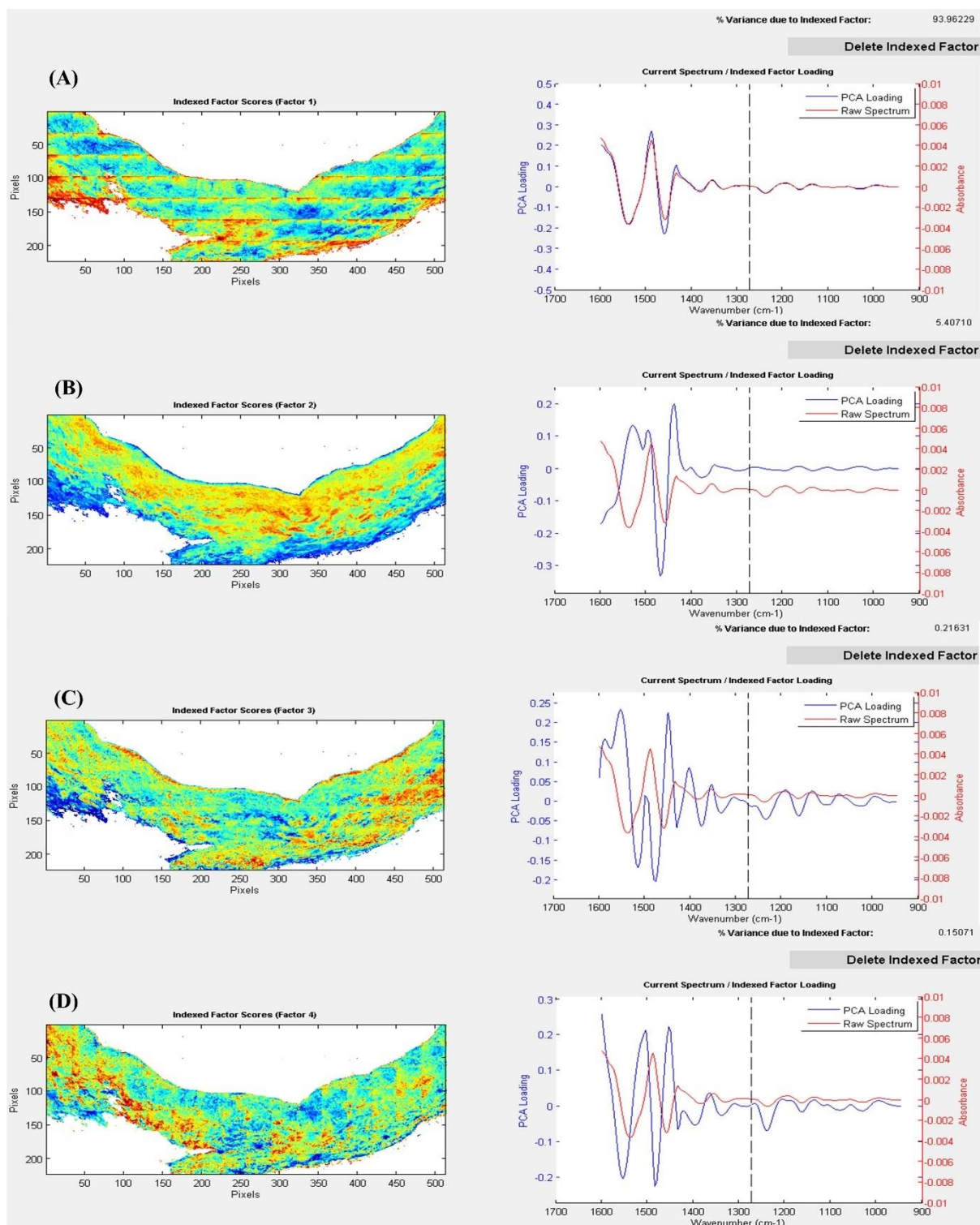


Figure A1 Details of all MCR-ALS results derived from the spectral regions 950–1600 cm⁻¹ and the % variance PCA for overview tissue. (A-D) presented modelled factor 1 to 4, respectively.

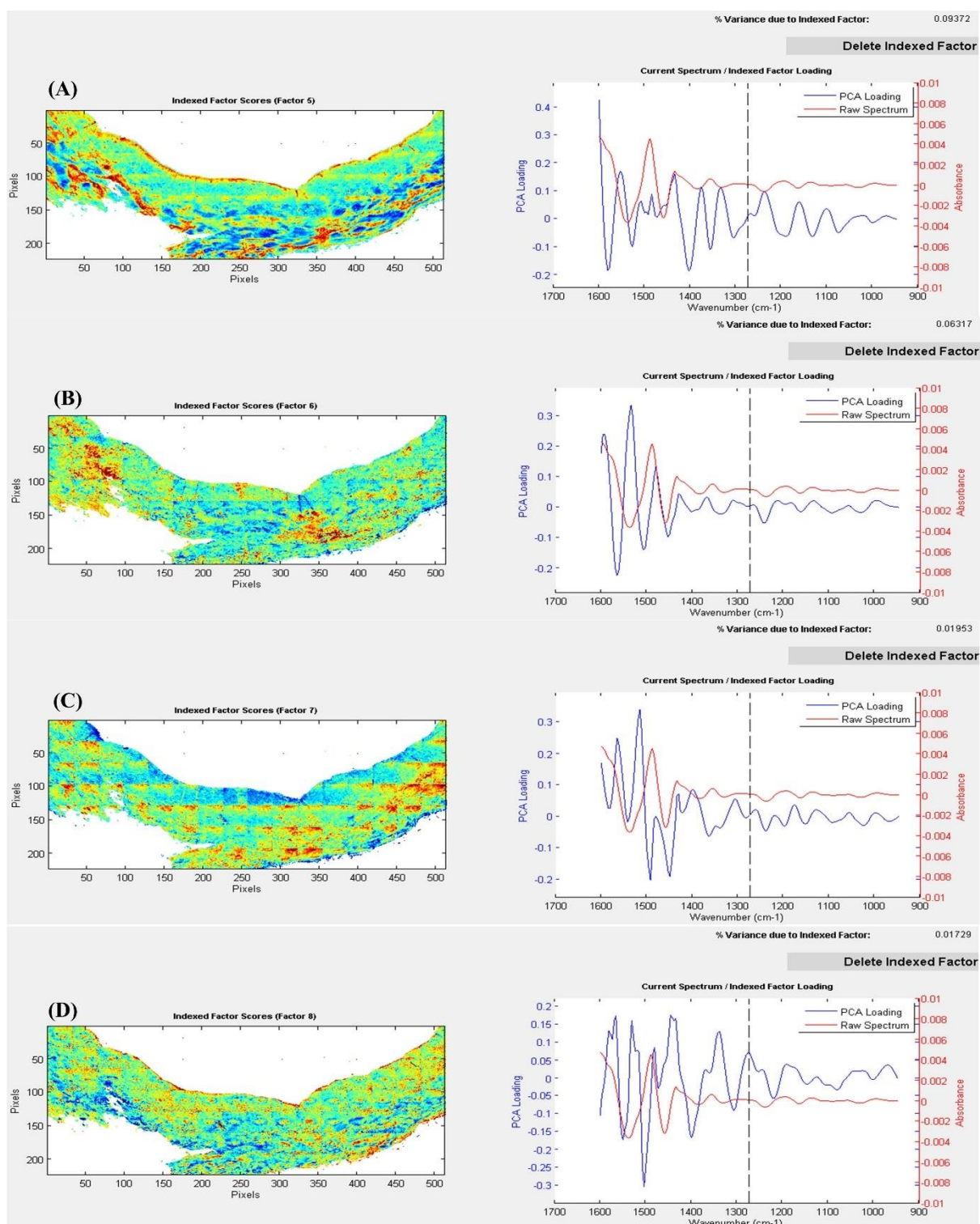


Figure A2 Details of all MCR-ALS results derived from the spectral regions 950–1600 cm⁻¹ and the % variance PCA for overview tissue. (A-D) presented modelled factor 5 to 8, respectively.

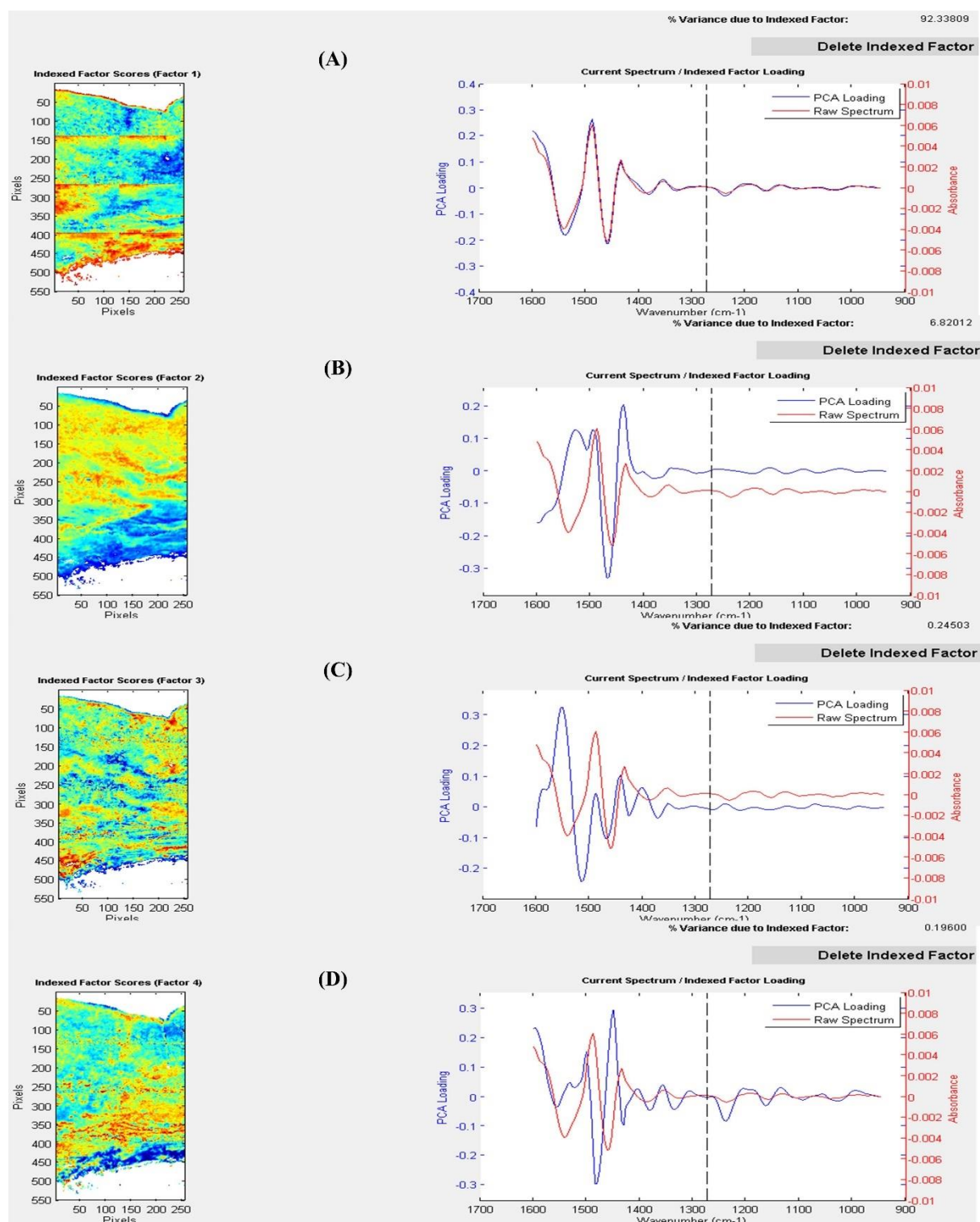


Figure A3 Details of all MCR-ALS results derived from the spectral regions 950–1600 cm⁻¹ and the % variance PCA for the transverse tissue. (A-D) presented modelled factor 1 to 4, respectively.

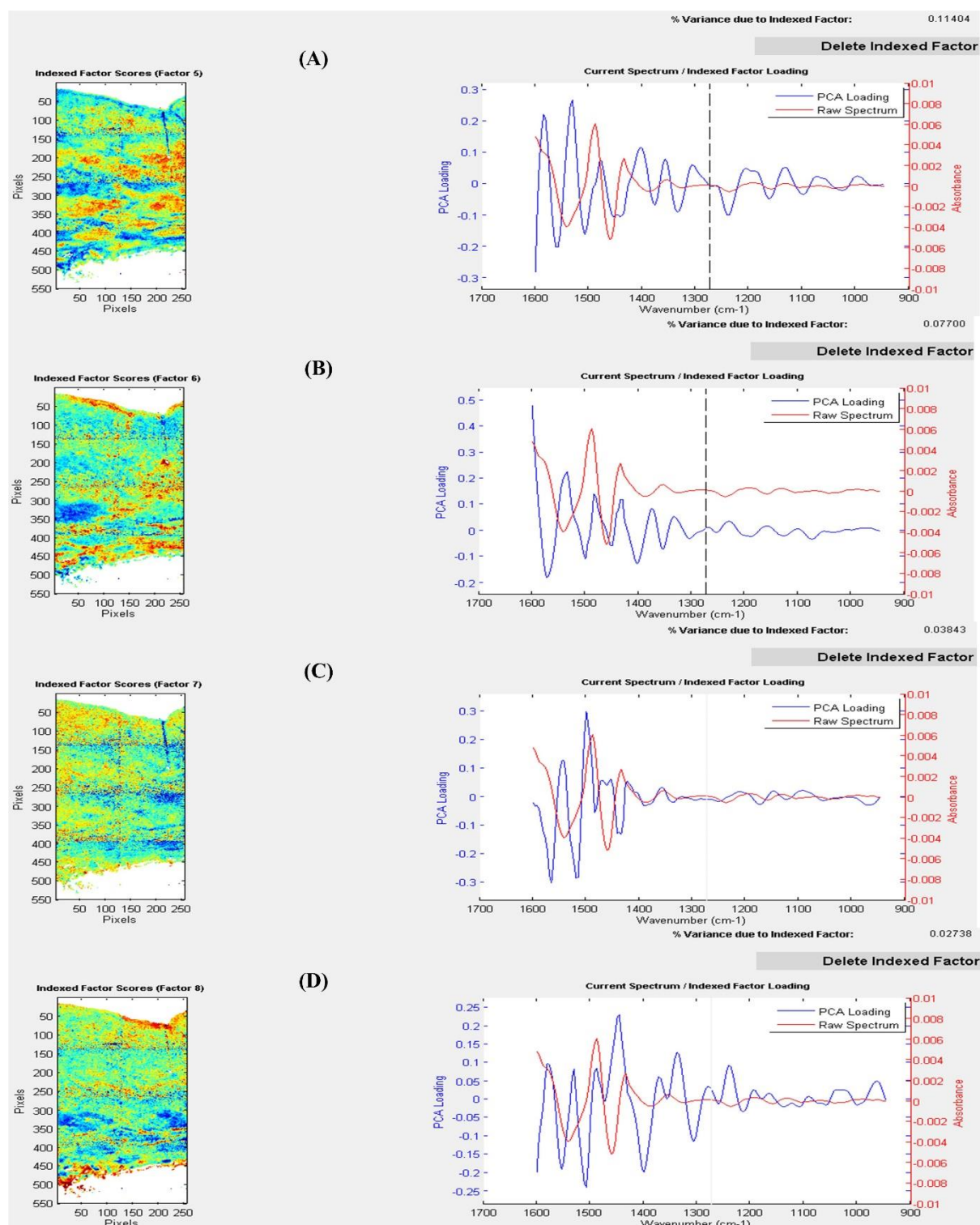


Figure A4 Details of all MCR-ALS results derived from the spectral regions 950–1600 cm⁻¹ and the % variance PCA for the transverse tissue. (A-D) presented modelled factor 5 to 8, respectively.

Appendix B

Table B1 The representative factor index after MCR-ALS analysis in the spectral region 950-1600 cm⁻¹ for the overview FTIR imaging data sets of patient 05-00064-18.

No. of factors used for model	Factor index after MCR	Component
4	F1	Reflective artefacts (gradual change in surface structure or reflective index change)
4	F2	Elastin
4	F3	Instrumental artefact (e.g. different illumination across the field of view)
4	F4	Collagen

Table B2 The representative factor index after MCR-ALS analysis in the spectral region 950-1600 cm⁻¹ for the overview FTIR imaging data sets of patient 05-00017-19.

No. of factors used for model	Factor index after MCR	Component
4	F1	Reflective artefacts (gradual change in surface structure or reflective index change)
4	F2	Instrumental artefact (e.g. different illumination across the field of view)
4	F3	Collagen
4	F4	Elastin

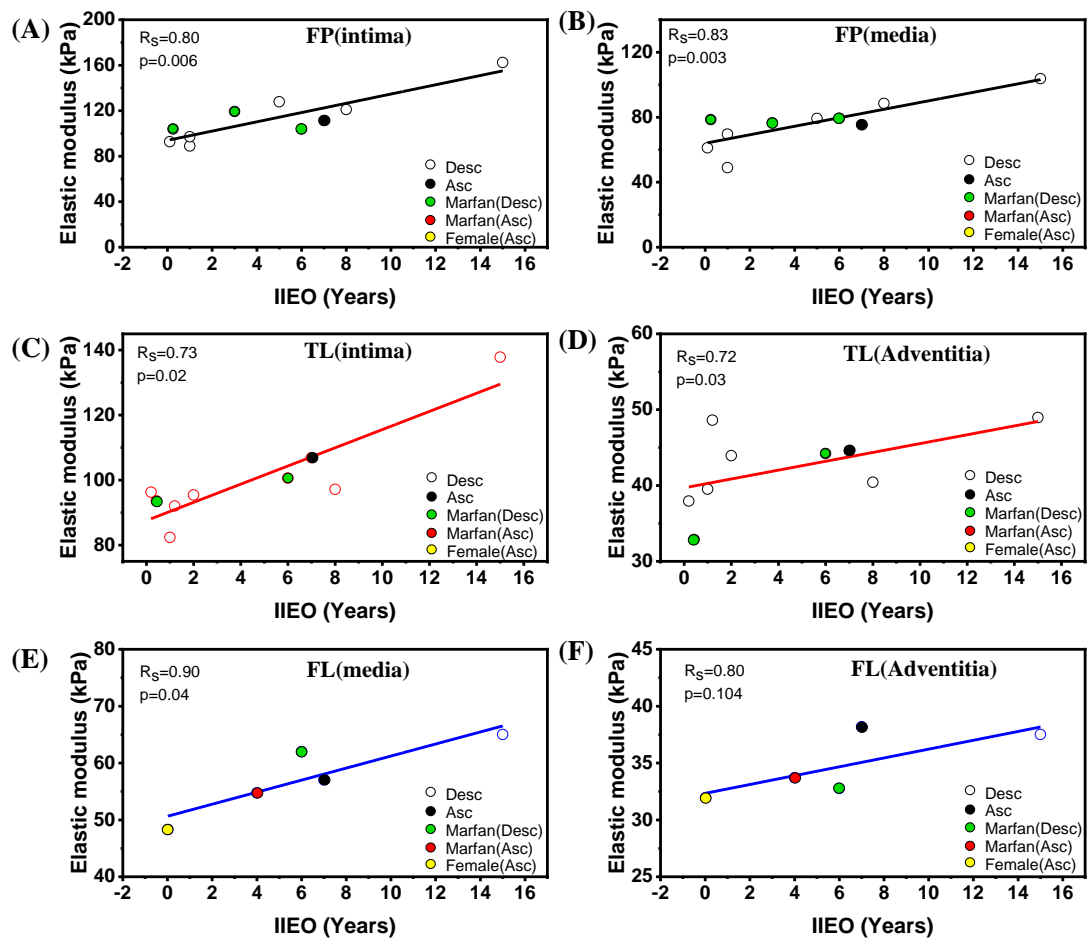


Figure B1 The correlation between elastic modulus for both sides of each chronic AD tissue type: FP (n=10 samples), TL (n=6 samples) and FL (n=5 samples) obtained from nanoindentation technique with IIEO. A, B correlation of IIEO with intimal and media surface for FP. C, D correlation of IIEO with intimal and adventitial surface for TL. E, F correlation of IIEO with medial and adventitial surface for FL(Spearman correlation coefficient, R_s).

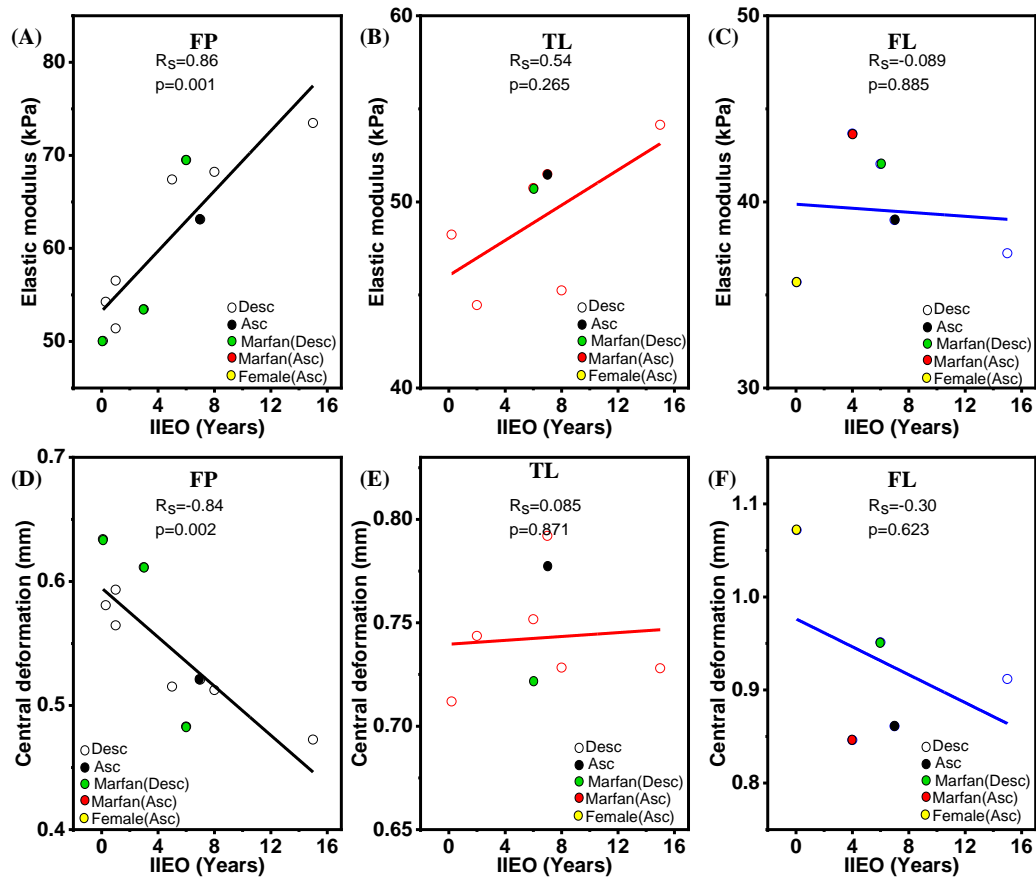


Figure B2 The correlation between elastic modulus and central deformation with interval of index event to operation (IIEO) for FP (n=10 samples), TL (n=6 samples) and FL (n=5 samples) are shown A-C and D-F, respectively (Spearman product-moment correlation coefficients: R_s).

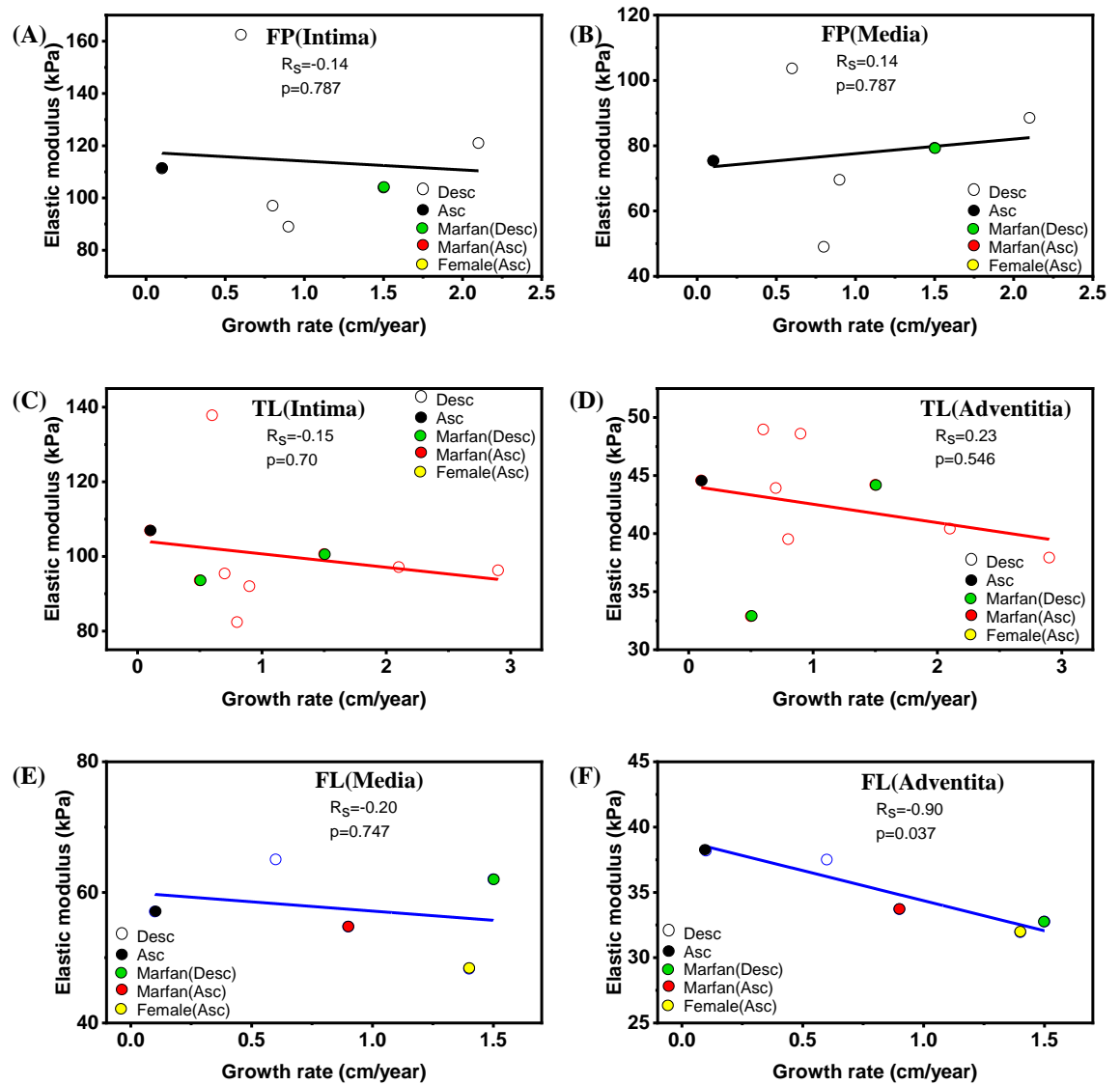


Figure B3 The correlation between local elastic modulus using nanoindentation technique and growth rate for FP (A, B) intimal and medial face, TL (C, D) intimal and adventitial face and (E, F) medial and adventitial face for FL.

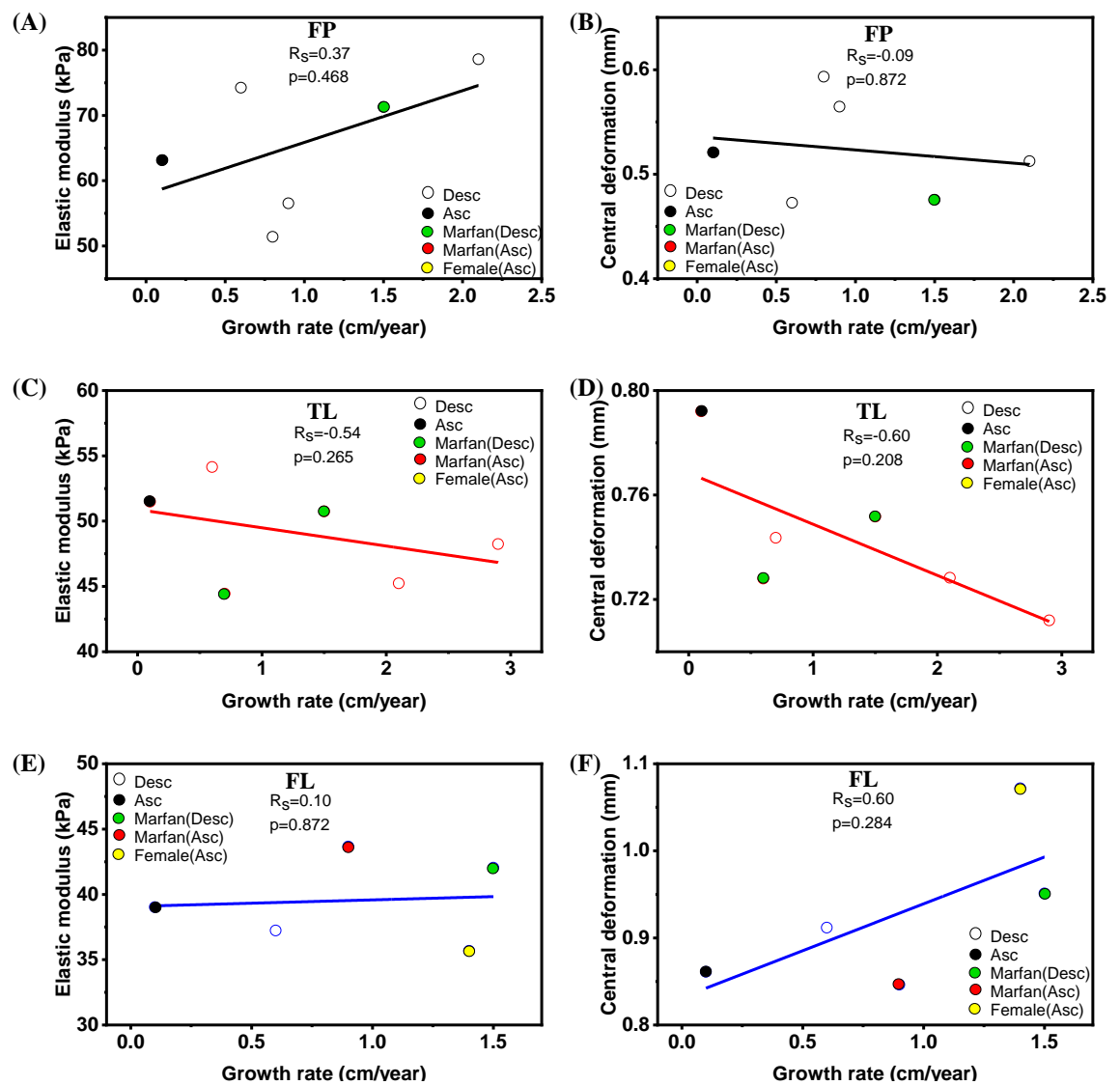


Figure B4 The correlation between elastic modulus and central deformation using ball indentation with growth rate: (A, B) for FP, (C, D) for TL and (E, F) for FL.

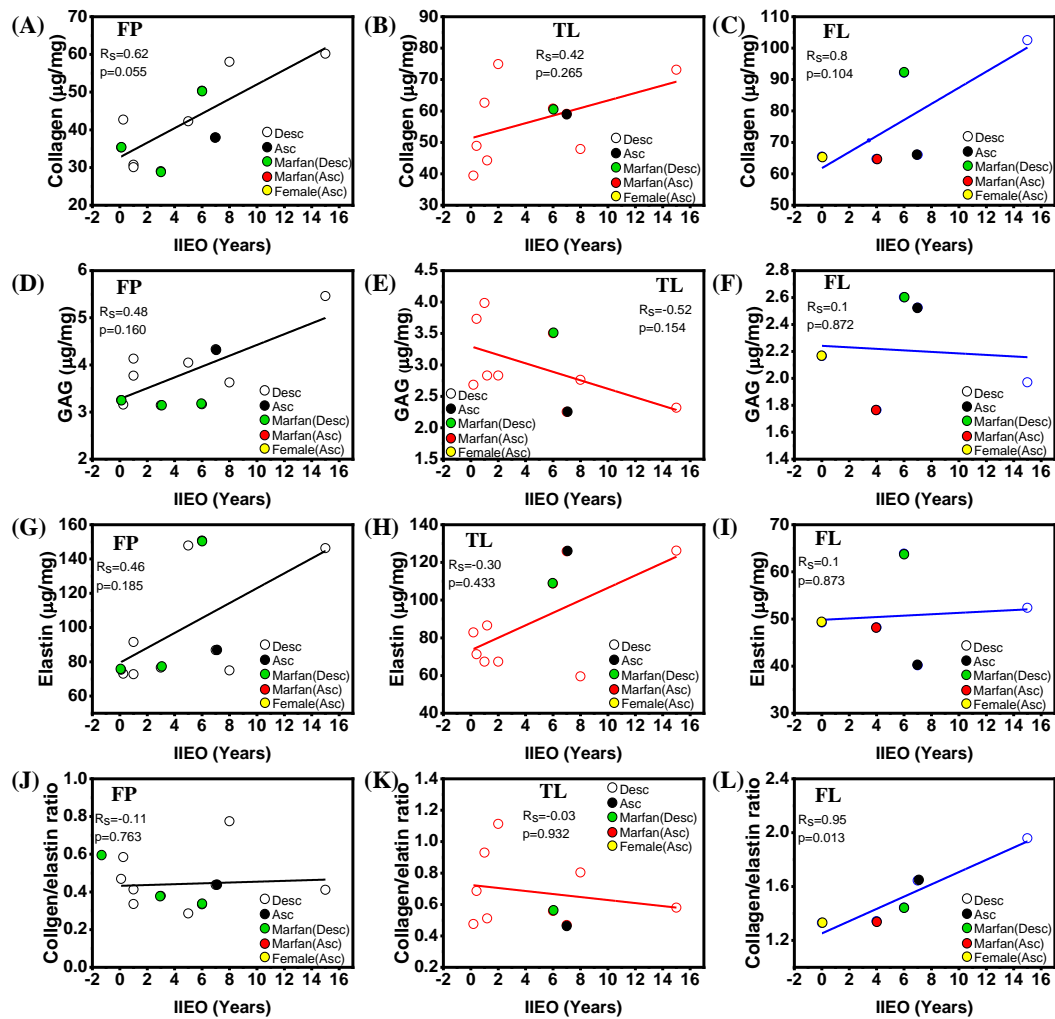


Figure B5 The correlation between biochemical data with IIEO for FP, TL and FL: (A-C) collagen, (D-F) GAG, (G-I) elastin and (J-L) collagen/elastic ratio.

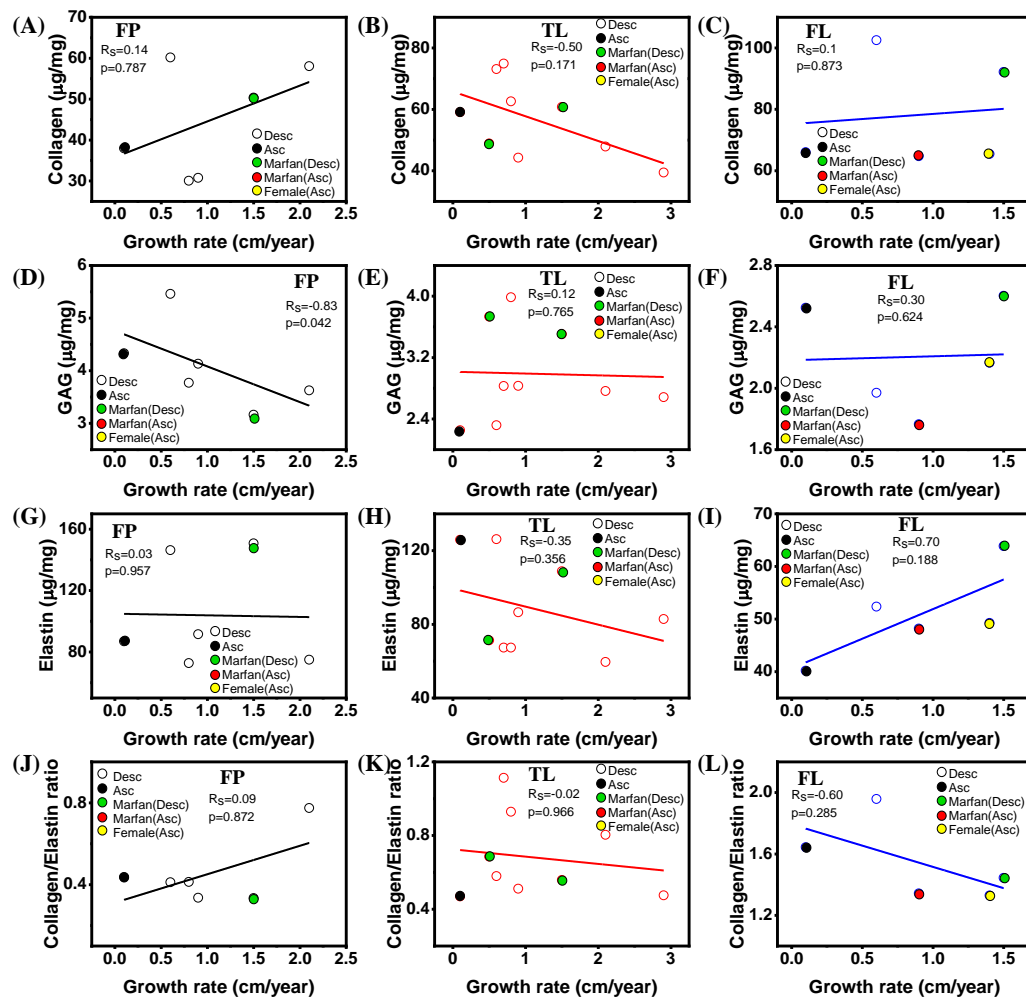


Figure B6 The correlation between biochemical data with the growth rate for FP, TL and FL: (A-C) collagen, (D-F) GAG, (G-I) elastin and (J-L) collagen/elastin ratio.